VALORISATION OF BIOMASS COMBUSTION ASH IN PREPARATION AND APPLICATION OF ACTIVATED CARBON FOR CO_2 ADSORPTION

A thesis submitted for the degree of

Doctor of Philosophy

by

Mikhail Gorbounov

Department of Chemical Engineering
Brunel University London

London, UK

November 2023

Abstract

Carbon capture and storage is a proposed pathway for mitigation of CO_2 emissions, suggesting bioenergy with carbon capture and storage to be a net-negative power generation technology. Combustion of sustainable biomass produces a waste residue, biomass combustion bottom ash, that is commonly landfilled. However, valorisation of biomass combustion bottom ash to prepare solid carbonaceous adsorbents can address the issues of both waste management as well as CO_2 emissions simultaneously. Therefore, in this thesis, extraction, activation (both physical and chemical) of BA-derived carbon followed by pelletisation and chemical modification of the adsorbents (accompanied by extensive characterisation of the different samples) have been investigated. These campaigns were conducted using appropriate design of experiments techniques to elucidate the main effects and any potential interactions of the plethora of studied parameters. It was found that chemical activation facilitated a nearly four-fold increase in CO_2 uptake (1.29 mmol/g at 1 bar and 50 °C) compared to the virgin extracted carbon (0.34 mmol/g), whilst physical activation allowed the uptake to double (0.69 mmol/g). However, the physically activated sample presented a high working capacity (96%) in addition to other promising (e.g. environmental, monetary) features. Therefore, it was selected for chemical modification and pelletisation studies. The conducted modification facilitated a ~35% increase in adsorption capacity, whilst investigation of different pelletisation routes revealed crucial differences between the approaches. For instance, the pelletised-then-activated (P-A) sample adsorbed 40% more CO_2 than its activated-then-pelletised counterpart. The latter pellet presented a crush strength of 0.794 N/mm, whilst the P-A carbon had inferior mechanical properties (below measurement threshold). As such, this thesis concludes valorisation of BA *via* extraction and preparation of carbonaceous sorbents to be feasible. Future work may now focus on development of the pelletisation technique (with industrial-grade equipment) as well as investigations of sorption properties from a synthetic flue gas stream.

Peer-Reviewed Journal Publications

1. **Mikhail Gorbounov**, Ben Petrovic, Serap Ozmen, Peter Clough, Salman Masoudi Soltani. Activated carbon derived from Biomass combustion bottom ash as solid sorbent for CO_2 adsorption. *Chemical Engineering Research and Design*. 2023; Vol. 194, June 2023, pp. 325–343. DOI: 10.1016/j.cherd.2023.04.057.

MG (first/lead Author): Writing (Original Draft & Editing), Methodology, Investigation, Data Analysis, Material Characterisation; **BP (2nd/contributing author)**: Methodology, Investigation, Data Analysis, Material Characterisation; **SO (3rd/contributing author)** Material Characterisation; **PC (4th/contributing author)** Resources, Material Characterisation; **SMS (corresponding author)**: Supervision, Funding Acquisition, Writing (Review & Editing), Resources, Conceptualisation, Project Administration.

2. **Mikhail Gorbounov**, Emilie Diaz-Vasseur, David Danaci, Salman Masoudi Soltani. Chemical Activation of Porous Carbon Extracted from Biomass Combustion Bottom Ash for CO2 Adsorption. *Carbon Capture Science and Technology*. 2023; Vol. 10, March 2024: 100151. DOI: 10.1016/j.ccst.2023.100151

MG (first/lead Author): Writing (Original Draft & Editing), Methodology, Investigation, Data Analysis, Material Characterisation; **EDV (2nd/contributing author)**: Writing (Original Draft), Investigation, Data Analysis, Material Characterisation; **DD (3rd/contributing author)** Writing (Review & Editing), Material Characterisation; **SMS (corresponding author)**: Supervision, Funding Acquisition, Writing (Review & Editing), Resources, Conceptualisation, Project Administration.

3. **Mikhail Gorbounov**, Jessica Taylor, Ben Petrovic, Salman Masoudi Soltani. To DoE or not to DoE? A Technical Review on & Roadmap for Optimisation of Carbonaceous Adsorbents and Adsorption Processes. *South African Journal of Chemical Engineering.* 2022; Vol. 41, July 2022, pp. 111–28. DOI: 10.1016/j.sajce.2022.06.001

MG (first/lead Author): Writing (Original Draft & Editing); **JT (2nd/contributing author):** Writing (Original Draft & Editing); **BP (3rd/contributing author):** Writing (Original Draft & Editing); **SMS (corresponding author)**: Supervision, Funding Acquisition, Writing (Review & Editing), Resources, Conceptualisation, Project Administration.

4. Ben Petrovic, **Mikhail Gorbounov**, Salman Masoudi Soltani. Influence of surface modification on selective CO_2 adsorption: A technical review on mechanisms and methods. *Microporous and Mesoporous Materials.* 2021; Vol. 312, January 2021:110751. DOI: 10.1016/j.micromeso.2020.110751

BP (first/lead Author): Writing (Original Draft & Editing); **MG (2nd/contributing author):** Writing (Original Draft & Editing); **SMS (corresponding author)**: Supervision, Funding Acquisition, Writing (Review & Editing), Resources, Conceptualisation, Project Administration.

5. Ben Petrovic, **Mikhail Gorbounov**, Salman Masoudi Soltani. Impact of Surface Functional Groups and Their Introduction Methods on the Mechanisms of CO_2 Adsorption on Porous Carbonaceous Adsorbents. *Carbon Capture Science and Technology.* 2022; Vol. 3, June 2022:100045. DOI: 10.1016/j.ccst.2022.100045

BP (first/lead Author): Writing (Original Draft & Editing); **MG (2nd/contributing author):** Writing (Original Draft & Editing); **SMS (corresponding author)**: Supervision, Funding Acquisition, Writing (Review & Editing), Resources, Conceptualisation, Project Administration.

6. Mohammad Reza Ketabchi, Shervan Babamohammadi, William George Davies, **Mikhail Gorbounov**, Salman Masoudi Soltani. Latest advances and challenges in carbon capture using bio-based sorbents: A state-of-the-art review. *Carbon Capture Science and Technology*. 2023; Vol. 6, March 2023:100087. DOI: 10.1016/j.ccst.2022.100087

MRK (first/lead Author): Writing (Original Draft & Editing); **SB (2nd/contributing author)**: Writing (Original Draft & Editing); **WGD (3rd/contributing author)** Writing (Original Draft & Editing); **MG (4th/contributing author):** Writing (Review & Editing); **SMS (corresponding author)**: Supervision, Funding Acquisition, Writing (Review & Editing), Resources, Conceptualisation, Project Administration.

7. Salman Masoudi Soltani, Abhishek Lahiri, Husain Bahzad, Peter Clough, **Mikhail Gorbounov** and Yongliang Yan. Sorption-enhanced Steam Methane Reforming for Combined CO2 Capture and Hydrogen Production: A State-of-the-Art Review. *Carbon Capture Science and Technology*. 2021; Vol. 1, December 2021:100003. DOI: 10.1016/j.ccst.2021.100003

SMS (first/lead/corresponding Author): Writing (Original Draft, Review & Editing) Supervision, Funding Acquisition, Resources, Conceptualisation, Project Administration; **AL (2nd/contributing author)**: Writing (Original Draft & Editing); **HB (3rd/contributing author)** Writing (Original Draft & Editing); **PC (4th/contributing author):** Writing (Original Draft & Editing); **MG (5th/contributing author):** Writing (Original Draft & Editing); **YY (6th/contributing author)**: Writing (Original Draft & Editing).

Peer-Reviewed Full Conference Proceedings

1. **Mikhail Gorbounov**, Ben Petrovic, Abhishek Lahiri, Salman Masoudi Soltani. Application of Nanoporous Carbon, Extracted from Biomass Combustion Ash, in CO_2 Adsorption. 2021. In: 2021 IEEE 21st International Conference on Nanotechnology (NANO). IEEE; 2021. p. 229-232. DOI: 10.1109/NANO51122.2021.9514288

MG (first/lead Author): Writing (Original Draft & Editing), Methodology, Investigation, Data Analysis, Material Characterisation; **BP (2nd/contributing author)**: Methodology, Investigation, Data Analysis, Material Characterisation; **AL (3rd/contributing author)** Material Characterisation; **SMS (corresponding author)**: Supervision, Funding Acquisition, Writing (Review & Editing), Resources, Conceptualisation, Project Administration.

2. **Mikhail Gorbounov**, Ben Petrovic, Serap Ozmen, Peter Clough, Dilyara Bekmuratova, Salman Masoudi Soltani. Development of Nanoporosity on a Biomass Combustion Ash-derived Carbon for CO_2 Adsorption. In: 2022 IEEE 22nd International Conference on Nanotechnology (NANO). IEEE; 2022. p. 245–248. DOI: 10.1109/NANO54668.2022.9928660

MG (first/lead Author): Writing (Original Draft & Editing), Methodology, Investigation, Data Analysis, Material Characterisation; **BP (2nd/contributing author)**: Methodology, Investigation, Data Analysis, Material Characterisation; **SO (3rd/contributing author)** Material Characterisation; **PC (4th/contributing author)** Resources, Material Characterisation; **DB (5th/contributing author)** Investigation; **SMS (corresponding author)**: Supervision, Funding Acquisition, Writing (Review & Editing), Resources, Conceptualisation, Project Administration.

3. **Mikhail Gorbounov**, Emilie Diaz-Vasseur, Rafal Panek, Salman Masoudi Soltani. Impact of Production Pathway on Nanoporosity of Carbonaceous Sorbents for CO_2 Adsorption. In: 2023 IEEE 23rd International Conference on Nanotechnology (NANO). IEEE; 2023. p. 249–254. DOI: 10.1109/NANO58406.2023.10231299

MG (first/lead Author): Writing (Original Draft & Editing), Methodology, Investigation, Data Analysis, Material Characterisation; **EDV (2nd/contributing author)**: Writing (Original Draft), Investigation, Data Analysis, Material Characterisation; **RP (3rd/contributing author)** Material Characterisation; **SMS (corresponding author)**: Supervision, Funding Acquisition, Writing (Review & Editing), Resources, Conceptualisation, Project Administration.

4. Ben Petrovic, **Mikhail Gorbounov**, Abhishek Lahiri, Salman Masoudi Soltani. Biomass Combustion Fly Ash-Derived Nanoporous Zeolites for Post-Combustion Carbon

Capture. 2021. In: 2021 IEEE 21st International Conference on Nanotechnology (NANO). IEEE; 2021. p. 233–236. DOI: 10.1109/NANO51122.2021.9514342

BP (first/lead Author): Writing (Original Draft & Editing), Methodology, Investigation, Data Analysis, Material Characterisation; **MG (2nd/contributing author)**: Methodology, Investigation, Data Analysis, Material Characterisation; **AL (3rd/contributing author)** Material Characterisation; **SMS (corresponding author)**: Supervision, Funding Acquisition, Writing (Review & Editing), Resources, Conceptualisation, Project Administration.

5. Ben Petrovic, **Mikhail Gorbounov** Serap Ozmen, Peter Clough, Salman Masoudi Soltani. Synthesis of Nanoporous Type A and X Zeolite Mixtures from Biomass Combustion Fly Ash for Post-Combustion Carbon Capture. In: 2022 IEEE 22nd International Conference on Nanotechnology (NANO). IEEE; 2022; p. 221–224. DOI: 10.1109/NANO54668.2022.9928679

BP (first/lead Author): Writing (Original Draft & Editing), Methodology, Investigation, Data Analysis, Material Characterisation; **MG (2nd/contributing author)**: Methodology, Investigation, Data Analysis, Material Characterisation; **SO (3rd/contributing author)** Material Characterisation; **PC (4th/contributing author)** Resources, Material Characterisation; **SMS (corresponding author)**: Supervision, Funding Acquisition, Writing (Review & Editing), Resources, Conceptualisation, Project Administration.

Oral Presentations at International Conferences

1. **Mikhail Gorbounov**, Ben Petrovic, Salman Masoudi Soltani. Biomass Combustion Ash in CO_2 Capture. UKCCSRC Spring 2021 Conference, 20-21 April 2021, Sheffield, UK.

2. **Mikhail Gorbounov**, Ben Petrovic, Abhishek Lahiri, Salman Masoudi Soltani. Application of Nanoporous Carbon, Extracted from Biomass Combustion Ash, in CO_2 Adsorption. 21st IEEE International Conference on Nanotechnology, 28-30 July 2021, online

3. **Mikhail Gorbounov**, Ben Petrovic, Serap Ozmen, Peter Clough, Dilyara Bekmuratova, Salman Masoudi Soltani. Development of Nanoporosity on a Biomass Combustion Ash-derived Carbon for CO_2 Adsorption. 22nd IEEE International Conference on Nanotechnology, 4-8 July 2022, Mallorca, Spain.

4. **Mikhail Gorbounov**, Ben Petrovic, Salman Masoudi Soltani. Cost effective waste-derived adsorbents for post-combustion carbon capture. International Conference on Carbon Capture Science and Technology 2022 (CCST2022), 21-23 July 2022, online.

5. **Mikhail Gorbounov**, Emilie Diaz-Vasseur, Rafal Panek, Salman Masoudi Soltani. Impact of Production Pathway on Nanoporosity of Carbonaceous Sorbents for CO_2 Adsorption. 23rd IEEE International Conference on Nanotechnology, 2-5 July 2023, Jeju, South Korea.

6. **Mikhail Gorbounov**, Emilie Diaz-Vasseur, Rafal Panek, Salman Masoudi Soltani. CO_2 Adsorbent Scale-up: from Powder to Pellet. International Conference on Carbon Capture Science and Technology 2023 (CCST2023), 21-23 July 2023, online.

7. **Mikhail Gorbounov**, Jessica Taylor, Ben Petrovic, Salman Masoudi Soltani. To DoE or not to DoE? A Roadmap for Improvement & Optimisation of Experimental Campaigns, 14th International Conference on Agrophysics 2023 (ICA 2023), 11-13 September 2023 Lublin, Poland.

Book Chapters

1. **Mikhail Gorbounov**, Valeriy Glebovich Larionov**. The impact of greenhouse gases on agriculture and carbon capture and storage as a way to avert disaster** in *"Global warming and its impact on the food security of Russia"* (**Влияние тепличных газов на сельское хозяйство и улавливание и хранение углерода как способ предотвращения катастрофы** в книге *"Потепление климата земли и влияние его на продовольственную безопасность России"*).

MG (first/lead Author): Writing (Original Draft & Editing), Conceptualisation; **VGL (corresponding author)**: Funding Acquisition, Writing (Review & Editing), Resources, Conceptualisation, Project Administration.

2. **Mikhail Gorbounov**, Valeriy Glebovich Larionov**. Use of agricultural waste as a precursor to activated carbon** in *"Management of the agro-industrial complex as an important component of Russia's food security"*, volume 2 (**Использование отходов агропромышленности в качестве прекурсора к активированному углю** в книге *"Управление АПК как важной составляющей продовольственной безопасности России"*, том 2).

MG (first/lead Author): Writing (Original Draft & Editing), Conceptualisation; **VGL (corresponding author)**: Funding Acquisition, Writing (Review & Editing), Resources, Conceptualisation, Project Administration.

Declaration

I do solemnly declare that all the material presented and contained in this thesis is my original work.

I do solemnly declare that the materials from this thesis have not been used in any other submission for fulfilment of any academic award.

I do solemnly declare that whilst being registered as a candidate for the research degree at Brunel University London, I have not been a registered nor an enrolled student for another award at Brunel University London or any other professional/academic institution.

I do solemnly declare that I have undertaken the programme of studies related to and in connection with the programme of research following the requirements associated with my research degree registration.

Acknowledgement

Firstly, I would like to acknowledge my supervisory team, namely, my Primary Supervisor – Dr Salman Masoudi Soltani, my Second Supervisor – Dr Svetlana Nikolaevna Ignatova, and my Research Development Advisor – Dr Peter Hewitson; their constant support throughout this research degree has played an immense role and is greatly appreciated.

Secondly, I would like to thank the Experimental Techniques Centre (ETC) at Brunel University London as well as the Wolfson Centre for facilitating access to analytical equipment and for providing a multitude of opportunities for my professional development.

Further, I would also like to recognise the UK Carbon Capture and Storage Research Community (UKCCSRC) for their support of this research and for organising a plethora of events that have supported my professional development.

Additionally, I would like to acknowledge Drax Group UK for continued generous support, with a special thanks to Dr James Hammerton and Dr Jeni Reeve.

Finally, I would like to thank and acknowledge all my co-authors for their great work and valued inputs.

Dedication

This thesis is dedicated to both Dr Dmitri Gorbounov and Prof Boris Gorbounov (my father and grandfather, respectively). Hopefully, this thesis finally constitutes a “proper degree in chemistry”.

Further, I would like to dedicate this thesis to my mother and little sister. Their love, support, questions and challenges have helped me become a better man.

I would also like to thank my supervisory team – Salman, Svetlana and Peter; for providing me opportunities to learn and develop in both personal and professional capacities as well as for always being there for me. Hopefully, my effervescent and vibrant character has not caused too much trouble and that I am now one step closer (to quote Salman) to “becoming a proper chemical engineer”.

Further, I would like to thank the members of the Department of Chemical Engineering at Brunel University London with a special thanks to our great research group. Your support throughout these past years is greatly appreciated. Go the “Mighty Salmons”!

Finally, I dedicate this thesis to my dearly beloved wife. Your love and mental (and sometimes physical) support have been my guiding light through immigration, COVID as well as everything else that life threw at us in past couple of years. Without you this whole thing is meaningless.

Table of Contents

Table of Figures

Table of Tables

List of Acronyms

AC	Activated carbon
ANOVA	Analysis of variance
ASTM	American society for testing and materials
BA	Biomass combustion bottom ash
BBD	Box-Behnken design
BCA	Biomass combustion ash
BE	Bioenergy
BECCS	Bioenergy with carbon capture and storage
BET	Brunauer–Emmett–Teller
BJH	Barrett-Joyner-Halenda
CAPEX	Capital expenses
CAS	Chemical abstract service
CCD	Central composite design
CCS	Carbon capture and storage
DEA	Diethanolamine
DI	Deionised
DIPA	Diisopropanolamine
EDS	Energy dispersive x-ray spectroscopy
FR	Flow rate
FTIR	Fourier transform infrared spectroscopy
GHG	Greenhouse gas
IPCC	Intergovernmental panel on climate change
IR	Impregnation ratio
IUPAC	International union of pure and applied chemistry
MEA	Monoethanol amine
MOF	Metal-organic framework
NRMSE	Normalised root mean square error
NSS	Not statistically significant
OFAT	One-factor-at-a-time
OPEX	Operational expenses
PBR	Packed-bed reactor
PFO	Pseudo-first order
PSA	Pressure swing adsorption
PSO	Pseudo-second order
PVA	Polyvinyl alcohol
PVSA (or VPSA)	Vacuum-pressure swing adsorption
PZ	Piperazine
RFG	Recycled flue gas
RR	Ramping rate
RSM	Response surface methodology
SEM	Scanning electron microscopy

SMR	Steam-methane reforming
SSE	Sum of square errors
TGA	Thermogravimetric analysis
TRL	Technology readiness level
TSA	Temperature swing adsorption
TVSA	Temperature-vacuum swing adsorption
VC	Virgin carbon
VCP	Virgin carbon pellet
VOC	Volatile organic compounds
VSA	Vacuum swing adsorption
WGS	Water-gas shift

1. Introduction

The world as we know it today still depends greatly on carbon-based fuels, despite the tendency to leave behind oil-based energy sources. Technological progress has enabled the human race to emit a myriad of greenhouse gases (GHGs) polluting our planet and causing global warming. Figure 1.1 depicts the temperature anomaly and portrays a trend of increasing average temperatures across the globe. The 2015 Paris accord [1] states the goal keeping the global temperature increase to under 2°C (or even 1.5°C) as this would definitely decrease the negative effects of climate change.

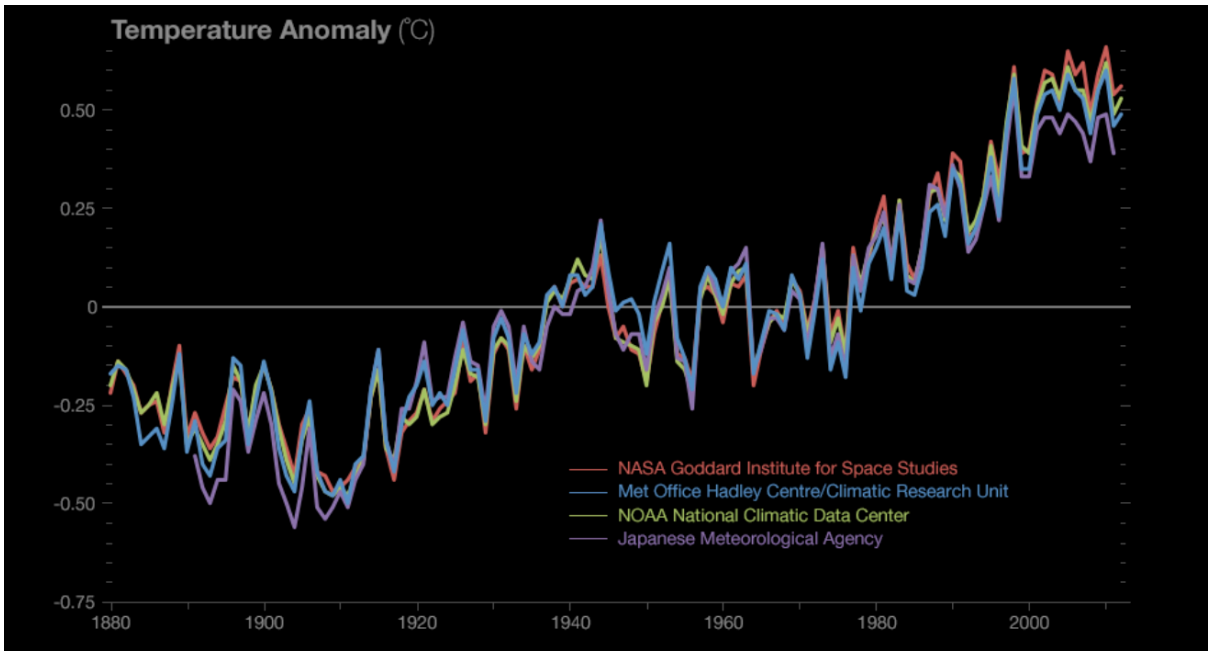

Figure 1.1:The rise of Earth's temperature overtime adapted from [2].

Norway, Sweden, France and the UK have legislation in place in order to battle this odious problem. For instance, the British government has passed the climate change act which is aimed at the target of net zero emissions by 2050 [3]. However, despite these efforts, there is still a lot to be done to mitigate climate change and global warming.

Greenhouse gases, such as carbon dioxide (CO_2), methane (CH_4), sulphur hexafluoride (SF_6), nitrous oxide (N_2O) and etc, are emitted into the atmosphere through various sources. These molecules absorb the energy in the lower atmosphere and then re-emit it, thereby altering the climate on our planet [4]. Amidst the formerly-mentioned gasses CO_2 is by far the most widely emitted pollutant and, therefore, cutting down on anthropogenic carbon dioxide release into the atmosphere is

considered to be an essential and pivotal point in the uphill battle against climate change.

The daily mean CO_2 concentration in May 2013 first surpassed 400 parts per million (ppm) [5] and has been on the rise ever since. In comparison, the concentration of carbon dioxide in the air for 1750 is believed to be around 277 ppm [6]. Figure 1.2 depicts these changes.

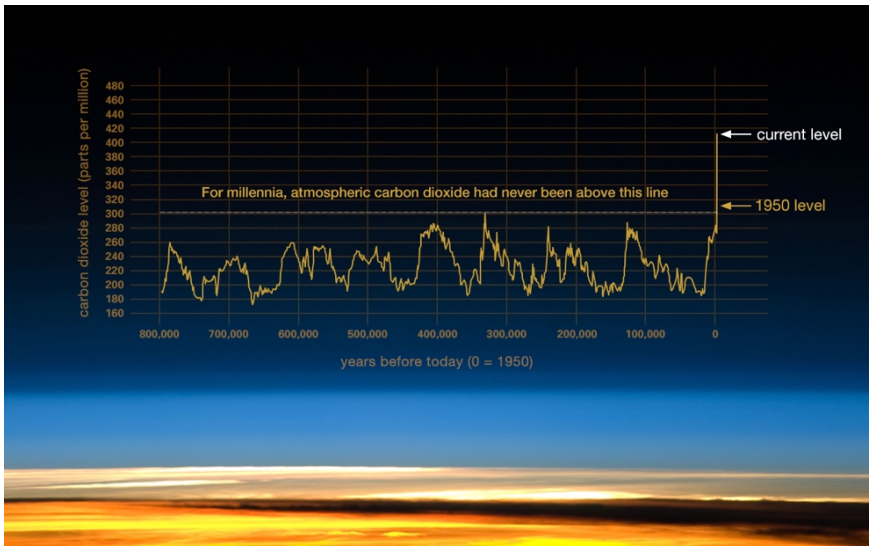

Figure 1.2: The levels of CO_2 in the atmosphere over time adapted from [7].

In 2018 the emissions from fossil fuel energy sources have reached 37.1 ± 1.8 gigatonnes of CO_2 [8] and they were prospected to increase in 2019 leading to a scenario well beyond the 1.5°C mark [9]. In order to digress from this grim trajectory, we, as a population, should look for ways of reducing our carbon footprint and implement these much-needed changes into not only the energy production cycle but also to other sources of CO_2 emissions scattered all over industry (around 21% of all global CO_2 emissions as seen from Figure 1.3), agriculture (24%) and transportation (14%).

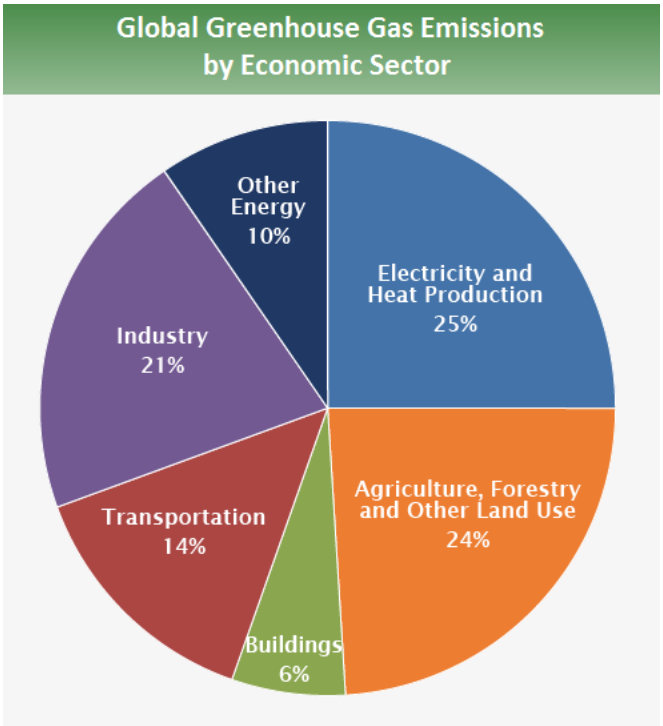

Figure 1.3: Global GHG emissions breakdown by sector adapted from [10].

Within the UK GHG emissions are distributed roughly in the same proportions as worldwide. For instance, electricity & heat production accounts for just a fifth of the nations' emissions (as can be calculated from Figure 1.4). However, transport emits a higher proportion of gases in the UK than globally, also approximately 25%.

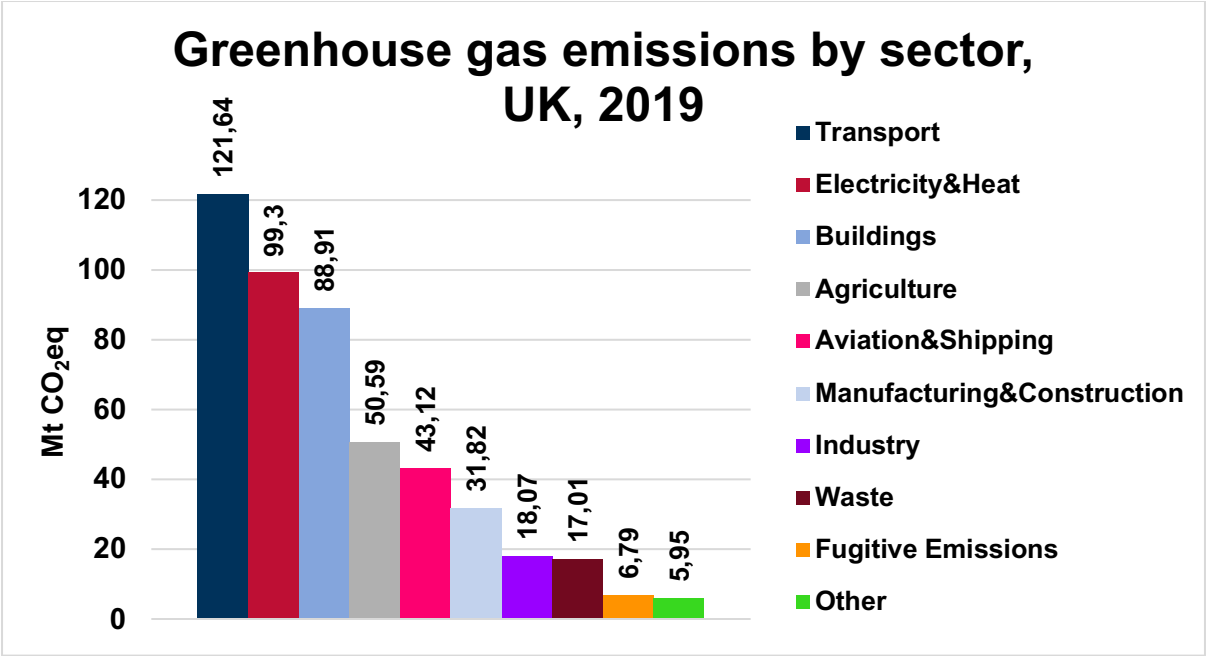

Figure 1.4: UK Emissions breakdown by sector, reproduced from [11].

One of the most formidable techniques of mitigating climate change is moving away from fossil fuels to alternative, less carbon-dependent energy sources i.e. wind, solar, hydro, nuclear. However, a one-to-one transition (from fossil to alternative) would not be smooth and would require a lot of investments as well as changes to the energy grid, especially in the developing countries which depend upon fossil fuel-derived energy much more than the western world and this reliance will probably increase over the coming years. Plus, we would not be utilising the energy potential and the facilities for fossil fuel energy production. Instead a more feasible and viable solution to the problem of the alternation of planet Earth's climate is carbon capture and storage (CCS). It is recognised as such not only by the scientific society but also by the political realm as governments worldwide are funding these initiatives. For instance, the British government has issued over £1 billion towards developing CCS in Britain, and Canada have invested more than Can$1.8 billion into carbon capture and storage funding [12]. Therefore, we cannot deny the importance of CCS in the process of mitigating climate change.

However, it is widely believed that the best, if not the only way, of achieving society's carbon curtailment goals is utilising CCS together with a shift towards building more renewable energy sites. For example, it has been estimated by Mai Bui et al [13] that for the UK to reach the decarbonisation targets, outlined by the Committee on Climate Change (recommending a significant decrease in carbon intensity on the grid by 2030 to 50 gCO_2/KWh from approximately 300 gCO_2/KWh in 2020 [14]), the country would have to achieve one of the four possible scenarios:

- 31GW of nuclear energy
- 56GW of wind + 18GW nuclear energy
- 30GW CCS + 13GW of nuclear energy
- 30GW CCS + 11GW nuclear + 56GW of wind energy.

CCS is a way to pave a smoother transition to a fossil fuel free world. This would allow developing countries to continue using highly carbonaceous fuels at the same time reducing their carbon footprint and not demanding an instant transition from the third world. However, as noted previously, society as a whole will, eventually, have to leave fossil fuels behind and transition to a "greener" energy source(s) in order to reach our goals of environmental protection. We ought to continue on the path towards net

zero emissions and saving our planet. An integral part of this journey would be implementing the concept of bioenergy with carbon capture and storage (BECCS). It is regarded as one of the most promising ideas for combating global warming. In fact, 101 out of 116 scenarios published in the IPCC report from 2014 [15] (leading to a "likely" chance of keeping the temperature rise at/below 2°C from the pre-industrial levels) heavily rely on deploying BECCS. This mitigation technique is grounded on two separate concepts: bioenergy (BE) and CCS. BE is power generated from carbon neutral sources of energy such as sustainable biomass. When being used as a primary fuel for power plants during combustion the material releases CO_2 that has been absorbed from surrounding air by the feedstock during its lifetime. This matter does not add "new" carbon dioxide and, therefore, such technologies are considered to be net zero. Furthermore, by adding CCS to the power plant we are creating a carbon-negative technology as it does not allow the GHG to be re-emitted into the atmosphere following combustion. Instead of being released into the atmosphere the CO_2 is taken out of the capturing unit and compressed for further transportation (usually via pipeline) to be deposited into the geosphere. Underground storage is not only safe but also durable, as it is believed that after being pumped into the storage site the gas will stay in place for thousands, if not millions, years. This work, however, is focused on capturing technologies, rather than storage or utilisation.

As per capturing the CO_2 from flue gases, there are three major routes that are being developed nowadays: oxy-fuel combustion, pre-combustion and post-combustion carbon capture. The third method can be fitted to most industrial plants and power stations, which is a great advantage in comparison to the alternative options. In this process, the combustion flue gas is typically sent to a decarbonisation unit after it has passed through the prior treatment stages e.g. flue gas desulphurisation. The flue gas comes in contact with the capturing media, which must have a high selectivity towards CO_2. The media binds the carbon dioxide and, therefore, allows for a green environmentally-friendly power plant or industrial factory. The GHG can be captured in a number of ways. The main processes today are adsorption, absorption and calcium looping. Absorption is the most widely used technology currently for this application. It is an industrially mature process that has been around since 1930, when a patent for a process for separating acidic gasses employing amines has been issued [16]. The most common material for the industrial

process of amine-based absorption is a 30% weight solution of aqueous monoethanolamine (MEA). It is well-suited for applications dealing with a low carbon dioxide partial pressure, i.e. flue-gas from coal-fired power plants. However, this material is not immune to thermal and oxidative degradation, as well as producing toxic waste and corroding the columns. Therefore, development of a more efficient CO_2 capture process, as an alternative to the conventional amine scrubbing process is essential to make CCS economically feasible.

In contrast to amine solvents, adsorbents are less widely used nowadays but do provide some clear advantages over the abovementioned materials. Generally speaking, the advantages of adsorption, compared to absorption, are as follows: a) high contact area, b) higher CO_2 loading [17]. Another benefit of most classical sorbents (i.e. zeolites, activated carbons (ACs), etc.) is that they normally do not lead to degradation of equipment, thereby cutting the operational costs. They also cover a wider range of temperatures (T) and pressures (P) and tend not to decompose so easily and to form toxic waste. Adsorbents, though, are not without their deficiencies. For instance, handling a large amount of solid material can be challenging and, therefore, a drawback preventing this technology from up-scaling as rapidly as is desired. An appropriate adsorbent material should have fast adsorption/desorption kinetics and a low heat of adsorption, a high CO_2 capacity and a high selectivity for CO_2/N_2, high hydrothermal and chemical stability, as well as good mechanical properties and a low cost of synthesis/raw material. The latter factor is of utter importance when considering, for instance, advanced novel metal organic frameworks (MOFs). Despite their colossal adsorption capacities, MOFs are cost-prohibitive and are not optimal for large-scale production (an adsorbent suitable for industrial CCS processes should aim to cost less than 10 $/kg [18], yet this value is also influenced significantly by the materials lifetime). Therefore, finding the balance between optimal adsorptive properties and manageable expenses (both operational and capital) is the main question in post-combustion carbon capture and, perhaps, the only route forward is to reduce costs. These economic drawbacks (associated with all carbon capture initiatives) can be diminished by utilising waste materials, such as biomass combustion ash, which is readily available at bioenergy power generating facilities (as combustion of sustainable biomass is associated with co-generation of ash – contributing to 6.8 wt.% of biomass feedstock on average [19]). Additionally, since BECCS is proposed

to have an immense impact in the uphill battle against the alteration of our climate, BCA may be of interest as a cheap, yet effective alternative to conventional capturing media. If implemented, companies may be enabled to avoid costs associated with logistics and waste management (as well as reduce their environmental burden), thereby reducing the price of each tonne of CO_2 captured and in turn preventing the electricity prices from skyrocketing.

Ashes, generated during combustion, can be divided into two different groups: fly ashes (the finer and lighter particles that rise up together with the flue gas) and bottom ashes (the much heavier and bigger particles that tend to stay at the lower end of the combustion unit). Both of these substances can potentially be used in building materials as additives to concrete. Alongside these current applications, there are also ways to include ash as a capturing media for post-combustion CCS. Coal ashes have already gained some traction in the scientific community either as adsorbents for CO_2 or as a precursor for zeolite synthesis. For instance, Brazilian researchers have found that the adsorptive properties of synthetic zeolites were quite similar to these of the commercially available (1.97 mmol/g and 2.39 mmol/g respectively) [20]. Although there have been several studies on the application of coal fly ash in post-combustion carbon capture, there is little research on the application of biomass combustion bottom ash in carbon capture. Not only does BCA generally contain a higher amount of alkali metals (which may be beneficial for CCS [21]), but also they normally contain lesser amounts of toxic metals, as opposed to coal ashes [22]. Apart from that, biomass substitutes coal as one of the worlds' leading fuel sources (thereby, producing more biomass ash rather than coal ash). In 2017 it is estimated that a little under 5% of energy production in the UK came from coal, and biomass just over 4% [23] (others say 6% [24]), whereas in the first quarter of 2020 biomass accounted for 6.7% and coal fell below 4% [25]. The British government has also received suggestions outlining an increased amount of biomass usage (more than 7%) for heat and electricity production by 2030 [26]. Currently in the UK, annual production of wood ash amasses to nearly 52 kilotonnes [27] and, with the country aiming to abandon unabated coal as fuel source by 2025 [28] this value is only poised to rise.

These facts pave the way for the rise of BCA usage as a capturing medium for carbon dioxide and therefore, this project will look into the applications of biomass

combustion bottom ash in the context of adsorption based post-combustion carbon capture.

1.1. Research Aims and Objectives:

This research aims to investigate the capabilities of BCA as carbon precursor for the synthesis of an AC adsorbent for efficient yet cost-effective CO_2 adsorption.

Based on the research aim set out above, the objectives of this research include:

1. To synthesise, activate and characterise various carbonaceous adsorbents derived from BCA;

2. To investigate equilibrium and kinetics of CO_2 adsorption on optimum samples *via* gravimetric methods;

3. To investigate the efficacy of different adsorbent pelletisation routes;

4. To chemically modify and characterise the optimum investigated activated carbon.

1.2. Thesis outline

The following chapter presents a comprehensive review of carbon capture technologies, focusing on the adsorption-based CO_2 separation and featuring a description of CO_2 adsorbents. Chapter 3 describes the main characterisation techniques employed across different chapters of this thesis. Chapter 4 features the extraction technique and characterisation of the virgin carbon derived from biomass combustion bottom ash. In chapters 5 and 6, the produced virgin carbon is activated chemically (Chapter 5) and physically (Chapter 6) with the respective optimum samples characterised. Chapter 7 investigates different pelletisation approaches for the produced physically-activated adsorbent, whilst Chapter 8 describes the chemical modification of the physically-activated carbon. Finally, the conclusions and proposed future work are presented in Chapter 9.

2. Literature Review

2.1. Carbon Capture: How to curb CO_2 emissions

As described in the previous chapter the main CCS technologies currently available for battling carbon dioxide emissions are oxy-fuel combustion, pre- and post-combustion carbon capture. Herein, the focus is mainly drawn to the latter highlighting

potential separation processes, their merits and drawbacks. In particular, adsorption is selected as the proposed alternative to the current state-of-the-art option of absorption with amine solutions. The latter technology is also elaborated on, discussing the current trends and benchmarks in solvent design, their respective performance is evaluated and cross-compared. Nevertheless, adsorption is believed to be superior to amine absorption as it does not require corrosive and/or toxic materials as well as is proposed to provide a lesser energy penalty associated with regeneration of the capture media [17].

Other CCS pathways, i.e. oxy-fuel combustion and pre-combustion carbon capture aim to approach to net-zero energy generation differently. Oxy-fuel combustion allows for capture from a highly concentrated flue gas stream (typically 75 – 80% [29]) as fuel is exposed to nearly pure O_2 (~95% purity) and recycled flue gas (RFG) as opposed to ambient air [30]. The RFG is introduced into the system as a heat absorbent, hence, slowing down the heat release rate [31] and decreasing the flame temperature from 3500 °C for pure oxygen to 1300 – 1400 °C, thus, potentially allowing to retrofit such a capture unit to an existing power plant [29]. However, that would require the atmosphere to consist of approximately two thirds of recycled carbon dioxide to mimic the typical combustion conditions [32]. Nevertheless, the absence nitrogen in the boiler lead to suppressed NO_x formation (nearly halved when compared to conventional air [33]) as well as lack of N_2 dilution of the flue gas, hence, CO_2 separation can be achieved *via* cooling and compression. However, major drawbacks for this method are associated with retro-fitting. The need to drastically lower the combustion temperature (and the large footprint of the equipment) hold back its further deployment [29]. Moreover, one of the biggest hurdles for oxy-fuel combustion is the significant CAPEX and OPEX of air separation.

Pre-combustion capture is another technique to help curb the CO_2 emissions and decarbonise the power-sector, which is based on the industrially mature processes of production of various chemicals and H_2 production [34]. This technology is applicable to, for instance, integrated gasification combined cycle power plants. Within this decarbonisation route the primary fuel is firstly gasified into syngas (a mixture of CO and H_2) *via* steam reforming at elevated pressures and temperatures. A prominent example of this chemical reaction is steam-methane reforming (SMR) for brown, grey and blue hydrogen production [35]. Following this step, if needed, the syngas is

subjected to cleaning from various trace contaminants (e.g. H_2S, OCS (carbonyl sulphide), HCl, Hg and etc. [36]) or is introduced into a cyclone for particulate removal [37] prior to being added to the shift reactor, where the water-gas shift (WGS) reaction takes place. During this process, carbon monoxide is further converted into carbon dioxide, leading to a concentration of in the range of 15 – 60% (dry basis) [34], which ease the separation process. Another benefit of this decarbonisation approach is the high-pressure nature of the processes upstream of the capture unit, leading to a lesser energy requirement for compression of CO_2 as well as (if using physical absorption) for solvent regeneration, due to higher efficiency of pressure reduction when compared to thermal treatment [29]. This technology is quite well-established in industry and could entail a cost reduction of nearly 25% compared to oxy-fuel combustion [38]; however, it is not without its significant disadvantages. The energy penalty associated with pre-combustion capture is a major limitation. The net electric efficiency would drop to approximately 37% [39]. The CAPEX and OPEX of such a plant would also be significant (especially if additional purification steps are needed prior to capture) and retro-fitting issues are also a serious limitation of this technology [29], [37].

2.1.1. Post-combustion Capture Methods

Post-combustion carbon capture systems are, as evident from the name, utilised downstream from the boiler and, currently, it is the most established strategy for CCS. Such systems are an end-of-pipe solution which makes them comparatively more attractive for wide industrial implementation. Here, carbon dioxide is captured from the flue gas before being emitted into the atmosphere. Thus, the conditions in the unit are less harsh than in the previously described techniques (i.e. oxy-fuel and pre-combustion), with the pressure being atmospheric and the temperature being within the range of 40 – 120 °C (with the exception of novel alternative technologies (e.g. calcium-looping) that operate at higher temperatures). The CO_2 concentrations, however, are also much lower (normally within the range of 3 – 20% [29]) and the flue gas also contains moisture, N_2 and other impurities (e.g. CO, SO_x, NO_x) with the exact type and concentration depending mainly on the energy source (but also on the completeness of the combustion process). For instance, coal off-gas contains approximately 15% CO_2 [40], whereas natural gas (NG) has a much lower partial pressure of CO_2 (in the region of 3 – 5% [41]) as well as less SO_x and NO_x [29], [42].

The system can also be implemented to other, non-power sector, emission sources with much higher carbon dioxide concentrations as cement plants (the kiln off gas can contain as high as 33% of CO_2 [32], [43]) or steel blast furnace flue gas (27.4%) [44]. This capability stems from the relevant ease of retrofitting of a post-combustion CCS unit to existing plants and factories, thus allowing for emission reductions across numerous sectors and industries. A block diagram of the basic post-combustion capture system is depicted below in Figure 2.1.

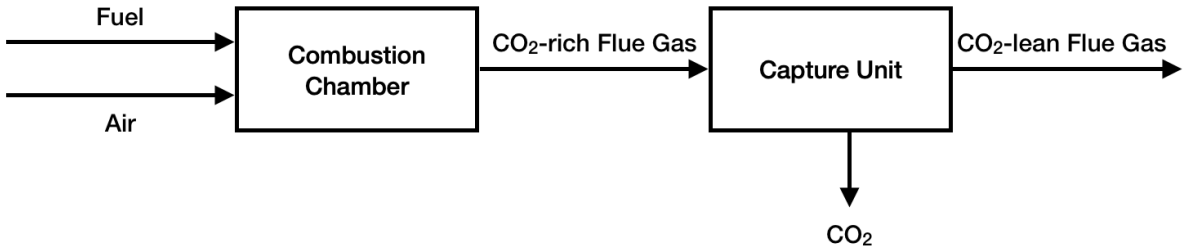

Figure 2.1: Basic schematic of a post-combustion capture process.

As mentioned earlier, one of the major, if not the most appealing aspect of post-combustion capture is the ability to retrofit this technology to existing power-plants. Such capability would allow for a smoother transition towards renewables as fossil fuels (i.e. coal, natural gas and oil derivatives) could still be utilised whilst their harmful GHG emissions could be largely minimised, thus, not affecting the environment. Post-combustion CCS may be of particular importance in the developing regions of the world, where dependence on fossil fuels is still rising. Wide deployment of this technology could advance the economic positioning of the emergent markets, making the “green” transition more attractive and viable.

Another benefit of post-combustion carbon capture processes (when compared to alternative CCS techniques) is the maturity of this process alongside the myriad research and development campaigns focused on further improving this method. However, post-combustion CCS is not without its limitations. Perhaps, the main disadvantage of this technology is the energy penalty needed for regeneration of the capturing media, as well as design challenges associated with unit footprint, cooling requirements and the OPEX required to process vast amounts of flue gas [29]. Additionally, since the high-purity CO_2 is produced at relatively low pressures, the captured gas has to be compressed prior to being transported to storage [37], thus, increasing the cost per tonne of CO_2.

Within the post-combustion capture network various approaches exist, each offering their own benefits and merits. The main examples are calcium looping technologies, and adsorption with solid sorbents. In this thesis, absorption with amines and membrane technologies are introduced, whilst adsorption is discussed at length.

2.1.1.1. Membrane Separation

Membrane separation technologies (industrially used for removing CO_2 from natural gas [45]), where the driving force is the pressure difference between either side of the membrane (the feed side and the permeate side) [29]. In such process, however, the stream is pressurised and the concentration of carbon dioxide can be quite high, leading to comparatively easy separation. Nevertheless, in order to be separated effectively, the flue gas should be pre-treated to eliminate the impurities and cooled to avoid thermal degradation of the membrane. The gas is also compressed (to approximately 20 bar) to assist with the separation process [29]. Addition of a RFG could also be beneficial for this separation technique [41].

These aspects are of utter importance for viability of the process when considering membranes for post-combustion capture [46]. The CO_2 content of the feed stream should be over 20%, though multi-stage operations can sufficiently capture CO_2 from a more dilute stream [29]. The biggest advantage of membranes is, most probably, lack of regeneration requirements [46] as well as the absence of flooding or foaming, channelling or entrainment [29]. On the other hand, within the post-combustion set-up, due to a lowered driving force, the capture efficiency is undesirable. Additional power is required to increase the total pressure of the gas stream. When comparing to a basic amine adsorption unit, the energy consumption would only be comparable at partial pressures of over 20% (and at 10% and lower, the difference in energy requirements is considerable) [47].

Membranes used for gas separation can be classified into different types, i.e. organic and inorganic. The latter offer lower CO_2 permeability (than the former) whilst organic (also referred to as polymeric) membranes are more applicable for CO_2/N_2 separation in part due to higher selectivity but also because of their higher permeability. Permeability for gas separation (expressed in units of barrer) is defined as the volume of a gas species passing through the membrane per unit time and area, whereas selectivity is the difference in permeability of the separated components [29].

2.1.1.2. Amine Absorption

CO_2 absorption with liquid solvents is an alternative option for CCS. A mature process known to humanity for nearly a century, with the patent for separation of acidic gases with alkanolamine solutions being registered in 1930 [16]. Upon contact with the gas, the CO_2 is chemically bound to the amine, then solvent regeneration (normally *via* thermal treatment) takes place in a desorption column (otherwise referred to as stripper). Generally, the alcohol group of the solvent increases the solubility in water whilst reducing the vapor pressure, whereas the NH_2 group provides the necessary alkalinity in aqueous solutions to promote the reaction with CO_2 [48].

Classically, a 30% monoethanolamine (MEA) aqueous solution is used as a benchmark for post-combustion carbon capture due to favourable qualities such as low cost and high chemical reactivity towards CO_2 [48]. The reaction involves formation of a carbamate according to the zwitterion mechanism, which is then followed by the hydration of carbon dioxide to form HCO_3^-/CO_3^{2-}, and accompanied by the hydrolysis of the carbamate [49]. The formed carbamate, however, is quite stable, hence the limited thermodynamic capacity to absorb CO_2 [48]. Secondary amines (such as diethanolamine (DEA), diisopropanolamine (DIPA), piperazine (PZ) and others) also react in this way. They have been proposed as MEA-alternatives since DEA is more resistant to degradation and shows lower corrosion levels, whereas DIPA has lower energy requirement for solvent regeneration than MEA [48]. A particular drawback of absorption with primary and secondary amines is the requirement of 2 moles of amine to capture one mole of CO_2. However, tertiary amines (e.g. methyldiethanolamine, triethanolamine and etc.), due to lack of an N-H bond, react in a different way, *via* formation of bicarbonate ion and protonated amine by the base-catalysed hydration [48]. Consequently, they have a higher theoretical capacity of one mole of CO_2 per mole of tertiary amine [50]. They are also characterised by a low reactivity and high stability [48], higher CO_2 solubility [51] as well as a lower absorption heat, hence, lower regeneration energy but slower reaction kinetics [52].

In order to harness the benefits of each type of amine, whilst minimising their respective limitations, amine blends have been proposed as novel solutions for absorption-based carbon capture. Such mixtures usually contain an activator or a promoter of the reaction. For instance, piperazine, a cyclical secondary diamine (hence, the ability to capture 2 moles of gas per 1 mole of solvent) without hydroxyl

groups, has kinetics that are 50 times quicker than MEA [48], leading to consideration of it as an activator.

Nevertheless, a 30 wt% MEA aqueous solution allows to achieve a capture efficiency of 90%, with the energy penalty associated with amine regeneration being approximately in the range of 4 GJ/tonne captured [13]. This number can be lowered by, for instance, increasing the stripper pressure; such change, however, promotes thermal degradation of the solvent [53]. MEA is also quite corrosive, hence, an additional reason to consider alternatives. A blend of 2-amino-2-methyl-1-propanol (AMP) with PZ (28/17 wt%) has been proposed to lower the required flow rate by 38% and provide an energy saving of 10% over the benchmark technology [54].

A lot of effort is put into minimising the energy requirements for solvent regeneration since an amine absorption unit is believed to consume around 20 – 30% of the energy output of a power plant [55]. Recent reports estimate the costs associated with capturing CO_2 with MEA solutions to be at ~$114.5/tonne of CO_2 [56]. The currently operational Boundary Dam capture unit is believed to achieve ~$115/tonne of CO_2 [57]. Whilst these costs are dominated by capital recovery, other operational expenses are also significant. For example, exclusively the aspects of solvent management were estimated to cost ~$10/tonne of CO_2 for another widely known capture facility – Petra Nova, Texas [58], thus, constituting a third of the targeted (by the Department of Energy in the US by 2030 [59]) $30 per metric tonne. Furthermore, solvent degradation is also a limitation of this capturing method, not only increasing the OPEX, but also causing secondary pollution. Additionally, SO_x, NO_x and other impurities also induce degradation of amine solvent, meaning such technologies struggle when dealing with contaminated flue gases (e.g. from oil refineries) [60]. Apart from the energy penalties, this technology also suffers from other drawbacks, such as an increase in plant footprint and corrosion [29]. The latter leads to the requirements of more chemically resistant building materials of the columns, thus increasing the CAPEX and maintenance costs [61]. Nevertheless, post-combustion CO_2 capture *via* amine absorption is the most widely adopted carbon capture technique currently.

2.2. Adsorption

A proposed alternative to the currently industrially used amine absorption is adsorption with solid sorbents. A 2nd generation technology, that has not yet reached

large-scale industrial deployment, with the technology readiness level (TRL) lower than 9 (commercial scale) of amine solvents [13]. The overall TRL is believed to be around 6–7 [62]. However, large pilot tests and Front-End Engineering Design studies are being conducted such as the Svante and Chevron project in the Kern River area in California or the Air Products Port Arthur SMR-CCS plant, all in USA [63], [64]. The former option entails Temperature Swing Adsorption (TSA), whereas the latter utilises Pressure Swing Adsorption (PSA) [63]. The main differences between these operational modes as well as benefits, drawbacks and examples are described in Section 2.2.2.1**Error! Reference source not found.**. Prior to the adsorption process considerations, a discussion of the fundamentals of adsorption is needed, to ensure logical and coherent understanding.

2.2.1. Adsorption Mechanisms

Different molecules have varying affinities to the surfaces of solid adsorbents. These properties can be associated with the electron densities, hence polarities of potential adsorbates. Since carbon capture can be (in the first approximation) viewed as separation of N_2 from CO_2, a cross-comparison of these molecules is appropriate. Although both molecules are non-polar, the latter is also a quadrupole hence, it is normally preferentially adsorbed owing to carbon dioxide's greater quadrupole moment and polarisability [65], [66]. Thus, the basic principle of adsorption is based on exploiting the differences between interaction strengths of adsorbates and the adsorbents [67]. However, morphological properties (porosity, surface area, pore size distribution and etc.) are also of utmost importance [68]. Similarly, process conditions (i.e. pressure and temperature) are major factors contributing to the equilibrium adsorption capacity [69]; whereas the kinetics are strongly impacted by the way the adsorbent material comes in contact with the flue gas (an often overlooked operational criterion) [70].

Adsorbent pore sizes are classified into and micropores (< 2 nm) , mesopores (2 nm – 50 nm) and macropores (> 50 nm) [71]. Upon contact with the sorbent, the adsorbate starts diffusing into the pore structure where the solute is then adsorbed onto the porous surface [72]. Within the first step, four mechanisms of mass transport are distinguished: molecular/bulk diffusion; Knudsen diffusion; surface diffusion; and Poiseuille flow [73]–[76]. The latter is dependent on the pressure difference across the adsorbent, whereas the other transport mechanisms are a function of temperature:

bulk diffusion is a function of $T^{3/2}$, while Knudsen diffusion is proportional to $T^{1/2}$ [73]. Surface diffusion has a stronger impact at higher surface loadings but decreases when the temperature rises (as adsorption favours lower temperatures) leading to a drop in the surface loading and an increased rate of molecular diffusion [77]. Molecular (bulk) diffusion usually takes place in macropores, whereas Knudsen diffusion would occur in cases when the mean free path of the molecule is greater than the pore diameter [73]. However, the diffusional mechanisms described above may occur simultaneously, competing with (or facilitating) each other depending on the structure of the material [78]. Nevertheless, adsorbents struggle from diffusion rate limitations if the adsorbate diameter is similar in size to the micropores themselves.

Having diffused into the pore, the second step i.e. surface adsorption, takes place. Adsorption is usually classified into physi- and chemisorption.

2.2.1.1. Physisorption

Physical adsorption is mostly governed by van der Waals intermolecular forces, which are sub-classified into Debye forces, Keeson interactions and London dispersion forces (with the latter strongly influencing CO_2 adsorption [79]). The sum of the different van der Waals intermolecular forces combined with the electrostatic interactions, result in the overall intermolecular force between the CO_2 molecule and the adsorbent [70]. Physisorption on carbonaceous adsorbents is classically governed by the intraparticle diffusion into the porous framework; thus, the size of the pores as well as the pore size distribution are of utter importance [69].

In case of CO_2 adsorption, the preferred pore size lies in the realm of ultramicropores (< 0.7 nm). Such pores facilitate the interaction between each side of the pore wall and carbon dioxide [80]. This phenomenon is observed as the potential energy surfaces overlap, thus, increasing the binding energy at approximately 0.7 – 0.8 nm [81]. As such, development of materials with larger ultramicroporosity is preferential.

In order to characterise the material and gauge if the produced porous structure fits the purposes, physisorption isotherms can be employed.

2.2.1.1.1. Physisorption Isotherms

The behaviour of the adsorbent-adsorbate system is often described using physisorption isotherms, an invaluable tool for characterisation of such porous

materials. The International Union of Pure and Applied Chemistry (IUPAC) has proposed 6 types of adsorption isotherms as shown in Figure 2.2.

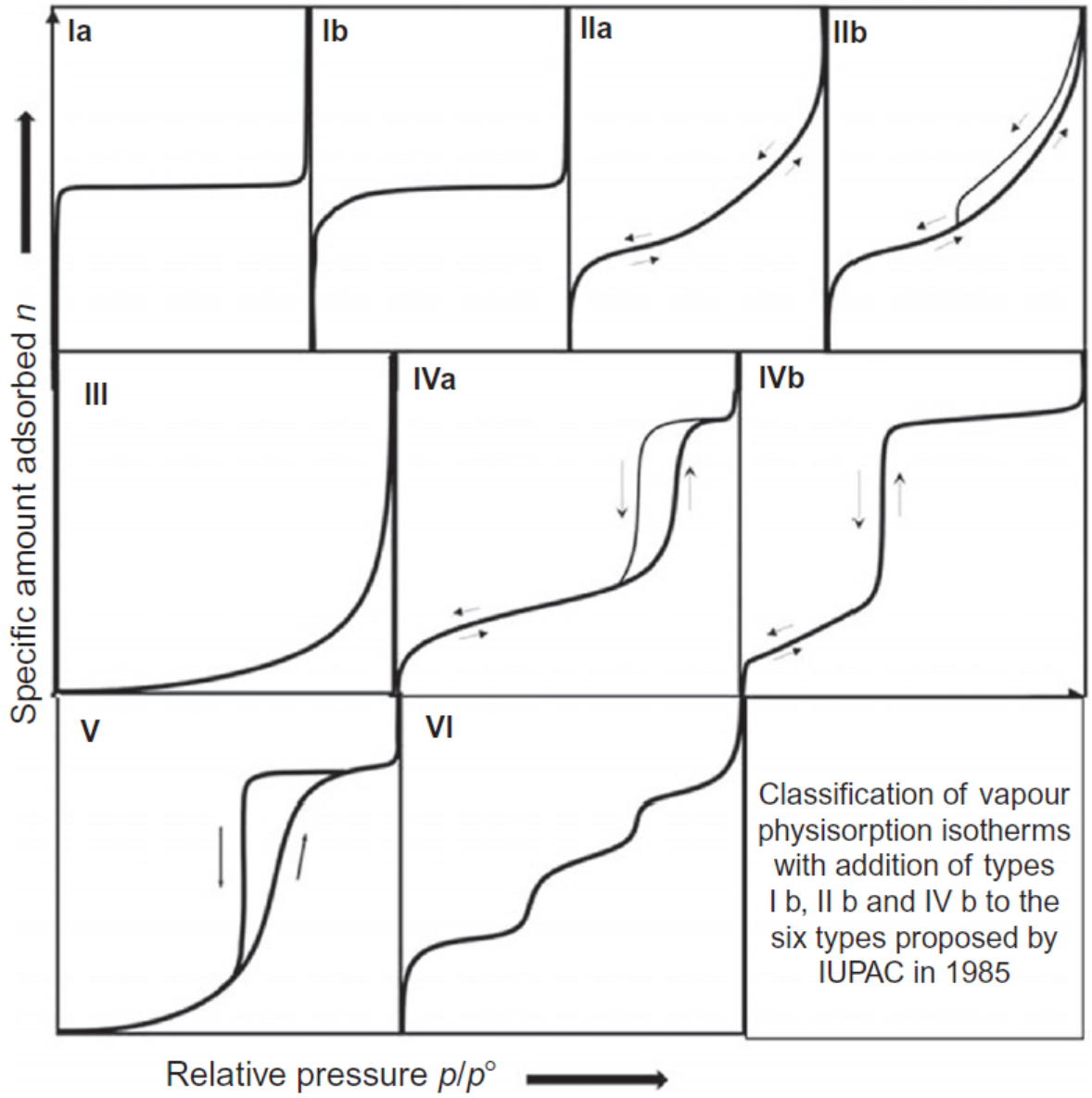

Figure 2.2: IUPAC Classification of physisorption isotherms adapted from [82].

Type I isotherms feature a steep rise in the adsorbed capacity until a plateau is reached that is maintained even at high relative pressures. They are associated with microporous materials showing micropore filling [83] and not monolayer coverage [84]. The former phenomenon is a distinctive feature of gas-phase adsorption in micropores which stems from the similar size of the sorbent's pore radius and the adsorbate molecule leading to the latter occupying the space within an adsorption force field, i.e. volumetric filling of the pore [85]. The filling of the micropores is not a form of capillary

condensation (due to a lack of phase-transition in micropore filling [85] hence, no meniscus is formed) but rather depends on the overlap of adsorption potentials [84]. Further, the plateau indicates the lack of multilayer adsorption. Additionally, if the micropores are of a decreased width, two phenomena would be observed, namely, a higher adsorption energy accompanied by a decrease in the pressure at which pore filling takes place [82]. Moreover, the shape of the “knee” of the isotherms can also be interpreted to provide further insight into the nature of the material. For instance, a sharp “step” would indicate the filling of rather narrow micropores could be sub classified into type Ia isotherm [82]. On the other hand, a wider “knee” (type Ib isotherm) suggests wider micropores [82] and even narrow mesopores (up to 7 nm) [84]. Examples of these subclassifications can also be seen in Figure 2.2. Further, if a nearly horizontal plateau is reached within a narrow range of relative pressures, the sample is believed to have a limited pore size distribution as well as a small surface area [82]. Moreover, for all type I isotherms, the available micropore volume is regarded as the limiting factor of the adsorption capacity [82]. Finally, type I isotherms are reversible.

An alternative to the discussed above isotherm is type II, which classically describes multilayer adsorption on non-porous or macroporous (> 50 nm) materials [83]. Here, the adsorbed layer is transformed into a bulk liquid once the equilibrium pressure reaches the saturation vapour pressure [82]. This isotherm starts out similar to the previously described model; however, instead of a horizontal plateau a quasi-linear portion is observed. The beginning of this section is considered to be the end of monolayer and the start of multilayer adsorption. Hence, this point could be regarded as the monolayer capacity [82]. Type II isotherms are also reversible; however, sometimes the desorption branch differs from the adsorption pathway, thus constituting hysteresis. This phenomenon leads to a subclassification within this type of isotherm: type IIa and IIb (without and with a hysteresis loop, respectively). Hysteresis is usually associated with the filling and then emptying of the mesopores *via* capillary condensation [82] and is discussed further in this chapter.

The next isotherm (i.e. type III) occurs when the interaction between the adsorbent and the adsorbate is weak as opposed to the interaction between the molecules of the gaseous (or liquid) phase [83]. They are, hence, found when dealing with non-porous samples and are relatively uncommon [82].

Type IV isotherms are used to describe mesoporous matter as they present characteristic hysteresis behaviour [83] (notably, for N_2 adsorption at 77 K hysteresis occurs for pores with a diameter of over 4 nm [86]), though, the exact shape of it varies. They are somewhat akin to type II isotherms as the initial portion of the graph follows a similar pattern. Further down the axis of relative pressures, however, type IV isotherms feature a distinctive saturation plateau (although it is sometimes found to be short or even reduced to a simple inflexion point [82]). However, some materials (notably, mesoporous silica MCM-41 [82]) follow this pattern and are completely reversible, i.e. lack a hysteresis loop. This is often found with samples possessing a pore width of < 4 nm [86]. As such, they are named type IVb and the classical pattern is called type IVa (as seen in Figure 2.2).

Further, similarly to type IV, type V isotherms present hysteresis. Nevertheless, type V can be distinguished from the former curve as they feature a nearly perpendicular section at relative pressures of ~ 0.5 suggesting presence of mesopores, where phase change (i.e. capillary condensation) occurs [83]. A further distinction stems from the nature of the relationship between the sorbent and the media, i.e. weak interaction. This leads to the graph being convex to the x-axis, similar to type III isotherms but applicable to micro and mesoporous materials [82]. Such isotherms are relatively rare [82].

Lastly, type VI isotherms describe multilayer adsorption of a “step-wise” nature (with the layers being more pronounced at lower temperatures) [83]. Such isotherms are comparatively uncommon but can be found when dealing with materials possessing a highly uniform surface structure, e.g. graphitised carbons [82].

2.2.1.1.2. Hysteresis Loops

Further information on the adsorbent can be acquired by examining the shape of the hysteresis loop. Its presence is often ascribed to capillary condensation, a phenomenon, which entails phase change and is evidenced by a delay in desorption as opposed to the adsorption step, i.e. adsorption at saturation vapour pressures and desorption at lower partial pressures. This may be associated with the saturation vapour pressure being different from (greater than) pressure upon evaporation from the meniscus [87], leading to harsher “evacuation” conditions (lower pressures) required for the condensed phase to convert back to gaseous state. Alternatively, the

differences between the adsorption and the desorption branch of the isotherms may stem from complex pore structures, where the desorption pathway could be altered by various effects or pore blocking [86]. For instance, an ink bottle-shaped pore (i.e. a wide pore with a narrow neck) upon desorption would “contain” the gas adsorbed inside until the “bottle neck” empties at a lower pressure [86]. As such, pore characteristics are preferably obtained by evaluating the desorption branch.

There is a variety of hysteresis loops recognised by IUPAC, which are shown in Figure 2.3.

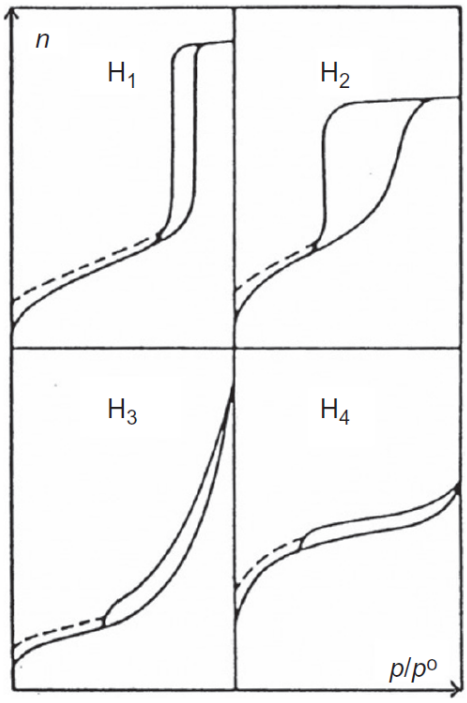

Figure 2.3: IUPAC Classification of hysteresis loops adapted from [82].

Type H_1 loops are normally found in mesoporous adsorbents with a strict/uniform pore structures (SBA-15 and MCM-41) [82], [86]. They feature steep, nearly parallel branches resulting in a quite narrow loop, suggesting delayed condensation [86].

Type H_2, on the other hand, are broad and present a plateau followed by a sharp drop on the desorption side. Network effects and pore blocking are believed to play a significant role here [86]. As such, samples with complex interconnected pores of varying shapes and sizes present such a form of hysteresis loops [82], but so can some ordered mesoporous silicas (SBA-16 and KIT-5) [86].

Further, type H_3 hysteresis is characterised by a lack of a plateau at elevated relative pressures, with the adsorption branch closely resembling type II isotherms. Hence, such loops would be anticipated for macroporous materials, where the macropores do not fill up completely with condensate [86].

Lastly, type H_4 hysteresis loops (similar to type H3) also do not plateau at higher pressures, though, the pronounced uptake at the start of the curve suggests micropore filling [86]. Such loops are often produced by carbonaceous adsorbents (although, after excessive burn off during their activation [84]) as well as other materials with slit-shaped pores of mainly micropore sizes [82].

2.2.1.2. Chemisorption

In contrast, chemisorption requires a formation of new chemical bonds, with binding energies normally exceeding 0.5 eV per molecule [88]. Therefore, this type of adsorption process is often referred to as “specific” or “selective” adsorption, since the CO_2 reacts with a particular adsorption site [82] (e.g. CO_2 will bond to specific functional groups, whereas the N_2 would not [89]). Carbon dioxide, being a (Lewis) acidic gas, is drawn to (Lewis) bases, hence, increasing the basicity of the adsorbent would enhance the affinity of the adsorbate towards the sorbent [90]. Since a variety of N-containing functional groups (examples are given in Figure 2.4) are of basic nature, they act as an electron-donor, thereby attracting the electron-deficient carbon atom of the CO_2 molecule, whereas O-functionalities (formed as a result of oxidative treatments) often impart electron-acceptor properties to the sorbent [69]. N-functionalisation (N-doping) leads to production of myriad functional groups, with low temperatures favouring amides, amines, imides, imines and nitriles [70]. At temperatures over 450 °C aromatic species will be the predominately produced, mainly pyridinic and pyrrolic surface functional groups, with the latter gradually converting into the former above 600 °C [91]. At adsorption temperatures of around 20 °C and low pressures (1 bar), physisorption in micropores is believed to be the governing mechanism controlling CO_2 adsorption, whereas at elevated temperatures (approximately 120 °C) the N-containing functional groups chemisorb the CO_2 *via* acid–base interactions [92]. This has been associated with a greater CO_2 transport rate through the pore structure which increases accessibility of the active adsorption sites at elevated temperatures [92]. This shift from physical to chemical adsorption leads to a decrease in the initial adsorption rate alongside the rise in adsorption

temperatures, with the presence of N-functionalities being the dominant driving force of the latter mechanism [93]–[97].

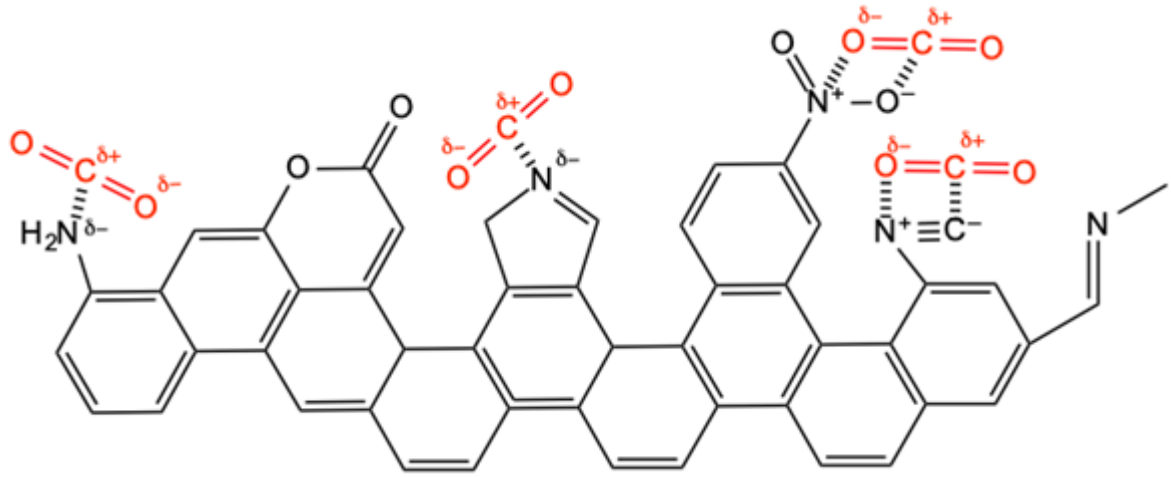

Figure 2.4: CO_2 attraction mechanisms for some N-based functionalities adapted from [73].

A metric often used to distinguish between these two types of adsorption is the different heat of adsorption values. Physisorption usually has quite low values for the heat of adsorption (also equivalent to the latent heat of the adsorptive) in the region of 8 – 40 kJ/mol, whereas chemisorption demonstrates much higher values of roughly 40 – 800 kJ/mol which are equivalent to the enthalpy of reaction [98], [99]. However, if heteroatoms are present within the framework of the carbonaceous sorbent, their impact on the polarizability of the sorbent might lead to an increase in the heat of adsorption to non-typical values of CO_2 physisorption [100].

In order to maximise the benefits of a given adsorption mechanism (and by extension material), other aspects have to be evaluated to ensure a suitable combination of system-adsorbent-pollutant.

2.2.2. Adsorption Process Considerations

Although, the adsorption process is spontaneous, a multitude of aspects have to be taken into consideration prior to deployment of this technology. In this thesis, some of these (namely, regeneration regime, reactor design and sorbent material itself) are elaborated on.

2.2.2.1. Regeneration Regime

The energy input within an adsorption process is associated with the removal of the adsorbed species off the surface of the adsorbent. The regeneration work is classically

supplied in form of a rise in temperature or a drop in the system pressure within the vessel (or as a combination of both). These changes/swings are the namesake of the processes: Temperature Swing Adsorption (TSA) and Pressure Swing Adsorption (PSA). It should be noted, that other forms of energy input have also been proposed, e.g. switching the gas chemical potential *via* introduction of differing gaseous species (namely, steam within the displacement purge cycle) or *via* microwaves and/or induction heating [101]. Further, within PSA systems, a sub-category of Vacuum Swing Adsorption (VSA) can be identified. The main distinction being the lack of (significant) gas pressurisation upstream of the adsorption column, i.e. the feed flue gas is introduced at pressures just above 1 atm. Thus, upon regeneration, the pressure is reduced to below atmospheric (typically ~ 0.3 bar absolute) to facilitate the evacuation of the adsorbed species. Industrially, this decrease would have to be achieved using mechanical vacuum generation as opposed to vacuum ejectors; the latter is not applicable for adsorption purposes due to the mixing of the product gas with the working fluid [62].

The choice of what process to employ often depends on not only the sorbent but also the surrounding conditions, i.e. the feasible footprint and availability of low-grade steam (a favourable property for TSA implementation). Alternatively, VSA cycles are proposed for post-combustion CCS due to a large amount of N_2 in the flue gas (compression of which is usually not cost-effective) as well as vacuum regeneration being more favourable than the positive pressure alternative [101]. Further, PSA/VSA processes would be more applicable to CO_2-rich flue gas streams, e.g. biogas upgrading, cement and steel productions as well as petrochemicals refining. On the other hand, TSA could offer higher working capacities relative to VSA [62] and, in contrast to PSA, TSA could be utilised for capture from highly diluted flue gas streams, as (similar to VSA) compression of feed gas is not required. Finally, to harness the respective benefits of the TSA and VSA processes and decrease the energy requirement for sorbent regeneration, a combination of these operational envelopes (i.e. TVSA) is also an option.

From the material standpoint, physical sorbents would typically favour PSA applications, due to an ease of regeneration *via* pressure reduction, whereas TSA would lend itself useful for chemical adsorption [89] as harsher conditions are needed to break the chemical bonds and remove the adsorbate [101]. Carbonaceous materials

are also considered to be promising adsorbents for TSA applications due to their high thermal conductivity [102]. Further, if the adsorbent is electrically conductive [103], electric swing adsorption can be evaluated as it allows for a lower energy consumption as well as faster heating and cooling rates [104]. However, regardless of the deployed technique, the system would then have to be optimised with regards to the process configuration (namely, cycle design and schedules as well as energy integration) [105] to maximise separation efficiency [106] as well as an appropriate reactor type and design.

2.2.2.2. Process Design

Apart from various modes of sorbent regeneration, the process design in terms of the configuration of the adsorbent unit (i.e. structure of the particle bed) has to be considered. These contactors have to be effective, affordable and easily retrofittable to an existing unit, whilst providing flexibility in operation [107]–[109].

The classical and most straight forward approach is a fixed-bed (also referred to as packed-bed) reactor (PBR). It has gathered a lot of attention in the scientific literature due to its ease of operation and design [110]–[112] furthered by its applicability towards different regeneration modes [107], [113], yet PBRs are deemed more suitable to PSA applications utilising physisorbents, due to moderate heat transfer properties of the set-up and low heats of adsorption [114]. The cycle times for a PBR TSA system are significantly longer, making them impractical at large scales due to their inadequate requirements in terms of unit size and/or footprint (i.e. number of columns) [89]. Fixed-bed configurations have a limiting factor in the feed gas flow rate due to the value of pressure drop across the bed; the pressure difference should not crush the adsorbent particles [62]. The matters of pressure drop, on the other hand, could be tackled by increasing the particle size of the adsorbent, though such approach hampers mass transfer [115]. Alternatively, the bed diameter, could be increased, which would facilitate an additional decrease in the superficial gas velocity (whilst maintaining it below the minimum fluidisation velocity of the adsorbent particles [62]).

Main process intensification lied in the ability to move the solid particles rapidly (facilitating heat and mass transfer) and providing acceptable equipment size [89]. This allows to capitalise on the increased working capacity that TSA offers, as well as

to enhance TSA's productivity [62]. A prominent example of such novel technologies are fluidised-bed reactors. In such a set-up, the feed flue gas is supplied from bottom up at an appropriate velocity and flow rate to force to solid particles to imitate a fluid. The sorbent then is circulated around the adsorber and the regenerator. This configuration results in an improved heat and mass transfer [107], [116], which (alongside the ability to recover or add heat to the bed [117]) suggest potential of fluidised beds for TSA applications [118]–[120]. Despite complexities associated with scale-up [116], fluidised-bed reactors offer increased gas-solid contact and faster kinetics, manageable values of pressure drop and are applicable to high flue gas velocities [121], [122].

An alternative adsorption set-up is the moving bed reactor configuration, which is known for smaller pressure drops (as opposed to equivalent PBRs) [123]. Further, TSA processes would benefit from lower cycling times during the heating and cooling steps [124]. However, the complex nature of this set-up (i.e. moving the adsorbent between "reactor A" and "reactor B") places significant limitations on its application towards PSA with another challenge stemming from the requirement of low feed gas velocities (in order to prevent fluidisation) [125]. The latter could also lead to poor heat transfer capabilities due to a lack of mixing. Nevertheless, these configurations are divided into two main categories, namely, conventional and rotary moving bed reactors. Both of these options could enable steady-state operations, yet the latter might face a challenge associated with sealing (hence, potential leaks of the flue gas) [107]. Classically, moving bed reactors are shorter than their fixed-bed counterparts leading to reduced pressure drops [123].

As such, applicability of a given process configuration depends greatly not only on the regeneration regime but also on the adsorbent used, since the aspects of adsorption capacity coupled with selectivity, production and operation cost as well as myriad other factors are at play when evaluating the efficiency and economics of a post-combustion capture system.

2.2.2.3. Adsorbent Materials

A multitude of various sorbents exist (e.g. zeolites, porous silicas, metal-organic frameworks (MOFs), covalent organic frameworks, zeolitic imidazole frameworks as well as a myriad activated and/or modified carbons) with colossal differences in their

proposed applications, properties, respective merits and challenges. Generally, the requirements for sorbents (in the context of carbon capture) include high working capacity and selectivity for CO_2, fast adsorption-desorption kinetics (with the latter step being conducted under preferably mild conditions), high mechanical and thermal stability, resistance to moisture (and other impurities present in the flue gas) as well as low cost of production and operation. One pathway for reducing the final price of a product is to utilise less costly substances for the synthesis process. Therefore, using existing waste and/or by-products as precursors to an adsorbent is a promising route. For instance, coal and biomass-derived fly ashes have been used to produce zeolitic materials for CO_2 adsorption [126]–[128]. Zeolites are aluminosilicates with alkali/alkaline-earth cations that are known for their superior dehydrating properties [129]. They are often referred to as molecular sieves due to their highly ordered uniform micropores (e.g. NaX < 0.7 nm, ZSM5 = 0.5 – 0.6 nm, RHO = 3 – 4 nm [130]). Zeolites' potential in the realm of carbon capture stems from their chemically inert and thermally resistant characteristics as well as strong affinities towards polar and polarisable molecules [126]. Yet their strong interactions with H_2O hamper their performance in applications with a wet flue gas stream.

MOFs, on the other hand, are nanomaterials that (at their core) have a metallic centrepiece (i.e. node) surrounded by various organic linkers (i.e. ligands). Thus, by changing the anchoring node and/or adjusting the ligands, highly tuneable and bespoke (e.g. desired functional groups and pore geometry) materials can be produced [131]. Hence, they can be applied not only in the realm of carbon capture by adsorption, but also for hydrogen storage [132], separation of hydrocarbons [133] as well as catalysis [134]. As such, MOFs generally outperform classical adsorbents in terms of selectivity, surface area and morphology as well as equilibrium uptake. An example of such sorbents' high adsorption capacities is Mg-MOF-74, reaching 5.5 mmol/g at 0.15 bar and 313K [135]. However, Mg-MOF-74 is believed to strongly adsorb moisture (similar to zeolite 13X) [136] and have a strong affinity towards N_2 [137]. Therefore, alternative materials, such as Calgary Framework-20 (CALF-20), a hydrophobic MOF, have recently been evaluated for the purposes of post-combustion carbon capture [136].

However, sorbents cannot be graded purely on their adsorption capacities [137]. Other parameters (e.g. stability, selectivity, cost and etc.) have to be considered to

evaluate the efficacy of a given material within industrial settings. Cost and thermal stability are the greatest challenges to MOFs' commercial deployment [138]. A particular focus could be drawn to the former as the disparity between commercially available "classical" adsorbents and MOFs is colossal. For instance, UTSA-16 (UTSA: University of Texas U.S.A) has been shown to cost as high as €83,200 per tonne [139]. There has, however, been recent progress in potential decrease in the costs due to economies of scale and innovations associated with continuous (as opposed to batch) production processes. For instance, CALF-20 has been shown to be scalable from a milligram-scale to ~300 kg [140]. Further, both BASF [141] and Promethean Particles [142] are believed to be capable of producing some MOFs on a tonne/year scale, leading to a considerable drop in their market price. More recently, a UK-based start-up (MOF Technologies; a spin-out company from Queen's University Belfast) also claiming the ability to produce on an industrial scale, have received substantial investment from Barclays Bank [143]. These efforts are bound to propagate MOF technologies further; however, the urgency of the climate crisis requires immediate attention, thus currently rendering these novel solutions challenging for immediate deployment. As such, research on development of cost-effective alternative yet efficient sorbents is urgent and highly timely at the moment.

2.3. Carbonaceous Adsorbents

The waste-to-value supply chain is wide-spread for production of carbonaceous adsorbents; often employing low-cost precursors such as tar, coal, pitch and etc. However, these substances do not align with the interests of green chemistry, circular economy and sustainable development, hence, have fallen out of favour and are being substituted by renewable and/or biomass-derived raw materials [144]. Additionally, biochars (as opposed to fossil-based carbons) generally have a higher chemical purity due to lower amounts (or even a lack) of heavy metals, nitrogen and sulphur [145]. Classically, an organic (e.g. pine saw dust [146], garlic peel [147], rice husk [148], sugar beet molasses [149], bamboo [150] or other agricultural [151]) residue undergoes a two-step treatment to become an activated carbon (AC). The first process is aimed at transforming the fibrous network to a carbonaceous one, hence, the name "carbonisation". The two common pathways for carbonisation are hydrothermal treatment and pyrolysis [144]. The former is based on low-temperature (~180–350 °C) processing of an aqueous dispersion of the precursor in an autoclave [152], thus

achieving a “hydrochar” with an elevated content of oxygenated surface functional groups – a suitable precursor for the production of chemically activated carbons [153]. Hydrothermal carbonisation is an attractive technique when dealing with wet biomass samples as the lack of a drying step constitutes energy savings [145]. Nevertheless, pyrolysis is more prominently employed as the carbonisation technique. This process is conducted under high temperatures (~400–800 °C) in an oxygen-free environment (classically achieved with N_2). Within this, four distinct types of pyrolysis are recognised, namely, slow, fast, flash and gasification pyrolysis [154]. However, the latter three are not most suitable for producing adsorbents due to low solid product yields and/or generation of wide pore structures [155]. Hence, slow (ramp rate of 5 – 7 °C/min [155]) pyrolysis is the most common carbonisation method [145]. During this process, an abundance of various chemical reactions occur (mainly cracking [156]) leading to the break-up of the precursor and production of solid carbonaceous substances (as well as gases) with pronounced porous structures.

In the context of post-combustion carbon capture, an investigation into carbonisation of date sheets (as an example of food waste valorisation) has shown a pyrolysis temperature of 800 °C to be more favourable than 500 °C as the harsher conditions resulted in a higher pore volume, smaller average pore size as well as an increased uptake (1.88 and 1.56 mmol/g, respectively) at 1 bar and 25 °C [157]. Conversely, lower pyrolysis temperatures have been shown to be better-suited for high pressure (7 MPa) CO_2 adsorption on other biomass precursors (namely, mangrove and palm-trunk) [158]. The samples pyrolysed at 500 °C, though, upon activation, have been shown to have a CO_2 uptake of approximately 15 – 20% larger than their 600 °C counterparts, which was also associated with greater pore volumes.

2.1.1. Activation of Carbons

Un-activated carbonised materials are rarely labelled as sorbents. Classically, the pyrolysed char is further processed in order to enhance/develop porosity in a process known as *activation*. Activation can be done *via* two distinct routes: physical and chemical. The former is considered to be more eco-friendly and relatively more cost-effective (due to the absence of any chemical reagents), whereas the latter is often quoted to produce materials with greater surface areas and a high degree of microporosity [159].

Physical activation describes a process during which the char is exposed to an environment of an activating gas (steam, CO_2 or their mixture are the most popular choices) at elevated temperature (typically above 700 °C) for a prolonged duration of time. Within this, employing CO_2 is believed to produce activated carbons with a higher degree of microporosity than steam which usually leads to a wide distribution of micro and mesoporosity [160]–[162]. As a result of this process, the surface morphology changes drastically, producing a much more porous material, i.e. increased porous surface areas and pore volumes. This was confirmed by evaluating physically activated carbon derived from anthracite coal, which had a S_{BET} of ~426.5 m^2/g and a total pore volume of ~0.217 cm^3/g [163]. Moreover, ACs derived from barley straw have been reported to achieve 789 m^2/g and 0.3268 cm^3/g, respectively, for activation with CO_2, and 552 m^2/g and 0.2304 cm^3/g for steam [161]. Further, the findings of this report suggest a higher degree of microporosity to be produced with CO_2 over steam, hence, this approach could be more favourable for the purposes of post-combustion carbon capture.

For instance, Ogungbenro *et al* [164] have physically activated their carbonised date stones with CO_2 to produce an AC that showed a capture capacity of ~2.9 mmol/g at room temperature. To reach this uptake, an hour-long activation had to be carried out at 900°C using 150 mL/min of CO_2. Similar results have been obtained by other researchers also using CO_2 as the activating gas and date stones as a precursor, though *via* a different approach. [165]. The raw precursor was first carbonised under 150 mL/min of N_2 at 600°C (ramping rate of 10 °C/min) for two hours. Thereafter, the gas was switched to CO_2, the activating gas, and the temperature was kept constant for the activation step which also lasted two hours. Following this procedure, the manufactured material adsorbed 1.44 mmol/g of CO_2 at 25 °C and 0.25 bar.

However, adsorbents from alternative organic precursors have also been activated with CO_2. For example, Rashidi *et al* [166] employed palm kernel shells as sorbent precursors, producing carbon that could adsorb 1.23 mmol/g and 0.89 mmol/g at 25 °C and 50 °C, respectively. Such capacities were achieved following an hour-long CO_2 activation at 850 °C. Their material was shown to outperform a commercial analogue, as the latter had a capture capacity of 1.08 and 0.75 mmol/g at the same adsorption temperatures.

Another popular organic waste precursor for ACs is coconut shells. In the work of Prauchner *et al.* [167] the outer layer of *cocos nucifera* was dried, crushed and sieved. Following this the size fraction of 2 – 2.83 mm was carbonised (100 mL/min of N_2 at 850 °C (heating rate of 2 °C/min) for 2 hours) and then activated. The procedure for the latter started with increasing the temperature in increments of 5 °C/min under 100 mL/min of nitrogen. Once the activation temperature of 750 °C was reached, the gas flow was switched to 100 mL/min of CO_2 for the desired activation duration. The choice of nomenclature of samples based on the degree of burn-off during activation hampers the identification of the evaluated activation times. Nevertheless, the material with the highest uptake (5 mmol/g at 1 bar and 0 °C) was achieved with the burn-off of ~35%. This phenomenon was attributed to prominently developed pore structure of this sample, namely, the highest number of pores that are on the lower end of the ultramicroporosity range. The smaller pore sizes were emphasised to be of particular importance since CO_2 was shown to be more efficiently adsorbed by them at the post-combustion partial pressures (i.e. 0.15 bar) [167]. This phenomenon was evidenced by a reduced uptake of the ACs with a higher degree of burn-off (i.e. possessing larger ultramicropores) at this gas concentration.

More recently, waste precursors such as post-consumer plastic have also been investigated as a potential starting point for carbonaceous adsorbents [168]. Ligero *et al.* have investigated activation of such waste plastic-derived chars. For physical activation a range of temperatures (680 – 840 °C) was studied, the ramping rate (10 °C/min) and the gas flow rate (200 mL/min) were fixed, whilst the activation gas itself has been varied (CO_2 and N_2). Within the respective experimental campaigns, the best performing materials (hence, the suggested activation temperatures) were identified to be produced at 720 °C. At these activation conditions CO_2 -activated AC was shown possessed a higher uptake at 30 °C of ~0.89 mmol/g versus ~0.76 mg/g for N_2 -activated sample. A similar trend was also observed across the whole evaluated temperature spectrum.

On the other hand, chemical activation is thought to produce more potent sorbents (in terms of morphology) even at lower treatment temperatures by using chemical activation agents. The activating agents can produce surface functional groups that would be beneficial for the purposes of carbon capture [70]. As such, a combination of a pronounced porosity alongside surface functional groups lead to materials with

high CO_2 adsorption capacities, although some of the functionalities may be alleviated from the carbon due to high temperature treatment. Classically, various acids (H_3PO_4, H_2SO_4 and etc.), salts ($ZnCl_2$, $FeCl_3$, K_2CO_3) and alkalis (KOH, NaOH) are regarded as chemical activating agents. The latter two are not the most preferable options as the metal ions constitute an environmental hazard (e.g. secondary pollution from the water used in the washing stage) [159]. However, potassium hydroxide (KOH) is believed to be the well-suited for microporosity development [169], hence more applicable for production of sorbents for with high CO_2 adsorption capacities. Nevertheless, other activating agents are also employed to produce CO_2 adsorbents.

For example, activation with H_3PO_4 and $ZnCl_2$ has been employed to develop adsorbents for CO_2 capture from coconut shells [167]. As a result of these treatments, the produced ACs adsorbed more CO_2 (i.e. 3.2 and 3.3 mmol/g, respectively for H_3PO_4- and $ZnCl_2$ -activated carbons) than the parent char (1.98 mmol/g) at 1 bar and 0 °C. However, their performance and degree of microporosity were inferior to the physically activated carbon also evaluated in their work. These findings corroborate the phenomenon of wider deployment of KOH as the activating agent most suited for CO_2 adsorbents due to its ability to develop of microporous materials. Consequently, it is frequently chosen as the preferred activating agent in the realm of CO_2 adsorption [170], [171].

For instance, activation with KOH of a biomass tar-based carbon produced an adsorbent that achieved an uptake of 4.1 mmol/g [172], whilst using acai stones as a precursor lead to an uptake of 6.1 mmol/g [173] both at 1 bar and 0 °C. Further, an adsorption capacity of 13.1 mmol/g (0 °C and 2 MPa) has been achieved for a KOH-activated AC from bituminous coal [174]. .

The bio-derived sorbents are quite prominently used as precursors [160]. For example, carbonaceous adsorbents derived from bamboo have also been investigated [150], [175]. In the first study [150], Ji *et al.* have physically (i.e. dry) mixed their material with the activating agent (KOH) in a ratio of 1:1. The mixed sample was then subjected to a flow of N_2 (100 mL/min) while the tube furnace was reaching (heating rate of 10 °C/min) the temperature of 700°C where it was held for an hour. The resulting AC was then evaluated as a proposed sorbent for post-combustion carbon capture from a coal-fired power plant. As such, the adsorption capacity was evaluated under a 15 volumetric % CO_2 concentration at 50 °C. Under these

conditions, the sample presented an uptake of 0.74 mmol/g. Further, the AC was shown to desorb fully at a relatively low temperature of 80 °C. In their subsequent study the authors have built up on these findings by investigating the impact of the impregnation ratio (IR), i.e. carbon to agent ratio on the produced adsorbent [175]. As such, they have selected to evaluate three different levels of impregnation, namely, 1:1, 1:0.5 and 1:0.2 with the rest of the production procedure being kept the same. A noticeable increase in the pore volume as well as surface area was observed for the sample with the highest IR, leading to a CO_2 uptake (at 25 °C and 1 bar under a pure gas stream) of 3.49 mmol/g. These findings suggest the need for a relatively high (i.e. ~ 50%) amount of activating agent to develop an effective AC for CO_2 adsorption; though excessive IRs (over 2) can be detrimental as they may decrease the volume of ultramicropores [176], [177].

An alternative approach of introducing the activating agent is wet mixing, i.e. introducing the activated agent as an aqueous solution. This may allow for a more homogenous impregnation of the sample, but also can lead to increased degradation of the ceramic activation vessel [178], hence, the KOH solution potentially/partially being spent on degrading the ceramic boat as opposed to activation of the carbon. Nevertheless, the wet impregnation method has been applied previously in the literature. In the case of vine shoots-derived ACs, for example, activation with a 4 M aqueous KOH solution was investigated evaluating the IR of 1:1 and 1:2 (C:KOH) with activation temperatures of 600 and 700 °C (ramping rate of 10 °C/min and N_2 flow of 100 mL/min) [179]. Their results show more prominently developed surface area (S_{BET}) and microporous volumes for the samples with the higher IR. In terms of uptake, the most promising results (2.46 mmol/g at 1 bar and 25 °C) were achieved following the harsher activation conditions (higher IR and activation temperature). Yet this sample presented a low apparent selectivity (molar basis) over N_2 of 8.5. In the same work, however, the authors have also conducted tests, where impregnation was achieved *via* dry mixing, although with different IRs, namely, 1:2 and 1:5. Unfortunately, a direct comparison between the mixing methods cannot be drawn as no adsorption data was reported for the dry mixed sample with the IR of 1:2; though some differences may be inferred based on the reported data for the AC with the IR of 1:5. The latter material possessed a drastically higher selectivity of 56.8 yet a lower adsorption capacity of 1.98 mmol/g at the same conditions [179]. The comparatively worse performance in

terms of uptake, however, as highlighted previously, may be attributed to an excessive amount of chemical activating agent used to produce the sample [176], [177].

A similar conclusion in terms of a balanced C:KOH ratio can be gathered when evaluating KOH-activated ACs from waste plastic, where an increase of IR from 1:1 to 1:4 led to the adsorption capacity being halved [168]. However, the optimum adsorbent was identified to be produced using an IR of 2:1 (or 1:0.5), thus highlighting the differences the precursor (alongside the activation procedure itself) plays as the work of Zhang *et al.* suggested lower levels of impregnation (i.e. more carbon than agent) to develop a modest pore framework [175]. Interestingly, the adsorption capacity of the optimum chemically activated sample in the work of Ligero *et al.* [168], i.e. IR of 2:1, was only minimally higher than that of the material produced using a 1:1 ratio of char to KOH. Finally, their work also suggested NaOH to be an inferior activating agent (in the context of CO_2 adsorption) compared to potassium hydroxide (in the 680 – 840 °C temperature range). The latter sentiment has also been expressed previously in the literature [180].

Apart from selection of appropriate activation/agent for a given adsorbate, the solid sorbent could be further chemically modified to tailor it for a particular application.

2.1.2. Surface Modification of Activated Carbons

Surface modification is an invaluable pathway that could facilitate an increased affinity towards target pollutants resulting in a higher adsorption capacity as well as a rise in the heat of adsorption of the material (e.g. transition from physisorption to chemisorption). As such, a plethora of pathways exist to achieve these results. Among these, grafting and impregnation have been the most-commonly investigated methods. Upon impregnation, the desired species is dispersed along the pores, hence, the loss of the modifier may occur during the regeneration of the sorbent [181]. As such, grafting is believed to produce more stable materials, constituting a more versatile approach to surface modification.

Generally, grafting could be divided into two categories: "*grafting-on*" and "*grafting-to*" [182]. The former achieves improved sorption characteristics by changing the existing surface functional groups of the parent carbon (e.g. oxidising the present hydroxyls to carbonyls or reducing the nitro-groups to amines). The alternative method (i.e. grafting-to) focuses on adding desired groups to the present functionalities. This

is often done by “opening up” double bonds and attaching an organic molecule with the desired functional group (i.e. transition from a *framework carbon-carbon π bond* to a *carbon-functional group σ bond*) to the surface of the sorbent. To simplify, *grafting-on* changes the groups, whereas *grafting-to* increases the length of the functional group’s chain.

Within the remit of carbon capture, grafting-to is employed when modifying terminal hydroxyls of mesoporous silicas with amine functionalities. However, for carbonaceous adsorbents, the OH-groups might not be sufficiently present to employ such a single-stage process (especially since activation often alleviates surface functionalities due to the high temperature (>500 °C) nature of the process). Hence, two-step grafting is employed. For example, oxidation of AC, followed by secondary treatment (e.g. with various amines [183] (including halogenated amines [184]), ammonia [181] and etc.). In other words, for activated carbons specifically, the most widespread in the literature grafting method is: *grafting-on* first, followed by *grafting-to*. Basic surface groups are often deployed due to the nature of CO_2 (Lewis acid) as amine moieties can selectively react to form a carbamate (Figure 2.5) similar to the approach used in amine absorption. Such surface modification has proven to be successful, especially for the purposes of direct air capture, where the increased affinity is paramount due to the inherently low CO_2 concentrations.

Figure 2.5: Amine functional group CO_2 chemisorption reaction.

One of the options for grafting an amine functionality to an AC is achieved by first oxidising the surface of the carbon in order to (step two) reduce the produced (in step one) acidic surface functional groups to amines. The latter step, however, involves hazardous/toxic reducing agents (e.g. $AlLiH_4$, $NaBH_4$) [182], hence, constituting a major limitation of this approach.

An abundance of literature exists on the topic of activation of carbons (and/or their chemical modification), yet the resulting materials present varying sorption and surface properties. These differences may stem from the employed precursors, set-ups, treatment conditions as well as myriad other factors. As such, in order to produce a

highly selective adsorbent with an appropriate porous structure and superior adsorption capacity, extensive experimental campaigns have to be carried out, focusing on the exact subject-matter at hand. Design of experiment (DoE) techniques could be effectively employed in order to minimise these efforts. In addition, DoEs significantly help to facilitate the optimisation of experimental campaigns, revealing any potential/hidden interactions among parameters, and assist with the identification of the optimum operating envelopes.

2.4. Design of Experiments & Statistical Analysis

When it comes to methods which are immensely useful in terms of allowing for processes' efficient evaluation, optimisation as well as interpretation through simultaneous investigations of a combination of input parameters and their interplay, DoE is an invaluable tool. Regardless of the stage of the process or its TRL, intelligently designed experimental campaigns can help address the questions at hand.

An intuitive approach to executing experimental studies is evaluating a single variable, whilst keeping others constant, thus revealing the effects of a select factor on the targeted output, is called the one-factor-at-a-time (OFAT) approach [185]. However, a significant limitation of this technique is a restricted design space.

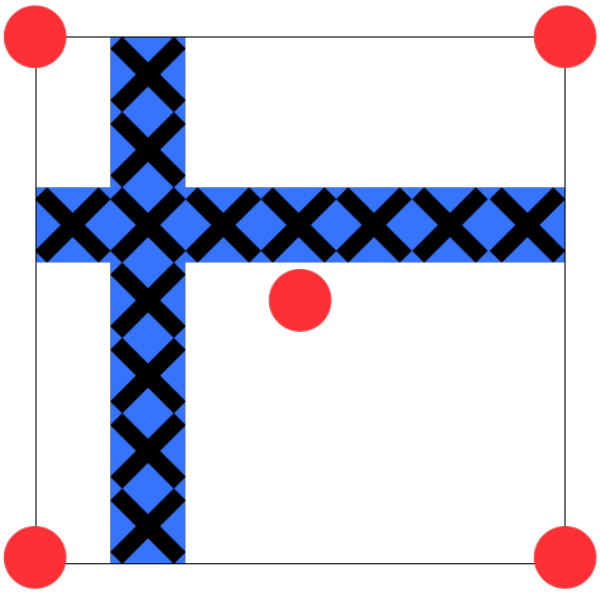

Figure 2.6: OFAT Design Space.

As seen in Figure 2.6, OFAT does not include the whole area of the possible design space; rather exclusively the portion, where the experimental points (black crosses)

have been acquired (blue stripes). An advanced experimental design, on the other hand, would capture the entirety of the studied area (i.e. black square), by strategically positioning the trial/experimental conditions (red circles).

Further, not considering (i.e. evaluating) any potential interaction between the input parameters (which may lead to differences in the interpretation of the data and the identified optimal conditions) is a further challenge of OFAT. On the other hand, an advanced experimental campaign design, would be able to reveal any impact derived from a simultaneous change in the inputs as well as provide a further benefit in form of a reduction in the number of experiments needed (as evident from Figure 2.6), hence, minimising the use of valuable resources (both natural and/or monetary). As such, a fantastic description of DoE has been provided by Smallwood: “planning of a number of experiments in order for their combined result to yield a maximum amount of information” [186]. This definition further highlights the value of considerable planning in order to properly optimise the process/material.

Within the context of carbonaceous adsorbents synthesis and applications, the predominant issues with their optimisation stem from the plethora of available precursors, processing/modification techniques as well as the particular separation technology and the given adsorbate species (i.e., process conditions, competing adsorption, the adsorbate itself, its concentration and etc). These aspects can have a significant impact on the appropriate factors (and their respective levels) as they may vary greatly, when switching a step of the production process or the proposed application. Within this, however, activation time (τ_{act}) and temperature (T_{act}) are frequently studied regardless of the activation method. In the cases of chemical activation, impregnation ratio (IR) is another frequently evaluated parameter, whilst for chemical modification both treatment time and temperature alongside other modification agent-related factors are often examined. On the other hand, investigations into the sorption process would often feature adsorption time (τ_{ads}) and temperature (T_{ads}) as the selected variables [185].

On the flip side, the dependant, i.e. response, variable is frequently selected to be a quantifier of the surface area (e.g. S_{BET}, iodine number, methylene blue number). However, ideally, the sorbent should “be married” to the process that maximises its potential [187]. As such, employing the target adsorbate uptake is, perhaps, a more suitable approach to optimisation of the synthesis (with similar logic applied to

optimisation of application). These output parameters are often optimised in conjunction with product yield, production and/or operation cost as well as removal, recovery and purity of the adsorbate and etc.

The optimum operation envelope is often defined using response surface methods (RSM). It has been posed to be extremely valuable [188] and can be employed for simultaneous identification of the frail points within the design space alongside visualisation of the impact of various factors on the response variable(s) [185].

RSM is utilised to develop an empirical statistical model to approximate how the response variable is influenced by the input parameters [189]. To produce a three-dimensional plot, each model parameter must be measured on a minimum of three levels. Designs that accommodate this number of levels are advised, as they could account for presence of curvature (i.e. non-linearity).

Prior to RSM, applying a statistical tool known as analysis of variance (ANOVA) is recommended as the RSM contour plots need only be produced in cases when the combined impacts are statistically significant (to eliminate the not statistically significant effects or to only focus on the impactful terms) [185]. ANOVA is a technique that separates and evaluates the variation related to the main effects in the design space with discrete the input factors (at/over three individual levels each) [190]. This is achieved by applying the least squares regression method. ANOVA requires the experiment runs to be randomised and, if the dataset contains replicates, they ought to be independent from one another [185]. Further, a normality test (e.g. Shapiro-Wilk, Kolmogorov-Smirnov test and etc.) is required to establish if the results follow a normal distribution [191]. Alternatively, normality could be assessed visually, though, this is approach is not as reliable [191].

Regardless, in order to analyse the data, it first has to be collected, preferably following an astute and robust DoE technique.

2.4.1. Common DoE techniques

A plethora of DoE techniques exist, though, the choice of which to opt for should be based on the target outcome. For instance, if aiming to screen through various parameters to determine the most statistically significant ones, factorial DoEs are preferred. Alternative designs, however, are suggested if the target is to optimise the

process and/or map the response surface. Further, some designs aim to accomplish both tasks simultaneously.

Factorial DoEs endeavour to consider all possible combinations of input parameters, hence are applicable when dealing with a moderate number of factors. There is a wide range of such matrices with a simple example (2^3 full factorial design) presented in Figure 2.7a. Alternatively, fractional factorial DoEs could be deployed. The latter designs are a variation on the former, which facilitate examining a larger number of input variables by reducing the number of experimental points (classically by focusing on the main terms) as clear from Figure 2.7b. These designs are the foundation for both Central Composite Designs (CCDs) and Taguchi frameworks.

Taguchi orthogonal arrays can be produced by overlaying two factorial designs over one another (i.e. inner and outer array) [185]. This can be visualised by examining Figure 2.7c. The key distinction is the positioning of the factors as noise variables are placed in the outer array, while the control variables are reserved for the inner array [192]. This facilitates increased control over the noise resulting in a more robust design. However, perhaps, the most valuable aspect of Taguchi frameworks (stemming from their orthogonal nature) is the ability to identify individual input parameters separately as well as some two-way interactions [185]. Further, the ability to group both categorical (i.e. qualitative) and quantitative factors together at different levels, without necessarily significantly increasing (doubling, tripling and etc.) the required amount of experimental trials, is a further benefit of these designs. These types of frameworks are called mixed-designs [185].

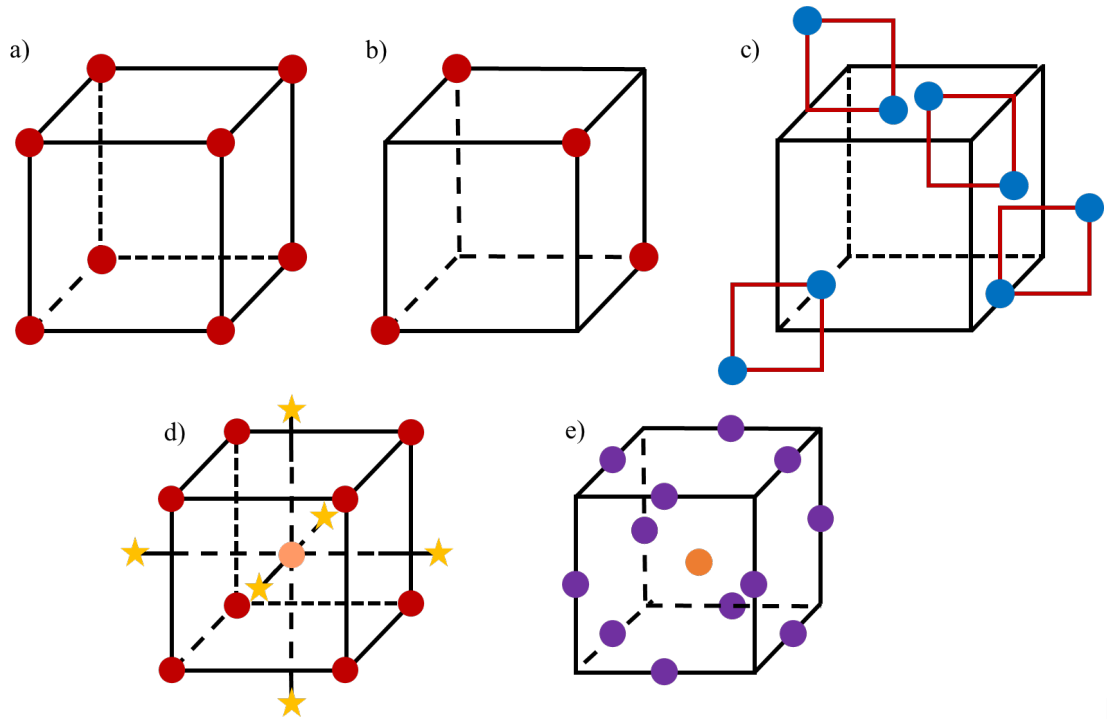

Figure 2.7: Examples of different experimental designs: a) Full factorial; b) Fractional factorial c) Taguchi; d) Central Composite; e) Box-Behnken, adapted from [185].

Central Composite Designs (CCD) frameworks are usually used when the aim is to optimise the response variable or map out the design space based on the dependent variable. These designs are preferred because of their exceptional ability to estimate non-linear relationships between the variables (i.e. curvature), hence, their proposed deployment in cases when a simpler linear model cannot accurately portray the design space. CCDs are produced using factorial designs as a foundation *via* an addition of axial (i.e. star) points as well as centre points [193]. Hence, if it is apparent that a (full/fractional) factorial DoE is insufficient for adequate modelling/optimisation of the given process, then building a CCD framework upon/around it could be an appropriate pathway for further examination. This overlap is pictured below (Figure 2.7d), where the grey circle in the centre represents the centre point experiment, the yellow stars stand for the axial (star) points and the red dots stand for the ever-present factorial design points (without any repetitions displayed in this picture) [185]. Such development allows the user to have a glance beyond the original matrix, therefore, expanding the design space, hence, response surface [185].

Another interesting DoE technique is called the Box-Behnken design (BBD) and is presented in Figure 2.7e. Opting for a BBD can be presumed as a more efficient design choice than CCD [194], [195] when dealing with a vast number of factors (classically,

over three) since it would require fewer runs to complete the experimental campaign. Hence, CCD is frequently preferred when considering few factors as it is more flexible when it comes to two-way interactions. Further, BBD struggles to meet the iso-variance per rotation criteria when working with three factors. A significant advantage of BBD is associated with the lack of experimental trials at the extremes of the design space. If the corner (classical factorial) points pose a risk to the operator/experimental setup or may result in loss of data, adopting BBD is a viable option for mapping the response surface [185].

Owing to the tangible benefits that are offered by this approach to executing experimental campaigns, they have found applications in various industries as well as in the context of AC synthesis as well as post-combustion CCS research.

2.4.2. DoE in Carbon Capture with Adsorbents

There is a number of examples in literature describing use of DoE for optimisation of AC production. For instance, Khalili *et al.* [196] have optimised their carbonaceous adsorbent from pine cones using a CCD. Their investigation examined the effect of three variables: H_3PO_4 to AC precursor ratio (0.66 – 2.34), activation temperature (381.82 – 718.18 °C) and time (69.55 – 170.45 min). The study revealed that all three variables and their interactions had a great impact on CO_2 adsorption capacity (p-values < 0.05), with impregnation ratio having the strongest antagonistic effect as indicated by the highest F-value. Their results suggest the optimum sample to be produced by impregnating the precursor with H_3PO_4 at an agent ratio of 2.2 and activating for 170.45 minutes under 488.82 °C. Higher activation times and temperatures led to increased CO_2 adsorption, which might be due to the formation of micropores yet this phenomenon might stem from the removal of tarry matter/disorganised carbon that was blocking the pores. Further, higher impregnation ratios led to a drop in CO_2 uptake that was associated with destruction of micropores, affecting the performance of the AC.

Alternatively, Yu *et al*. [197] used BBD to analyse the impact of the same three factors: the mass ratio of the activating agent to carbon precursor (although, this study looked at KOH as the agent and coal tar pitch as the parent material), the activation time and temperature each at three different levels (1:0.5 – 2.5; 0.5 – 2 hours; and 650 – 850 °C, respectively). The results suggested that increasing the temperature led to

a decrease in yield due to the enhanced degree of polycondensation reactions, while the interaction of time and temperature became increasingly significant as the temperature was raised. This phenomenon was associated with the strengthened reaction between the KOH and carbon precursor. Additionally, the creation and widening of pores was found to play a vital role in defining the adsorption capacity of the material. The authors also noted a shift towards pore widening at elevated activation temperatures, whilst lower temperatures favoured pore creation. Thus, their optimal conditions for the maximum capture capacity were proposed at 650 °C for 1.25 hours with the impregnation ratio of 2.5 to 1.

In another study [198] BBD was used to optimise a single-step physical activation process for palm kernel shells. The investigation focused on three independent variables: activation time (60 – 120 min) and temperature (750 – 950 °C) as well as the CO_2 (activating gas) flow rate (150 – 450 mL/min). The results indicated temperature to be the most significant factor in determining the yield of the final product, since thermal activation techniques lack an activating agent. However, the optimum conditions for producing their AC were found to be 850 °C under the maximum flow rate and minimum time investigated, chosen based on maximum adsorption capacity rather than a combination of capacity and product yield. These conditions were chosen as they provide an adequate final product yield that exceeds the minimum industrial target (which is suggested to be ~20% [198], [199]). However, it is preferable to use a desirability function when evaluating multiple responses to maximise all targeted variables simultaneously. This study also utilised randomisation of trial sequences, which is a recommended practice for intellectually designed experimental campaigns to avoid uncontrollable luring variables [185].

Apart from synthesis of the carbonaceous material, its application as an adsorbent for CO_2 has also been studied. For instance, García *et al.* [200] completed a three-level two-factor full factorial experimental campaign which included four replicates at the centre of the design. They investigated the combined impact of CO_2 partial pressure (1 – 3 bar) within a total pressure of 5 to 15 bar and the adsorption temperature (25 – 65 °C) on the uptake and breakthrough time. The study concluded that partial pressure had the greatest impact on both of the dependent variables yet no interactions between the factors were determined. Further, Baldovino *et al.* [201], conducted an investigation into carbon capture by nitrogen-functionalised graphene-

oxide looking into adsorption temperature (40 – 120 °C), inlet flow rate (100 – 300 mL/min) and adsorbent loading (4 – 8 mg). The optimum conditions were found to be at 80°C, 100 mL/min and 8 mg. The relatively high suggested optimum temperature of 80°C is associated with the nitrogen-functionalities present on the adsorbent surface as they require elevated temperatures to interact with the CO_2 molecule.

2.5. Pelletisation

Having optimised the synthesis procedure for a given sorbent (most often in powder form), in order to be used at a larger (industrial) scale separation facilities, a transition to mm-scale particles (e.g. beads, pellets and etc.) from fine μm-scale powders is required [202]. This is an essential aspect of adsorbent deployment in a fixed-bed column that facilitates ease of material handling [203], increased heat transfer rate [204] and a lower pressure drop across the bed. Despite powder-form adsorbents' ability to be employed in fluidised-bed systems, fixed-bed units are often opted to avoid issues associated with determination of appropriate fluidisation velocity, as well as, potentially, particle agglomeration within the system. As highlighted previously, advanced reactor configurations do provide benefits of enhancing the heat and mass transfer, though, are generally more CAPEX&OPEX intensive. Therefore, classic fixed-bed systems are preferable for ease of deployment within industry and as such, powder-form materials have to be upscaled not only in terms of production output but also in their particle size. Within the literature on waste-derived carbonaceous sorbents, the aspect of particle size increase is largely overlooked as some bio-residues (especially agricultural by-products) can be used in the "as-received" form (since waste seeds are in a quasi-granular shape). Alternatively, a manual grinding procedure prior to carbonisation (or activation) can be employed resulting in a powder that would require post-processing (e.g. pelletisation) to be deployed in an adsorption column. Another restriction on such a direction of research is the fact that chemically activated carbons employ a tail-end washing stage, which could destroy the particle formed using a water-soluble binder. For these reasons, many works opt for the *activate-then-pelletise* approach utilising a variety of binders (e.g. polyvinyl alcohol (PVA) [204], ionic liquids [205], organic and inorganic binders [206], [207]) and ground/powder-form precursors (e.g. textile industry waste [203], commercial ACs [204]–[206], hazelnut shells [207]).

On the other hand, activation of shaped particles has been investigated for some coal-based [208], [209] and sewage sludge-based ACs [210] as well as other organic precursors (eucalyptus wood [211]; olive stones, rice straw and etc. [212]). These works focused on the alternative *pelletise-then-activate* pathway, with some opting for grinding and then briquetting the char (between the carbonisation and activation steps) while others start by producing shaped materials to be activated.

Regardless of the approach, pelletisation is commonly achieved using a binder solution. Prior art has investigated inorganic binders as a potential options due to their thermal resistance and inertness [207], [213]–[215]. However, these have been shown to produce materials with more modest mechanical properties compared to organic alternatives [215]. Further, they would significantly increase the (inert) ash content of the adsorbent, hence, can be assumed to lead to a drastic drop in specific adsorption capacity. Organic alternatives, on the other hand, may alleviate some of these concerns. Such binders are also more favourable when considering carbonaceous adsorbents' end-of-life (i.e. incineration [209]) as they would partake in the combustion process. Further, binders should be eco-friendly, effective and economical [209]. As such, agricultural waste or recycled plastics could be an avenue to explore in the transition from powder to pellet. One of such proposed materials is polyvinyl alcohol (PVA), which has been previously employed in the context of adsorbent binding [204], [216]. PVA can be opted for since it is low-cost, readily available, non-toxic and biodegradable as well as water soluble [217], [218] (facilitating ease of operation/processing). Further, the hydroxyl groups of the polymer may also assist CO_2 adsorption [73]. For these reasons in this thesis PVA was opted for as the binder.

2.6. Research Gap

Within the research on pelletisation of ACs, the questions of which approach (namely, *pelletise-then-activate* versus *activate-then-pelletise*) to select and why are not addressed. Many studies have overlooked the comparison of the two and have therefore, seemingly randomly chosen a pathway without a complete understanding of the underlying reasoning. Therefore, in this thesis, this question is addressed.

Prior to the pelletisation aspects, however, the matters of suitable and appropriate adsorbent development have to be addressed, preferably aligning with the interests of green chemistry and circular economy. With biomass combustion arising as an

evermore prominent approach for energy generation, this industrial sector may benefit significantly from feasibility studies on waste valorisation to materials for CO_2 adsorption. Therefore, biomass combustion bottom ash (BA) has been used in this thesis as the starting material (i.e. precursor) for production of carbonaceous sorbents, thus valorising this emerging waste stream into value added products *via* a cost-effective yet efficient novel approach.

Further, this thesis examined the applicability of different sorbent production techniques to the BA-derived carbon, namely, physical and chemical activation as well as surface chemical modification. The latter is, classically, aimed at tethering NH_2 functionalities to the surface of the sorbent and is done *via* a two-step technique with the latter involving toxic/hazardous reduction agents [182]. In this thesis, an alternative (more facile and environmentally-friendly) modification method is proposed that is aimed at generating novel functional groups (namely, nitro) on the BA-derived adsorbent. This modification should positively impact the regeneration energy penalty as no chemisorption would be involved.

Finally, in order to optimise the preparation procedure and to elucidate the factors impacting the final product, the experimental campaigns were conducted employing appropriate DoE frameworks. Most literature employs the OFAT approach that does not truly optimise the synthesis as this methodology is not wholistic. As such, this thesis also describes the good practices for applying DoEs as well as highlight limitations and/or benefits of particular designs.

3. Characterisation Techniques

A number of analytical instruments and techniques have been employed, aiming at defining and describing the materials' composition, surface properties and their affinity towards CO_2. For instance, surface morphology has been analysed *via* scanning electron microscopy (SEM). The composition has been analysed using a plethora of methods, namely:

- Surface elemental composition has been gauged *via* energy dispersive X-ray spectroscopy (EDS);
- Bulk composition has been evaluated with proximate analysis as well as ultimate (CHN) analysis;
- Data on surface functional groups has been collected *via* Fourier transform infrared spectroscopy (FTIR);
- Crystallinity of the carbonaceous adsorbents has been analysed with Raman spectroscopy.

The CO_2 adsorption capacities have been collected using thermogravimetric analysis (TGA). The surface porosity and equilibrium adsorption isotherms have been investigated with a sorption apparatus following the methods described in the previous chapter.

These analytical characterisation techniques are briefly discussed below.

3.1. Scanning Electron Microscopy (SEM) & Energy Dispersive X-ray Spectroscopy (EDS)

The Scanning Electron Microscopy (SEM) & Energy Dispersive X-ray Spectroscopy (EDS) are non-destructive analytical techniques which can be used to elucidate the surface morphology of the sample as well as its surface elemental composition. This is achieved *via* subjecting the specimen to a focused (*via* electromagnetic lenses) beam of electrons that interact with the material resulting in a plethora of electrons being emitted off its surface [219]. The variety of emitted electrons are then collected by the detector and based on their properties, data about the material is gathered. For instance, the secondary electrons (ejected inelastically off the surface of the sample) facilitate visualisation of the sample topography (i.e. physical features of the sample

surface), whilst the backscattered incident electrons (emitted due to elastic interactions of the incident particles with atoms located deeper in the specimen) are also used for morphology information as well as provide data on the atomic number (the larger the atom the brighter the portion of the SEM image due to stronger scattering). In order to achieve such phenomena, an electron gun supplies the high-energy beam that accelerates to 10 – 20 kV while the experiment chamber is usually put under a high vacuum > $1x10^{-4}$ mbar. The vacuum serves to prevent the incident beam interacting with particles from ambient air as well as to preserve the filament.

Sputter-coating of SEM samples with conductive particle (e.g. C, Au) layer of up to ~20 nm can be considered as part of sample preparation. In this process, the sample is covered with a thin layer of conductive matter to facilitate conductivity, negate charging and to increase the number of secondary electrons emitted of the surface [220]. In this thesis, however, the samples were not sputter-coated with gold as the studied carbonaceous adsorbents are conductive. Further, in order to avoid confusion between the elemental aluminium as part of the ash impurities and the aluminium sample stub material (i.e. background of the scanned surface), the specimens were placed onto copper plates. Following a similar logic, the use of carbon tape as the adhesive has been avoided. Instead, isopropanol has been opted for which was allowed to evaporate prior to analysis.

Nevertheless, EDS (also often referred to as EDX) employs characteristic x-rays emitted from the specimen to analyse material composition. The number of emitted x-rays and their energy is picked up by the detector, thus allowing for quantitative and qualitative analysis (respectively) of the sample's elemental composition (as they correspond to particular "jumps" of specific atoms). However, EDS struggles to accurately quantify the atoms with low atomic masses and numbers (generally, lower than Na with ~23 amu and z = 11), e.g. elemental carbon. This is associated with weaker signals (i.e. longer wavelengths of x-rays) from lighter atoms that may even be absorbed within the specimen itself [221]. Further, this technique is focused on the surface chemical composition. Therefore, particular bulk analysis techniques were also employed to quantify the carbon content of the adsorbents, such as ultimate and proximate analysis.

3.2. Ultimate Analysis

Another elemental analysis technique employed in this thesis is called ultimate analysis, otherwise known as CHN analysis, a destructive bulk analysis technique for indirect determination of elemental carbon, hydrogen and nitrogen contents based on their respective final combustion products (i.e. CO_2, H_2O and N_2, respectively). In order to achieve complete combustion, the test is conducted at elevated temperatures (> 900 °C) in a pure (N5.5) oxygen environment (with He being employed as the carrier gas) following the Pregl-Dumas method [222]. Upon combustion, the gas mixture passes through copper to remove excess of oxygen as well as to reduce any nitrogen oxides (in cases when final thermodynamic combustion state has not been achieved) to N_2. Afterwards, the gases are separated *via* gas-phase chromatography and quantified (for example, using thermal conductivity detectors). Various adsorbents and catalysts can also be added to remove any potential contaminants and to facilitate combustion, respectively [222].

In this thesis, ultimate analysis has been conducted employing a Thermo Scientific Flash 2000 Organic Elemental Analyzer and using acetanilide as the reference material.

3.3. Thermogravimetric Analysis

A thermogravimetric analysis (TGA) equipment is an invaluable apparatus as it allows for continuous measurements of sample mass over a period of time whilst controlling both the gaseous environment as well as temperature in the chamber. Classically, the sample is positioned into an inert crucible which is then put into the furnace on a sensor-equipped sample holder. High temperature applications (e.g. proximate analysis) require thermally stable (i.e. alumina) crucibles, whereas low temperature tests (e.g. adsorption-desorption) can be conducted with aluminium crucibles. Regardless, the sample holder is connected to a high-precision microbalance that allows for continuous recoding of mass change. This compensation balance is usually equipped with a counter weight and a magnet that compensates for the weight of the sample at a given moment/temperature. The sample temperature is measured using thermocouples located in the immediate vicinity of the sample.

Herein, a TGA apparatus has been employed for measuring CO_2 adsorption capacity of the sorbents as well as for proximate analysis. It is noteworthy, that both of the tests were conducted at atmospheric pressures.

3.3.1. Proximate Analysis

Another destructive bulk analysis technique (aimed at material composition characterisation) deployed in this thesis is proximate analysis. This established analytical procedure aims to elucidate the quantities of (in alphabetical order) ash, fixed carbon, moisture and volatile organic compounds (VOCs) in a carbonaceous material. In this thesis the employed method follows ASTM D7582 [223] (and can be visualised from Figure 3.1) employing a thermogravimetric analyser Mettler Toledo TGA 2 system to allow for continuous monitoring of mass change.

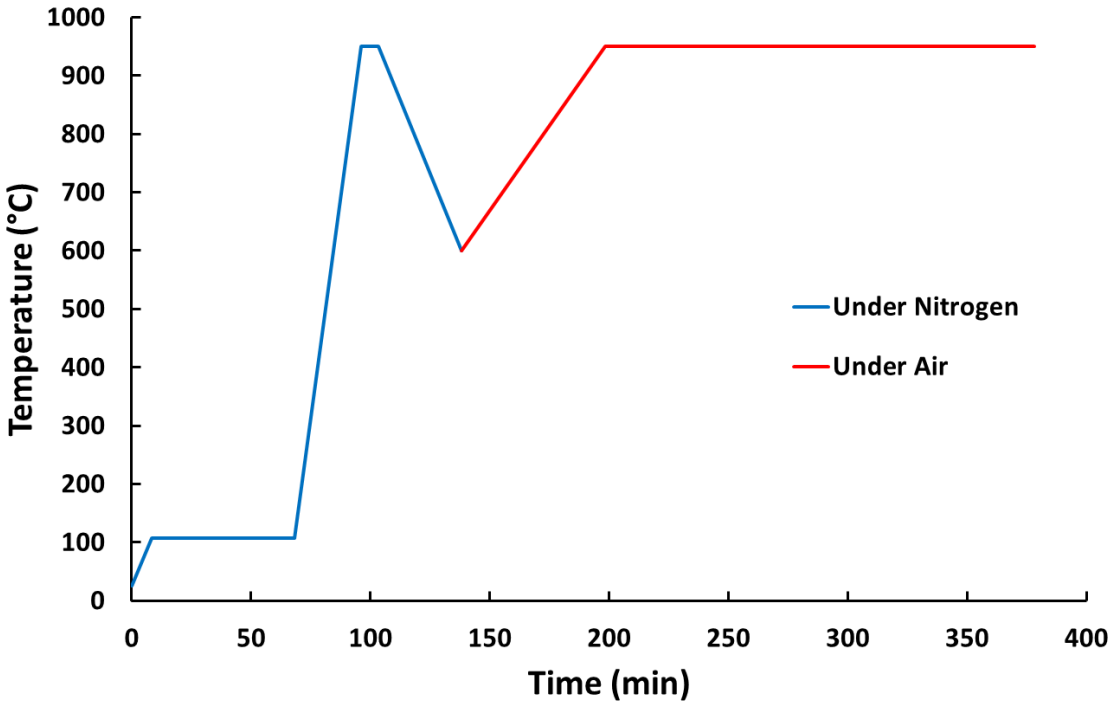

Figure 3.1: Temperature profile of proximate analysis.

In order to determine the moisture content, the sample was heated to 107 °C under N_2 (22 mL/min), where it was kept for one hour. Then the temperature was raised to 950 °C with a ramping rate of 30°C/min, whilst supplying the same (inert) gas flow rate. After a seven-minute isothermal step, the VOC content is determined. Prior to the final stages of the analysis, the sample has to be cooled down to 600 °C at which point the atmosphere should be switched to an oxidising gas (i.e. air at 22 mL/min). Upon changing the gas, the material was heated to 950 °C at 6 °C/min (i.e. the final

temperature is reached over a period of 60 min). At this point the sample was left for a three-hour hold with the resulting residue allowing for quantification of the ash content. Finally, the fixed carbon content is calculated by taking away the mass of each of the other constituents from the initial sample mass.

3.3.2. CO_2 Adsorption Capacity Tests

Adsorption of CO_2 has been evaluated using a TGA apparatus. However, in these tests the focus is drawn towards the increase of mass upon supply of the adsorbate gas. In order to quantify the adsorption capacity, the material was placed into a crucible and onto a balance arm located inside the furnace chamber. For tests at different temperatures the employed program was slightly adapted yet the generalised approach is presented in Figure 3.2.

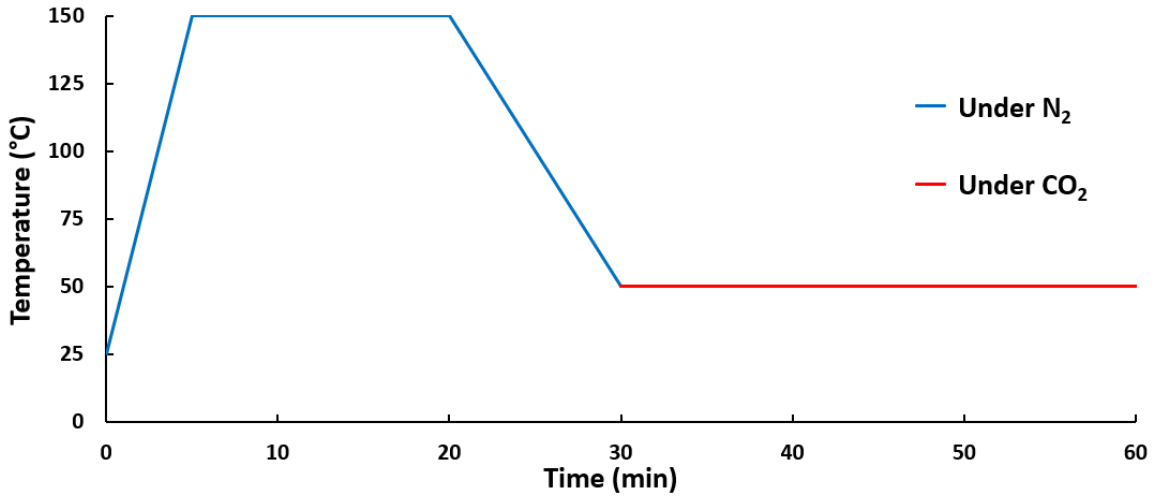

Figure 3.2: Temperature profile of a CO_2 adsorption capacity measurement.

As evident from the temperature profile of these tests, the initial step was a 15-minute-long desorption conducted under an inert gas flow (i.e. 50 mL (value selected to minimise use of resources and due to independence from volumetric flow as per initial trials) of N_2) at 150 °C. This allows for loss of any pre-adsorbed from ambient air species (e.g. moisture, CO_2) whilst avoiding decomposition of VOCs present in the material. Having purged the adsorbent, the sample was then cooled down (-10 °C/min) to the desired temperature (in Figure 3.2 – 50 °C) where the gas flow was switched to 50 mL of CO_2, hence, initialising the adsorption step which lasted for another 30 minutes. A sharp rise in sample mass followed by a plateau (mass increase of <0.005 mg/min) at a particular value would be noted, which constituted the adsorbent to reach its equilibrium uptake. This reading would then be related to the sample mass providing

a specific value for the CO_2 adsorption capacity. The continuously recorded mass change data would then also be used to investigate the kinetics of the adsorption process.

3.3.3. CO_2 Adsorption Kinetics

Kinetics of adsorption have a major impact on the adsorption unit capital costs as well as the bed size [160]. As such, there is a vast amount of literature focusing on this aspect of adsorption.

The two most prominent kinetic models used for investigations into the kinetics of physisorption are the pseudo-first order (PFO) and pseudo-second order (PSO). A striking majority of published literature is inclined to favour the latter over the former owing to a number of issues arising as a consequence of the implemented mathematical technique. These aspects are elaborated on in the literature and an improved methodology is proposed that utilises fractional coverage (facilitates comparison between models) [224]. Kinetics of CO_2 adsorption can be evaluated using the models described in Table 3.1.

Table 3.1: Examples of kinetic adsorption models.

Name	Equation (non-linear form)	Description
PFO	$F = \frac{q_t}{q_e} = 1 - e^{-K_1 t}$	q_t (mg/g) – uptake at time t (s) q_e – equilibrium uptake (mg/g) K_1 – the PFO rate constant (1/s) F – fractional coverage
PSO	$F = \frac{q_t}{q_e} = \frac{q_e K_2 t}{1 + q_e K_2 t}$	q_t (mg/g) – uptake at time t (s) q_e – equilibrium uptake (mg/g) K_2 – the PSO rate constant (g/mg s) F – fractional coverage
Ritchie's Equation	$F = 1 - (1 + (n-1)K_R t)^{\frac{1}{1-n}}$	F – fractional coverage t – time (s) K_R – Ritche's rate constant (1/s) n – the number of sites occupied by the adsorbate molecule

Elovich	$q_t = \frac{1}{\beta}\ln(1+\alpha\beta t)$	α (mg/g) and β – the Elovich fitting parameters q_t (mg/g) – uptake at time t (s)
Intraparticle Diffusion	$q_t = C + K_D t^{0.5}$	q_t (mg/g) – uptake at time t (s) K_D – the diffusion rate constant (g/mg $s^{1/2}$ C – thickness of the boundary layer (mg/g)

3.4. Volumetric Adsorption Analysis

3.4.1. Surface Area & Porosity Analysis

Another concept extensively employed in describing porous matter is the porosity and surface area analysed *via* proxies (e.g. methylene blue number, iodine number). In realm of gas adsorption this is commonly done by means of evaluation of the physisorption isotherms, their types and features (e.g. hysteresis). The data for this analysis is commonly collected from the N_2 adsorption isotherms at -196 °C. Alternative gasses (i.e. Ar and Kr at 87 K) also may be applied for this analysis; however, liquid nitrogen is significantly less costly [86]. Nevertheless, Prior to the measurement, however, the specimen is degassed under vacuum at elevated temperatures (in this thesis the procedure of initial purge for surface area and porosity analysis entailed a quick (15 °C/min) ramp to 200 °C, followed by maintaining these conditions for six hours). Then, upon cooling to analysis temperature, the adsorbate is supplied incrementally until the pressure reaches 1 bar. Based on the resulting adsorption isotherm, the surface area is determined *via* the Brunauer-Emmett-Teller (BET) equation (though, only using the data in the partial pressure range of 0.05 – 0.35 [86]).

$$\frac{p}{v(p_0 - p)} = \frac{1}{v_m C} + \frac{C-1}{v_m C}\left(\frac{p}{p_0}\right) \qquad \text{Eq. 1}$$

where, v (cm^3/g) is the specific quantity of the gas adsorbed at a relative pressure p/p_0, C is the BET constant and v_m (cm^3/g) is the specific quantity of the gas adsorbed that constitutes monolayer coverage.

There are a number of methods (e.g. t-plot, Dubinin-Astakhov, Dubinin-Radushkevich) to determine the micropore volume and surface area. Most commonly used approach in the literature is the t-plot method due to its versatility. This technique relies on estimating the surface area based on the thickness of the produced

adsorbate layer , *t* (nm), which is also often referred to as statistical thickness, [225] as compared to a reference non-porous material. There are a number of equations aimed at calculating the statistical thickness but for carbonaceous adsorbents the Carbon Black equation [226] below is preferred.

$$t = 0.88\left(\frac{p}{p_0}\right)^2 + 6.45\left(\frac{p}{p_0}\right) + 2.98 \qquad \text{Eq. 2}$$

The provided coefficients are appropriate for N_2, hence, allowing the BET data to be reinterpreted, although, the Carbon Black equation should be linear in the relative pressure range between 0.2 and 0.5 [225]. By plotting the adsorption capacity over the thickness, one can obtain the micropore volume and surface area.

However, this method has been shown to underestimate the microporous area [227] as well as face limitations due to the presence of curvature associated with a varying adsorbed layer thickness which depends on the diameter of the pore itself [228].

A further paramount parameter of an adsorbent is its pore size distribution which is commonly found by repurposing the same data (N_2 isotherm at 77 K) at near saturation partial pressures levels (P/Po ≈ 0.99) *via* the Barrett-Joyner-Halenda (BJH) equation [229], [230]. This information could be employed in Eq. 3 to calculate the pore sizes.

$$V_{pn} = \left(\frac{r_{pn}}{r_{Kn} + (\Delta t_n/2)}\right)^2 \left(\Delta V_n + \Delta t_n \sum_{i=1}^{n-1} Ac_i\right) \qquad \text{Eq. 3}$$

In the above equation V_{pn} (cm^3/g) stands for the volume of the n-th pore; r_{pn} (nm) and r_{Kn} (nm) are the pore and inner capillary radii, respectively; ΔV_n (cm^3/g) is the volume desorbed; Δt_n (nm) is the change in thickness of adsorbed N_2 layer; Ac_i (m^2/g) is the average exposed area of the pores where the physically adsorbed gas is lost.

The BJH analysis of the pore size distribution is often used in the literature as a way to describe the material's surface, despite some proposed alternatives (e.g. density functional theory) and limitations when dealing with smaller mesopores [86] as well as non-uniform pore structures [82]. The latter however, could be overcome by using other isotherms of adsorption (e.g. Toth [231]) or with kinetic models (e.g. Elovich [232]) that can help assess adsorbent surface heterogeneity as well as other fundamental models that facilitate comprehensive material characterisation.

3.4.2. Equilibrium Adsorption Isotherms

Equilibrium adsorption isotherms which in this thesis have been employed to characterise the adsorbents are shown in Table 3.2 below:

Table 3.2: Examples of equilibrium adsorption isotherms.

Name	Equation	Description
Langmuir	$q_e = \frac{q_{max} K_L P}{1 + K_L P}$	q_{max} – maximum uptake (mmol/g) P – adsorbate pressure (Pa) K_L – adsorption affinity/Langmuir constant (1/Pa) q_e – equilibrium uptake (mmol/g)
Multi-site Langmuir	$q_e = \sum_{i=1}^{z} \frac{q_{max(i)} K_{L(i)} P}{1 + K_{L(i)} P}$	$q_{max(i)}$ – maximum uptake at the appropriate site (mmol/g) P – adsorbate pressure (Pa) $K_{L(i)}$ – adsorption affinities/Langmuir constants (1/Pa) q_e – equilibrium uptake (mmol/g)
Freundlich	$q_e = K_F P^{1/n}$	K_F – Freundlich constant (mmol/(g*Pa$^{1/n}$)) P – partial pressure of the gas (Pa) q_e – equilibrium uptake (mmol/g) n – the dimensionless heterogeneity factor
Toth	$q_e = \frac{q_{max} K_T P}{(1 + (K_T P)^n)^{1/n}}$	q_{max} – maximum uptake (mmol/g) P – adsorbate pressure (Pa) K_T – Toth constant (1/Pa) q_e – equilibrium uptake (mmol/g) n – the dimensionless heterogeneity factor

These isotherm models identify a plethora of factors that inform the process model and to evaluate the properties of the material (e.g. adsorbent-adsorbate interactions, adsorption mechanism, adsorbent surface homo- or heterogeneity, the porous structure and etc. [233]–[235]). Langmuir and Freundlich isotherms are most

commonly used [236], [237]. Alternatively, the Toth isotherm model is often employed for adsorption in gaseous media due to its ability to overcome some of the challenges associated with the mentioned above models [238], [239] as well as Multi-site Langmuir [240]. The latter models benefit from a larger number of fitting parameters, which may facilitate a more accurate fit. On the other hand, they are more prone to overfitting (i.e. fitting random noise). As such, to select the most appropriate model evaluation of not only the regression coefficient (R^2) but also other indicators (e.g. normalised root mean square error (NRMSE), the predictive and adjusted regression coefficients (R^2_{pred} and R^2_{adj}, respectively)) is advisable.

In addition, in order to fit the experimental data to the models, non-linear regression can be deployed owing to the fact that most of the isotherm models possess more than two fitting parameters [231]. Moreover, transformation of non-linear equations into their linear forms might result in a skew towards a parameter/condition, i.e. leading to biased interpretation [241].

3.5. Spectroscopic Analysis

Two spectroscopic analysis techniques have been employed in this thesis, namely, Raman and Fourier-Transform Infrared (FTIR) spectroscopies.

3.5.1. Fourier-Transform Infrared Spectroscopy

Infrared (IR) spectroscopy is a versatile non-destructive method for gathering data on the surface functionalities of carbonaceous adsorbents. This approach to material characterisation is based on the phenomenon of absorbance of a particular IR wavelength by a particular covalent bond leading to a change in the IR light received by the detector. This technique is not usually employed for characterisation of inorganic matter as ionic bonds are not strongly excited (i.e. do not change their dipole moment during internal vibrations) upon being subjected to IR spectra [242]. Nevertheless, it is invaluable for characterisation of surface functional groups of carbonaceous adsorbents.

IR absorption induces molecular vibration. Depending on the bond and the applied frequency of the IR light, various vibrational modes (e.g. (a)symmetrical stretching/bending) for different molecules would be noted leading to identification of the surface functionalities. Within this, FTIR is commonly conducted either by employing potassium bromide (KBr) or *via* the attenuated total reflection method. The

former is employed as the sample carrier as, firstly, KBr does not absorb IR light in the FTIR range (i.e. the wavenumbers of ~400 – ~4000 cm^{-1}) and secondly, it dilutes the black carbonaceous matter allowing the detector to receive more IR radiation. In the attenuated total reflection method, the sample is directly in contact with the crystal anvil of the spectrometer. The IR beam is supplied through the crystal and is reflected off the sample towards the detector. However, the interaction with the sample occurs through an evanescent field/wave, where the absorbance of the IR light occurs. As such, the reflected beam lacks the specific wavelengths, hence, is reduced/attenuated. This technique is believed to be quite sensitive when good contact between the crystal and the sample is achieved [243], does not require additional chemicals as well as is easier in practical implementation.

3.5.2. Raman Spectroscopy

A further spectroscopic technique used in this thesis is Raman spectroscopy, which is somewhat a complimentary technique to FTIR in this research. It is a non-destructive method that can been used to assess the crystallinity of the produced carbonaceous adsorbents. This is achieved by evaluating the intensity of the G- and the D-band carbon peaks. The latter is used as an indication of the defects of the structure and/or disordered/sp^3-hybridised C atoms as well as the edges of graphene layer sheets, whereas the former describes the graphitic/sp^2-hybridised C atoms [244], [245]. In order to obtain this data, a monochromatic incident beam (in this thesis – a green laser with the wavelength of 532 nm) has to be shone onto the sample. Upon contact with the specimen, some of the light would be absorbed, exciting the bonds, and then be reemitted elastically (at same frequency), i.e. Rayleigh scattering. However, a small proportion of it would be scattered inelastically, resulting in a change of frequency/colour (hence, the phenomenon of Raman shift) of the wave. The latter occurs if the scattered photon returns (upon relaxation) to a higher/lower vibrational energy level [246]. A visualisation of this phenomenon is provided in Figure 3.3.

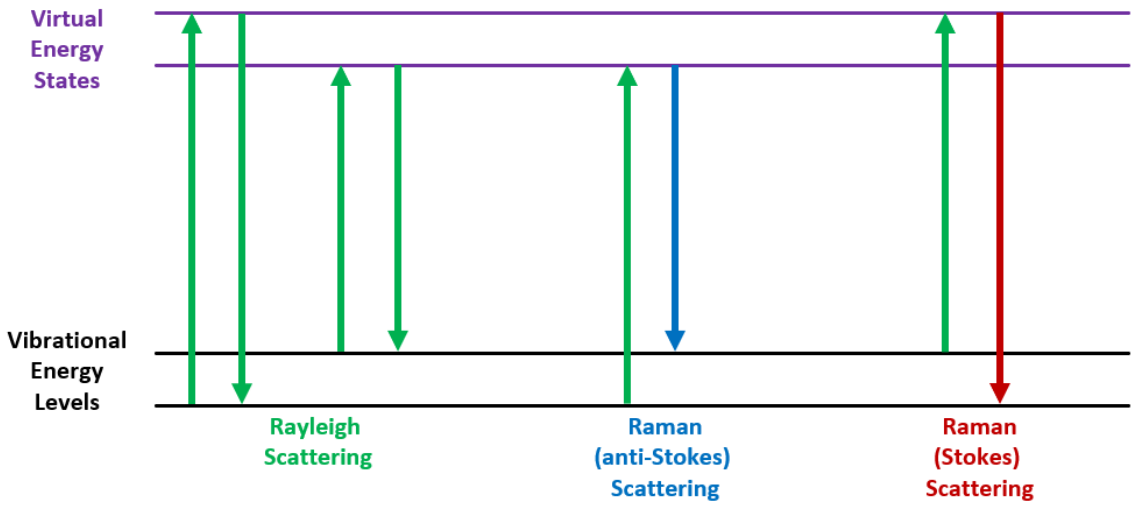

Figure 3.3: The energy transition of Raman spectroscopy.

Raman spectroscopy does not facilitate analysis of non-polarisable molecules (i.e. a distortion of the electron cloud around the atoms is required) [247]. As such, highly polar bonds (e.g. O-H) would only produce weak Raman scatters, whereas a bond with a relatively evenly distributed electron cloud (e.g. graphitic C=C) can vibrate strongly. The latter rather symmetric bonds are not as prominently shown on an FTIR spectrum; therefore, Raman can complement IR analysis.

4. Virgin Carbon

4.1. Introduction

Sustainably sourced biomass is viewed as a potential fuel for producing net zero emissions energy as the carbon dioxide released during combustion has been previously absorbed by the plant matter from the atmosphere during its growth [248]. Further, this approach has a strong potential of becoming a net-negative emissions technology if the emitted CO_2 is captured and subsequently stored underground. As such, the concept of bioenergy with carbon capture and storage (BECCS) is an emissions mitigation strategy that is heavily relied upon in 85% of the scenarios described in the reports from the Intergovernmental Panel on Climate Change (IPCC) that meet targets of keeping global warming below the 2 ºC target [15].

However, combustion of sustainable biomass is associated with co-generation of ash – contributing to 6.8 wt.% of biomass feedstock on average [19]. In the case of the UK, annual production of wood ash amasses to nearly 52 kilotonnes [27] and, with the country aiming to abandon unabated coal as fuel source by 2025 [28] (due to conversions of coal-fired units into their biomass-combusting counterparts within the UK power sector [249]) waste biomass combustion ash management is poised to become a more pressing issue due to it inherently different physicochemical properties to that of coal's.

Therefore, biomass combustion bottom ash (BA) has been used in this thesis as the starting material (i.e. precursor) for production of carbonaceous sorbents for CO_2 adsorption, thus valorising this emerging waste stream into value added products *via* a cost-effective yet efficient novel approach.

4.2. Extraction of Carbon from Biomass Combustion Bottom Ash

BA has been utilised as the adsorbent precursor in this project. The BA has been collected from a biomass-fired power plant operated by Drax and located in North Yorkshire, UK. However, as can be inferred from Figure 4.1, the raw BA is, firstly, moist (40 – 60%), and secondly, presents a significant degree of heterogeneity. This is, however, to be expected, as the varying nature of waste streams is an ever-present obstacle in the "waste-to-value" chain. As such, in order to extract the carbon, the raw BA was first dried overnight (12 hours) at 110 °C in an oven (Fisher Scientific 825F).

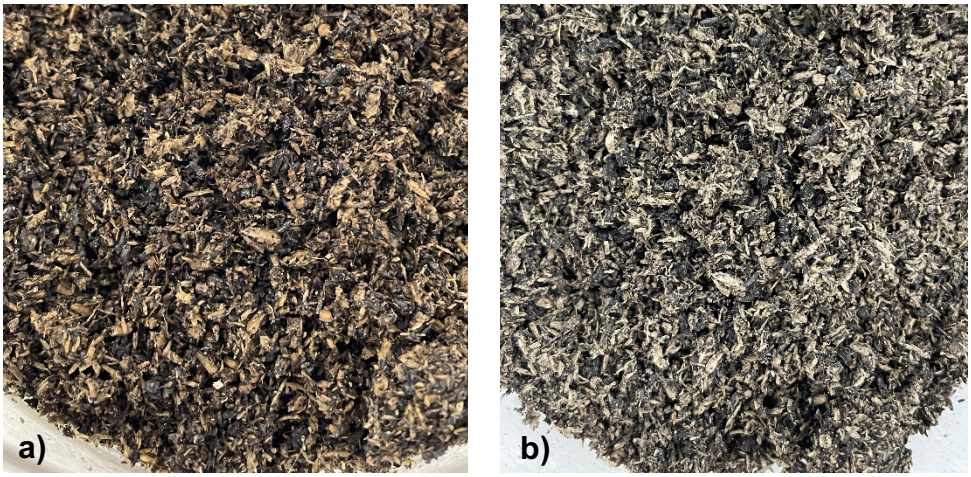

Figure 4.1: Images of raw bottom ash; a) wet, b) dried.

The resulting dry bottom ash (Figure 4.1b) was then ground using a lab-scale ball mill (Capco Ball Mill Model 2) *via* a two-step process. Initially, an hour-long crude grind (at ~ 120 rpm) in a 1-L alumina jar (with the appropriate charge) was conducted. The matter was then separated through a standard sieve with an aperture size of 1.4 mm (mesh size: 14) to alleviate the bigger particles. The fraction that passed through the sieve was used for further processing in this research, whereas the retained fraction (containing mostly unburnt biomass) was left untouched. This reclaimed material could possibly be reintroduced into the boiler in order to offset some of the cost associated with sorbent production or regeneration. Nevertheless, the bottom fraction was transferred into a 0.5 L jar (with the appropriate loading) for the fine grinding step (1 hour at ~140 rpm). Following this, a stack of standard sieves (aperture range 0.1 – 1.4 mm) was manually shaken. The desired carbonaceous fraction (i.e. the virgin carbon) was extracted from the bottom of the stack, hence, the name of BA-100-P, which stands for “Bottom Ash – 100 µm – Passed through the sieve”. The mass yield of BA-100-P resulting from this dry extraction process ranged between 4 – 11%. This fraction was then taken for characterisation and used as the precursor for all of the investigations described in this thesis.

However, alongside the variation in mass yield of the dry extraction process, the CO_2 capture capacity and the exact composition of the material presented some differences. As such, prior to characterisation, a satisfactory “baseline” material had to be produced, hence, the material variation has to be assessed and minimised.

4.3. Material Variation

Similar to the BA itself, BA-100-P also presented some degree of material variation, which is expected of materials derived from heterogenous waste. This may stem from a plethora of factors occurring upstream (i.e. at the biomass combustion facility) including changes in the fuel composition, operation of the boilers as well as the exact boiler at Drax from which the BA was collected and etc. However, the latter can be identified as the potential culprit due to the findings described in the following section. As such, investigations into this hypothesis have been conducted and the variation between different virgin carbons (i.e. different samples of BA-100-P) has been assessed in terms of the composition of BA-100-P as well as the adsorption capacity of the produced sorbent.

Composition of the produced carbonaceous fractions was firstly analysed *via* Proximate analysis as per ASTM D3172 [250]. This technique is an established method of quantifying the moisture content of the material followed by the volatile organic compounds (VOC) and fixed carbon quantities coupled with the ash content of the sample. Proximate analysis is often applied to characterise the nature of carbonaceous matter [251]–[255], hence, the results of analysis of BA-100-P from different boilers is described in Table 4.1.

Table 4.1: Results of proximate analysis of BA-100-P from individual boiler units.

Boiler	Moisture, wt%	VOC, wt%	Fixed C, wt%	Ash, wt%
U-1	2.5	38.23	34.77	24.5
U-2	2.33	41.84	30.5	25.33
U-3	2.67	37.83	35.67	23.83
U-4	3.83	36.17	24.67	35.33

As evident from Table 4.1, some variation in BA-100-P may be attributed to the exact boiler (U1 – 4) from which it has been collected with the strongest discrepancies stemming from boiler U-4. Further, a significant portion of the as-received ash has been supplied by Drax without specifying the exact unit where the BA was collected. As such, in order to minimise some of this variation, the bottom ash was mixed prior to ball milling whilst excluding boiler U-4. This procedure results in a decrease in the variation between the different virgin carbon batches. However, other lurking variables would still impact the dry extraction process, leading to some deviation as can be seen

in Table 4.2. The outmost left column denotes the batch number. Each of the batches employed the same mixing procedure.

Table 4.2: Results of proximate analysis of BA-100-P from mixed BA.

Batch Number	Moisture, wt%	VOC, wt%	Fixed C, wt%	Ash, wt%
1	3.23	35.47	35.13	26.17
2	3	38	32.25	26.75
3	3.17	36.83	34.5	25.5
4	3.5	38.17	36	22.33
5	4.25	37	34	24.75

Similar tends have been observed for the equilibrium CO_2 adsorption capacity. The virgin carbon derived from boiler U-4 presented the lowest uptake (9.579 mg/g) of the three other boilers. Discarding the outlier and having mixed the BA from the three other units (U1-3) allowed for a repeatable BA-100-P fraction to be extracted with the adsorption capacities presented in Table 4.3. Further, in order to minimise the impact of the variation inherent to a heterogeneous waste-derived product, the sample crucibles used for the adsorption tests (conducted *via* TGA) were filled to the brim, hence, maximising sample mass to present a more accurate average value. A lower sample mass may have presented a (slightly) different adsorption capacity that would also be more prone to variation.

Table 4.3: CO_2 adsorption capacity at 50 ºC for different batches of BA-100-P.

Batch Number	CO_2 Uptake, mg/g	CO_2 Uptake, mmol/g	Relative Standard Deviation
1	15.689	0.356	2.36%
2	15.227	0.346	
3	14.677	0.333	
4	14.949	0.340	
5	15.461	0.351	

The derived virgin carbons present an acceptable degree of variation considering their heterogeneous waste parent material (i.e. biomass combustion bottom ash). Nevertheless, each experimental campaign presented below has been conducted utilising a single given batch of BA-100-P, hence, the negligible changes in the virgin carbon baseline adsorption capacity in each of the modification/processing chapters.

Prior to this, however, BA-100-P derived from the first batch has been fully characterised.

4.4. Virgin Carbon Characterisation

A number of analytical instruments and techniques have been employed, aiming at defining and describing the material composition, surface properties and its interaction with CO_2. Having partially described the composition of BA-100-P in Section **Error! Reference source not found.**, a further description of the elemental components is provided in the following section.

4.4.1. Scanning Electron Microscopy (SEM) & Energy Dispersive X-ray Spectroscopy (EDS)

SEM and EDS analysis (JOEL IT200) has been conducted employing copper plates as background in order to differentiate the elemental aluminium present in the ash impurities from the Al in the sample stub. Additionally, the sample was fixed on the plate using isopropanol as opposed to carbon tape to avoid similar issues with confusion of elemental composition of the sample and the scan background.

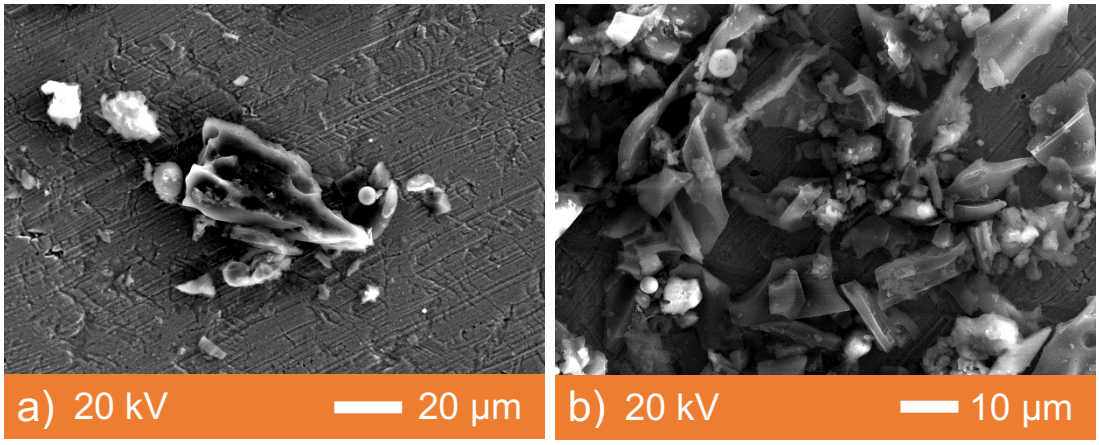

Figure 4.2: SEM images of BA-100-P.

As can be visualised from Figure 4.2, the produced sorbent is a fine heterogenous powder, containing both carbonaceous species (shard-like shapes) and ash impurities (aluminosilicate cenospheres). The latter are believed to be typical of ashes [128] with their form stemming from the amorphous coating arising from the abrupt quenching of the material [256].

The hypothesis of the aluminosilicate nature of the spheres was corroborated by the EDS. The results presented in Table 4.4 were averaged from 10 discrete points along the surface of the sample.

Table 4.4: Surface elemental composition of BA-100-P.

Element	Weight %
C	72.7
O	24.6
Ca	1.4
Si	0.7
Al	0.4
Mg	0.2

It should be noted that, firstly, EDS is a surface analysis technique, as such, might not be representative of the bulk of the material. Secondly, EDS struggles to estimate the quantities of elements with a low atomic number and mass. Hence, good practice guidelines suggest not to rely on the composition for elements that are below Na (i.e. atomic number < 11) in Mendeleev's periodic table; in this case the percentage of elemental C may be overestimated. As such, ultimate analysis can be employed to overcome both of these limitations and more accurately quantify the elemental carbon content.

4.4.2. Ultimate Analysis

Ultimate analysis (Thermo Scientific Flash 2000 Organic Elemental Analyzer) (otherwise known as CHN-analysis) has confirmed successful extraction of carbon from the biomass combustion ash waste stream.

The virgin carbon was shown to contain nearly 60% (by weight) of carbon atoms, ~ 3% of H and just under 0.5% of elemental nitrogen as per Table 4.5.

Table 4.5: Ultimate (CHN) analysis results of BA-100-P.

Element	Weight %
C	60.07
H	3.16
N	0.42
Other	36.35

These results agree with the proximate analysis data (Table 4.2) as the total elemental carbon content comprises both fixed C and the elemental carbon found in the VOCs, thus comprising approximately 60 wt%.

4.4.3. Spectroscopic Analysis

BA-100-P has also been studied *via* spectroscopic analysis techniques, namely, Fourier-Transform Infrared (Perkin Elmer Spectrum One) and Raman (Renishaw Invia Raman Spectroscope) spectroscopies.

4.4.3.1. Fourier-Transform Infrared Spectroscopy (FTIR)

BA-100-P has produced a quite vivid spectra containing a multitude of different bonds as seen in Figure 4.3. The spectrum was acquired *via* the standard attenuated total reflection method.

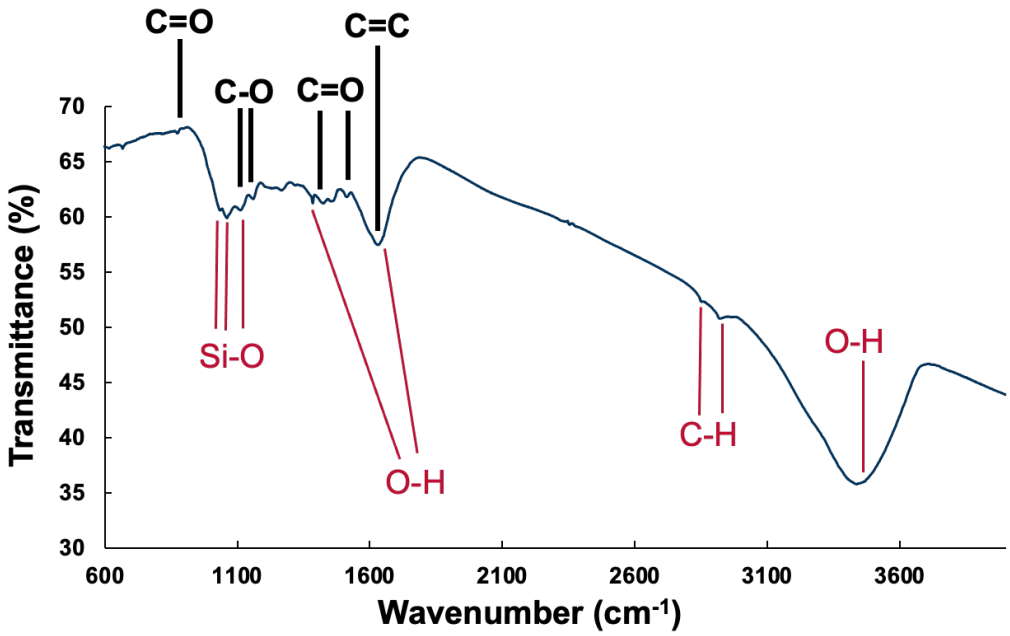

Figure 4.3: FTIR spectrum of BA-100-P.

The peaks located at wavenumbers of 873 cm^{-1}, 1425 cm^{-1} as well as 1515 cm^{-1} could all be assigned to various vibrational modes and/or different configurations of the C=O bond found in carbonyl functionalities and/or metal carbonates [242], [257], [258]. Further, a prominent band representative of the hydroxyl group is visible at ~ 3450 cm^{-1} [259]–[261] as well as the stretching vibrations [259] and bending vibrations found at 1383 cm^{-1} and 1634 cm^{-1}, respectively [242]. The latter, however, could be reassigned to stretching of aromatic C=C bonds found in graphene-like structures [261] with other graphitic (namely, graphene oxide) peaks being the C-O stretch at 1114 cm^{-1} and 1160

cm^{-1} [261], [262]. Another wavenumber associated with the C-O bond (though, from epoxy groups [244]) is located at ~ 1062 cm^{-1}. The latter three peaks (as well as the band at 1036 cm^{-1}) can be alternatively described by asymmetric stretching vibrations of the Si-O bonds [242] which could stem from the ash impurities in the sample with their different positions possibly occurring due to presence of both pure silicon- and Al/Si-based structures (the Si-O-Al bond would lead to a "red shift", i.e. decrease, of the wavenumber) as well as both crystalline and amorphous particulates within BA-100-P [263]. Finally, the wavenumber of 2857 cm^{-1} and 2930 cm^{-1} are associated with the aliphatic C-H bonds [261], [262] and a peak at 2355 cm^{-1} is visible due to presence of CO_2 from ambient air in the background of the scan [264].

4.4.3.2. Raman Spectroscopy

Raman spectroscopy is a complimentary technique to the FTIR method of gauging the crystallinity and the surface defects on the sample. Figure 4.4 clearly displays two peaks around 1353 cm^{-1} and 1585 cm^{-1} representing the D-band and G-band carbons, respectively. The former is ascribed to the defects on the graphene plane or as edges of graphene sheets as well as disordered carbon atoms in a sp3 hybridisation state, whilst the latter is associated with the graphitic sp2-hybridised atoms [244].

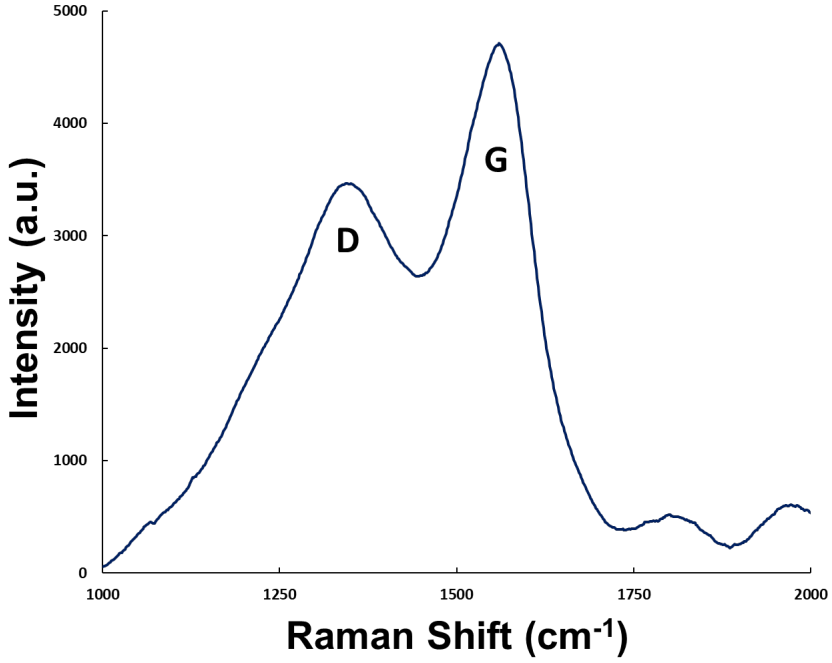

Figure 4.4: Raman spectrum of BA-100-P.

The ratio of the intensities of the aforementioned peaks (ID/IG) can be employed to

gather information on the defects and the crystallinity of the carbon sample. In case of BA-100-P, the ID/IG ratio is 0.73. This number, firstly, further confirms successful extraction of carbon from BA (due to the presence of D- and G-bands) as well as will serve as a baseline for comparison of the crystallinity of the adsorbents upon activation.

4.4.4. Surface Area Analysis

Surface area and porosity analysis has been conducted following the N_2 adsorption isotherm at 77K using the Micromeretics ASAP 2020.

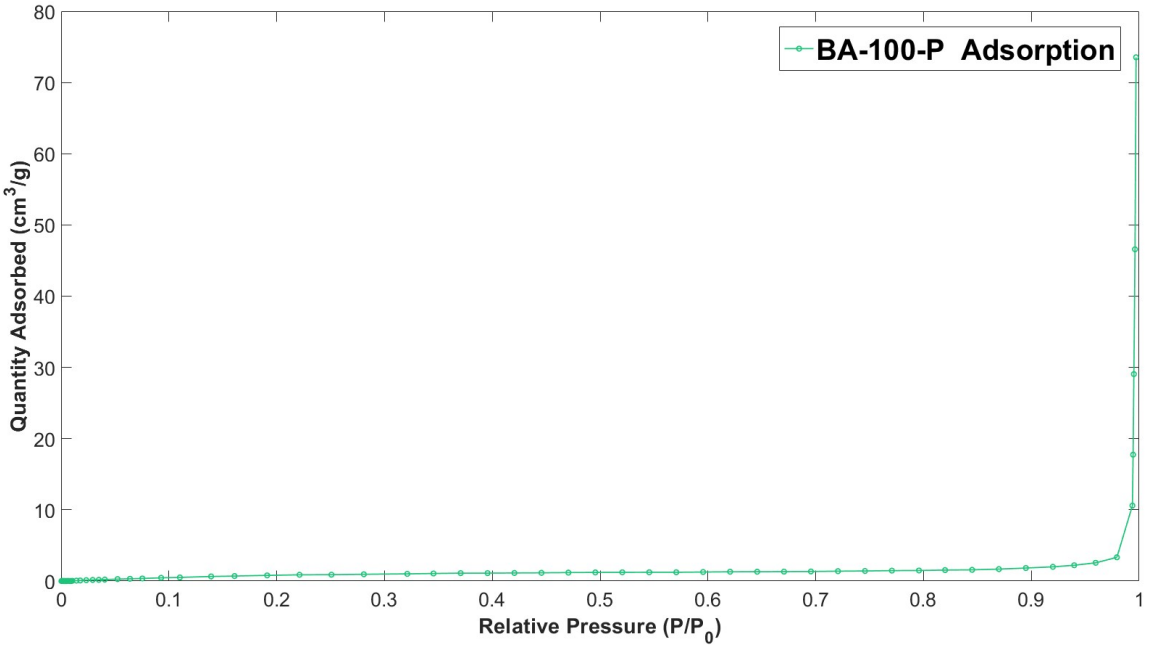

Figure 4.5: N_2 adsorption isotherm (at 77K) of BA-100-P.

Based on the measurements from Figure 4.5:, the S_{BET} of BA-100-P is 4.6 m^2/g. Further, the virgin adsorbent presents an IUPAC's type I physisorption isotherm with a low plateau [86]. Such behaviour, however, is expected of microporous materials with modest external surface areas [86]. This hypothesis is corroborated by the t-plot microporous surface area of BA-100-P, namely, 3.1 m^2/g. As such, approximately 65% of the surface area stems from the sample's microporosity.

Moreover, the pore size distribution and the pore volumes are shown in Figure 4.6: .

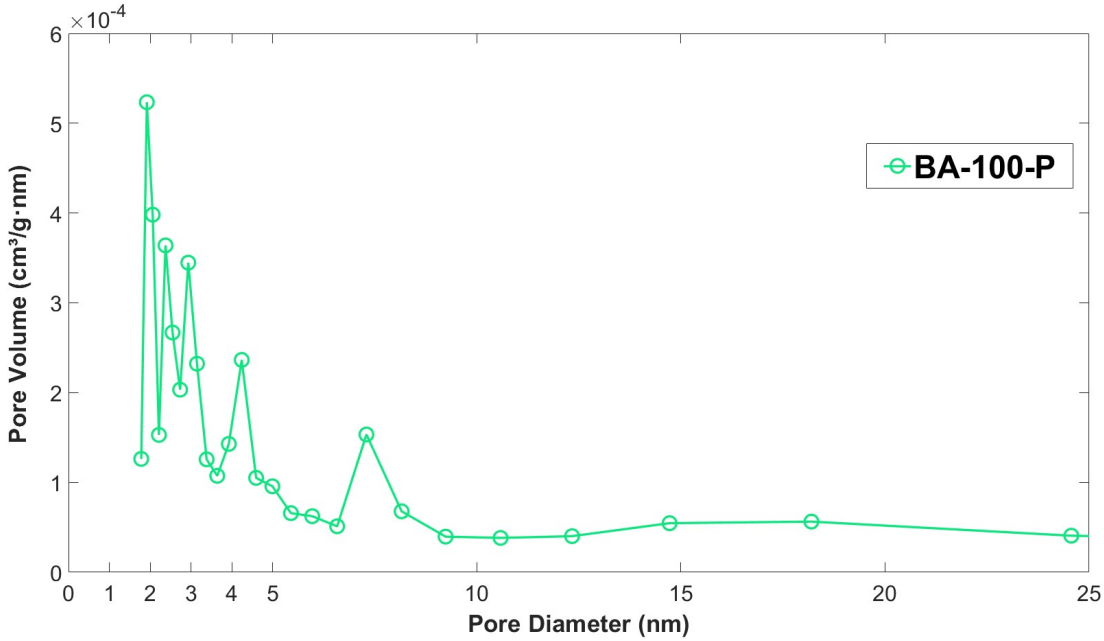

Figure 4.6: Pore size distribution plot of BA-100-P.

The pore volume of BA-100-P was calculated to be 0.00575 cm³/g (following the BJH method) with most of that volume stemming from pore sizes located in the region of < 5 nm. The modest pore volume and surface area values are to be expected as the extracted carbon has not been treated thermochemically to establish a pronounced porous structure. Nevertheless, the ability of the material to adsorb CO_2 has been investigated in order to be used as a baseline for comparison and evaluation of the activated carbonaceous adsorbents.

4.4.5. CO_2 Adsorption by the Virgin Carbon

Adsorption of CO_2 on BA-100-P has been evaluated in terms of the uptake at various temperatures, the kinetics of the process as well as the equilibrium adsorption isotherm model that produced the best fit.

4.4.5.1. Adsorption Capacity

The equilibrium adsorption capacity data was acquired *via* thermogravimetric analysis (TGA) using a Mettler Toledo TGA 2. The tests were conducted under a pure (N2.8 grade) flow (50 mL/min) of CO_2 at atmospheric pressure. Prior to this the samples have been purged under N_2 (purity of N4.8) at 150 °C. The gasses were procured from BOC. The tests were conducted in triplicates using a full (100 µL) aluminium crucible to minimise the variation within the sample. Different sample sizes were not investigated.

Given the temperature-dependent nature of the adsorption process, the uptake is expected to decrease with a rise in temperature. As expected, BA-100-P follows this trend as shown in Table 4.6.

Table 4.6: Results of BA-100-P CO_2 adsorption tests at different temperatures.

Uptake at 25 °C, mmol/g	Uptake at 50 °C, mmol/g	Uptake at 75 °C, mmol/g
0.53	0.34	0.14

However, to further envisage the properties of the adsorbent-adsorbate systems, investigations into the appropriate isotherm models have been conducted.

4.4.5.2. Equilibrium Adsorption Isotherms

The produced BA-100-P has been further studied in order to identify the most well-suited equilibrium adsorption isotherm. These tests were done employing a 3P Meso 222 Analyser. First, the material has been degassed/purged at 200 °C for 6 hours (ramp rate of 15 °C/min) under vacuum, then the CO_2 was supplied at the appropriate test temperature. The quality of fit has been assessed based on the normalised root mean square error (NRMSE) as well as the regression coefficient (R^2). The former parameter has been calculated *via* Eq. 4:

$$NRMSE = \sqrt{\frac{\sum_{i=1}^{n}(X_{exp,i} - X_{mod,i})^2}{n}} \Big/ \overline{X_{exp}} \qquad \text{Eq. 4}$$

where $X_{exp,i}$ is the i^{th} observed experimental results, whereas $X_{mod,i}$ is the value predicted by the model, n – the number of total observations and $\overline{X_{exp}}$ is the average of the observed experimental values across the dataset.

The choice of the most suitable isotherms has been based on the minimal values of both the NRMSE and R^2 with the results presented in Table 4.7:. It is noteworthy, that non-linear fitting was employed in order to more accurately represent the employed non-linear models and to provide more accurate estimation of parameters [232].

Table 4.7: BA-100-P equilibrium adsorption isotherm fits.

Isotherm Model	R^2	NRMSE
Langmuir	0.9836	0.03381
Freundlich	0.9992	0.00747

Double-site Langmuir	0.9999	0.00344
Triple-site Langmuir	0.9924	0.00350
Toth	0.9984	0.01541

Out of the multiplicity of adsorption isotherms that were fitted (i.e. Langmuir, Freundlich, Toth, Bi- and Tri-site Langmuir), BA-100-P leans towards the Double-site Langmuir (i.e. Bi-site Langmuir).

Table 4.8: BA-100-P equilibrium adsorption isotherm data.

Temperature	**Isotherm Model**	**Identified parameters**
0 °C	Double-site Langmuir	$q_{max\ (1)}$ = 4.524 mg/g $K_{L\ (1)}$ = 12.04 1/bar $q_{max\ (2)}$ = 72.18 mg/g $K_{L\ (2)}$ = 0.6438 1/bar
25 °C	Double-site Langmuir	$q_{max\ (1)}$ = 6.011 mg/g $K_{L\ (1)}$ = 7.83 1/bar $q_{max\ (2)}$ = 54.29 mg/g $K_{L\ (2)}$ = 0.2126 1/bar

This phenomenon suggests the presence of two distinctive types of adsorption sites, which, in this case, may be ascribed to the presence of both crystalline (e.g. adsorption on the edges/defects of the graphitic structure) and amorphous (the slightly porous network) structures within the carbonaceous adsorbent (supported by the collected Raman spectrum). An alternative interpretation might stem from the presence of various functional groups (as per FTIR) that influence the polarity of a given pore or due to micropores and mesopores on the surface of the virgin BA-100-P carbon (based on the N_2 adsorption isotherm at 77 K).

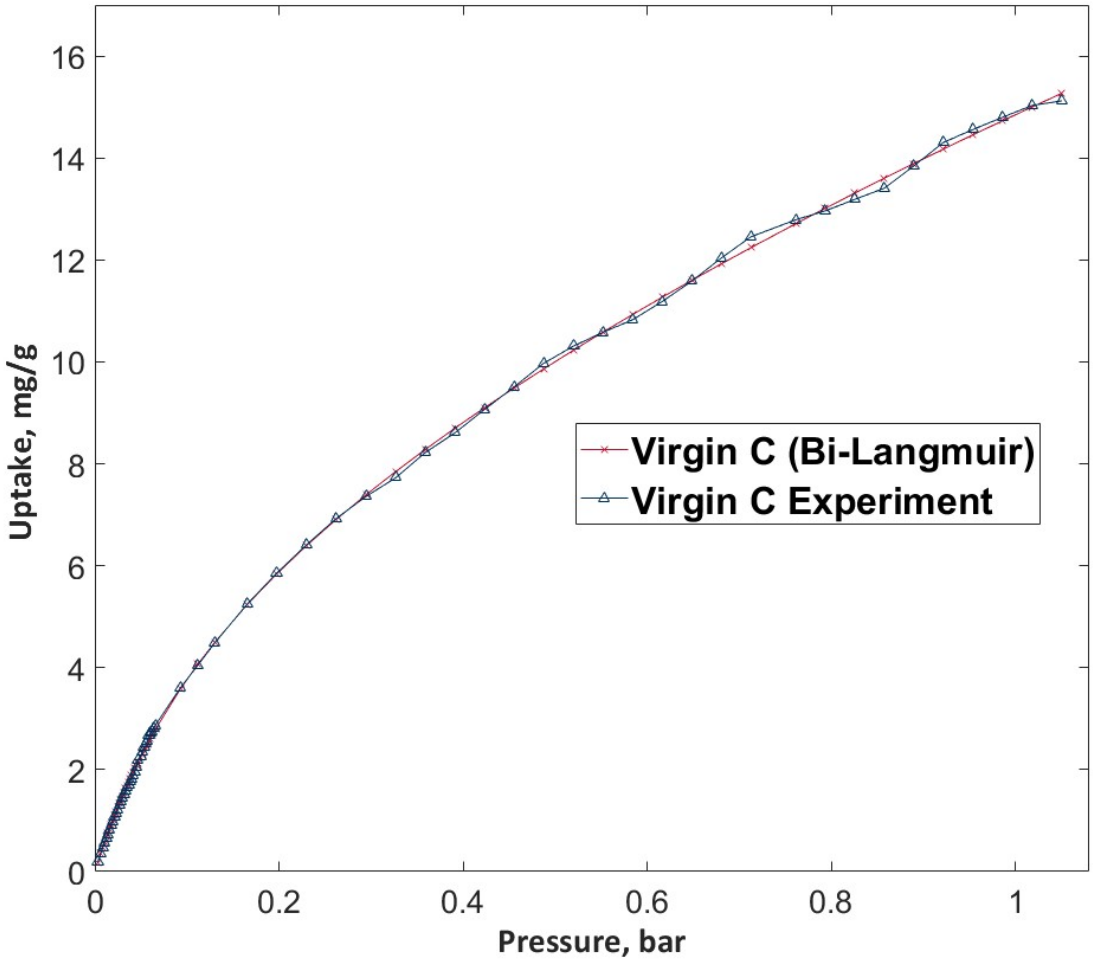

Figure 4.7: BA-100-P isotherm and experimental data.

4.4.5.3. Adsorption Kinetics

Apart from the equilibrium isotherms, the kinetics of the process were also investigated. This was achieved by fitting appropriate models (i.e. Pseudo-First Order (PFO), Pseudo-Second Order (PSO), Modified Ritchie, Intraparticle diffusion, Avrami, and Elovich models) to the TGA data. The goodness-of-fit was analysed based on R^2 and NRMSE utilising non-linear regression to improve accuracy and minimise any bias [224], [263].

Table 4.9: CO_2 adsorption kinetic model fits.

Kinetic Model	R^2	NRMSE
Pseudo-First Order (PFO)	0.9927	0.0230
Pseudo-Second Order (PSO)	0.9239	0.0439
Modified Ritchie	0.9481	0.0363

Intraparticle diffusion	0.8045	0.0704
Avrami	0.9705	0.0273
Elovich	0.9695	0.0278

Table 4.10: CO_2 adsorption kinetics on BA-100-P at 50 ºC.

Kinetic Model	**Identified parameters**
Pseudo-First Order (PFO)	$K_{(1)}$ = 0.006633

The PFO model produced the best fit of the data, which may be caused by few active adsorption sites [232] on the surface of BA-100-P which is to be expected as this carbonaceous sorbent did not undergo activation. Further, it also suggests the adsorption process to be controlled by external and/or internal diffusion [232], [237].

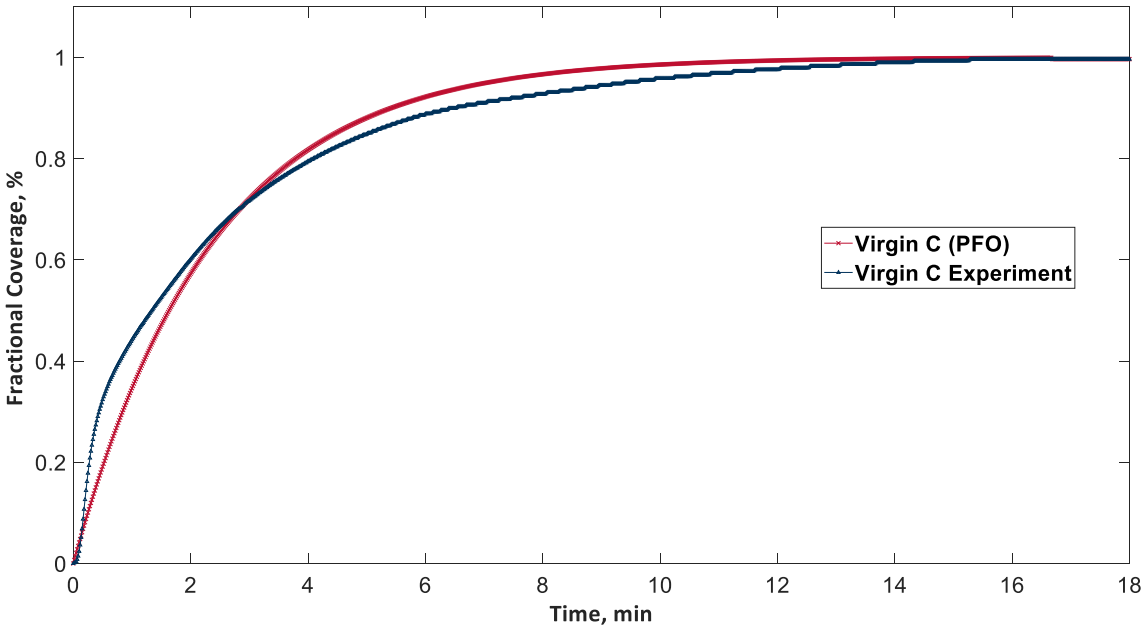

Figure 4.8: BA-100-P kinetic model and the experimental adsorption data.

Industrial applications classically favour an adsorbent with fast kinetics. Apart from this requirement, the high working/cyclic capacity is also of utter importance.

4.4.5.4. Working Capacity

BA-100-P working (i.e. cyclical) adsorption capacity has been assessed on a fractional coverage (Θ, %) basis with the uptake after first cycle constituting 100%. When an adsorbent has reached the end of its work life is system specific, and would depend on the economics of the process (and the material), the values of the adsorption capacity itself as well as a myriad of other factors. In this thesis the

adsorbent was deemed to be exhausted once (and if) the drop in the capture capacity reached 15%, i.e. Θ = 85%. This benchmark was developed to facilitate comparison between the produced BA-derived sorbents. The carbonaceous material could then be reactivated or burnt for energy purposes. Nevertheless, the cyclic adsorption capacity tests at 50 °C (the purge and desorption procedure kept the same as in Section 4.4.5.1) have been conducted.

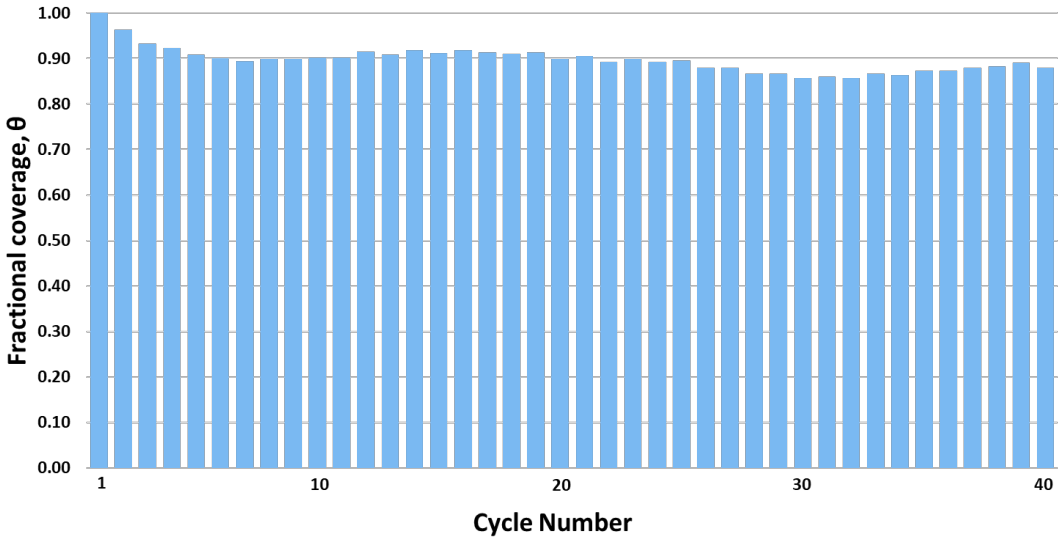

Figure 4.9: Working capacity of BA-100-P.

As can be visualised from**Error! Reference source not found.**, BA-100-P has not reached the generalised benchmark of 20% drop in over 40 cycles. Initially, a steep decline is observed from the first cycles until the third, losing 4% and a further 3% of uptake, respectively. This phenomenon might be associated with the release of other pre-adsorbed species on the surface of the sample that have not been alleviated during the initial purge. Afterwards, a gradual decline until ~89% is noted; then the factional coverages varies within the range of 89 – 92% until cycle 25. From there onward another decrease is observed as far as cycle 30, where the fractional coverage hovers between 86% and 89% of the original adsorption capacity until the end of observation.

The sharp drop in the first cycles, suggests the sample to retain moisture stronger than CO_2 as during these steps both the initial sorbent mass and the mass increase due to adsorption (i.e. uptake) decrease simultaneously. The other cycle steps, however, present mostly a decrease in adsorbed mass and a smaller drop in adsorbent mass (as can be visualised from Figure 4.10), proposing CO_2 to be easily desorbed off

BA-100-P. The latter property is imperative for to minimise the energy penalty required for sorbent regeneration.

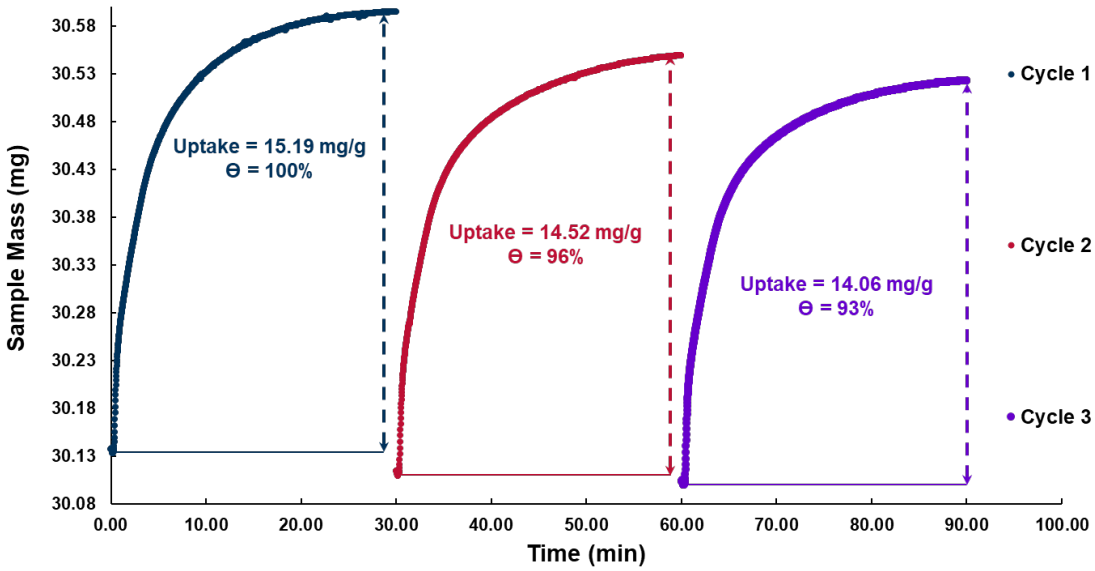

Figure 4.10: First three adsorption/desorption cycles of BA-100-P.

4.4.5.5. Heat of Adsorption

Isosteric heat of adsorption (Q_{st}) is a valuable metric used to quantify the energy requirement associated with the regeneration of the sample. This property is also employed as an indicator of the nature of the process, i.e. physisorption (weaker adsorbent-adsorbate interaction) or chemisorption (stronger bonding) and is generally acquired following the the Clausius–Clapeyron approach (Eq. 5).

$$Q_{st} = -R \left[\partial \ln p \Big/ \partial \left(\frac{1}{T}\right) \right]_{q_e} \qquad \text{Eq. 5}$$

Here, p_i is the pressure where a given (same) coverage or uptake (q_e) has been reached (this q_e includes multi-layer adsorption, capillary condensation and etc.), T_i is the temperature of the isothermal measurement and R is the universal gas constant. Employment of two isotherms (with a maximum ΔT of 20 °C) is suggested as an minimum (or three isotherms spread 10 °C apart) [265]; though, to achieve higher accuracies more measurements (four or five volumetric adsorption isotherms within 10 – 15 °C of each other) may also be deployed.

In order to calculate the value of Q_{st} at a given coverage, an appropriate isotherm model can be used allowing for the results to be presented in Figure 4.11.

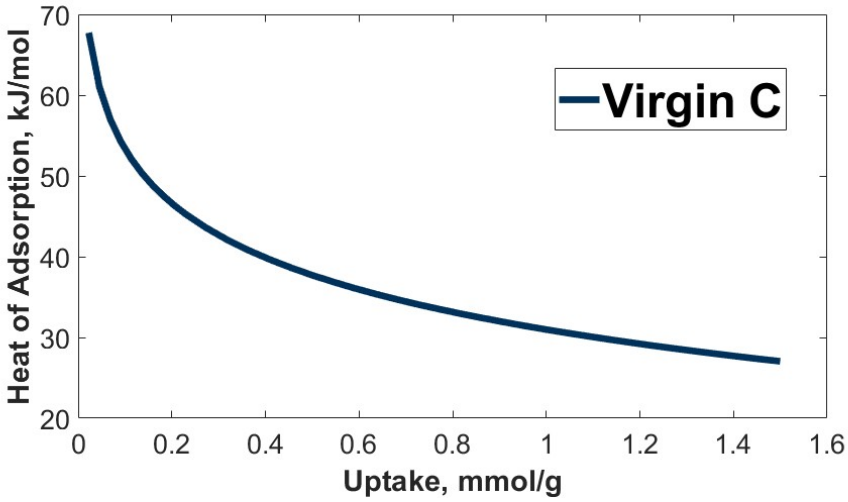

Figure 4.11*:* Heat of CO_2 adsorption of BA-100-P.

The curve for the virgin BA-100-P carbon follows a commonly observed trend for heterogenous sorbents of a strong dependence of Q_{st} on coverage. The higher values during the initial seconds (i.e. at lower uptakes) stem from the thermodynamically favoured (high-energy) adsorption sites being first/preferentially occupied. This is followed by a sharp drop associated with adsorption on pores with lesser affinity towards CO_2 [266]. Therefore, initial Q_{st} may vary significantly from the energy released (as adsorption is exothermic) at the final stages [265]. This can also play a role in the decrease in working capacity of sorbents (as shown in Section 4.4.5.4) as CO_2 may not have been alleviated from the high-energy sites (or "trapped" in micropores [267]). Further, a sub-optimal enthalpy of adsorption may also preclude the sorbent from retaining a high cyclic capacity [268].

In the case for BA-100-P, Q_{st} value stabilises at ~ 27 kJ/mol suggesting the sample to be a physisorbent. However, since the observed value is much larger than the enthalpy of vaporisation for CO_2 (16.4 – 17 kJ/mol at pressures of 1 bar and within the temperature range of 267 – 304 K [269]–[271]), capillary condensation is believed not to have taken place at the experimented conditions.

4.5. Conclusion

A promising carbonaceous adsorbent has been successfully derived from industrial-grade biomass combustion bottom ash, following a facile and low-cost dry extraction technique. The produced virgin carbon (labelled BA-100-P) has been extensively

characterised in terms of both bulk and surface composition, surface area and morphology as well as the adsorbent's interaction with CO_2.

The results suggest that approximately 25% (mass) of the produced material to be ash, with VOC and fixed carbon representing ~35% (mass) each, thus, resulting in a total elemental C content of 60% by weight. BA-100-P is highly heterogenous, possessing both amorphous and graphitic structures as well as various surface functional groups. The presence of surface heterogeneity was also evidenced by the Dual-site Langmuir model.

Moreover, analysis of BA-100-P's surface suggests the carbon to be microporous (65%) yet with a moderate surface area of 4.6 m^2/g. Despite such modest numbers, the produced virgin carbon could adsorb ~15 mg/g (from a pure CO_2 stream at 1 bar and 50 °C) and maintain a high working capacity of 86% after 40 adsorption-desorption cycles. Additionally, the sample was shown to adsorb CO_2 physically as the heat of adsorption was calculated to be 27 kJ/mol.

Future work may focus on further developing the extraction technique (aiming to enhance the purity and/or yield of BA-100-P) as well as activating the surface of this virgin carbon to improve adsorption capacity, kinetics and other sorption properties. The latter aspects have been investigated in the following chapters.

5. Chemical Activation

5.1. Introduction

The exact KOH activation mechanism is still actively debated within the scientific community [272]. There is agreement, however, that the process can be somewhat closely resembled by an overall summarising reaction [272]–[274]:

$$6KOH + 2C \rightarrow 2K + 2K_2CO_3 + 3H_2 \uparrow \qquad \Delta H_R = +428\ \mathrm{kJ/mol}$$

This reaction is thermodynamically possible at elevated temperatures [274], [275] and presents a negative Gibbs energy values (-7.6 kJ/mol C; -22.8 kJ/mol C and -47.0 kJ/mol C at 630, 730 and 830 °C, respectively) [276]. Within that, however, a multitude of other reactions involving KOH, the molecules produced during the process and various by-products are also thought to take place, further contributing to the development of the surface with some examples (non-exhaustive list) provided below [148], [272], [277]–[279].

$$2KOH \rightarrow K_2O + H_2O \uparrow \qquad \Delta H_R = +245\ \mathrm{kJ/mol}$$

$$K_2CO_3 + C \rightarrow K_2O + 2CO \uparrow \qquad \Delta H_R = +565\ \mathrm{kJ/mol}$$

$$C + CO_2 \rightarrow 2CO \uparrow \qquad \Delta H_R = +172.5\ \mathrm{kJ/mol}$$

$$C + H_2O \rightarrow CO \uparrow + H_2 \uparrow \qquad \Delta H_R = +131\ \mathrm{kJ/mol}$$

$$K_2O + C \rightarrow 2K + CO \uparrow \qquad \Delta H_R = +430\ \mathrm{kJ/mol}$$

$$K_2O + C \rightarrow K + C - O - K$$

These may or may not occur depending on the precursor [272] and temperature (i.e. activation conditions) [280] at hand. For instance, temperatures over 700 °C are believed to be required for the carbon (or hydrogen) to reduce potassium oxide to elemental K and CO (or H_2O) [272]. This can be corroborated by observed metallic K in the furnace [276]. This elemental potassium, however, is not necessarily in “free form” as it can penetrate into the carbonaceous framework *via* intercalation into the lattice, where it resides either between carbon layers or existing as quasi-chemically bound potassium-oxygen functional groups within the sorbent [281], [282] (as

represented by the final equation from above). Such (intercalated or chemically bound) K moieties may not be alleviated during the post-activation washing (that is aimed at eliminating any residual metallic substances) and would remain as part of the sorbent.

Therefore, BA-100-P (the biomass combustion bottom ash-derived virgin carbon) has been chemically activated (with KOH) to develop microporosity and evaluate its potential deployment as a CO_2 adsorbent. This has been achieved *via* a Taguchi L9 orthogonal array to envisage the statistically significant parameters and their interactions. This particular DoE framework was selected as it facilitates more control over noise variables and is highly efficient in evaluating systems with many potentially impactful factors [185].

5.2. Materials and Methods

5.2.1. Materials

The virgin (BA-100-P) carbon powder was chemically activated with KOH (85% pure; CAS 1310-58-3; Alfa Aesar). The effectiveness of activation was evaluated using CO_2 uptake as the dependent variable deploying the same methodology and characterisation methods as in the previous chapter.

5.2.2. Preparation of Chemically Activated Carbon

The experimental procedure began with the precise measurement of the required amounts of materials, specified as part of the randomised L9 experimental matrix. These materials were then placed in a ceramic mortar and manually mixed with potassium hydroxide, i.e. dry mixing. The amount of KOH was predetermined based on the DoE framework. This parameter was incorporated into the design in form of C:KOH Impregnation Ratio (IR). The resulting substance was transferred to a ceramic boat (i.e. activation vessel) and positioned in the centre of an insulated Inconel tube within a furnace (Carbolite Gero TF1 12), where the activation temperature (T_{act}) was achieved using a prescribed ramping rate (RR). Once T_{act} (i.e. furnace set point) was achieved the sample was held in the furnace for the appropriate activation time (τ_{act}) for each experiment. Thereafter, the AC was left to cool to room temperature inside the furnace. During the whole process, a continuous flow of N_2 (BOC, purity: N4.8) at a rate of 300 mL/min was maintained to ensure evacuation of any gaseous species from the reactor in under a minute. The next step entailed the samples being washed *via* deionised (DI) water in a Büchner flask-funnel system until the pH of the filtrate

reached ~7. The optimisation was carried out applying both Response Surface Methodology (RSM) and assessing the Signal-to-Noise (S/N) ratio. Statistical analysis as well as the development of the experimental matrix were conducted using Minitab (version 18).

5.3. Results and Discussions

5.3.1. Activation and Optimisation Campaigns

To investigate the design space a randomised L9 Taguchi orthogonal array matrix was produced consisting of four different factors at three levels each as depicted in Table 5.1.

Table 5.1: Factors and levels studied *via* the L9 Taguchi design.

Factors	**Levels**		
Time (τ_{act}), min	30	60	90
Temperature (T_{act}), °C	400	625	850
Ramping Rate (RR), °C/min	5	10	15
C:KOH Impregnation Ratio (IR)	1:1	1:2	1:3

The obtained data was assessed *via* ANOVA, with the CO_2 adsorption capacity as the dependent variable. The regression coefficient (R^2) of the developed model was calculated to be 0.9995, indicating a strong fit of the model. However, the predictive ability of the model, denoted as R^2_{pred}, was found to be weaker, with a value of 0.9429. It is essential to consider R^2_{pred}, especially when the R^2 is high, as it can reveal if the model is overly complex and is fitting random noise alongside the actual response signal(s). In order to calculate R^2_{pred}, each individual data point is removed from the dataset, and then the regression equation estimates that specific removed point. This process helps assess the predictive capabilities of the model. The results of the statistical analysis are presented in Table 5.2.

Table 5.2: Results of ANOVA for chemical activation experimental campaign.

Factors	**F-Value**	**p-Value**	**Significance**
Activation Time (τ_{act})	25.67	0.124	NSS
Activation Temperature (T_{act})	241.31	0.041	3
Ramping Rate (RR)	470.01	0.029	2
C: KOH Impregnation Ratio (IR)	29.57	0.116	NSS

Quadratic Interaction of τ_{act}	162.18	0.050	4
Quadratic Interaction of T_{act}	1152.88	0.019	1
Quadratic Interaction of IR	43.69	0.096	NSS

The data given in Table 5.2 indicates the presence of non-linear relationships within the design space. Notably, the quadratic term of T_{act} is the most statistically significant one, followed by the linear effects of RR, T_{act} and non-linear τ_{act}^2. A similar pattern emerges when examining the S/N ratios illustrated in Figure 5.1. The S/N ratio serves as a measure of process robustness, assessing how resistant it is to variations in input parameters. Given that the objective of this experimental campaign was to maximise the CO_2 uptake of the produced AC, the "larger is better" method, as expressed in (Eq. 6), was selected for analysing the S/N ratios.

$$\frac{S}{N} = -10 \cdot \log\left(\sum\left(\frac{1}{y^2}\right) / n\right) \qquad \text{Eq. 6}$$

In Eq. 6, *y* represents the response variable derived from a particular parameter-level combination, and *n* is the number of such responses for that specific parameter-level combination.

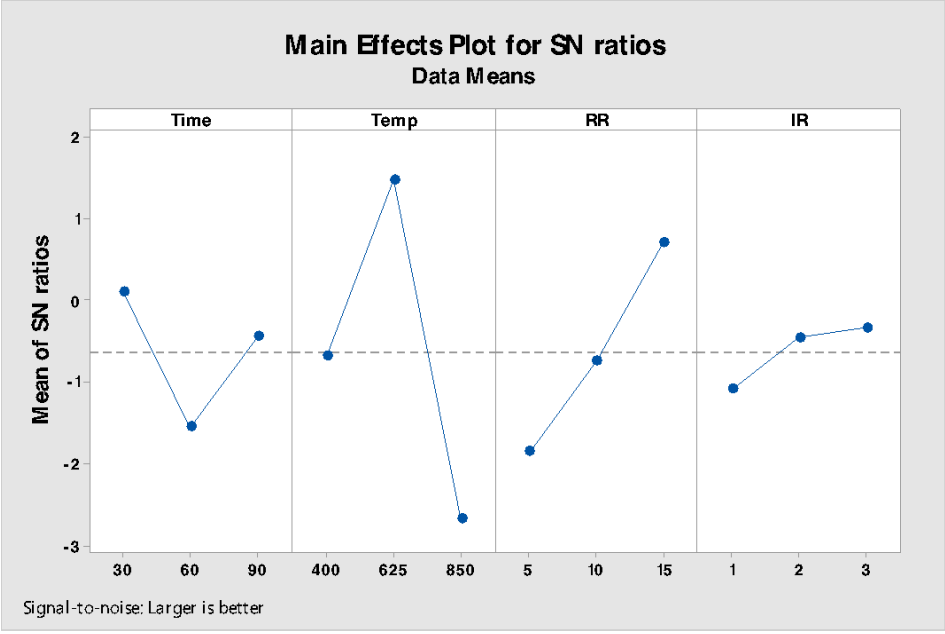

Figure 5.1: The S/N ratio for the evaluated L9 array.

Based on the data gathered and the analysis conducted, it is evident that activation temperature (T_{act}), activation time (τ_{act}), and the RR have a strong impact on the adsorption uptake. The trends in Figure 5.1 indicate that both τ_{act} and T_{act} behave non-

linearly. Within that, for the areas around the extremum point of T_{act}, the activation process has either been carried out to such an extent where the generated micropores have (presumably) collapsed into larger mesopores or that activation has not reached is maximum capabilities (as evident by the lower capacities as lower temperatures). Further, the RR presents a steadily rising trend. This indicates a negative impact on the sorbent's uptake if the material is treated thermo-chemically for an unnecessary large amount of time. As such, more rapid RR would allow for a more attractive and economically attainable adsorbent. Moreover, IR was (interestingly) determined to be NSS, though, similar conclusions can be drawn from assessing the data available in the literature [148]. This phenomenon could be due to the inherent heterogeneity of dry mixing. Therefore, future research efforts may consider avoiding the use of this technique and opt instead for wet mixing. However, this introduces its own set of challenges. Aqueous KOH solutions have the potential to etch the ceramic boat/crucible used in the activation process, rather than activating the carbonaceous sorbent to its (agent's) full potential. This could introduce additional sources of variation (in form of a lurking variable) and degradation of the activation vessel. Furthermore, activation with alkaline solutions may lead to a reduction in the quantities of the main exchangeable cations present in the material [283]. In the case of biomass combustion bottom ash-derived carbons, Ca^{2+} ions may be particularly affected by this phenomenon. A decline in such cations might result in a lower electrostatic potential of the adsorbent, thus, leading to a reduced capacity for capturing CO_2 through physisorption mechanisms.

Nevertheless, the trends from Figure 5.1 suggest the highest RR and lowest τ_{act} to be most appropriate for increasing uptake (within the evaluated design space). This combination suggests a potential opportunity to reduce the energy requirements for the thermochemical synthesis of AC by further decreasing the activation time and enhancing the ramping rate. This hypothesis is supported by the contour plots (Figure 5.2Figure 6.4:), which are a part of the RSM.

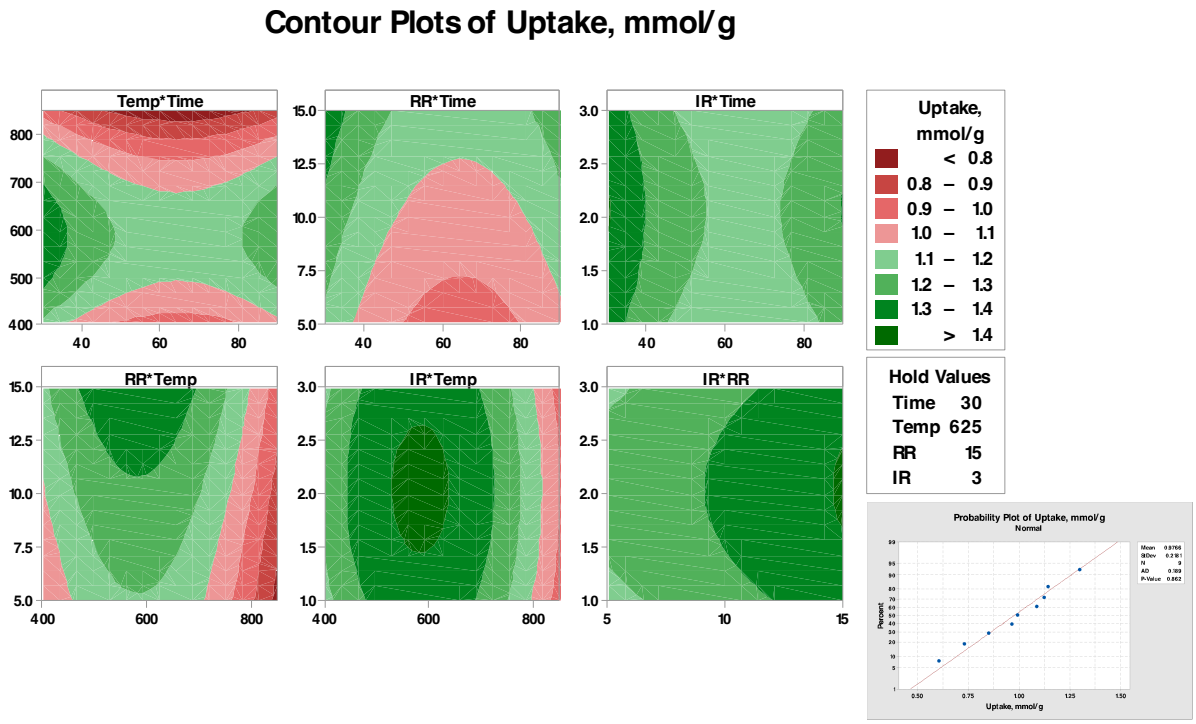

Figure 5.2: Contour plot of CO_2 uptake with the normality plot on the bottom right.

When utilising a Taguchi DoE to determine optimal conditions, the calculated S/N ratio is used as the key performance indicator. In this case, as the goal is to maximise the dependent variable, the suggested levels for the parameters would be 30 minutes τ_{act}, 625°C for T_{act}, 15°C/min for RR, and IR of 1:3. On the other hand, the RSM optimisation proposed slightly different conditions, specifically a temperature of 595.5°C and IR of 1:2.23, while RR and τ_{act} remained the same. However, neither of the proposed conditions (based on conducted trials) resulted in the values predicted by the model uptake. This outcome might be attributed to the inherent uncontrollable variation in waste materials or, as mentioned earlier, the heterogeneity associated with the dry mixing process, as well as potential limitations in the model's predictive capability. In future research, it may be beneficial to incorporate repeated runs, typically at the centre points of the design, to account for the inherent heterogeneity of dry mixing within the design space. Additionally, when working with an L9 array and analysing four factors at three levels each, the model is overfit, meaning there are fewer degrees of freedom than estimated terms. In such cases, reducing the model by eliminating terms, such as interactions and the quadratic effect of RR, could enable more robust statistical analysis and potentially improve the model's predictive accuracy.

Despite the challenges in optimisation, the experimental campaign did yield sorbents with significantly higher CO_2 adsorption capacity, and one sample stood out as particularly promising and was chosen for further examination and characterisation. The selected material was obtained using the following parameters: 30 minutes of chemical activation at 625°C, a ramping rate of 10°C/min and a C:KOH Impregnation Ratio of 1:2. Following the prescribed activation conditions, a resulting sample was obtained (mass yield of 36%) which was labelled as ChAB.

5.3.2. Characterisation of Optimum Sample

5.3.2.1. Scanning Electron Microscopy (SEM) & Energy Dispersive X-ray Spectroscopy (EDS)

As SEM/EDS are widely employed analytical techniques for investigating both the surface morphology and the elemental composition of a given sample, their application in analysis of ChAB as demonstrated in Figure 5.3 and Table 5.3.

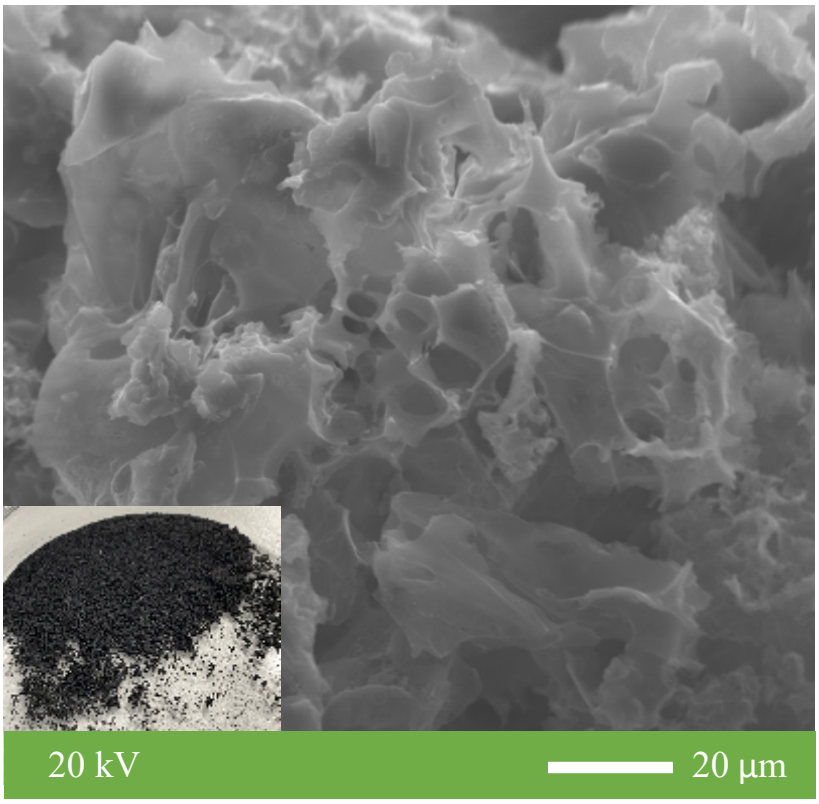

Figure 5.3: SEM images of ChAB and a full-scale photo as insert (bottom left).

The morphology of ChAB is, as anticipated, a finely powdered texture with a notably rough surface. This surface roughness can be attributed to a combination of factors, arising from both the characteristics of the original virgin BA-100-P carbon and from

the chemical activation. Another noteworthy impact of the chemical activation process becomes evident when assessing the surface elemental composition of ChAB.

Table 5.3: Surface elemental composition of ChAB.

Element	Weight %
C	70.2
O	28.2
K	1.6

Table 5.3 reveals the presence of residual potassium that was not completely removed during the post-activation washing step. This phenomenon is associated with DI water primarily removing by-products of the activation process (e.g. potassium carbonate, potassium oxide) [282]. However, during the activation process, K-containing species can also diffuse into the internal structure of the carbon, contributing to pore creation, opening and widening [283]. Additionally, free potassium can penetrate between the graphene layers of the AC [277]. These intercalated K atoms are believed to occupy positions between the centres of the C hexagons in adjacent graphitic layers [284]. This intercalation has been shown to enhance the AC's affinity to CO_2 and increase its surface polarity [282], which may occur due to electron transfer from the metal to the delocalised π-electron cloud of the graphene sheets. It is worth noting that quantities of slightly over 1% of K have been suggested to provide the maximum benefit from intercalation [282]. In the case of ChAB, elemental potassium is relatively scarce and sparse, accounting for only 1.6 wt% in the analysed sample. Interestingly, no Si or Al was detected in the single-point measurements. This could be attributed to the surface-sensitive and site-specific nature of EDS. As a result, bulk analysis techniques would be more suitable for a holistic investigation of ChAB and for quantifying inorganic elements. Alternatively, aluminosilicate-based ash impurities may have been partially eliminated due to their reaction with KOH during the activation process, leading to the formation of water-soluble salts that were removed during the final washing stage of AC production. As such, the impurities are more accurately assessed *via* proximate analysis (Section 5.3.2.3). Moreover, EDS has intrinsic limitations when quantifying elements with atomic masses lower than that of sodium as lighter elements emit weaker signals that may be absorbed by the specimen before reaching the detector. Therefore, to arrive at more accurate

estimations of C and O contents, ultimate (Section 5.3.2.2) has also been deployed in characterisation of ChAB.

5.3.2.2. Ultimate Analysis

One of the bulk analyses commonly used for characterising materials like ChAB is elemental analysis, which is often referred to as CHN(S)-analysis or *ultimate analysis*. This analytical method enables the estimation of elemental C, H, and N quantities, providing a more accurate assessment of carbon content compared to EDS. Therefore, data from the ultimate analysis is presented in Table 5.4.

Table 5.4: Ultimate analysis data for ChAB.

Element	Weight %
C	39.34
H	2.05
N	0.00
Other	58.61

The reduction in C content in comparison to the parent BA-100-P is anticipated and can be attributed to the inherent effects of the activation process (e.g. burn off). The absence of nitrogen in ChAB is also not surprising, as KOH activation is not known to introduce nitrogen-containing functional groups. The decrease in nitrogen and hydrogen contents, when compared to the parent virgin carbon, may indeed be linked to the loss of volatile organic compounds (VOCs). This phenomenon is further elaborated in Section 5.3.2.3.

5.3.2.3. Proximate Analysis

A comprehensive bulk analysis technique, namely, proximate analysis [250] was also used to investigate the nature of ChAB (Table 5.5).

Table 5.5: Proximate analysis data for ChAB.

Moisture, wt%	VOC, wt%	Fixed C, wt%	Ash, wt%
13.5	20	33	33.5

As anticipated, the chemical activation process has led to a noticeable reduction in the percentage of fixed C and VOCs (compared to the BA-100-P) since the yield of ChAB is 36%. The fixed carbon content aligns well with the data obtained from the ultimate analysis. The reduction in volatiles (and fixed C) is primarily attributed to the

activation process being conducted at elevated temperatures, which causes the release of VOCs (and fixed C) from the surface of the adsorbent. The decline in these constituents of ChAB have also contributed to the increased ash content. Finally, the higher level of retained moisture in the sample may be attributed to the elevated surface area of the material and the presence of surface functional groups, as can be observed from spectroscopic analysis (Section 5.3.2.4). These analytical techniques can also provide insights into the nature of the ash impurities present in the sample.

5.3.2.4. Spectroscopic Analysis

5.3.2.4.1. Fourier- Transform Infrared Spectroscopy (FTIR)

The existence of silica-based ash impurities has been further confirmed *via* FTIR. Furthermore, the spectrum generated for ChAB also exhibits several other discernible peaks (Figure 5.4).

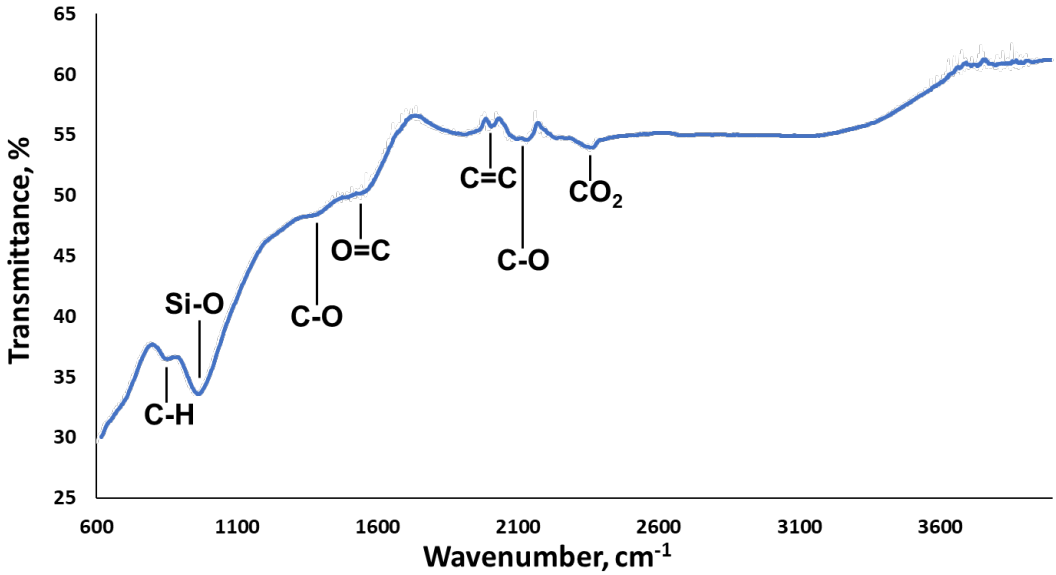

Figure 5.4: Infrared spectrum of ChAB.

Starting from the left in the spectrum, the first peak, located at ~830 cm^{-1}, can be attributed to the bending vibrations of the C-H bonds present in the sample [285]. Moving on, the next identifiable peak at around 957 cm^{-1} corresponds to the vibrations of Si-O bonds, which are indicative of ash particulates [258]. This is anticipated since the AC is derived from biomass combustion ash, which naturally contains such impurities. Furthermore, two peaks associated with C-O functionalities are observed at approximately 1306 cm^{-1} and 2100 cm^{-1} [285], [286]. These peaks may arise from quasi-chemical bonds that enable potassium to persist within the adsorbent in the form

of a C-O-K functionality even after washing with deionised water [282]. In addition, peaks representing O=C and C=C bonds appear at 1530 cm^{-1} and 1992 cm^{-1}, respectively. The former may originate from keto- or quinone-like structures [287], while the latter is associated with the asymmetric stretching of C=C [288]. Lastly, the peak observed at approximately 2358 cm^{-1} can be attributed to background CO_2 [264].

The observed peaks also align closely with the typical FTIR peaks associated with KOH-activated carbons [283]. However, it is worth mentioning that some surface functional groups may undergo degradation in the presence of KOH as proposed in the literature [148].

5.3.2.4.2. Raman Spectroscopy

Raman spectroscopy has also been employed as a complimentary technique to FTIR for the purposes of ChAB analysis. Based on the spectrum in Figure 5.5, the I_D/I_G has been identified to be 0.88, suggesting an increased number of sites with defects (sp^3-hybridised) compared to BA-100-P. A higher I_D/I_G proposes the sample to possess a higher degree of surface roughness, which in turn can be associated with more pronounced porosity, therefore, CO_2 uptake.

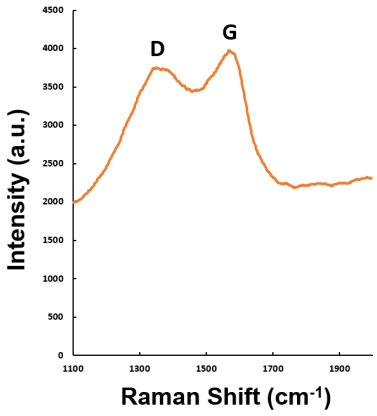

Figure 5.5: Raman spectrum of ChAB.

Though, these indications of porosity are valuable, a more appropriate approach for description of the porosity and adsorbent characterisation relies on N_2 adsorption isotherm at 77 K presented in the following section.

5.3.2.5. Surface Area Analysis

BET analysis is a widely employed method for assessing the surface area of a given sorbent. With ChAB, the S_{BET} has been determined to be 643.6 m^2/g. This is a

substantial rise compared to the parent carbon, which has a surface area of 4.6 m²/g, and is ascribed to the successful chemical activation. The N_2 adsorption isotherm, which provides insights into this analysis, is presented below.

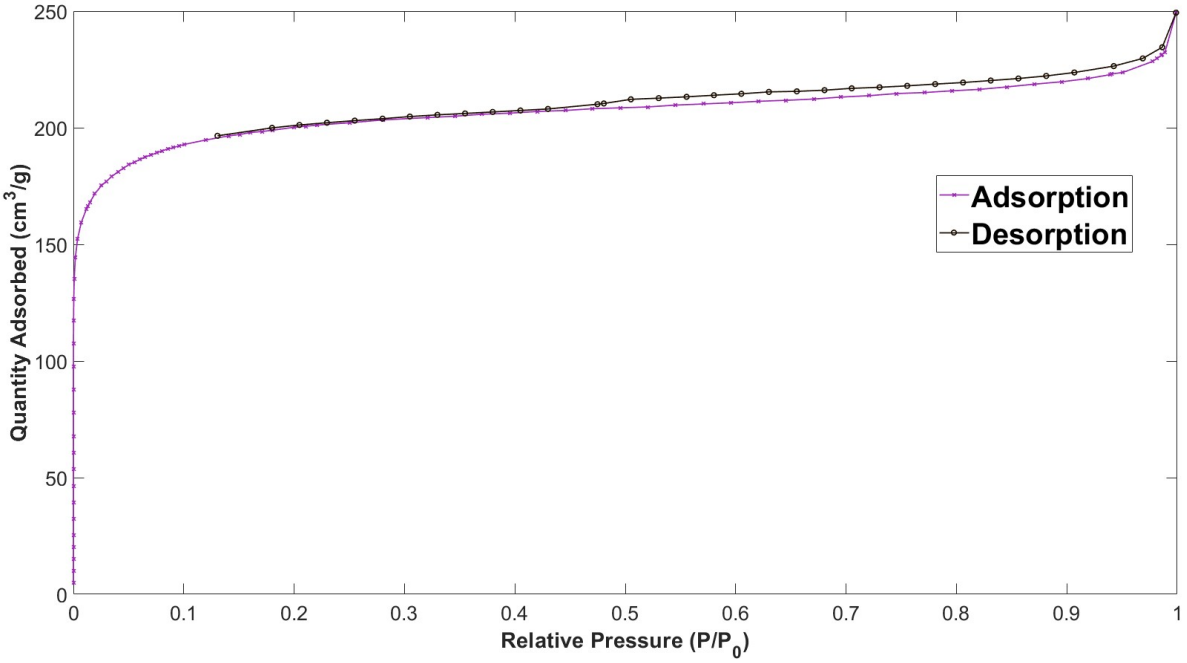

Figure 5.6: BET physisorption isotherm of ChAB.

As shown in Figure 5.6, ChAB exhibits a type IV physisorption isotherm with an H4 type hysteresis loop. Such patterns are commonly observed in carbonaceous adsorbents, particularly when there is a significant reduction in material mass during activation (as is the case for ChAB which had a 36% mass yield) [84] . These loops typically occur in materials with slit-shaped micropores [82]. The hypothesis that KOH activation results in highly microporous powdered ACs [169] is further supported by ChAB's t-plot microporous area (597.9 m^2/g). However, in general, the presence of a hysteresis loop indicates the existence of pore sizes larger than 4 nm on the AC's surface [86]. The observations are corroborated by the pore size distribution plot depicted in Figure 5.7.

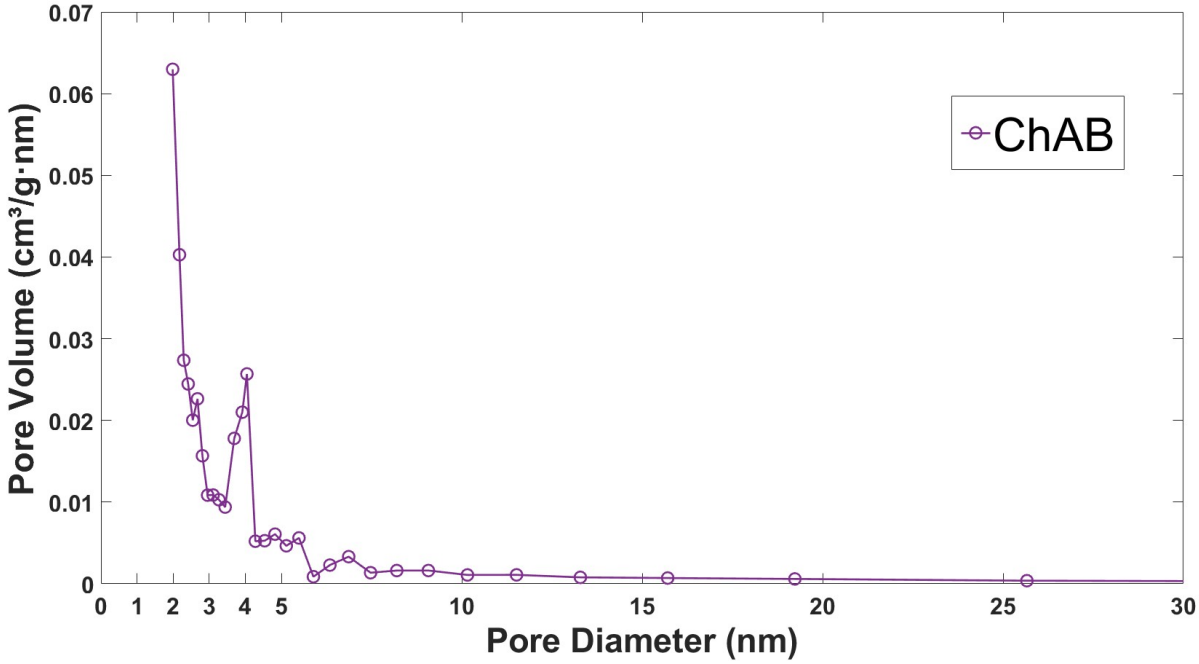

Figure 5.7: Pore size distribution plot of ChAB.

Consequently, following the chemical activation conditions proposed in this thesis, a highly micro-mesoporous material can be obtained. The high degree of microporosity is a competitive advantage for ChAB as they enhance affinity to gaseous adsorbates [70], [80], hence, play a crucial role in determining the adsorption capacity of an AC [289].

5.3.2.6. CO_2 Adsorption Experiments

The adsorption capacity as well as the affinity of ChAB towards CO_2 have been examined based on a plethora of different experiments pertaining towards CO_2 adsorption.

5.3.2.6.1. Adsorption Capacity

ChAB's CO_2 uptake has been examined at different temperatures with the data shown in Table 5.6, where the increased capacity at lower temperatures suggests the nature of adsorption to be physical [263].

Table 5.6: Results of ChAB CO_2 adsorption tests at different temperatures.

Uptake at 25 °C, mmol/g	Uptake at 50 °C, mmol/g	Uptake at 75 °C, mmol/g
1.93	1.29	0.84

Chemical activation with KOH resulted in a significant increase in CO_2 uptake compared to the virgin carbon powder. At 25 °C and 50 °C, the uptake is approximately

four times higher than that of the parent material, while at 75 °C, ChAB adsorbed 6 times more CO_2 than BA-100-P, thus outperforming a commercial alternative examined at the same conditions [263]. However, beyond these values, it is crucial to examine the applicable equilibrium adsorption isotherms (Section 5.3.2.6.2) to understand the capacity and behaviour at concentrations of carbon dioxide more relevant to post-combustion CCS. Additionally, kinetic studies (Section 5.3.2.6.3), cyclic adsorption studies (Section 5.3.2.6.4), and heat of adsorption data (Section 5.3.2.6.5) are frequently overlooked but are essential for industrial deployment.

5.3.2.6.2. Equilibrium Adsorption Isotherms

To further investigate the surface of ChAB a myriad of adsorption isotherms were fit to the experimental data with the results provided in Table 5.7.

Table 5.7: ChAB equilibrium adsorption isotherm fits at 0 ºC.

Isotherm Model	R^2	NRMSE
Langmuir	0.9515	0.2004
Freundlich	0.9994	0.0201
Double-site Langmuir	0.9981	0.0375
Triple-site Langmuir	0.9999	0.0094
Toth	0.9977	0.4111

As evident from Table 5.7, the Triple-Langmuir provides the best fit (based on maximum R^2 and minimal NRMSE), suggesting the surface to be heterogenous. More details on the fit of the Triple-site Langmuir model is given in Table 5.8 and Figure 5.8.

Table 5.8: ChAB equilibrium adsorption isotherm data at 0 ºC and 25 ºC.

Temperature	Isotherm Model	Identified Parameters	
0 °C	Triple-site Langmuir	$q_{max\ (1)}$ = 11.91 mg/g	$K_{L\ (1)}$ = 5978 1/bar
		$q_{max\ (2)}$ = 34.49 mg/g	$K_{L\ (2)}$ = 33.46 1/bar
		$q_{max\ (3)}$ = 241.4 mg/g	$K_{L\ (3)}$ = 0.9483 1/bar
25 °C	Triple-site Langmuir	$q_{max\ (1)}$ = 58.36 mg/g	$K_{L\ (1)}$ = 2.097 1/bar
		$q_{max\ (2)}$ = 27.14 mg/g	$K_{L\ (2)}$ = 2.119 1/bar
		$q_{max\ (3)}$ = 11.68 mg/g	$K_{L\ (3)}$ = 2.172 1/bar

The best fit of this isotherm proposes ChAB to possess three different and distinct adsorption sites with (possibly) varying adsorption mechanisms. These might be

ascribed to sites with various and varying (and/or without) surface functional groups (as evidenced by the FTIR in Section 5.3.2.4.1). Alternatively, this phenomenon may be assigned to presence of both amorphous and crystalline phases (as per Raman spectroscopy in Section 5.3.2.4.2). Further, the different mechanisms of adsorption in meso and micropores (i.e. capillary condensation and volumetric filling, respectively) can facilitate fitting of the Triple-site Langmuir isotherm.

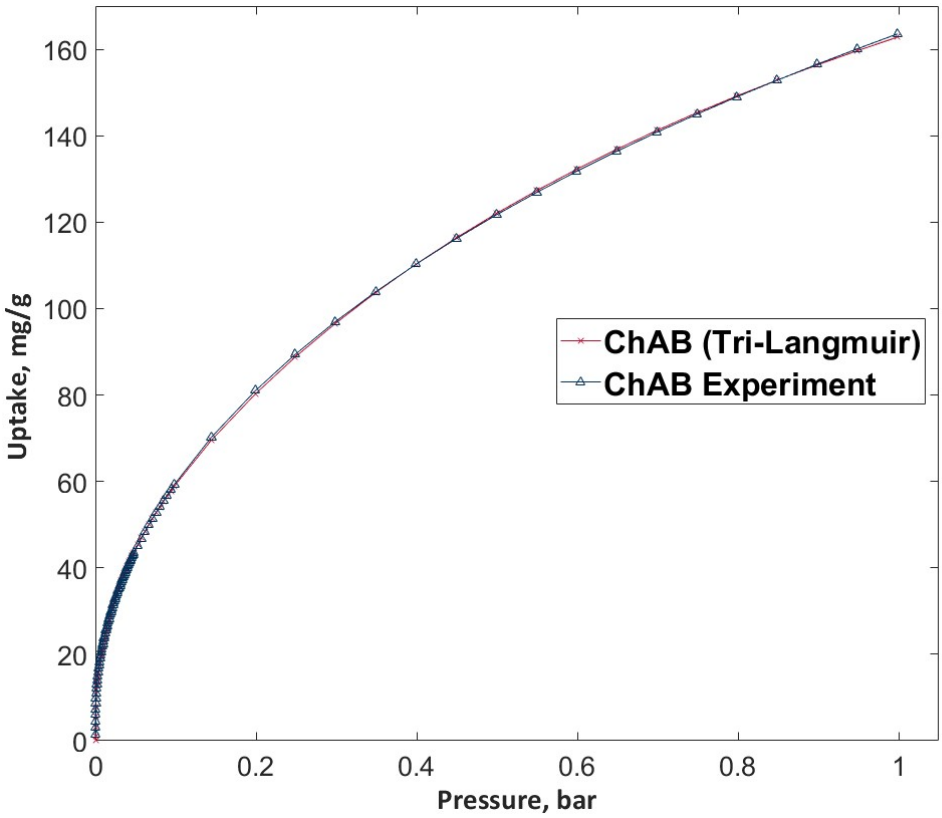

Figure 5.8: Experimental data (triangles) and the equilibrium isotherm model (crosses) ChAB at 0 °C under pure CO_2.

In the case of volumetric filling, to the overlapping adsorption potentials/force fields of the walls of the pore [84] facilitate the gaseous CO_2 molecule(s) to take up the pore space fully since the adsorbate (kinetic diameter of CO_2 = 0.33 nm [290] and the micro- (<2 nm) and, especially, ultramicropores (<0.7 nm) are of similar diameters [85] and does not involve a phase transition of CO_2. Capillary condensation, on the other hand, entails phase-change. As the saturation vapour pressure for the confined adsorbate (in mesopore) is larger than the condensation pressure due to a reduction in free energy of the adsorbate in the pore coupled with surface tension effects [289]. Therefore, as the larger gap between mesopore walls cannot be filled with a single

molecule or a layer of molecules, multilayer adsorption followed by condensation of CO_2 and formation of a meniscus-bridge occurs [291].

Apart from the equilibrium isotherm adsorption studies, adsorption kinetics have also been investigated.

5.3.2.6.3. Adsorption Kinetics

Similar to the evaluation of equilibrium isotherms, the fitness of the kinetic models (presented in Table 5.9) was assessed using non-linear regression and employing R^2 and NRMSE as the goodness-of-fit criteria. The equations yielded results that exhibited a trend of (in descending order): Avrami, Elovich, Modified Ritchie, Intraparticle Diffusion, PSO and PFO. Firstly, since the evaluated diffusion-oriented models did not provide a compelling fit, CO_2 adsorption on ChAB is believed not to be diffusion restricted [237]. This is anticipated as the chemical activation allowed to overcome some diffusion limitations that BA-100-P (the virgin carbon) encountered due to less pronounced porosity of the surface. Secondly, the Avrami equation is considered to provide the best fit for the system of CO_2 and ChAB. Although its applicability to adsorbate-adsorbate systems has met its portion of criticism [292], it's application towards adsorption is prominent in the literature [160], [293]–[297] as it facilitates determination of factionary kinetic orders [296]. The calculated fitting parameters are outlined in Table 5.10 Table 6.*12*:and Figure 5.9.

Table 5.9: CO_2 adsorption kinetic model fits for ChAB at 50 ºC.

Kinetic Model	R^2	NRMSE
Pseudo-First Order (PFO)	0.5397	0.0885
Pseudo-Second Order (PSO)	0.6065	0.0690
Modified Ritchie	0.7966	0.0496
Intraparticle diffusion	0.6968	0.0606
Avrami	0.9470	0.0328
Elovich	0.9007	0.0347

Table 5.10: CO_2 adsorption kinetics on ChAB at 50 ºC.

Kinetic Model	Identified parameters
Avrami	K_A = 0.0152 n_A= 0.4276

The calculations indicate that n_A is, indeed, fractional. In such instances, the Avrami model is considered to be multi-pathway and complex [293], possibly following different kinetic orders and possibly altering while the adsorbent-adsorbate system is in contact [297]. Current observation aligns with the best fit of the Triple-site Langmuir equilibrium model (Section 5.3.2.6.2).

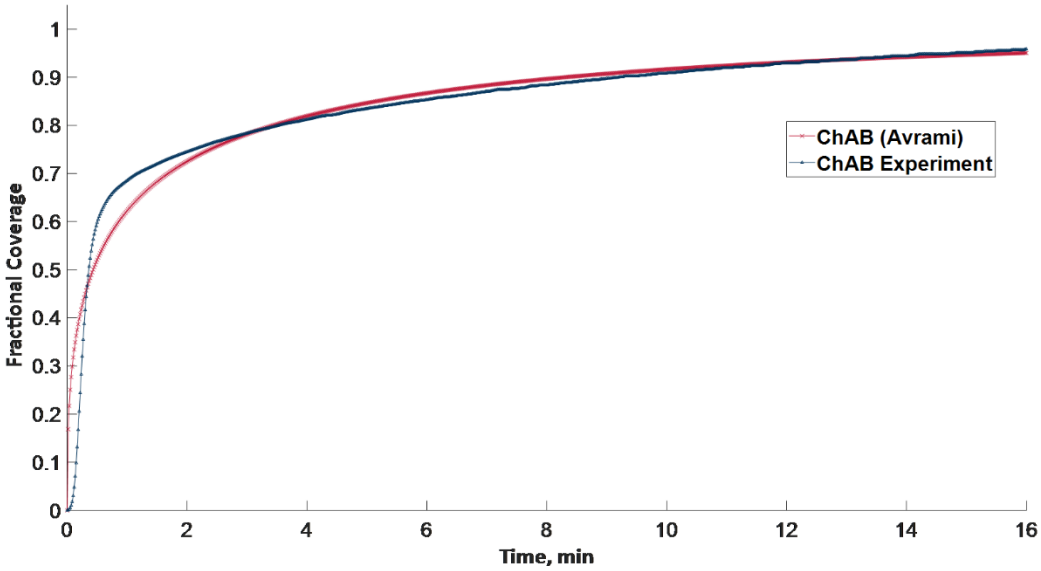

Figure 5.9: Experimental data (triangles) and the kinetic model (crosses) for pure CO_2 adsorption on ChAB at 50 °C and 1 bar.

Further to the kinetic studies, another key aspect for deployment of adsorbents has been evaluated, namely, cyclic adsorption capacity of the material (Section 5.3.2.6.4).

5.3.2.6.4. Adsorption Working Capacity

The performance of ChAB in terms of its working capacity is shown in Figure 5.10.

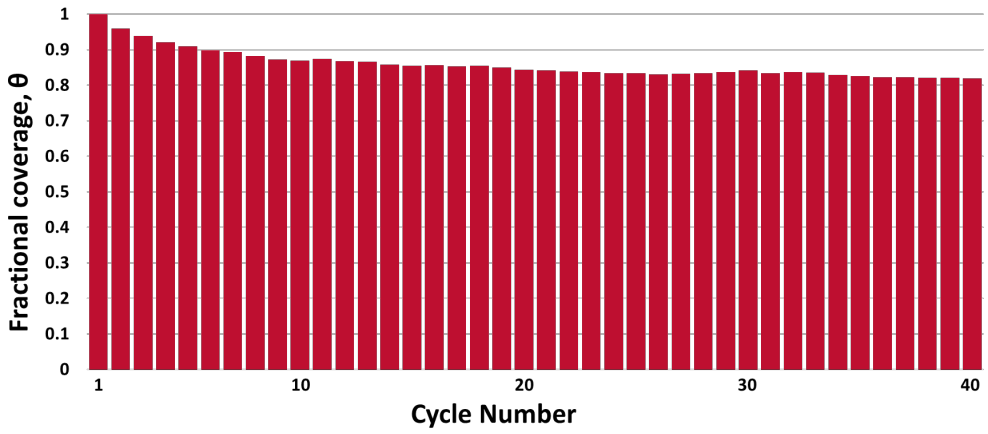

Figure 5.10: Working capacity of ChAB over 40 adsorption-desorption cycles.

The cyclic adsorption capacity of ChAB exhibits a notable decrease over the investigated 40 successive cycles. There is a sharp drop in fractional coverage (Θ) of 4% between the first and second cycles, further highlighting the significance of such cyclic evaluations in the realm of adsorption research. The rate of decline subsequently slows down, resulting in a 2% decrease between cycles 2 and 3, then leading to a capacity of 90% after 10 cycles, followed by 87% after 20 cycles until it eventually levels off at ~85% coverage between cycles 30 and 40. Thus, the work-life of ChAB has been exceeded over 40 successive adsorption-desorption cycles.

ChAB manifests a significantly lower working capacity after 40 cycles compared to the parent BA-100-P. However, it outperforms alternative adsorbents like tetraethylenepentamine functionalized SBA-15 [298]. An alternative amine-modified mesoporous silica, when evaluated in a pressure swing adsorption set-up, exhibited a 4% loss in Θ over 5 cycles [299], which is similar to the performance of ChAB.

The observed diminishing working capacity is likely linked to incomplete (partial) desorption of CO_2 from cycle to cycle. Such phenomenon may have resulted in the blockage of some pores and facilitated a diminished working capacity. This decrease may stem from high energy adsorption sites strongly tethering the adsorbate molecule. Therefore, heat of adsorption studies have also been conducted.

5.3.2.6.5. Heat of Adsorption

The chemically activated bottom ash-derived carbonaceous adsorbent has also undergone investigations into its isosteric heat of adsorption.

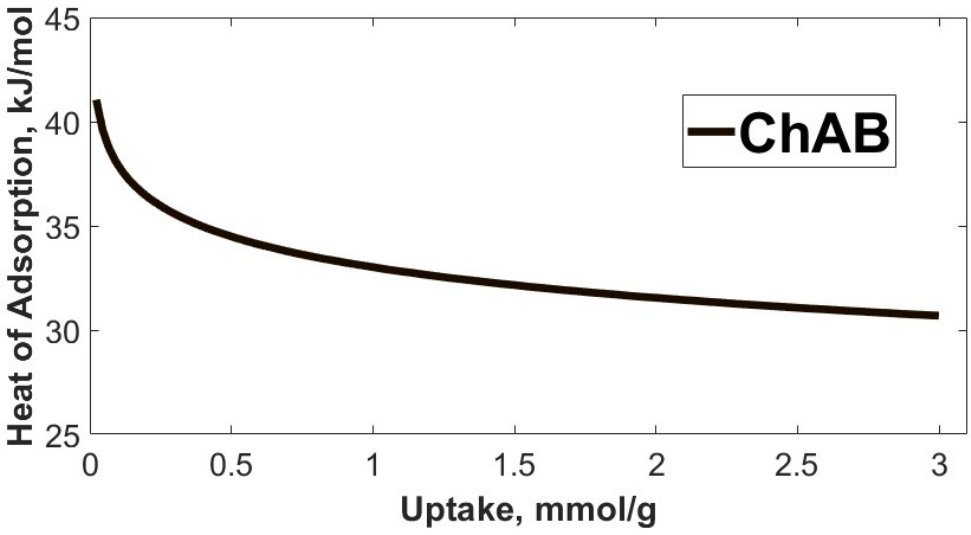

Figure 5.11: Heat of CO_2 adsorption of ChAB.

As is visualised in Figure 5.11, ChAB's heat of adsorption (Q_{st}) follows a declining trend, going from ~ 41 kJ/mol at near zero coverage to ~ 30.5 kJ/mol at an adsorption uptake of ~ 3 mmol/g. These values are higher than those of BA-100-P, thus showing that whilst adsorbing more CO_2, ChAB also would necessitate a higher energy penalty associated with regeneration of sorbent. With regards to alternative materials, the values for this chemically activated biomass combustion bottom ash-derived AC fall within the general range of KOH-activated ACs. For instance, polyacrylonitrile-based ACs presented heats of CO_2 adsorption in the range of 29.73 – 41.61 kJ/mol [300]. Other KOH-activated ACs from rice husk were shown to possess a Q_{st} ranging between ~25 and ~26.5 kJ/mol [148] and 27.3 to 41.3 kJ/mol [301]. Interestingly, within the latter work, one material was exclusively KOH-activated (Q_{st} = 27.3 – 34.9 kJ/mol), while a second sample underwent an additional processing step, namely, impregnation with more potassium hydroxide. This further conditioning of adsorbent facilitated an increase of the heat of CO_2 adsorption to 33.8 – 41.3 kJ/mol. The authors posited that since the *initial* Q_{st} values of over 40 kJ/mol have been observed, chemisorption was taking place [301]. Although, large heat of adsorption values are, indeed, seen in chemisorbents (e.g. amine-modified silicas [299]), they alone do not necessitate chemical adsorption. Such claims have to be (and, indeed, were) evidenced by, firstly and foremostly, presence of matter that could chemically bind CO_2 as well as other analysis techniques (in the case of Wang *et al*. [301] the methods of *in-situ* FTIR and X-ray diffraction after the adsorption step were employed). Therefore, in the case of ChAB, despite having an initial heat of adsorption of over 40 kJ/mol (and a final recorded Q_{st} value of ~ 30.5 kJ/mol), chemisorption is not believed to have taken place. This would lead to a diminished energy penalty compared to other sorbents, yet, as mentioned previously, higher than for the virgin BA-100-P.

5.4. Conclusion

Biomass combustion bottom ash-derived virgin carbon was subjected to chemical activation with KOH following a Taguchi L9 array examine the effects of various parameters on the CO_2 adsorption capacity. The experimental campaign proposes that KOH is a suitable activating agent for developing adsorbents for CO_2, as a high degree of microporosity was developed on the carbon's surface. Specifically, it was found that moderate activation time (30 minutes) and temperature (625 °C) with a relatively high ramp rate (10 °C/min) and an C:KOH impregnation ratio of 1:2 were the

most favourable conditions. Based on this activation procedure, the adsorbent's CO_2 uptake has quadrupled to 1.29 mmol/g at 1 bar and 50 °C (pure CO_2 stream), which was higher than the value obtained for a commercial analogue. Additionally, based on the BET isotherm measurements, a drastic increase in both surface (643.6 m^2/g) and micropore (597.9 m^2/g) area has been noted, which is believed to be the primary cause of such a substantial increase in uptake.

However, such high capacity could not be maintained fully over 40 adsorption-desorption cycles, with Θ dropping to 85% (effectively, the threshold for work-life of adsorbent). Further, an isosteric heat of adsorption of 30.5 kJ/mol has been noted for ChAB.

The impact of chemical activation with KOH has also been seen in terms of a lesser carbon content (elemental = 39.34% mass; fixed = 33% mass). Moreover, ChAB was shown to possess more ash (33.5% mass) as well as retain more moisture (13.5% mass) than the parent BA-100-P material.

Additional research in this area could focus on investigating (and probably enhancing) the selectivity of the adsorbent, over both N_2 and moisture. Alternatively, a more appropriate optimisation envelopes (based on applicable DoE frameworks [185] and the findings presented in this chapter) may be studied to further increase the surface properties and adsorption uptake of chemically activated biomass combustion bottom ash-based adsorbents. Moreover, there is a need to scale up the production process and adsorption technologies, considering factors such as the shape and size of adsorbent particles (e.g., pellets, tablets, beads) and etc. This scaling up process is crucial for developing adsorption reactor process models that closely mimic the conditions of particular post-combustion carbon capture systems. Developing accurate and sophisticated process models based on this proposed further research would, in turn, enable thorough techno-economic analysis, helping to determine the feasibility and economic viability of these technologies.

6. Physical Activation

6.1. Introduction

The waste-to-value supply chain can be viewed as a potential pathway to minimise these costs as well as mitigate issues of disposal *via* avenues of waste valorisation. The biomass combustion bottom ash-derived carbonaceous adsorbents reported in this thesis are a prime candidate for such applications due to the inherent minimal costs for the virgin BA-100-P carbon or the pronounced porosity and affinity towards CO_2 of ChAB (the chemically activated sorbent). However, these approaches are not without their respective limitations, namely, the modest adsorption capacity of the former and the higher production costs of the latter. Moreover, ChAB employs KOH as the activating agent, which produces a secondary waste stream and, thus, constitutes a further environmental concern [302]. Therefore, to strike a balance between the benefits of activation coupled with economical and eco-conscious production approaches [159], physically activated carbons may be viewed as a viable and promising alternative.

Therefore, the waste-derived virgin carbon (BA-100-P) has been activated physically to examine its potential applications in CO_2 adsorption. This has been done *via* employing a DoE framework in order to facilitate the understanding of the process and identification of most significant parameters, as well as revealing any interactions among them. Crucially, the choice of activating gases used in this thesis, namely, CO_2 and N_2, stem from the novelty and cost-effectiveness of the latter and the renowned ability of the former to generate microporous ACs. The respective activation mechanism are also discussed in this chapter.

6.1.1. Materials and Methods

6.1.1.1. Materials

The virgin carbon (BA-100-P) powder was used as the starting (parent) material for the physical activation. The CO_2 uptake was analysed following the same methodology as in the previous chapter; similarly, the characterisation methods were kept the same.

6.1.1.2.Preparation of Physically Activated Carbon

The physical activation investigation was carried out in two steps. Initially, a screening study was conducted using a Taguchi-based L18 orthogonal array to identify the most significant parameters influencing the CO_2 uptake of the adsorbent. Subsequently, two CCDs were developed and executed based on the statistically significant factors to optimise the CO_2 adsorption capacity of the sample *via* RSM. The DoE matrices were generated and statistical analyses were performed using Minitab (version 18).

The experimental campaign was performed employing an insulated tube furnace (Carbolite Gero TF1 12). ~0.4 g of BA-100-P was placed in the centre of an Inconel tube with the desired gas passing over the sample at a predetermined flow rate (FR). The tube was insulated to lessen temperature variations. The activation temperature (T_{act}) was reached by controlling the ramping rate (RR) in each experimental trial. Upon reaching T_{act}, the sample was held in the tube for a given activation time (τ_{act}) under a desired FR of the specified (for the particular experiment) activating gas. Upon completion of the thermal treatment, the sample was allowed to cool down to ambient temperatures inside the tube furnace, using the same gas and flow rate employed during the activation process itself.

6.2. Results and Discussions

6.2.1. Activation and Optimisation Campaigns

To access the influence of five different factors at various levels, a mixed-level L18 Taguchi orthogonal array design was created. The factors consisted of one qualitative parameter investigated at two levels and four quantitative variables at three levels each. The experimental factors and their respective levels are presented in Table 6.1.

Table 6.1: Factors and levels studied *via* the L18 mixed-level Taguchi design.

Factors	**Levels**		
Gas	N_2 or CO_2		
Time (τ_{act}), min	30	50	70
Temperature (T_{act}), °C	700	800	900
Flow Rate (FR), mL/min	100	200	300
Ramp Rate (RR), °C/min	5	15	25

The outcomes of this screening have been thoroughly examined *via* ANOVA with CO_2 adsorption capacity employed as the response (results displayed in Table 6.2).

Table 6.2: Results of ANOVA for the screening experimental campaign.

Factors	F-Value	p-Value	Significance
Gas	55.2	0	1
Time (τ_{act}), min	1.31	0.322	5
Temperature (T_{act}), °C	22.46	0.001	2
Flow Rate (FR), mL/min	2.38	0.154	4
Ramp Rate (RR), °C/min	4.77	0.043	3

Based on the p and F-values obtained from the model (with a regression coefficient (R^2) of 0.936), conclusions were drawn regarding the significance of each parameter. The results indicated that τ_{act} had no statistically significant impact on the process. This observation can be associated with AC having been exposed to inherently longer thermal treatments in the cases of slower RRs. Consequently, the ramping rate has had a stronger influence on the sorbent. This proposes pore-unclogging (involving the release of VOCs) to occur at temperatures lower than 700 °C (i.e. lower investigated level) during the activation of BA-100-P. Thus, the impact of RR is exacerbated, while the importance of τ_{act} decreased. Additionally, during CO_2 activation, the same temperature marks the point at which the *reverse* Boudouard reaction [303], proposed as the mechanism for CO_2 activation, starts to favour production of CO. This process removes some surface carbon atoms and generates porosity within the material.

Boudouard reaction $2CO \rightleftharpoons CO_2 + C$ ($\mathbf{\Delta}H_{298\,K}$ = 172 kJ/mol) Eq. 7

However, within that, formation of surface oxides (lacking a singular definitive description of their chemistry [304]), denoted as C(O), also occurs. These surface oxide complexes can largely be viewed as a combination (or cluster) of more basic (in terms simplicity, *not* acidity) functional groups. They act as an inhibitor of the reaction rate as well as an intermediate product of the gasification process [304]. C(O) may decompose releasing carbon monoxide and/or dioxide [305], [306]; thereby resembling (or contributing to) the reverse Boudouard reaction. Additionally, an active carbon site is produced. However, a free carbon site can then adsorb a CO molecule and slow down gasification of the remaining carbon structure [307].

On the other hand, the surface oxide may stabilise on the carbon surface, leading to formation of oxygen-containing surface functionalities [304] (illustrated as C-O in

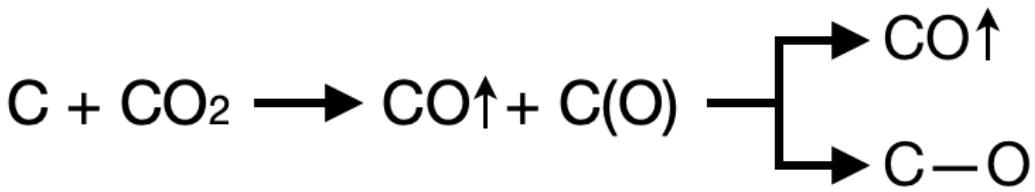

Figure 6.*1*:) that may impact the overall adsorption capacity. For instance, presence of functional groups can alter the electrostatic potential of the surface and/or block access to micropores.

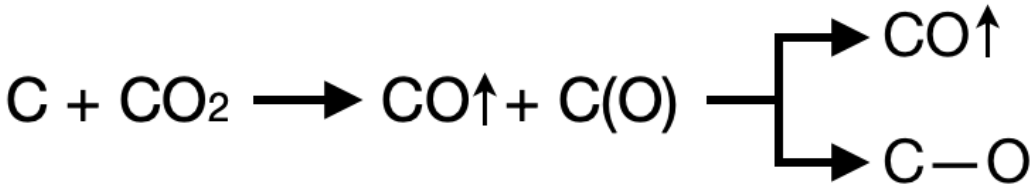

Figure 6.1: Schematic of potential mechanism of CO_2 activation.

This plethora of variations can arise from various factors. For example, the organic precursor, the nature of the carbon (e.g. graphitisable and anisotropic or non-graphitisable and isotropic [304]) and etc. Furthermore, ash impurities can also have an influence as they may act as catalysts for certain reaction(s) pathways. The size, nature, composition, and distribution of these catalyst particles within the carbonaceous material are important considerations. Such variations have been observed to impact the CO_2 activation process [304]. Moreover, the location of these reactions can also contribute to the variations, occurring either between the basal planes of graphene layers or by interacting with the edge carbon atoms as well as the type of the resulting surface complexes formed during the activation process all can play a key role in determining the overall adsorption behaviour [263].

Another important observation is the lack of CO_2 uptake for the AC generated at the highest activation temperature utilising CO_2 as the activating agent. Regardless of other investigated factors and their levels, the samples activated at the highest T_{act} (i.e. 900 °C) presented a very modest yield as well as had a significant visual difference (grey powder) compared to the other samples (black powder), as depicted in Figure 6.2:. This led to the theory that these materials are not primarily composed of carbonaceous matter but rather ash. Thus, the sample depicted in Figure 6.2:b is

assumed to be derived as a result of the reverse Boudouard reaction propagating to an "extreme extent", hence, (near) total loss of carbonaceous matter from the AC upon activation. This hypothesis was further corroborated by EDS and proximate analysis, confirming the inorganic nature of the material activated at 900 °C under CO_2. These samples possessed a nil CO_2 uptake. However, the samples activated at 800 °C with the same gas also performed poorly. Their modest CO_2 adsorption capacity could be attributed to the generation of larger micropores through pore widening, hence, less suitable for CO_2 adsorption. Additionally, these samples also had a low yield of AC. Hence, for physical activation with CO_2, temperatures below 800 °C were more appropriate for producing sorbents with larger CO_2 uptakes.

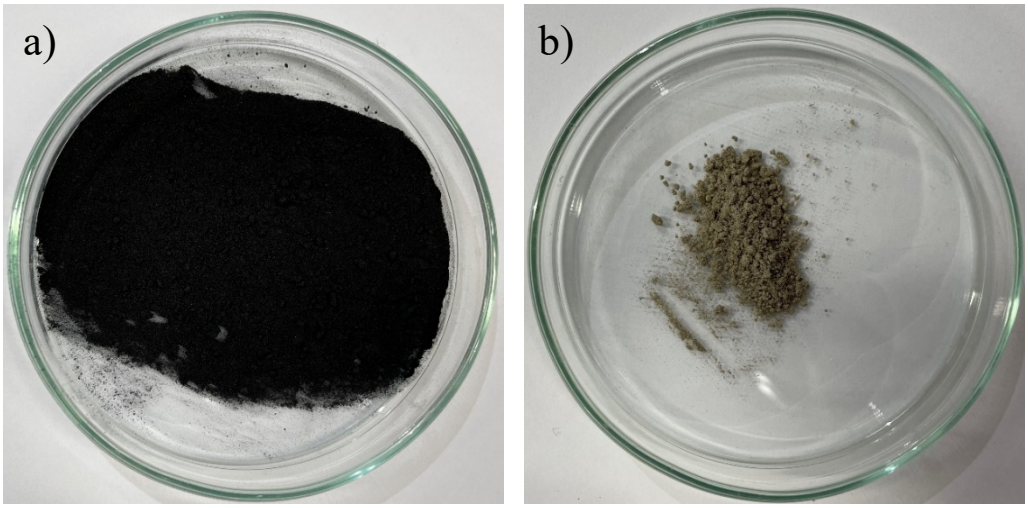

Figure 6.2: Samples activated at 700 °C (a) and at 900 °C (b) adapted from [263].

After the initial Taguchi-based screening campaign, the statistically significant factors (within the boundaries of the investigated levels) were subjected to further examination using two separate CCDs. This design choice was made in order to explore beyond the lower boundary of the activation temperature *via* the axial/star points as well as due to the enhanced ability of this framework type to capture any potential “curvature” within the design space [185]. The former point is particularly vital as it could facilitate an increase in uptake while minimising the energy needed for activation. As such, two separate CCDs were developed for each activating gas, where the statistically significant factors were varied and others were maintained at their lowest values (i.e. τ_{act} = 30 min, FR = 100 mL/min) to align with the principles of green chemistry. Additionally, to verify the repeatability of the outcome, both of the

designs included three repetitions at the “centre point” conditions. Figure 6.3: provides a visual representation of the new design space.

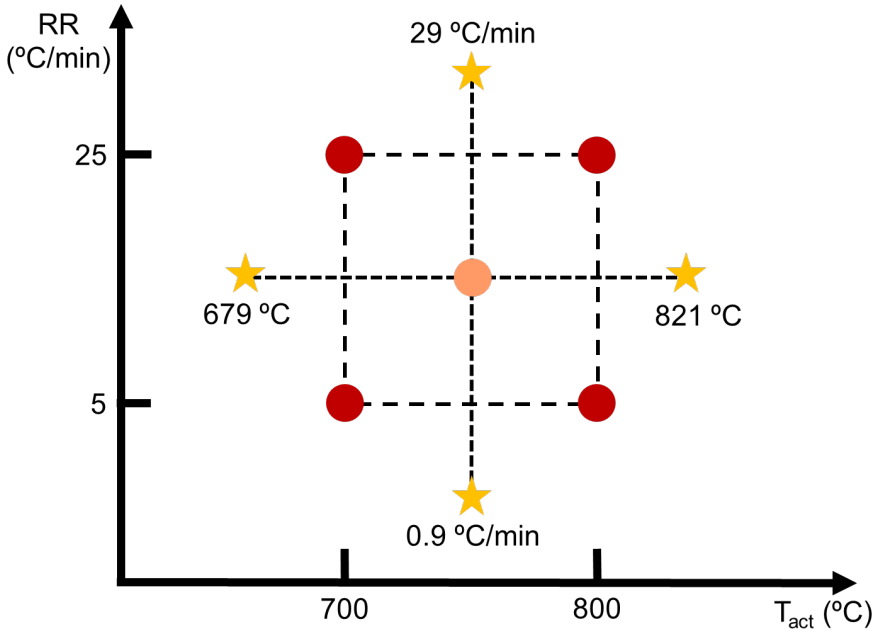

Figure 6.3: The design space used for the optimisation of BA-100-P activation with CO_2 and N_2 adapted from [263].

The results obtained from the CCD experimental campaigns were analysed utilising a similar approach as the initial screening. The identification of optimum points and analysis of the models were conducted using Minitab. The findings of the model (R^2 = 98%) for CO_2 activation are presented in Figure 6.4: in the form of a contour plot.

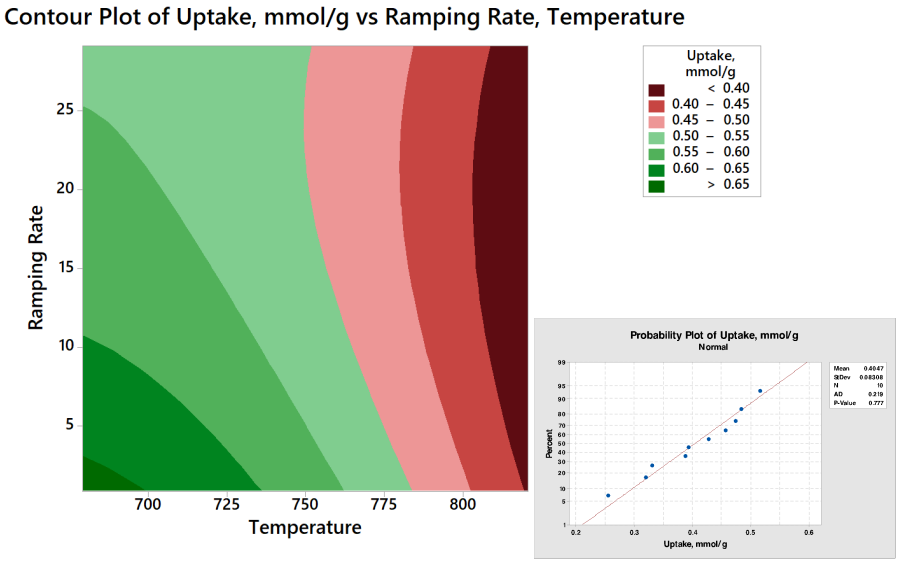

Figure 6.4: Contour plot of CO_2 uptake vs RR and T_{act} for the CO_2 activation with the normality plot as insert (bottom right corner) adapted from [263].

The contour plot in Figure 6.4: clearly shows a trend of enhanced adsorption skewing towards the bottom left corner. This suggests that the "true" optimum activation conditions for maximising uptake may lie outside of the investigated design space. This phenomenon can be attributed to the proposed pore unclogging process, which occurs without damaging the surface morphology at $T_{act} \leq 700$ ºC. Above this temperature, the equilibrium of the Boudouard reaction shifts towards the production of CO [307], which increasingly influences the carbon structure. The contour plot reveals the following observations: in the temperature range of approximately 700 – 750 ºC, a slight decrease in both uptake and yield is observed due to a degree of pore widening. This is followed by a significant drop in both these variables in the range of around 750 – 800 ºC. At temperatures ~ 800 – 850 ºC, severe destruction of the pore structure is believed to have occurred, resulting in a minimal CO_2 adsorption capacity. Lastly, at temperatures of approximately 850 – 900 ºC, complete oxidative degradation of the carbon is noticed, leading to a lack of CO_2 uptake and a very low product yield (as previously shown in Figure 6.2:). Therefore, both of the investigated factors are statistically significant as indicated by the F and p-values presented in Table 6.3:. Further, the presence of a degree of non-linearity of the contour plot may stem from the quadratic effect of T_{act} having a p-value just above of the 0.05 threshold.

Table 6.3: ANOVA results of the CO_2 activation campaign.

Effect	F-Value	p-Value
Temperature	161.98	0
Ramping Rate	17.01	0.015
Temperature*Temperature	6.93	0.058
Ramping Rate*Ramping Rate	2.87	0.166
Temperature*Ramping Rate	1.92	0.238

The optimised conditions for maximising the uptake are believed to be 679 °C and a RR of 0.9 °C/min. This sample exhibited an increased CO_2 adsorption capacity of 0.689 mmol/g under pure CO_2 at 50 °C. Additionally, a favourable product yield of 62.3% was achieved. However, based on the trend observed from the contour plots,

a further improvement of the capture capacity may be reached by activating the BA-derived carbon at temperatures below 679 °C.

On the other hand, the activation under N_2 experiments and optimisation did not suggest a lower activation temperature. Activation with N_2 can be somewhat compared to conventional pyrolysis as it lacks an oxidising atmosphere. Changes to surface chemistry occur at temperatures lower than those evaluated in this study. For instance, between 300 and 500 °C, condensation/dehydration takes place, resulting in the loss of oxygen and hydrogen, thus discarding alcohol [308] or phenolic groups [309], though, the latter can withstand temperatures up to 650 °C [310]. The hydroxyl-containing (-OH) surface functional groups may also convert to COOH *via* oxidation (carboxylation) reactions below 500 °C [311]. However, carboxylic groups are also known to decompose at temperatures below 400 °C, whilst for carbonyl (C=O) functionalities the temperature range is between 700 and 900 °C [310] evolving CO_2 and CO, respectively [309]. Figure 6.5 provides a simplified description of these processes.

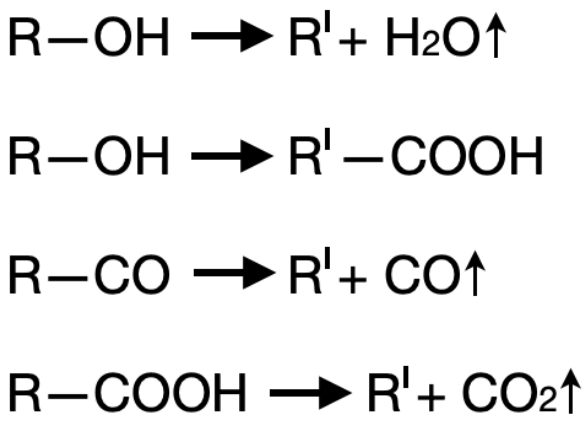

Figure 6.5: Some descriptive surface functional groups' reactions.

Other decomposition products (e.g. H_2O) as well as VOCs (e.g. saturated/unsaturated light hydrocarbons, alcohols, aldehydes, ketones and etc.) can also be released within the wide temperature range described above. Additionally, at temperatures over 900 °C, the micropore structures of the carbon may shrink, resulting in a loss of surface area, which has been observed in previous studies and assigned to the loss of free sites and defects due to high-temperature annealing [312]. In the activation under N_2 campaign, the inert atmosphere acts as a carrier gas, removing the evolved VOCs from the carbon surface, thereby preventing their adsorption and

recondensation. The produced model showed a R^2 value of 91.5%. The contour plots for CO_2 adsorption versus T_{act} and RR in the activation under N_2 campaign are presented in Figure 6.6.

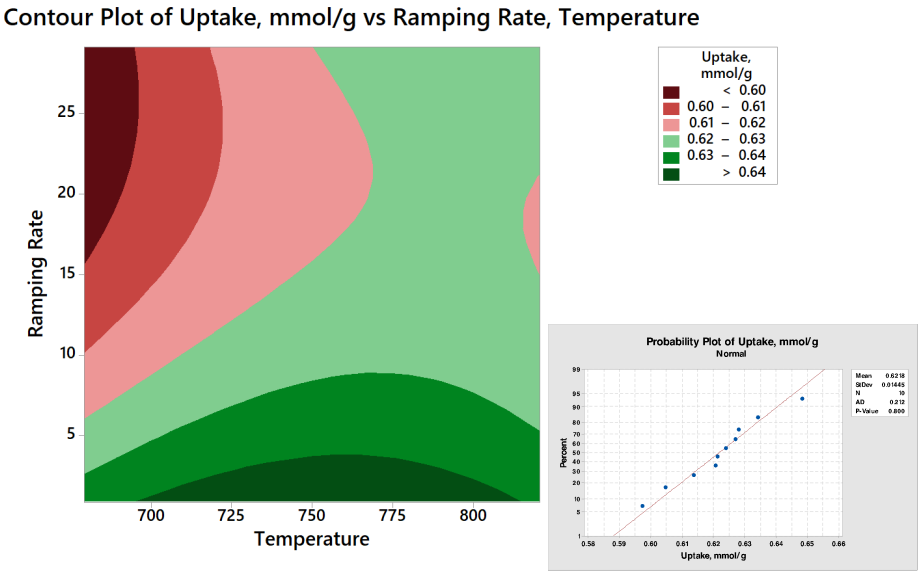

Figure 6.6: Contour plot of CO_2 uptake vs RR and T_{act} for the activation under N_2 with the normality plot as insert (bottom right corner) adapted from [263].

The analysis of Figure 6.6 reveals the presence of curvilinear relationships within the studied design space for nitrogen activation. Additionally, ANOVA confirmed that both the RR and T_{act}, were of statistical significance, as indicated by the F and p-values provided in Table 6.4:. Further, the optimised activation conditions were proposed to be at 748 °C and 0.9 °C/min.

Table 6.4: ANOVA results of the activation under N_2 campaign.

Effect	F-Value	p-Value
Temperature	9.03	0.04
Ramping Rate	18.92	0.012
Temperature*Temperature	3.03	0.157
Ramping Rate*Ramping Rate	4.77	0.094
Temperature*Ramping Rate	1.63	0.271

The outcome of both the CO_2 and N_2 activation campaigns lead to a greater adsorption capacity compared to the virgin carbon. Interestingly, the N_2-activated sample showed similar results to the CO_2-activated AC in terms of uptake and product yield. However, since the CO_2-activated sample presented a lower energy requirement

for activation (due to a lower T_{act}) and the potential for further reduction, it was selected for further characterisation and analysis under the name AC-Opt.

6.2.2. Characterisation of Optimum Sample

6.2.2.1. Scanning Electron Microscopy (SEM) & Energy Dispersive X-ray Spectroscopy (EDS)

SEM/EDS analysis was conducted to examine the surface morphology and elemental composition of the produced material. Figure 6.7 presents the results of SEM imaging.

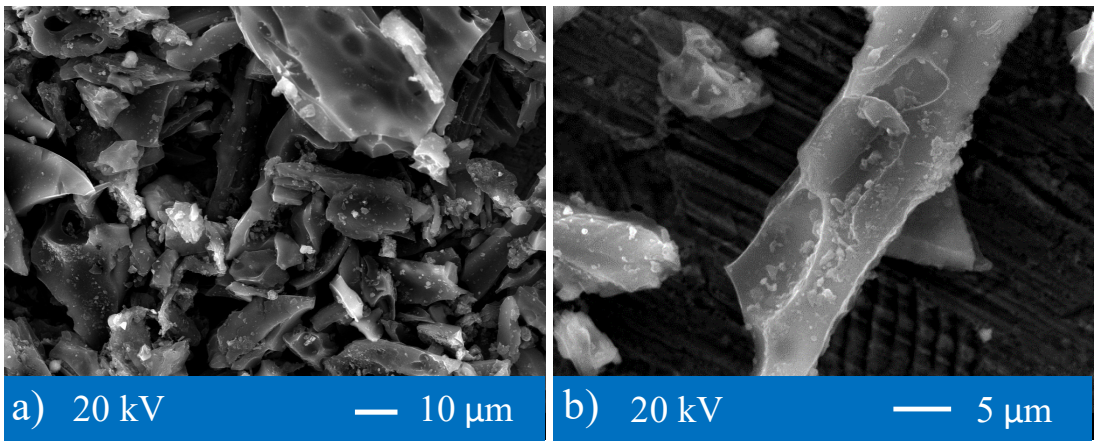

Figure 6.7: SEM images of AC-Opt.

Similarly to BA-100-P, a heterogenous surface morphology is noted for AC-Opt, including carbonaceous particles of varying sizes accompanied by the spherical particles of aluminosilicate origin. However, AC-Opt displays a more pronounced surface roughness and heterogeneity (Figure 6.7b) compared to the parent material. Moreover, there is a slight change in the elemental composition, indicated by a decreased amount of elemental carbon in Table 6.5:. This change was expected and was accredited to the loss of carbonaceous matter as part of the activation process, commonly referred to as burn-off.

Table 6.5: Surface elemental composition of AC-Opt.

Element	Weight %
O	72.0
C	26.7
Ca	0.6
Si	0.3

Al	0.2
Mg	0.1
K	0.1

However, more reliable bulk analysis methods (as opposed to surface techniques such as EDS) are preferred for more accurate estimation of carbon content.

6.2.2.2. Ultimate Analysis

The CHN analysis, also known as ultimate analysis, has corroborated the hypothesis of loss of elemental C (compared to the virgin carbon) as well as provided a more accurate qualitative estimate. The results suggest the activated sample to have a lower carbon content (approximately 54.5%) compared to the virgin sample, as well as reduced levels of hydrogen and nitrogen by weight. These decreased values can be attributed to the removal of carbonaceous matter during the thermal treatment (i.e. activation). The detailed results of the ultimate analysis can be found in Table 6.6:.

Table 6.6: Ultimate analysis results of AC-Opt.

Element	Weight %
C	54.47
H	1.00
N	0.26
Other	44.27

As for quantification of the impurities, proximate analysis is the preferred method.

6.2.2.3. Proximate Analysis

Proximate analysis [250] was conducted on the sample to determine the levels of ash impurities, fixed C, VOC and moisture content. The results of this analysis are presented in Table 6.7:.

Table 6.7: Proximate analysis results of AC-Opt.

Sample name	Moisture, wt%	VOC, wt%	Fixed C, wt%	Ash, wt%
AC-Opt	1.5	7	49	42.5

The results of proximate analysis support the notion of volatile compound release from the virgin carbon as part of the activation process, leading to an inflated amount of fixed carbon and ash contents. Interestingly, the low moisture content may suggest

the material to possess a low affinity towards H_2O, an important characteristic of an adsorbent suitable for post-combustion carbon capture.

6.2.2.4. Spectroscopic Analysis

6.2.2.4.1. Fourier- Transform Infrared Spectroscopy (FTIR)

AC-Opt was also analysed *via* FTIR with the spectrum shown in Figure 6.8.

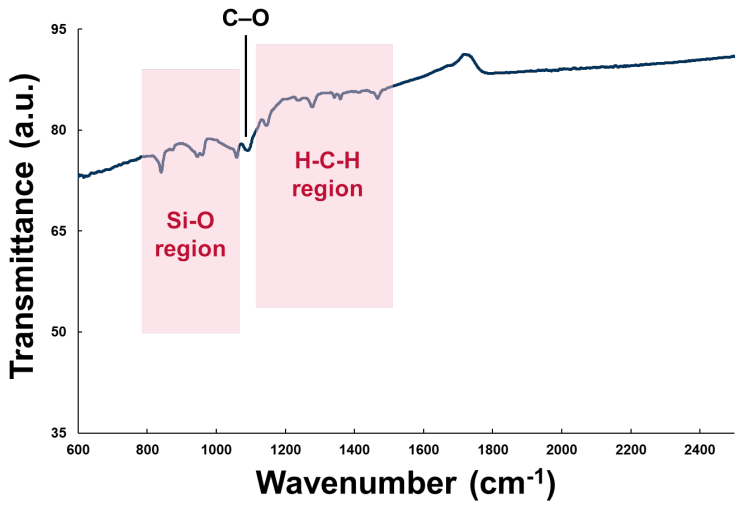

Figure 6.8: Infrared spectrum of AC-Opt.

The produced spectrum indicates a significant reduction in surface functionalities after heat treatment under CO_2. Instead, AC-Opt possesses mostly C-H bonds as evidenced by various vibrations associated with such groups (i.e. 1240, 1279, 1342, 1360 and 1467 cm^{-1}). For instance, the peak at 1360 cm^{-1} may correspond to symmetric bending of CH_3 [264], while the peak at 1467 cm^{-1} may represents scissoring (in-plane bending) vibrations of CH_2 [264]. This splitting of peaks could also be indicative of the presence of semi-crystalline structures within the sample. Despite the loss of many surface functionalities, some functional groups have survived the activation process. The C-O graphitic stretch is still present at 1147 cm^{-1} [261], [262], [313], indicating the persistence of carbon-oxygen bonds of the graphitic structure. Additionally, the 1060 cm^{-1} band may be ascribed to an epoxy-type C-O bond [244]. However, the latter (alongside the peaks at 946, 961 and 1090 cm^{-1}) lays in the Si-O region also, hence, may indicate the presence of silicon-oxygen bonds from the ash impurities. The minor shifts in the wavenumbers after activation could be attributed to transformations in the Si-O bonds or to the inherent structural disorder of both the AC and the virgin carbon precursor. Overall, the FTIR analysis of AC-Opt confirms the elimination of most surface functionalities and shows mostly presence of vibrational

modes associated with methylene-type groups. These phenomena may be associated with the slow ramping rate that allows the functional groups to be alleviated from the surface of the carbon (as per Section 6.2.1). Nevertheless, the persistence of C-O bonds and the presence of Si-O bonds suggest the retention of some specific functional groups during the activation process as well as ash particles.

6.2.2.4.2. Raman Spectroscopy

Herein, the Raman spectrum (Figure 6.9:) has been used as an additional indicator of potentially developed porosity. Since the I_D/I_G ratio is commonly used as a measure of structural disorder or defects in carbon materials, a higher I_D/I_G ratio indicates a greater degree of heterogeneity and a higher number of defects, hence, possibly greater surface roughness and porosity. The activation with CO_2 lead to an enhancement of the I_D/I_G ratio to 0.81, suggesting development of a more prominent surface area. However, the increase in the I_D/I_G ratio could also be a sign of a partial transformation from sp^2 to sp^3 hybridisation state (from C=C or C=O bonds to C-H).

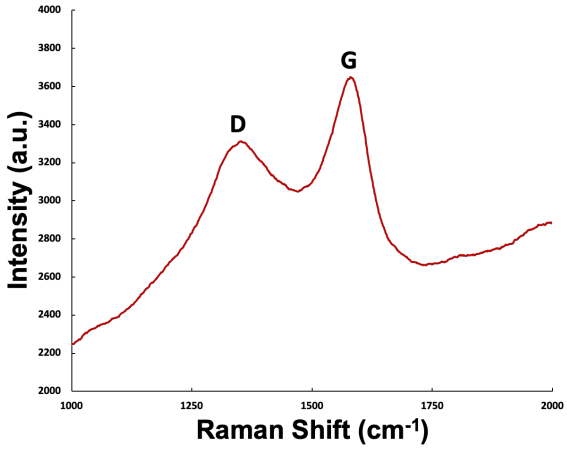

Figure 6.9: Raman spectrum of AC-Opt.

6.2.2.5. Surface Area Analysis

A substantial increase in BET surface area is observed due to physical activation with CO_2, rising from ~4 m^2/g to 248 m^2/g (BA-100-P and AC-Opt, respectively). The N_2 physisorption isotherm of AC-Opt exhibits a type IV behaviour, which is indicative of a mesoporous structure [82]. Type IV isotherms typically show a saturation plateau (just like type I) but saturation may also present itself as a simple inflection point [82], which is the case of AC-Opt as evidenced by Figure 6.10:. Furthermore, AC-Opt displays a type H4 hysteresis loop, which is characteristic of micro-mesoporous

carbons [86]. Indeed, ~ 74% of the sample's surface area (i.e. 183 m^2/g) is attributed to micropores, as determined by the t-plot method.

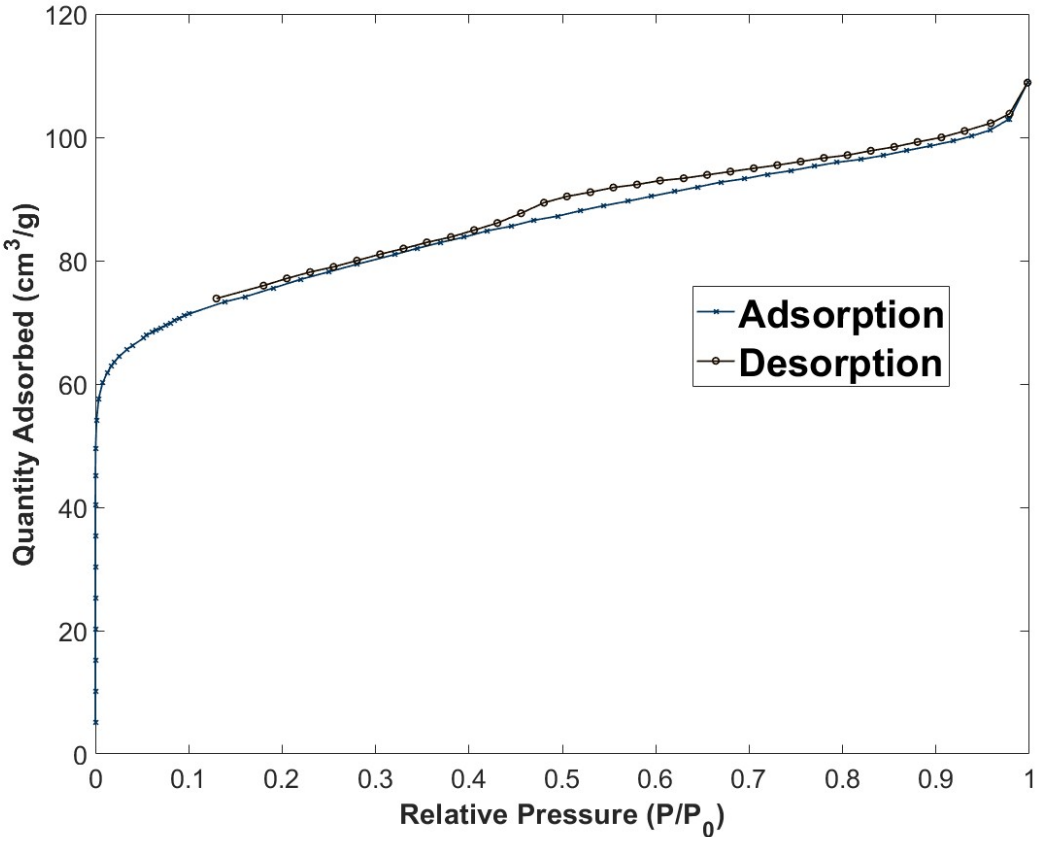

Figure 6.10: BET physisorption isotherm of AC-Opt.

The micropore volume was also drastically enhanced: from 0.00087 cm^3/g for BA-100-P to 0.0936 cm^3/g in the case of AC-Opt. This substantial rise indicates the successful development of microporosity upon CO_2 activation. In gas-phase adsorption, a greater pore volume is considered to be beneficial because it largely determines the total adsorption capacity of an AC [289]. Moreover, the average pore diameters have experienced a drastic change (dropping from 14 nm to 3.7 nm) as a consequence of generation of micropores. However, smaller mesopores would also contribute to the decrease of the BJH (desorption branch) average pore diameter value. Their existence is consistent with the phenomenon of the hysteresis loop appearing due to presence of pores greater than ~ 4 nm [86]. These findings are confirmed by the pore size distribution plot in Figure 6.11.

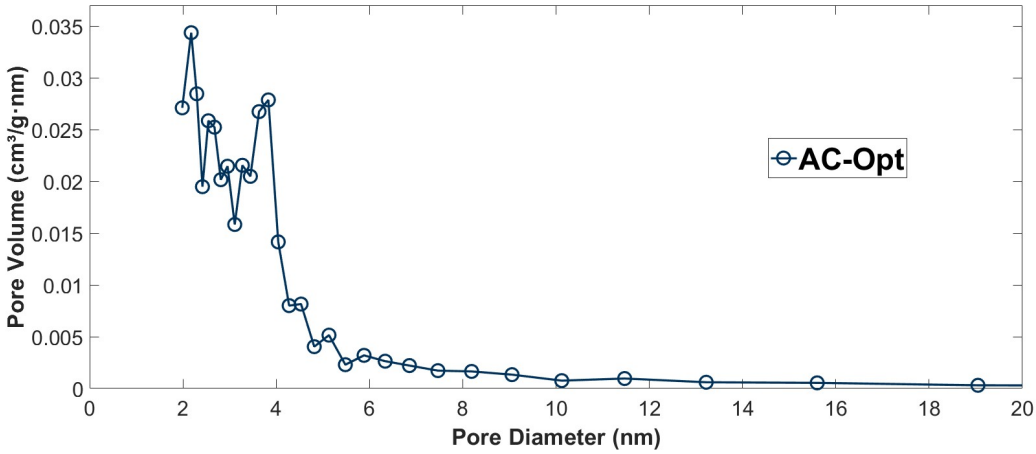

Figure 6.11: Pore size distribution plot of AC-Opt.

However, apart from a prominent surface area, an appropriate adsorbent should possess a strong affinity to the adsorbate.

6.2.2.6. CO_2 Adsorption Experiments

The effectiveness of CO_2 activation can be assessed by examining the equilibrium capacity of the produced sample.

6.2.2.6.1. Adsorption Capacity

The exothermic nature of adsorption on AC-Opt can be visualised by examining the trends shown in Table 6.8: a drop in uptake with an increase in temperature.

Table 6.8: Results of AC-Opt CO_2 adsorption tests at different temperatures.

Uptake at 25 °C, mmol/g	Uptake at 50 °C, mmol/g	Uptake at 75 °C, mmol/g
1.04	0.69	0.43

CO_2 activation at the optimum conditions facilitated a doubling of the adsorption capacity (within the examined temperatures) compared to the parent virgin BA-100-P. Further, AC-Opt exhibits a comparable uptake to a commercially available analogue, even surpassing this alternative AC in the temperature range suitable for post-combustion carbon capture (i.e. 50 and 75 °C) [263].

However, to further analyse the physically activated carbon, the equilibrium adsorption studies have also been executed.

6.2.2.6.2. Equilibrium Adsorption Isotherms

A variety of adsorption isotherms has been fitted to the gathered experimental data (Table 6.9).

Table 6.9: AC-Opt equilibrium adsorption isotherm fits at 25 ºC.

Isotherm Model	R^2	NRMSE
Langmuir	0.9911	0.0433
Freundlich	0.9965	0.0269
Double-site Langmuir	0.9998	0.0071
Triple-site Langmuir	0.9948	0.0348
Toth	0.9999	0.0042

Out of the examined models, AC-Opt favours the Toth model due to the highest R^2 value alongside the minimal NRMSE. This isotherm is therefore, expanded upon in Table 6.10: and Figure 6.12.

Table 6.10: AC-Opt equilibrium adsorption isotherm data at 0 ºC and 25 ºC.

Temperature	Isotherm Model	Identified parameters
0 °C	Toth	q_{max} = 906.2 mg/g K_T = 26 1/bar n = 0.1826
25 °C	Toth	q_{max} = 286.3 mg/g K_T = 3.423 1/bar n = 0.3171

This observation (coupled with the high quality of fit for the Double-site Langmuir model) proposes the material to exhibit surface heterogeneity, hence, possess a non-uniform pore structure (which can also be evidenced by the pore size distribution plots in Figure 6.11). However, the activation process has resulted in a more intricate and potentially non-discrete heterogeneous surface, which may be the reason behind the better fit of the Toth isotherm. Further, this finding aligns with the increased number of defects observed on the surface of AC-Opt, as discussed in Section 6.2.2.4.2.

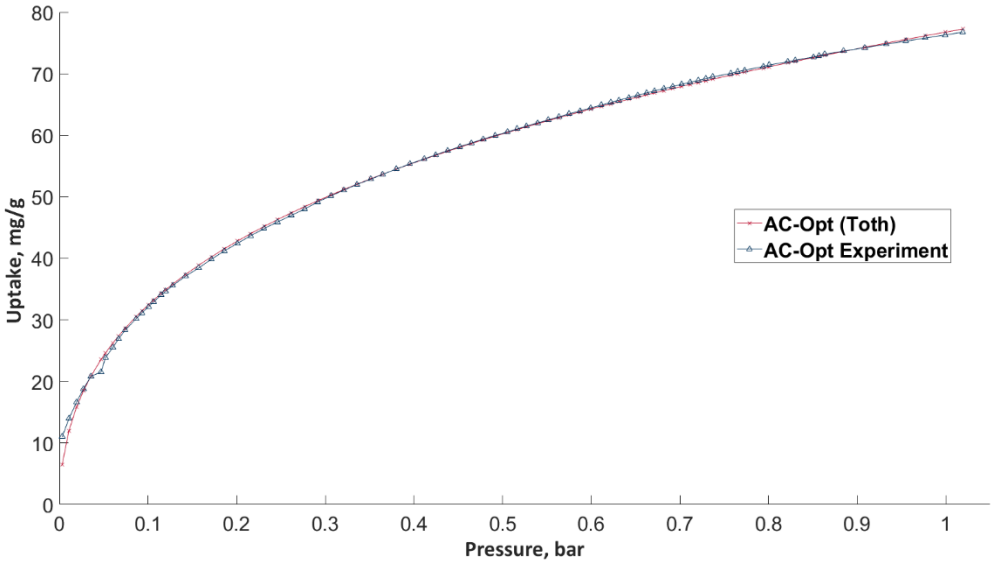

Figure 6.12: Experimental data (triangles) and the equilibrium isotherm model (crosses) AC-Opt at 0 °C under pure CO_2.

However, relying solely on the criteria of equilibrium adsorption capacity is insufficient to determine the suitability of the material for a given application. Therefore, the kinetics of AC-Opt have also been investigated.

6.2.2.6.3. Adsorption Kinetics

When comparing suitability of the PFO and PSO models, AC-Opt demonstrated a better fit to the latter (across the range of evaluated temperatures), suggesting that the adsorption process is not diffusion controlled [237] but rather more strongly dependent upon presence of active adsorption sites [263]. This is to be expected as activation has produced both mesopores and micropores on the surface of the sample (as highlighted in Section 6.2.2.5), thus facilitating (intraparticle) diffusion into the framework as well as acting as accessible adsorption sites. However, when comparing across the plethora of kinetic models (Table 6.11:) applied in this thesis, the Modified Ritchie equation (Figure 6.13 and Table 6.12:) is suggested to be the most appropriate kinetic model.

Table 6.11: CO_2 adsorption kinetic model fits for AC-Opt at 50 ºC.

Kinetic Model	R^2	NRMSE
Pseudo-First Order (PFO)	0.8634	0.1617
Pseudo-Second Order (PSO)	0.9621	0.0238
Modified Ritchie	0.9741	0.0177

Intraparticle diffusion	0.3356	0.0900
Avrami	0.9247	0.0290
Elovich	0.6542	0.3523

Table 6.12: CO_2 adsorption kinetics on AC-Opt at 50 ºC.

Kinetic Model	**Identified parameters**
Modified Ritchie	$K_{(R)}$ = 0.08875 β= 0.8259

It should be noted that the Modified Ritchie model includes a term for initial particle loading (β), suggesting incomplete purge of the sample before adsorption took place. Nevertheless, the presence of an additional parameter in the equation may have also facilitated better fit of model.

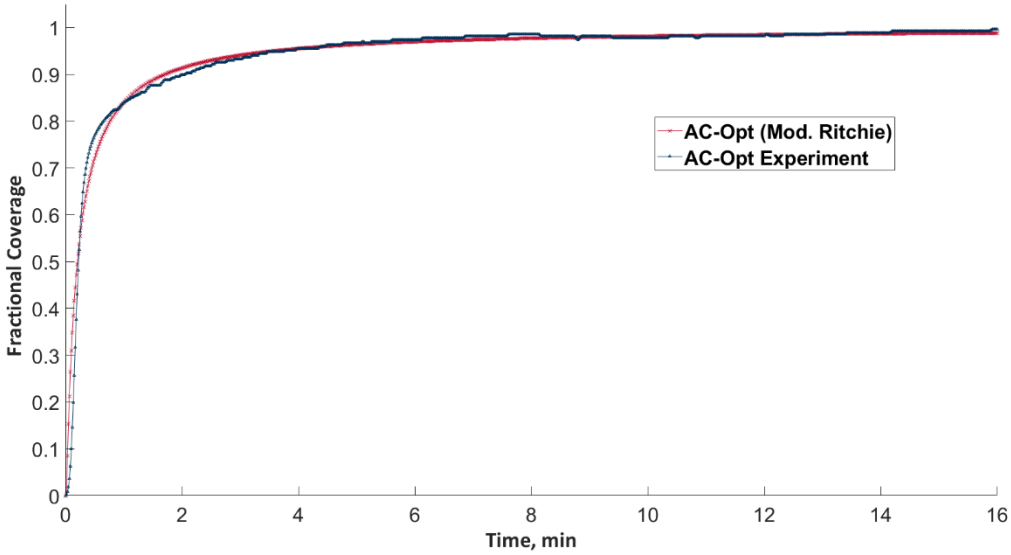

Figure 6.13: Experimental data (triangles) and the kinetic model (crosses) for pure CO_2 adsorption on AC-Opt at 50 °C and 1 bar.

A fast adsorption rate is paramount for a suitable adsorbent as this would enable rapid cycling, resulting in a lesser residence/contact time (hence, bed size), which in turn allows the adsorption column to be smaller, thus constituting reduced capital costs [119], [314]. However, all these benefits are derived from an ideal breakthrough curve (straight vertical line as opposed a more classical/real-world S-shaped curve), a theoretical concept that would necessitate instantaneous adsorption across the whole bed (thus, also meaning complete utilisation of all of the adsorbent bed for both the adsorption and regeneration steps), hence, facilitating a smaller bed size.

Another key factor in preparation of a suitable adsorbents is the cycling/working capacity of the material. This has been investigated in the next section.

6.2.2.6.4. Adsorption Working Capacity

Figure 6.14 indicates the excellent performance of the prepared AC-Opt in terms of cyclic adsorption-desorption studies.

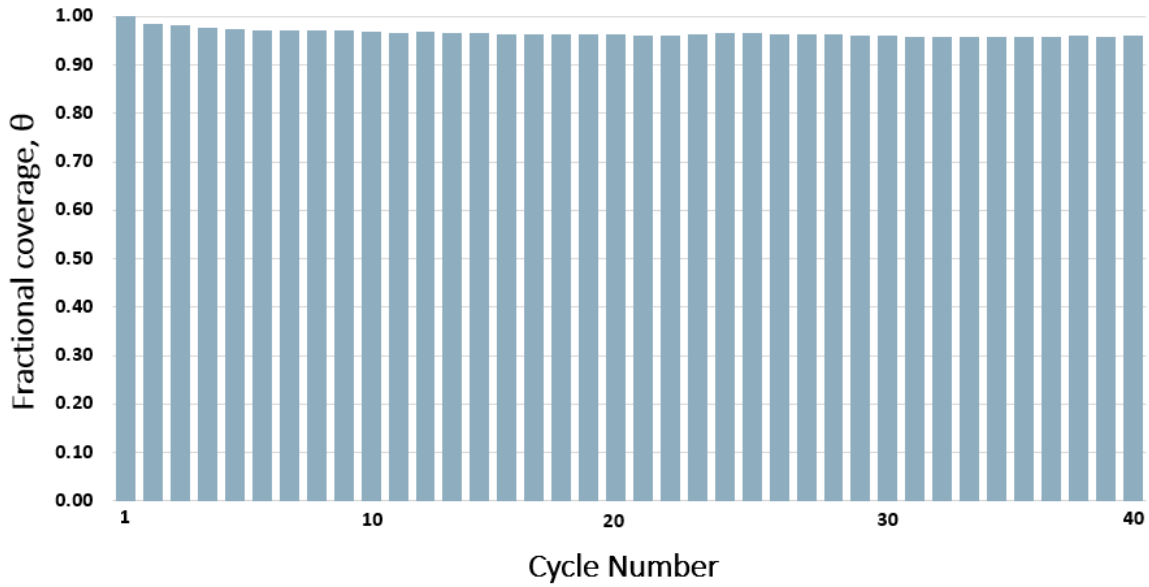

Figure 6.14: Working capacity of AC-Opt over 40 adsorption-desorption cycles.

AC-Opt shows a minimal loss of adsorption capacity throughout the evaluated range, maintaining a fractional coverage above 96%. The sharpest decline of nearly 1.5% is observed after the first cycle which could be due to CO_2 molecules being only partially desorbed (perhaps, as part of incomplete capillary evaporation) from the surface of AC-Opt as opposed to the gaseous species from ambient air that have been purged off prior to the initial cycle. Following which, a slow and steady decline (ranging between 0.5 and 0.1%) is noted stabilising at ~96% original uptake at cycle 15 until cycle 40 (i.e. end of observation). Within that, minor fluctuations are noted which may be attributed to the sample not completely desorbing CO_2 at 150 °C (as suggested by the Modified Ritchie equation fit in Table 6.11: and Table 6.*12*:).

Regardless, activation under the optimum conditions resulted in a material with a more favourable cyclic performance than the virgin sorbent. Further, similar performance to a commercial AC used for comparison in this study was observed [263]. Further, AC-Opt possess either a similar or a significantly higher working capacity than some other alternative (carbon nanotubes and functionalised zeolites

and silicas) sorbents reported in the literature [298], [315], [316]. Notably, the decline between the first and second cycle is much lower than the 10 – 16% that can be found for some other recently reported advanced carbonaceous adsorbents for CO_2 [267]. However, it is important to highlight the fact that in order to make a fair comparison between different adsorbents, the materials should undergo adsorption under the same conditions or, alternatively, within their respective ideal/optimum operation envelope. The former may result in some adsorbents not reaching their equilibrium/not being properly purged, while using the preferred operational envelopes would require prior knowledge of the most advantageous conditions for each sorbent. These obstacles limit the ability to conduct an unbiased and fair comparison among different sorbents. However, the cyclic capacity test on a commercial AC [263] were conducted following the exact same procedure as the one deployed in this thesis to allow for consistency in comparison.

With regards to the parent BA-100-P, the stronger cyclic performance of AC-Opt may be due to its more extensive thermal treatment, specifically physical activation, which enhanced its ability to withstand increases in temperature.

6.2.2.6.5. Heat of Adsorption

The physically activated biomass combustion bottom ash-derived carbonaceous adsorbent has also been investigated in terms of the isosteric heat of adsorption of CO_2.

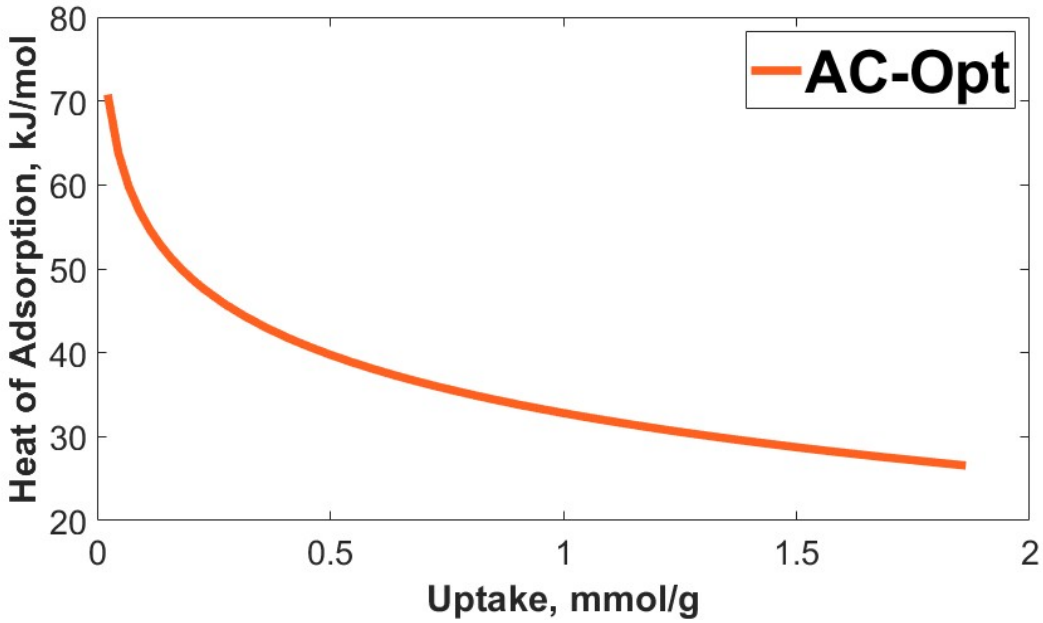

Figure 6.15: Heat of CO_2 adsorption of AC-Opt as a function of CO_2 uptake.

As can be noted from in Figure 6.15, a steady decline can be observed for the heat of adsorption of CO_2 on AC-Opt. Based on the model isotherms Q_{st} presents a decline that levels at approximately 26.5 kJ/mol. These values are on par with heats of CO_2 adsorption for some commercial ACs (e.g. 16.2 – 25.7 kJ/mol [317]) and outperform alternative, recently reported carbonaceous materials (30 – 38 kJ/mol [267]) as well as was well below the values for various zeolites [266], [318], [319] and amine-loaded silicas [299].

Further, a Q_{st} value of 26.5 kJ/mol suggests AC-Opt to physiosorb carbon dioxide, hence, allowing for a weaker bond (as opposed to chemisorption), leading to a lesser energy requirement for regeneration than the chemically activated carbon investigated in this thesis (ChAB). This would constitute a substantial benefit in terms of the economic aspect of deploying this AC.

6.2.3. Economic Evaluation

The procedure for estimating manufacturing expenses in relation to the final product price is, unfortunately, not well-established [320]. However, BA-derived sorbents have the potential to be more cost-effective compared to commercially available alternatives due to the following reasons:

- Lack of a carbonisation step. Conventional AC production pathways involve a demanding (in terms of energy consumption) carbonisation step. As part of AC production, electricity consumption constitutes approximately 15-50% of total manufacturing cost [321]–[323]. Within that, the pyrolysis step itself accounts for a significant portion of the final production cost (around 20% [324], 27% [325] or 39% [326]). BA-derived sorbents avoid this step, thus constituting an advantage (in terms of cost) to current commercial alternative ACs.
- Absence of transport/logistics costs if deployed *in-situ*. With the BA being readily availability on-site of the biomass combustion facilities, the need for transportation of the capture media is removed, resulting in additional cost savings. The logistics costs estimates in the literature vary from approximately 3% [327] to 10% [326] of the production cost.
- Waste management and valorisation. ACs are often derived from waste materials, making them readily accessible at minimal or no cost. However, by

utilising BA-derived materials, there is an additional advantage in terms of waste valorisation, as it aids in reducing landfill costs associated with waste ash. In the UK, as of 1st April 2023, the standard landfill tax rate is £102.1/tonne and £3.25/tonne for inert/non-hazardous waste. Moreover, UK government guidance also emphasises minimising biomass waste whilst simultaneously maximising its value as a resource [328].

- The carbon extraction process involves grinding and separation by size. As part of the sieving process, the residual top fractions (particle sizes over 500 μm) primarily consist of unburnt biomass. This pulverised biomass can be reintroduced into the boiler as fuel, effectively improving the overall energy/fuel efficiency of the power plant, thus constituting an additional monetary benefit of such application. An alternative option would be to use this reclaimed fuel in a separate unit dedicated to sorbent regeneration (or AC production), thereby further decreasing the parasitic energy requirement associated with post-combustion carbon capture (or the production cost of sorbent).
    - In addition, reclaiming the top fractions not only enhances the utilisation of biomass but also leads to a decrease in the amount of waste ash sent to landfill. This also aligns with the government's guidance on minimising biomass waste/maxising biomass value [328] and offers an extra financial incentive by further reducing waste disposal costs.

Furthermore, there are additional aspects to the physically activated BA-derived carbon described in this thesis, namely:

- Lack of specific chemical activating agents leads to a more cost-effective and eco-friendly approach as opposed to chemical activation, where the activating agent has to be procured and generates secondary waste (which leads to additional waste management issues). Industrial-scale viability and carbon neutrality potential have been demonstrated with physical activation utilising CO_2 for waste plastic ACs [329]. Additionally, comparisons between physical activation with steam and with CO_2 for oil palm waste indicate the latter route as a more economical method [330]. Furthermore, the captured CO_2 can be recycled as the activating gas, further optimising the process and aligning with the principles of a circular economy approach.

- Potential for further decreasing the T_{act}, hence, less demanding activation conditions.

6.3. Conclusion

Physical activation of the virgin carbon has been examined employing a two-step approach. Initially, a singular mixed-level L18 Taguchi DoE framework has been employed to screen for statistical significance of five parameters (one qualitative (gas) at two levels and four quantitative at three levels each). These results informed the further experimental campaign, i.e. optimisation campaign. Therefore, statistically significant factors, namely, gas type, RR and T_{act} were selected for further investigation using two separate CCDs (as this framework does not allow for incorporation of both categorical and quantitative parameters). Based on the outcomes from the second step, the activation conditions that allowed to maximise the CO_2 uptake of the bottom ash-derived sorbent were as follows: τ_{act} of 30 min at a T_{act} of 679 °C achieved at a RR of 0.9 °C/min under a CO_2 flow rate of 100 mL/min. This process produced a 62.3% yield of AC-Opt with an uptake double that of the precursor at the same conditions (i.e. 0.69 mmol/g from a pure CO_2 stream at 1 bar and 50 °C) and slightly over a commercial AC. AC-Opt could also maintain a high working capacity of 96% over 40 adsorption-desorption cycles, thus, outperforming both the parent and chemically activated (ChAB) bottom ash-derived carbons.

Additionally, AC-Opt was extensively characterised. Namely, physical activation was shown to decrease the amount of VOC (7% mass) and elemental carbon (54.47% mass) within the sample, hence, elevating the fixed carbon (49% mass) and ash (42.5% mass) contents. Within this, a lower moisture content (1.5% mass) was noted, suggesting the material to be more hydrophobic than the parent BA-100-P and its chemically activated counterpart (ChAB). Since resistivity to moisture is of utter importance for industrial flue gas treatment, AC-Opt was deemed superior (in this and other aspects) than the alternative sorbents described in this thesis.

Similar to the parent BA-100-P, AC-Opt is heterogeneous with presence of both amorphous and graphitic phases, yet without a variety of surface functionalities. The latter was ascribed to the low RR of the proposed activation process and the former was confirmed with the best fit of the Toth isotherm as well as the calculated heterogeneity factor. Further, this model suggests a plethora of various pores to be

present on the surface of the AC which was corroborated by analysis of the N_2 isotherm at 77 K. Other valuable information was also gathered based on this isotherm. A substantial increase in BET surface area (248 m^2/g) and microporous surface area (183 m^2/g) was noted alongside a smaller average pore size (3.7 nm), suggesting physical activation with CO_2 to have successfully developed a micro-mesoporous AC.

Moreover, the heat of adsorption for AC-Opt was calculated to be 26.5 kJ/mol, thus, constituting a further benefit of this activation approach as opposed to chemical activation (in the case of BA-derived carbons) for the purposes of CO_2 physisorption.

Based on the described above properties in conjunction with the lack of secondary pollution from activation agents, ease of production as well as unique economic benefits of AC-Opt over alternative sorbents discussed in this thesis, AC-Opt was selected for further chemical surface modification as well as a preliminary pelletisation study.

However, future work can also aim to investigate the behaviour of the produced sample under CO_2 concentrations more representative of an industrial flue gas. Such studies can also be coupled with investigations into moisture resistance, competitive adsorption and selectivity of the material over other flue gas components as well as different regeneration regimes (e.g. in a pressure swing adsorption set-up).

Further, as AC-Opt performed similarly in terms of CO_2 uptake to the sample activated with N_2, future studies may investigate the examined alternative activation pathway deeper as this would enable a further reduction in final product cost due to a wider availability and relatively lower costs of nitrogen gas, in general.

7. Pelletisation

7.1. Initial pelletisation investigation

To produce the organic binder solution, PVA (Sigma-Aldrich; CAS 9002-89-5; Mw = 85,000 – 146,000) was dispersed in DI water using a ratio of 5:95 = PVA:H_2O and was stirred at 400 rpm continuously overnight under reflux at 90 ºC (Radley's Findenser). This resulted in a 5 wt% PVA mixture. Additionally, a 10 wt% PVA solution was also produced following the same pathway (with adjusted ratios) to be used as an alternative binder. The resulting viscous liquids were employed in the process of pelletisation. The resulting samples were afterwards evaluated in terms of CO_2 uptake, as well as mechanical properties.

This experimental campaign was conducted employing a mixed-level full factorial design with the investigated parameters being the mass ratio of C:Binder Solution (in the levels of 1:0.5; 1:1 and 1:1.5) alongside the different PVA-based binders (i.e. 5% and 10%). The resulting samples were labelled as Pellet_X%PVA_1:Y with the used binder solution being denoted by X, whereas Y stood for the ration of carbon to binder. The pelletisation process started with the virgin carbon powder being first mixed with the appropriate aqueous binder solution in the desired ratio as per the design framework. Upon mixing and prior to extrusion additional amount of DI water was added to the samples that necessitated it in order to produce an extrudable paste. Following this step, this intermediate material was manually extruded (using a syringe) onto a receiver surface (i.e. a petri dish) and dried overnight in an oven at 60 ºC. The resulting adsorption capacities can be found in Table 7.1.

Table 7.1: Results of the initial pelletisation campaign.

Name	Adsorption capacity, mg/g	Decrease in Uptake, %
Virgin Carbon Powder	15.2	N/A
Pellet_5%PVA_1:0.5	12.4	~18.5
Pellet_5%PVA_1:1	11.3	~26.0
Pellet_5%PVA_1:1.5	10.9	~28.0
Pellet_10%PVA_1:0.5	12.9	~15.0
Pellet_10%PVA_1:1	11.2	~26.0

Pellet_10%PVA_1:1.5	9.6	~37.0

Generally, the loss in adsorption capacity of approximately 20 – 30% is anticipated when transitioning from powder to pellet. Based on this criterion alone, all of the samples except for Pellet_10%PVA_1:1.5 could be taken for further consideration. However, the mechanical strength of the produced pellets is also a key dependent variable. Producing a resilient pellet (i.e. with acceptable crush strength, resistance to attrition and etc.) would enhance materials' work- and shelf-life as well as ease its handling. As such, this crucial aspect could not be overlooked. In terms of mechanical strength, only the samples with the highest amount of binder used, could be analysed or even handled. Others, with lesser binder amounts used, would deform, crumble and break upon any significant handling. Similar sentiments have been reported in the literature, suggesting the requirements of high amounts of binder [206]. As such the sample which was prepared using the 5% PVA binder and the C:Binder ratio of 1:1.5 was taken for further examination (since only this sample satisfied both highlighted aspects) and is henceforth called: Virgin Carbon Pellet (VCP).

7.2. Second pelletisation investigation

Having produced such an adsorbent (i.e. VCP), it could be then activated, hence the *pelletise-then-activate* approach. This or a similar pathway (i.e. activation of pre-formed shapes) has been previously utilised in the literature [208]–[212]. However, this option would not suit chemically activated carbons, due to presence of the washing step or issues with mixing the chemical activating agent as these steps could destroy the shaped form. For such materials (as well as the physically activated carbons), the *activate-then-pelletise* pathway can be employed. However, not much research has focused on the differences between them, employing a comparative framework.

As such, two different materials have been produced, namely the activated-then-pelletised (A-P) and the pelletised-then-activated (P-A) samples. The latter was obtained by activating the VCP sample (with the same activation conditions as AC-Opt), whereas the former was produced by pelletising AC-Opt powder following the same approach as for the VCP.

7.2.1. Scanning Electron Microscopy (SEM)

The produced pellets have been evaluated *via* SEM with the results presented below.

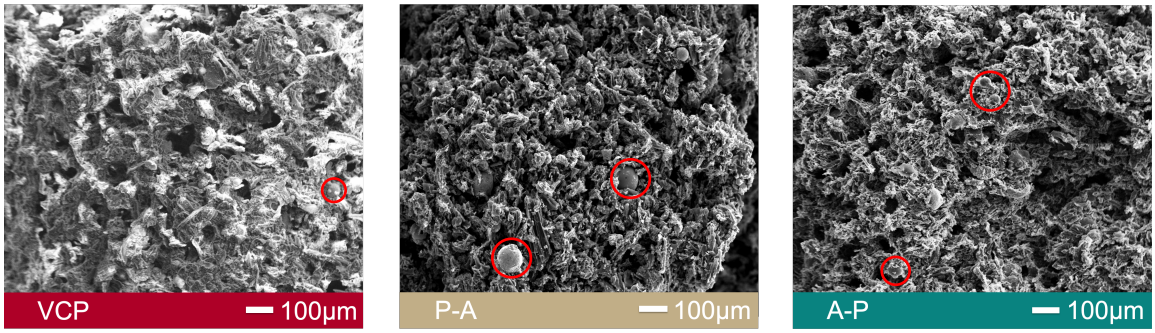

Figure 7.1: SEM images of the three produced pellets.

As can be visualised from Figure 7.1, the pelletisation process led to large openings forming on the surface of the adsorbent. This is more pronounced for A-P (far right) and VCP (far left). Additionally, the incorporation of the aluminosilicate raw ash impurities can also be seen in all of the samples (highlighted using red circles).

7.2.2. Proximate Analysis

Proximate analysis has been employed to quantify the ash impurities as well as the fixed carbon, the VOC and moisture contents. The data obtained for these three samples is presented in Table 7.2: .

Table 7.2: Results of proximate analysis of the pellets.

Sample name	Moisture, wt%	VOC, wt%	Fixed C, wt%	Ash, wt%
VCP	2.0	40.5	36.0	21.5
P-A	1.0	8.5	57.5	33.0
A-P	1.0	14.5	53.5	31.0

The increased fixed carbon and ash contents of the activated pellets (both A-P and P-A) can be ascribed to loss of volatiles upon activation. Moreover, Table 7.2*:* corroborates the proposition that the lower VOC content of P-A may stem from the decomposition of PVA upon thermal treatment (suggesting a lesser mechanical stability). These observations (i.e. passing of the organic binder into the gas-phase at elevated temperatures) are in-line with similar works reported in the literature [212].

7.2.3. Surface Area and Porosity Analysis

The impact of the order of processes onto the surface area and pore structure of the sorbent has also been studied with the results shown in Table 7.3.

Table 7.3: Surface area analysis results.

Sample name	S_{BET}, m^2/g	Total pore volume, cm^3/g	Average pore size, nm
VCP	4.0	0.0066	4.5
P-A	334.0	0.0778	3.5
A-P	120.2	0.0194	3.3

As has been highlighted earlier in the manuscript, activation significantly enhances the porous structure of the adsorbent. Same phenomenon can be noted for the investigated pellets, leading to a considerable rise in both the surface area and pore volume. Additionally, CO_2 activation has also been shown to develop microporosity, hence the shift of the average pore sizes to a decreased value as can be visualised from Figure 7.2:.

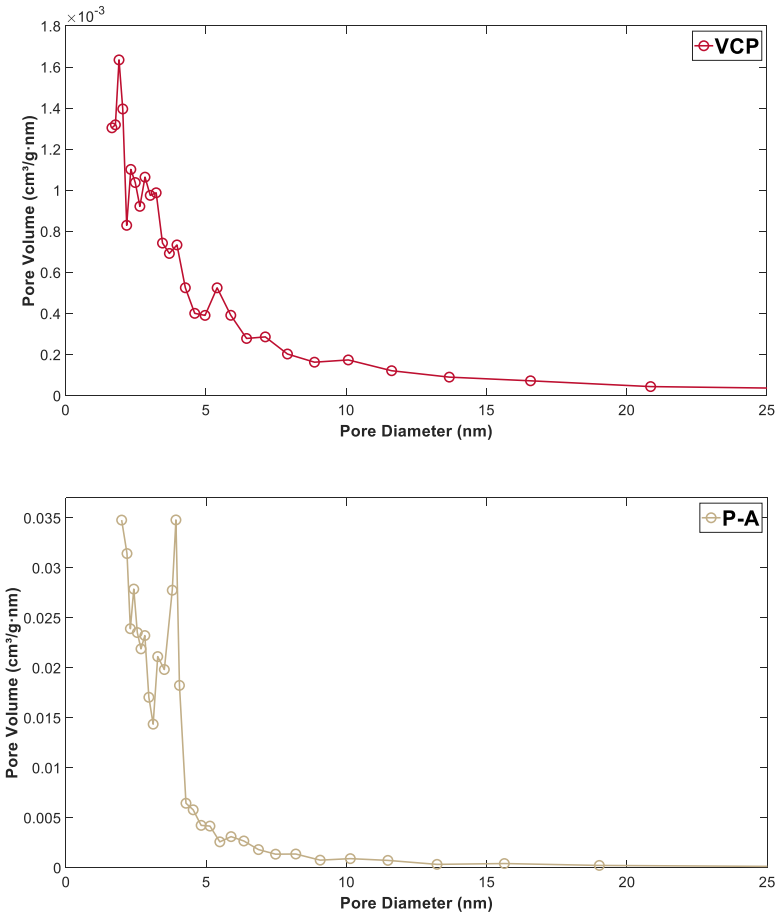

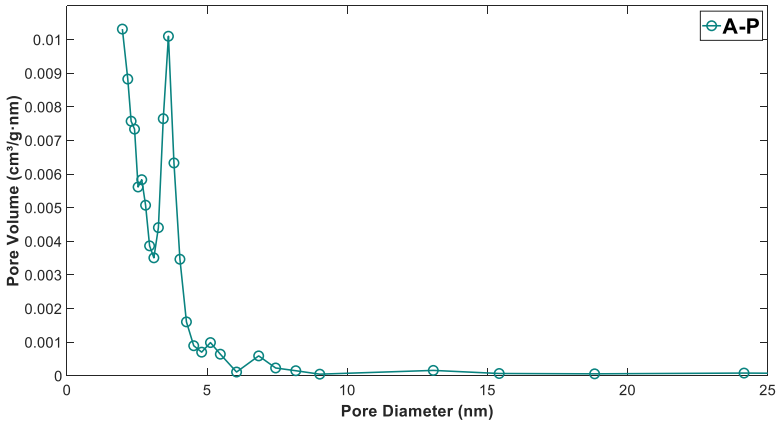

Figure 7.2: Pore size distribution of the pelletised samples: VCP (top; red), P-A (middle; beige) and A-P (bottom; turquoise).

However, the activated samples differ significantly from one another. For instance, S_{BET} of A-P is (approximately) half of the parent AC's surface area, whereas P-A possesses a greater surface area than the powder-form AC. This mainly suggests the following: a) PVA has been partially lost upon activation, leading to increased pore volume and S_{BET} of the P-A pellet; and b) A-P sample might incur some pore-blockage from the binder molecules, decreasing adsorbent's porous, structural properties.

7.2.4. Fourier-Transform Infrared Spectroscopy (FTIR)

The infrared spectra of the three carbon pellets were produced following the attenuated total reflection methodology between 600 – 4000 cm^{-1} using a 4 cm^{-1} step size. The acquired FTIR spectra are presented in Figure 7.3:.

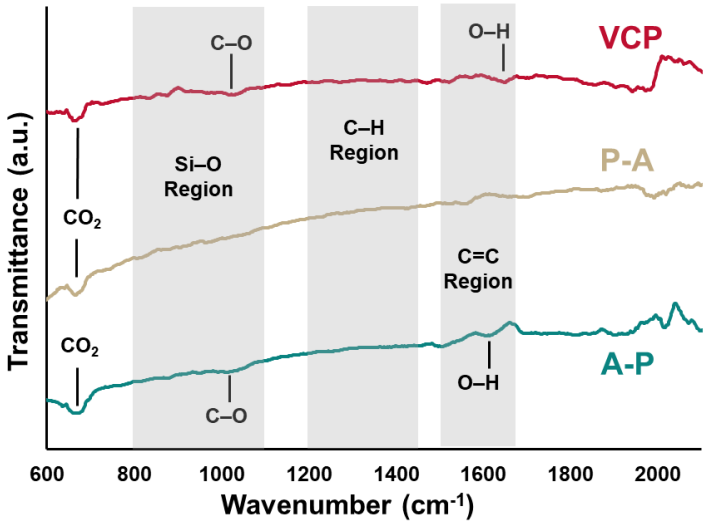

Figure 7.3: Infrared spectra of the pelletised samples: VCP (top; red), P-A (middle; beige) and A-P (bottom; turquoise).

With the materials having similar origins, they are expected to possess the same/similar peaks, e.g. the bands in the area between ~800 cm^{-1} and ~1100 cm^{-1} are commonly found across all of the samples and are associated with the ash impurities, i.e. Si-O bonds [242], [260], [264]. Within that region, though, the VCP and A-P pellets present peaks (around 1030 and 1050 cm^{-1}, respectively) that could alternatively be ascribed to stretching vibrations of the C-O functionality [286]. Further, another common feature can be found around the wavenumber of ~ 669 cm^{-1}, which is associated with the background CO_2 from the scan [331]. Moreover, the region between ~1200 $cm^{-1}$and ~1400 cm^{-1} is riddled with different C-H vibrations [264], whereas the range of ~1500 – ~1700 cm^{-1} could be described by the C=C bonds [183], [261], [285]. Within that, an alternative option (though, only for VCP and A-P) is to assign the peak located at ~1630 cm^{-1} to the hydroxy-bond potentially stemming from the PVA.

Notably, as was the case with AC-Opt, physical activation led to a decrease in surface functionalities as volatiles are largely eliminated during thermal treatment. As such, the P-A spectrum does not present O-H or C-O bonds associated with the binder, whereas the other samples do. This is a clear indication of the impact of the different production pathways, which could also suggest a lower crush strength of the P-A sorbent. On the other hand, their presence on the VCP and A-P pellets, confirms incorporation of the binder into the material. However, the spectra did not produce prominent peaks in the 3300 – 3400 cm^{-1} regions where the main stretching vibration is believed to lie (hence, the cut off of the spectra at 2100 cm^{-1} to highlight the present peaks). This fact might suggest a low amount of binder added to the parent carbon, potentially signifying inadequate mechanical properties of the pellets.

7.2.5. Adsorptive properties and Characteristics

Additionally, the impact of the pelletisation and activation of the samples has been evaluated in terms of their affinity towards CO_2.

Table 7.4: Results of the equilibrium adsorption capacity tests at 50 ºC.

Sample Name	CO_2 Uptake, mg/g
VCP	10.9
P-A	31.4
A-P	22.4

Table 7.4 presents the results of the TGA studies, suggesting the materials that have undergone pelletisation last (i.e. VCP and A-P) to possess a lower (~30%) CO_2 uptake that their powder counterparts. As with the surface area analysis, these changes might stem from covering/clogging of the pores by the PVA-binder. Further, physical activation of the pellets resulted in an enhanced adsorption capacity (similar to the transition between the virgin BA-100-P and the AC-Opt). Based on these findings, the presence of surface hydroxyl functionalities does not seem to necessarily facilitate CO_2 uptake. The variation in the porosity of the samples is believed (in this case) to have a stronger impact on the differences in adsorption capacity.

Further, non-linear fitting of the PFO and PSO kinetic models has also been undertaken to further investigate CO_2 adsorption by the pellets. Interestingly, all of the samples were more accurately described by the latter equation, hence, the results of the PSO fitting are shown in Table 7.5.

Table 7.5: Results of the kinetic modelling for the CO_2 adsorption tests at 50 ºC.

Sample Name	k_2*	R^2	NRMSE
VCP	0.01054	0.9711	0.003338
P-A	0.08456	0.9495	0.003443
A-P	0.02136	0.9885	0.001635

The acquired data further highlights the differences between the produced pellets. Namely, regardless of the order of the activation and pelletisation processes, the activated pellets present faster sorption kinetics than VCP. Within that, k_2* (the rate constant) for the P-A adsorbent is quadruple that of the A-P sample. As such, under dynamic adsorption conditions in a fixed-bed column, the former should theoretically produce “steeper” breakthrough curves, thus, maximising the use of adsorbent bed (i.e. increasing operational efficiency). This is currently one of the main challenges of CCS *via* adsorption.

7.2.6. Mechanical Properties and Crush Strength

Another key hurdle preventing wide industrial deployment of this technology in the CCS context is the acceptable mechanical properties of adsorbent materials. As such, investigations into the crush strength of the produced pellets have been conducted; the results of which are shown in Table 7.6. This study adhered to the methodology of

ASTM D6175 [332]. However, the samples were dried at a lower temperature (i.e. 60 °C) to minimise the thermal treatment, hence, loss of volatiles instead of purely moisture.

Table 7.6: Crush strength test results.

Sample Name	Crush Strength, N/mm
VCP	1.054
P-A	N/S
A-P	0.794

The studied samples vary significantly between one another in terms of their resistance to crushing. Mainly, the P-A samples possessed such a low mechanical stability that the crush strength could not be registered by the employed test rig (Mecmesin MultiTest-dV). In fact, even manual handling was challenging as the P-A pellets would crumble readily upon pick-up or any other minor impact/force. This phenomenon was attributed to degradation of the organic binder (PVA) upon thermal treatment of the extrudate. In order to overcome this issue, an inorganic medium (e.g. clay, bentonite) could be employed as the binder for the "*pelletise-then-activate*" approach. Alternatively, further research can explore usage of industrial-grade extruders or other methods of particle forming (e.g. freeze-drying, high-pressure moulding) to enhance the mechanical stability of the sorbents. Nevertheless, the pellets that have been only dried and not activated (i.e. VCP and A-P) present crush strengths that are on par with extruded carbonaceous adsorbents reported previously in the literature [333] alongside the minimum requirements for extruded alumina catalysts [334].

However, in order to be deployed on an industrial scale, the crush strength of the pelletised adsorbents has to be improved. The minimum requirements are believed to be at least 4 N/mm [335], though a crush strength of > ~ 8 – 10 N/mm would be preferred [334], [336], [337]. For these samples, similarly to P-A pellets, industrial-grade solutions can be further studied to attain the requirements from industry.

7.3. Conclusion

A preliminary pelletisation study has been conducted investigating binder solution (i.e. PVA) ratios and concentrations as well as comparing two different pellet forming

approaches (i.e. activate-then-pelletise (A-P) and the pelletise-then-activate (P-A) pathways) for BA-derived adsorbents.

Based on the initial screening, high ratios (>50% by mass) of organic binder were required to produce pellets that could withstand handling and not crumble upon manual contact by the operator. Such adsorbents would lose ~ 30% of their adsorption uptake compared to their powder analogue. Both findings are in line with the results from the literature.

Within the second (comparative) investigation, as expected, high temperature physical activation led to a substantial rise in sorption properties (i.e. surface areas and CO_2 uptakes) for both powders and pellets. However, significant variation in terms of the mechanical stability of the produced pellets was noted.

Mainly, despite the preferable adsorption capacity (31.4 mg/g) and kinetics of the P-A samples, their extremely low mechanical stability (in terms of crush strength values that could not be registered by the employed equipment) hampers their deployment in fixed-bed adsorption reactors in their current state (i.e. pellets). This phenomenon was attributed to loss of organic binder due to physical activation, which was evidenced by decreased VOC content (8.5% by weight as opposed to 14.5% for A-P) and lack of PVA-associated bonds on the FTIR spectrum. Decomposition of binder, in turn, decreased pore blockage, hence, facilitating greater adsorbent loading with CO_2. Therefore, future research on this production pathway may focus on deploying inorganic binders to overcome these limitations of the P-A approach as well as investigate alternative particle/pellet forming methods (e.g. high-pressure moulding).

The A-P sample, on the other hand, possessed an improved affinity towards CO_2 as evidenced by a two-fold enhancement of both kinetic parameters and uptake (22.4 mg/g) over VCP (10.9 mg/g). Alongside preferable sorption characteristics, A-P sample presented a relatively similar crush strength to its virgin counterpart (i.e. 0.794 N/mm for A-P and 1.054 N/mm for VCP) and comparable ACs from the literature yet both A-P and VCP were deemed sub-performing for wide industrial deployment. Future investigations may focus on attaining this value *via* utilisation of industrial-grade extruders and pelletisers. Alternatively, other binders and/or particle shapes and forming techniques may also be of interest.

8. Chemical Modification

8.1. Introduction

In the literature, oxidation of carbonaceous matter is often achieved using HNO_3 and employing an one-factor-at-a-time approach [184], [254], [338], [339]. This method, however, does not investigate the interactions between the studied parameters as well as does not benefit from a stronger acidic agent namely, a mixture of H_2SO_4 and HNO_3. The proposed in this thesis approach would not only facilitate a deeper understanding of the factors at play but also allow to produce alternative, yet widely overlooked surface functional groups (in the CO_2 adsorption literature) that could theoretically prove effective in surface modification of activated carbons.

8.2. Materials and Methods

8.2.1. Materials

The physically activated BA-derived carbon (AC-Opt) was used as the precursor for this work. HNO_3 (>68% pure; CAS 7697-37-2; Fisher Scientific) and H_2SO_4 (98% pure; CAS 7664-93-9; Fisher Scientific) were used as the modification reagents. The characterisation of the sample followed the exact same methodology as for the other produced BA-derived sorbents in this thesis.

8.2.2. Preparation of Chemically Modified Carbon

The chemical modification was conducted based on a Box-Behnken experimental design (BBD), totalling 27 experiments, examining the modification time, temperatures, acid mixing ratio and the individual acid concentrations within each solution. BBD was selected in order to avoid running experiments at the extreme conditions of all of the factors simultaneously (in this case, maximum temperature at maximum time with maximum acid concentrations to minimise generation of brown gas, i.e. NO_2) as well as to benefit from centre points incorporated in the framework. As with the previous experimental campaigns, the dependent variable in the design was the CO_2 uptake capacity.

The modification started by heating up a three-necked round bottom flask containing the desired acid mixture (in the amount of 210 mL) to the prescribed temperature whilst stirring at 250 rpm under an air-cooled condenser (Radley's Findenser). The three-necked flask was pivotal for this experimental campaign as such

a set-up enables continuous temperature measurements (far left in Figure 8.1), condensation of vapours (central neck in Figure 8.1) as well as a port for addition of AC-Opt (far right in Figure 8.1). It should be noted that the right neck was only open to atmosphere during the addition step of adsorbent to the glass reactor; all other time it was closed with an appropriately sized glass stopper (as is the case in Figure 8.1).

Figure 8.1: Experimental set-up for surface modification of AC-Opt.

Once the prescribed temperature was reached, 0.5 g (±0.001 g) of AC-Opt was added to the flask, marking the beginning of the modification (residence/contact) time. After this step, the reaction mixture was separated using a Buchner funnel-flask system and washed with deionised water until neutral pH. The sample was then placed into an oven to dry overnight (12 h at 80 ºC) and then characterised.

8.3. Results and Discussions

8.3.1. Modification and Optimisation Campaigns

A mixture of HNO_3 and H_2SO_4 is commonly referred to as the “nitration mixture” in the realms of organic chemistry due to the ability of sulfuric acid to protonate the nitric acid (Eq. 8) facilitating nitration (*via* the electrophilic aromatic substitution mechanism [340]) of organic/carbonaceous matter. And, since NO_2 groups are also believed to be beneficial for attracting (*via* electrostatic forces) the electron deficient (δ+) carbon atom of CO_2 [73], this acid mixture has been opted for over pure HNO_3 solutions that mostly

oxidise the surface (although it has been reported that even for the investigated acid mixture, nitration may be transient and oxidation also occurs (especially over prolonged periods of time) [341]).

$$HNO_3 + 2H_2SO_4 \rightarrow NO_2^+ + H_3O^+ + 2HSO_4^- \quad \text{Eq. 8}$$

As such, the nitration acid mixture ratios and the individual acid concentrations within each mixture are shown in Table 8.1 alongside the times and temperatures used for chemical modification.

Table 8.1: Factors and levels studied *via* the Box-Behnken design.

Factors	**Levels**		
Time, h	1	2	3
Temperature, °C	30	60	90
Acid Ratio (vol)	2	3	4
Concentration, M	1	6	11

The results of the modification study were examined in a similar fashion to the parent AC-Opt, i.e. using CO_2 adsorption capacity as response and *via* ANOVA.

Table 8.2: Results of ANOVA for the screening experimental campaign.

Factors	**F-Value**	**p-Value**	**Significance**
Time	2.63	0.131	NSS
Temperature	57.01	0	1
Acid Ratio	3.26	0.096	NSS
Concentration	43.3	0	2
Time*Time	0.83	0.379	NSS
Temperature*Temperature	1.61	0.229	NSS
Ratio*Ratio	0.66	0.433	NSS
Concentration*Concentration	3.37	0.091	NSS
Time*Temperature	0.67	0.43	NSS
Time*Ratio	1.35	0.268	NSS
Time*Concentration	0.1	0.753	NSS
Temperature*Ratio	1.29	0.278	NSS
Temperature*Concentration	0.19	0.67	NSS

Ratio*Concentration	4.47	0.056	NSS

The results of the model (R^2 = 0.911, R^2adjusted of 0.808 and a predictive ability of 0.499) in Table 8.2 suggest only the temperature and acid concentration to be statistically significant employing the literature-standard of p-values less than 0.05. This p-value would constitute a 5% chance of mistake in ascribing the measured effects to the proposed factor, hence, a 95% confidence in statistical significance. This significance level can also be corroborated by the "2σ rule" that suggests ~ 95% of the values to be within two standard deviations from the dataset mean. Therefore, only the concentration of the acid mixture and the reaction temperature are believed to have had a statistically significant impact on the CO_2 uptake. Sometimes the literature may contain threshold p-values over 0.05. This practice is not advisable and is colloquially referred to as "p-hacking" as it allows for increased statistical significance of factors (be it additional or only one). In the case of AC-Mod, for instance, if changing this threshold to 0.06, then the interaction between the acid ratio and their (acids) individual concentrations also would have been statistically significant; and if evaluating only 90% of the cases, then the list would also include the acid ratio itself (linearly) coupled with the quadratic effect of concertation; and so on. As such, it is advisable to use the commonly-employed 0.05 bar for statistical significance. Nevertheless, the obtained experimental data allowed for a contour plot to be modelled (displayed in Figure 8.2).

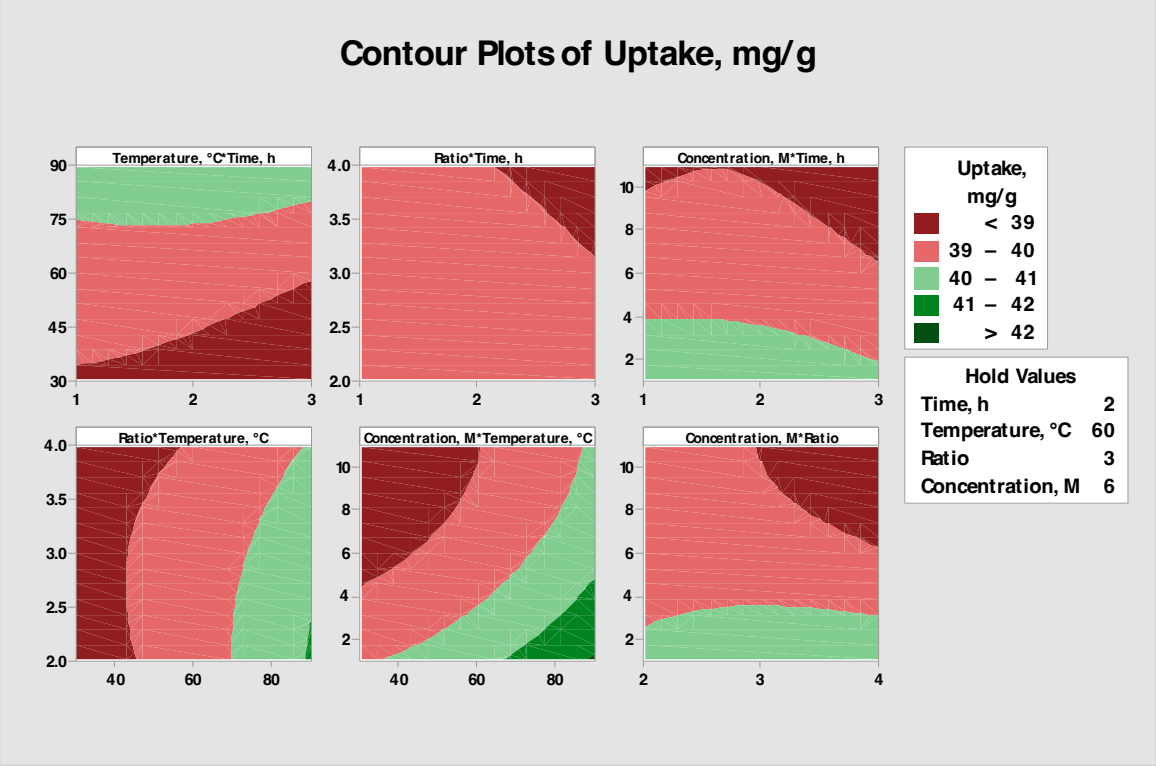

Figure 8.2: Contour plot of CO_2 uptake vs investigated parameters.

As can be visualised from Figure 8.2, the CO_2 uptake increases towards the edges of the design. This may not be necessarily true, as lack of experimental points at the corners of the design space necessitates estimation and extrapolation. However, in the case of the described above chemical modification, the optimum point that maximised CO_2 uptake was, indeed, found to be at maximum studied time (3 h) and temperature (90 °C) and minimum acid ratio (1:2) with minimum concentration (1 M). Lower acid mixing ratios have been previously shown to be beneficial in enhancing CO_2 uptake [340], which was ascribed to an increased nitrogen content of the samples. On the other hand, enhancing the treatment time and temperature can facilitate dissolution of ash species (Section 8.3.2.3), hence, lesser impurities and, in turn, higher adsorption capacities. Further, lower acid concentrations (as highlighted in 8.3.2.4.1) facilitate presence of nitro groups as opposed to O-heteroatom based (e.g. hydroxy, keto and etc.) groups [342], [343]; and, since, the NO_2 functionality has a higher polarity than C=O [73], this would contribute to a more electrostatically robust surface that would attract more CO_2 molecules. Although, to confirm these hypotheses, analysing all of the samples using various dependent variables (e.g. N-content, surface acidity and etc.) is advisable. Nevertheless, based on the highest

uptake values (coupled with the reasoning above) this edge-point optimum sample was labelled AC-Mod and used for characterisation.

8.3.2. Characterisation of Optimum Sample

8.3.2.1. Scanning Electron Microscopy (SEM) & Energy Dispersive X-ray Spectroscopy (EDS)

AC-Mod was examined *via* SEM/EDS with the images presented in Figure 8.3.

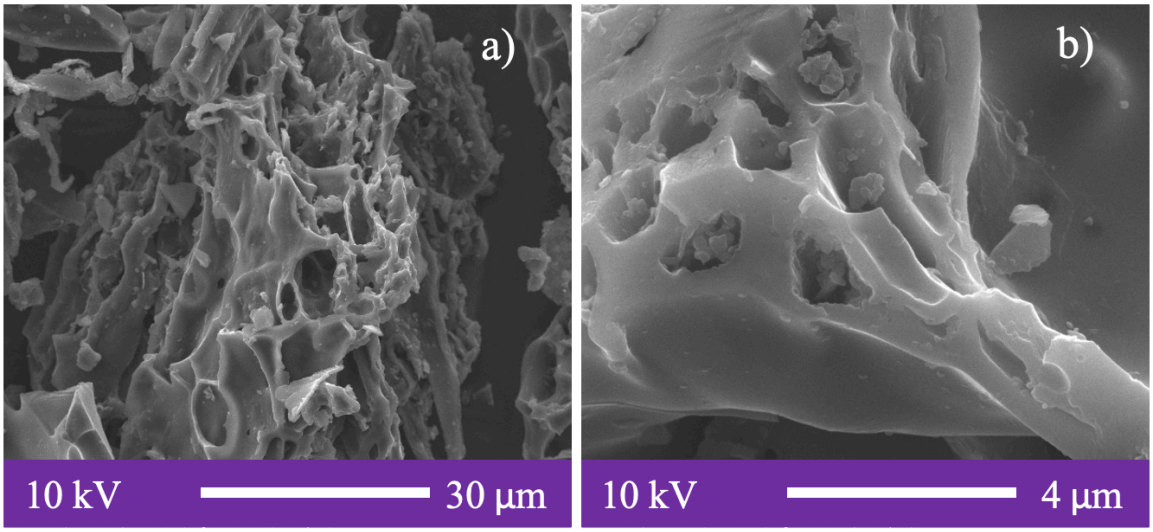

Figure 8.3: SEM images of AC-Mod.

As with the parent AC, this material presents significant surface roughness and heterogeneity.

The surface elemental composition of AC-Mod has also been investigated.

Table 8.3: Surface elemental composition of AC-Mod.

Element	Weight %
C	77.6
O	21.3
Ca	0.4
Si	0.4
Al	0.2
S	0.1

As can be gathered from Table 8.3, the acidic treatment has had an impact on the material. Most notably, the presence of sulphur (albeit in only 0.1% mass) has been measured on the surface of AC-Mod. This is to be expected as some residual species

may have persisted after the washing with deionised water. Interestingly, no nitrogen has been found on the surface of AC-Mod. This, however, may stem from the inadequacy of this analytical technique to quantify, both the bulk of the sample as well as to accurately measure elements with a low atomic mass (<23 amu of sodium) [221]. Therefore, CHN analysis was performed to elucidate the N and C contents of AC-Mod (next section). Finally, EDS confirmed presence of inorganic species on the surface of AC-Mod; yet, an alternative more reliable method, namely, proximate analysis, is preferred for accurate (bulk) quantification of inorganics as part of the carbonaceous adsorbent.

8.3.2.2. Ultimate Analysis

Ultimate analysis has been employed for characterisation of AC-Mod with the data presented in Table 8.4.

Table 8.4: Ultimate analysis results of AC-Mod.

Element	Weight %
C	65.45
H	1.38
N	1.43
Other	31.74

The modification of the carbon resulted in a notable increase in nitrogen content, namely, from 0.26% to 1.43%. This rise is ascribed to the presence of N-containing surface functionalities as a result of nitration. On the other hand, minor increases in C and H content (AC-Opt showed 54.47% and 1.00%, respectively) may stem from the dissolution of ash because of the acid treatment This theory is corroborated by results of proximate analysis in the next section.

8.3.2.3. Proximate Analysis

Proximate analysis [250] was used to evaluated the produced sorbent against the efficacy of modification. Table 8.5 suggests AC-Mod to possess a moisture content of 7.2% which is much higher than that of the parent physically activated AC (1.5%). This may indicate that the modified sample has a higher affinity to moisture than the parent material. Further, an increase in VOCs can be noted (from 7.2% to 21.3%) which can be attributed to the combined oxidation and nitration of the surface, leading to

increased content of volatile functional groups. In turn, a decreased ash content (42.5% for AC-Opt) which may stem from the dissolution (and subsequent wash) of some ash species upon exposure to the nitric and sulphuric acid mixture. All the described above changes would have impacted the resulting fixed carbon content.

Table 8.5: Proximate analysis results of AC-Mod.

Sample name	Moisture, wt%	VOC, wt%	Fixed C, wt%	Ash, wt%
AC-Mod	7.2	21.3	58.4	13.1

8.3.2.4. Spectroscopic Analysis

8.3.2.4.1. Fourier- Transform Infrared Spectroscopy (FTIR)

The FTIR spectrum (Figure 8.4) corroborates the hypothesis of successful nitration and oxidation as the associated N-O (1557 cm^{-1}) and O-H (3192 cm^{-1}) stretching vibrations [285] are present on AC-Mod, whilst spectrum of the parent AC-Opt did not possess such bands. Additionally, neither ChAB, nor virgin BA-100-P did not present nitro groups on their respective spectra. Based on the trends for pure nitric acid modification, oxidation with higher concentrations of HNO_3 favours more strongly acidic functionalities (i.e. carbonyl and then carboxyl groups) [342] with lesser concentrations allowing for persistence of nitro groups [343], which is in line with the lowest acid concentrations employed for the analysed sample.

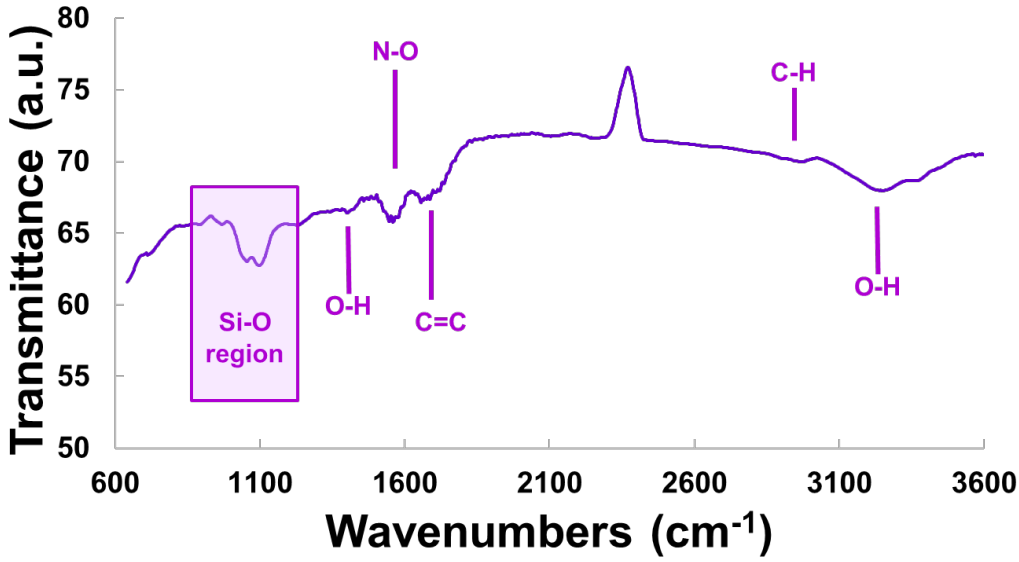

Figure 8.4: Infrared spectrum of AC-Mod.

Additionally, the C=C bond at 1652 cm^{-1} has been noted alongside C-H stretching vibrations at 2959 cm^{-1} and Si-O peaks at wavenumbers of 1019 and 1080 cm^{-1} [285].

8.3.2.4.2. Raman Spectroscopy

Raman spectroscopy was employed in complementary characterisation of the produced AC-Mod. Based on the spectrum presented in Figure 8.5, the I_D/I_G ratio is believed to be 0.66 (constituting a ~18% decrease compared to parent AC), which is somewhat unexpected. The I_D/I_G ratio has been previously shown to be highly (and non-linearly) treatment time sensitive (for carbon fibres treated at 60 °C with a concentrated H_2SO_4/HNO_3 mixture at a volumetric ratio of 3:1) [341], yet in all of those cases a rise in the D-band was noted. Perhaps, this increase may stem from the use of non-activated/virgin pristine fibres, that did not possess surface defects, whereas in this thesis, a material (AC-Opt) with a high D-band intensity was employed for modification. Alternatively, the produced surface functional groups (assuming they are placed at the more easily accessible edges and defects of the graphene sheets) could have adsorbed some of the shone light. This would prevent inelastic (Raman) scattering of the "defective" carbon atoms. Corroborating this theory is the fact that the produced functionalities (namely, nitro and hydroxyl) would not appear on the Raman spectrum as a distortion of the electron cloud around the atoms is required [247], hence, a lack of polar groups (in this case, the nitro and hydroxyl) in Figure 8.5. Nevertheless, analysis of all of the produced during the experimental campaign samples may elucidate the mechanisms at play and provide more information on the changes of the I_D/I_G ratio dependent on treatment temperature and time as well as acid concertation and mixing ratio.

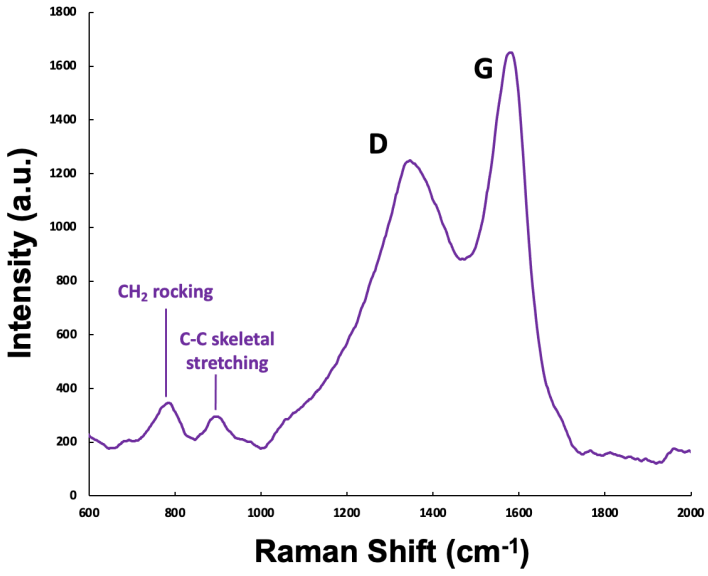

Figure 8.5: Raman spectrum of AC-Mod.

Additionally, CH_2 rocking has been noted alongside C-C skeletal stretching at a Raman shift of ~775 and ~879 cm^{-1}, respectively [344].

8.3.2.5. Surface Area Analysis

Following acid treatment, changes to the surface area of the sample have also been observed. As is the case with the parent carbon (AC-Opt), AC-Mod presents a type IV isotherm and a hysteresis loop (Figure 8.6). Interestingly, the initial sharp increase (associated with volumetric filling) reaches the point of inflexion earlier for AC-Mod than for the parent AC, whilst the maximum registered uptake is lower.

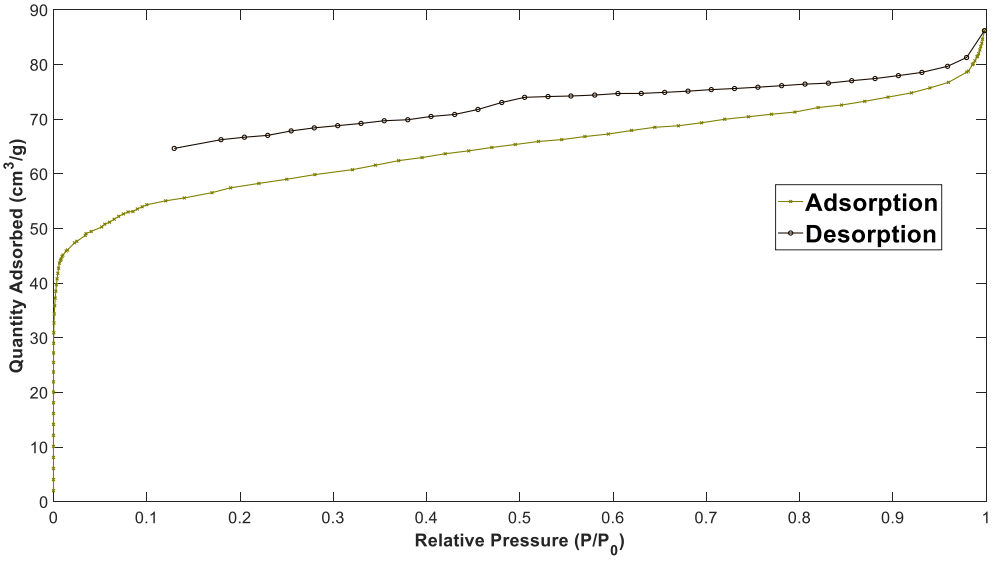

Figure 8.6: BET physisorption isotherm of AC-Mod.

The observation of a smaller initial rise suggests AC-Mod to possess lesser micropore volume and a lower total quantity adsorbed – a lower total BET surface area. The BET surface area (and micropore volume in brackets) of AC-Mod is 221 m^2/g (0.0633 cm^3/g) compared to 248 m^2/g (0.0936 cm^3/g) for the parent physically activated carbon. This is largely to be expected as surface modification causes pore blockage by the produced functional groups leading to smaller surface areas and micropore volumes.

Furthermore, the BET physisorption isotherm of AC-Mod features an open hysteresis curve, i.e. adsorption and desorption branches do not reconnect at lower relative pressures. Such discrepancy can be ascribed to “pore swelling” [82], i.e. deformation of the shape of the pore accompanied by enlargement of the pore volume [345]. Within this, the carbon scaffold may be irreversibly damaged by the adsorbate

during desorption (due to collapse of the polyaromatic structure of an AC) leaving some gas molecules trapped in the solid phase [346], thus, further highlighting the value of cyclic studies (Section 8.3.2.6.4). It's also noteworthy that chemisorption of adsorbate may also cause an open hysteresis loop [82] yet for N_2 adsorption isotherms, pore swelling would be a more probable cause.

Moreover, since the average pore size of the optimum sample has not changed significantly upon acidic treatment (3.6 nm as evidenced by Figure 8.7), the treatment is believed not to have generated new surface pores but rather enhanced the electrostatic properties of the surface.

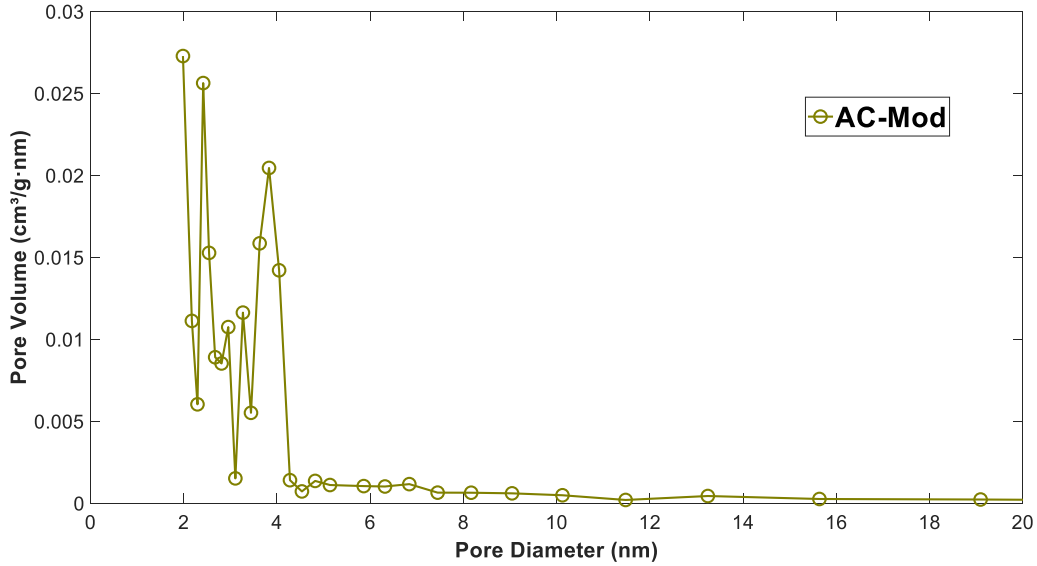

Figure 8.7: Pore size distribution plot of AC-Mod.

Such changes to the surface have also impacted the CO_2 uptake.

8.3.2.6. CO_2 Adsorption Experiments

The effectiveness of surface modification with the nitration mixture has also been assessed based on the interaction between CO_2 and AC-Mod.

8.3.2.6.1. Adsorption Capacity

Similarly to the parent sample, AC-Mod's adsorption of CO_2 follows the classical physisorption trend of increased capacity at lower temperatures as per Table 8.6.

Table 8.6: Results of AC-Mod CO_2 adsorption tests at different temperatures (pure CO_2 flow rate of 50 ml/min).

Uptake at 25 °C, mmol/g	Uptake at 50 °C, mmol/g	Uptake at 75 °C, mmol/g

1.39	0.96	0.61

Based on the data from Table 8.6, an approximately 35% increase has been observed across the evaluated temperature range. Therefore, the proposed modification allows the adsorbent to overcome an analogous commercial activated carbon [263].

Moreover, apart from the adsorption capacity, the equilibrium adsorption isotherms have also been studied.

8.3.2.6.2. Equilibrium Adsorption Isotherms

Table 8.7 contains the equilibrium adsorption isotherm fits for AC-Mod at 0 °C. Here, apart from the previously used in this thesis R^2 and NRMSE, the sum of square errors (SSE) is included to be used as a further indicator of goodness-of-fit. This feature is employed here due to the similarities in the results of fitting for some isotherms.

Table 8.7: Equilibrium adsorption isotherm models fitted to experimental data at 0 ºC (AC-Mod).

Isotherm Model	R^2	NRMSE	SSE
Langmuir	0.9813	0.1168	660.4
Freundlich	0.9876	0.0124	438.6
Double-site Langmuir	0.9998	0.0050	6.251
Triple-site Langmuir	0.9999	0.0017	0.698
Toth	0.9999	0.0026	2.788

The Triple-site Langmuir model was found to have the best fit for the analysed experimental data (though, the Toth model is a close second). As such, the values for the identified isotherm parameters are presented in Table 8.8, while Figure 8.8 displays a comparison between the experimental data and the Triple-site Langmuir isotherm model fitted to the experimental isotherm data.

Table 8.8: AC-Mod equilibrium adsorption isotherm models' parameters at 0 ºC and 25 ºC.

Temperature	Isotherm Model	Identified Parameters
0 °C	Triple-site Langmuir	$q_{max\ (1)}$ = 91.23 mg/g $K_{L\ (1)}$ = 0.9663 1/bar $q_{max\ (2)}$ = 11.73 mg/g $K_{L\ (2)}$ = 157.6 1/bar $q_{max\ (3)}$ = 54.05 mg/g $K_{L\ (3)}$ = 14.39 1/bar

25 °C	Triple-site Langmuir	$q_{max\ (1)}$ = 124.4 mg/g	$K_{L\ (1)}$ = 0.5429 1/bar
		$q_{max\ (2)}$ = 38.77 mg/g	$K_{L\ (2)}$ = 11.63 1/bar
		$q_{max\ (3)}$ = 0.67 mg/g	$K_{L\ (3)}$ = 711.1 1/bar

The high quality of fit for the Triple-site Langmuir (i.e. the high R^2 and NRMSE coupled with the minimal SSE) suggests the sample to possess a significant degree of surface heterogeneity, especially considering the "second best" fit of the Toth isotherm. The variations in active adsorption sites can be ascribed to different functional groups, pore shapes and sizes (both stemming from the parent physically activated carbon and as a result of acidic treatment). On the other hand, a higher number of fitting parameters also facilitates better fit of this model.

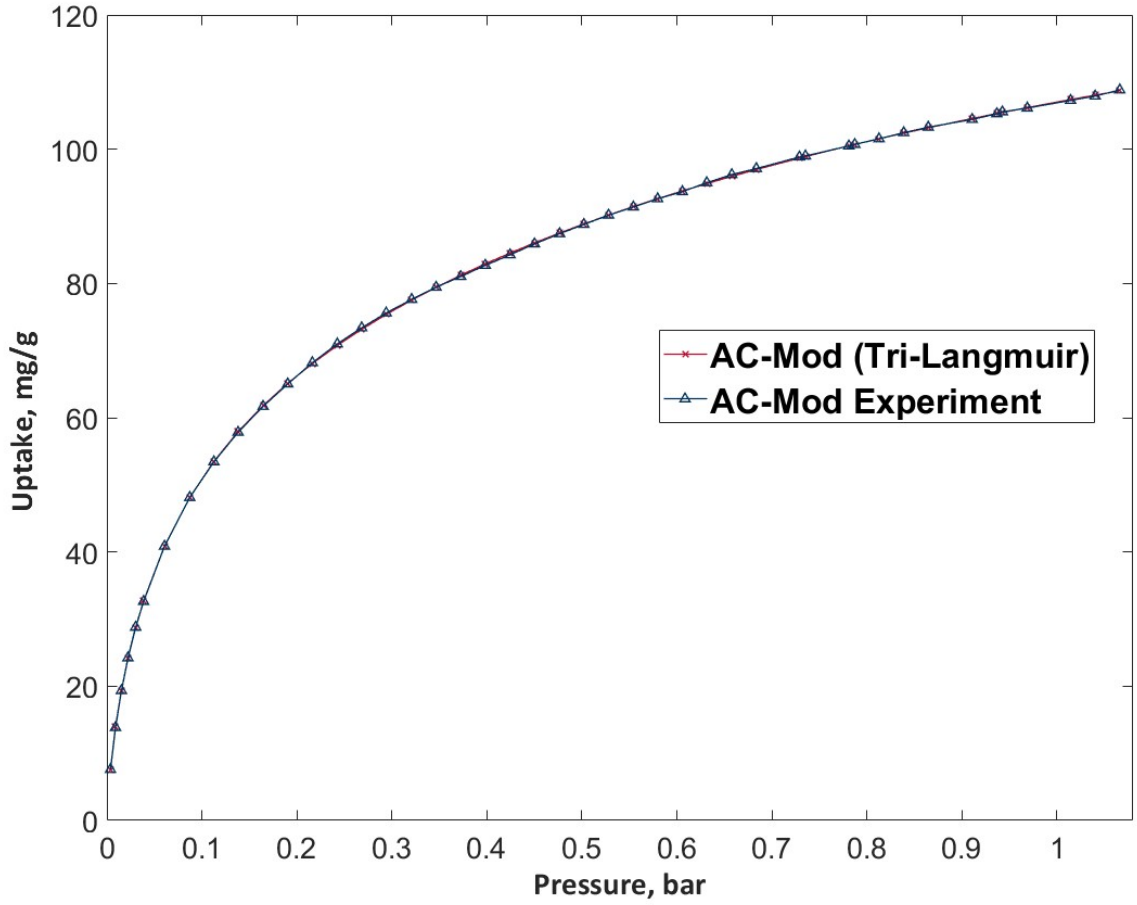

Figure 8.8: Experimental data (triangles) and the equilibrium isotherm model (crosses) for AC-Mod at 0 °C under pure CO_2.

Apart from this, CO_2 adsorption kinetics have been evaluated.

8.3.2.6.3. Adsorption Kinetics

Similarly to the parent AC, the PSO and Modified Ritchie provide the (by far) best fit as per Table 8.9. This suggests adsorption to be contingent upon active adsorption sites [263]. The modification is believed to have impacted the surface electrostatic potential by introducing new functionalities (as highlighted in Section 8.3.2.4.1).

Table 8.9: CO_2 adsorption kinetic model fits for AC-Mod at 50 ºC (flow rate: 50 ml/min).

Kinetic Model	R^2	NRMSE
Pseudo-First Order (PFO)	0.6526	0.0869
Pseudo-Second Order (PSO)	0.9838	0.0188
Modified Ritchie	0.9843	0.0185
Intraparticle diffusion	0.6608	0.0858
Avrami	0.9595	0.0297
Elovich	0.9093	0.0444

Between the two models, though, the Modified Ritchie equation is believed to have a better fit (therefore, this model is presented in Figure 8.9 and Table 8.10) which may stem from inclusion of a model term (associated with the initial particle loading) that helps this model fit more accurately to the experimental data.

Table 8.10: CO_2 adsorption kinetics on AC-Mod at 50 ºC.

Kinetic Model	Identified Parameters	
Modified Ritchie	$K_{(R)}$ = 0.02264	β= 1.155

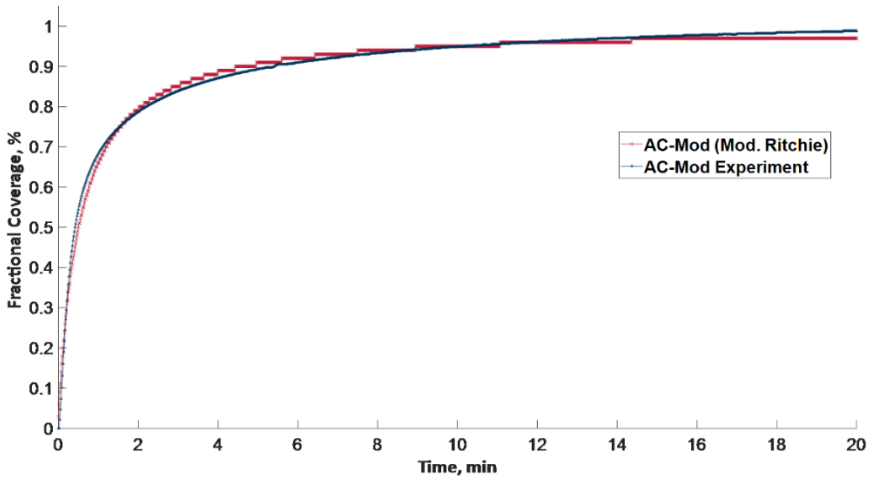

Figure 8.9: Experimental data (blue triangles) and the kinetic model (red crosses) for pure CO_2 adsorption on AC-Mod at 50 °C and 1 bar.

Apart from the kinetics of the adsorption process, the adsorbent's cyclic capacity has also been investigated.

8.3.2.6.4. Adsorption Working Capacity

The working CO_2 uptake of AC-Mod can be understood from Figure 8.10.

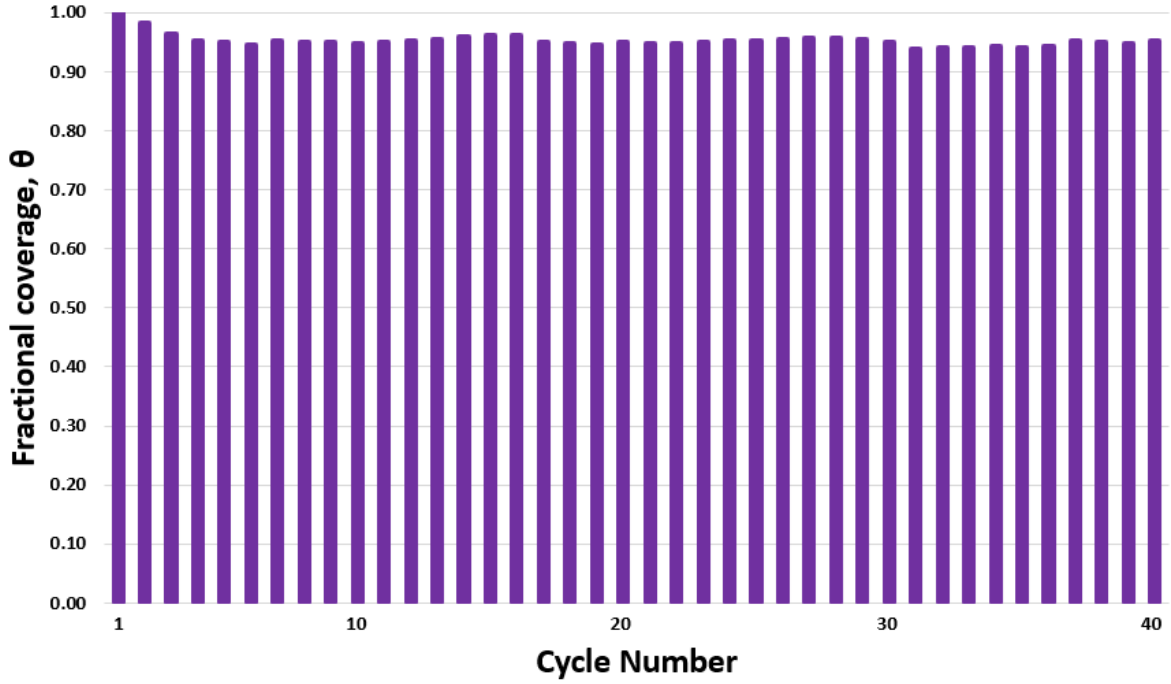

Figure 8.10: Working capacity of AC-Mod over 40 adsorption-desorption cycles.

As expected, a decrease in adsorption loading can be noted after the first cycle. Upon exposure to a stream of pure CO_2, the highest energy adsorption sites may not be alleviated from the adsorbate during the desorption step, leading to a drop in capacity from the first cycle to the second one. As such, AC-Mod adsorbed 2% less in the second cycle. Following this, another 2% decrease in uptake is noted for cycle three, constituting the last sharp decline observed. From cycle four onwards, fluctuations between 95 and 96% coverage were recorded until cycle 30, where the fractional coverage (θ) drops to below 95% for six consecutive adsorption steps. This is followed by a return to 95% coverage at the end of the cyclic adsorption-desorption studies.

A potential explanation to such fluctuations may stem from incomplete desorption (as posited in Section 8.3.2.6.3 based on the Modified Ritchie equation) of various heterogeneous adsorption sites (as per the Tri-site Langmuir fit described in Section 8.3.2.6.2) with different adsorption energies (discussed in Section 8.3.2.6.5).

Nevertheless, AC-Mod performs similarly to the parent AC-Mod, preserving a high fractional loading even after 40 adsorption-desorption cycles.

8.3.2.6.5. Heat of Adsorption

Figure 8.11: presents the modelled heat of adsorption for AC-Mod based on the CO_2 adsorption isotherms, by applying the Clausius-Clapeyron equation (Eq. 5) to the experimental isotherm data at temperatures between 0 – 40 °C.

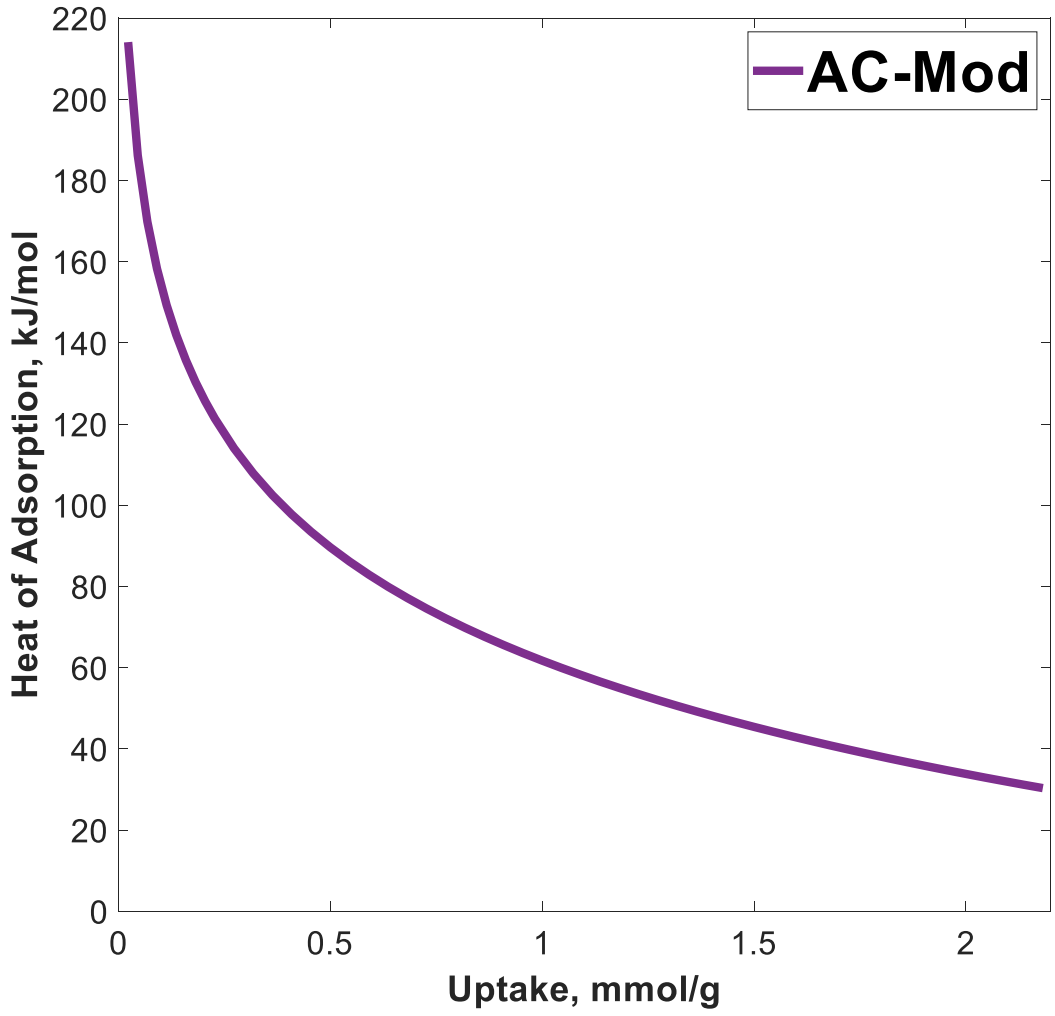

Figure 8.11: Heat of CO_2 adsorption on AC-Mod as a function of CO_2 uptake.

As expected, the modelled curve in Figure 8.11: follows a decreasing trend as the uptake and coverage rise. This is associated with the sample reaching bulk adsorption conditions as the low energy sites are being occupied. This continues until the heat of adsorption reaches 30.5 kJ/mol at a CO_2 uptake equal to 2.18 mmol/g. As such, AC-

Mod has a stronger affinity towards the target adsorbate than its parent material, i.e. AC-Opt.

Additionally, in Section 8.3.2.6.4, the theory of a sharper drop in working capacity of AC-Mod than AC-Opt may be corroborated by a higher heat of adsorption at (near) zero coverage. Although a high Q_{st} is often associated with chemisorption, this is not believed to be the case for AC-Mod (due to a lack of functionalities (Section 8.3.2.4.1) with potential to chemically bind CO_2). Further, zero loading heat of adsorption values are not as reliable as their higher coverage counterparts due to lesser collected experimental data points [265]. Despite the initial numbers in Figure 8.11: being triple than those modelled for AC-Opt, further investigations employing alternative analytical means (e.g. *in-situ* FTIR) would be able to elucidate if chemisorption is taking place.

8.4. Conclusion

This chapter investigated a surface modification technique (of the physically activated carbon – AC-Opt), resulting in an alternative (to the conventional amines) functionality, namely, nitro groups, *via* HNO_3 and H_2SO_4 treatment. This was done by employing a Box-Behnken experimental design (selected to minimise brown gas generation), investigating four different parameters at three levels each (including repeated runs at the centre point). Based on the experimental data, the point that increased CO_2 adsorption was found to be achieved at the maximum contact time (3 hours) and temperature (90 °C) studied in this work, and at the minimum acid ratio (1:2) with minimum concentration (1 M). Following the optimised procedure, a substantial increase in the CO_2 adsorption capacity of AC-Mod (compared to the parent carbon) was noted, namely 0.96 mmol/g from a pure CO_2 stream at 1 bar and 50 °C. This rise may be associated with a diminished ash content (13.1% mass) coupled with an increased elemental (65.45% mass) and fixed C (58.4% mass) contents as a result of acid treatment and subsequent washing.

This modification is believed not to have had a significant detrimental impact on the surface morphology, despite a decreased BET surface area (221 m^2/g) and micropore volume (0.0633 cm^3/g). Further, successful grafting of NO_2 groups was evidenced by increased elemental N content (1.43% mass compared to 0.26% for parent AC) and *via* FTIR spectroscopy.

However, such modification is not without its inherent limitations. For instance, compared to the parent AC-Opt, the modified carbon presents a larger isosteric heat of adsorption (30.5 kJ/mol at the final acquired coverage value) and a higher moisture content (7.2% mass), which suggest not only a stronger affinity towards CO_2 (resulting in a higher regeneration penalty) but also to H_2O (meaning potential *selectivity* issues when exposed to actual flue gases), respectively.

Future work may assess the elemental S content of AC-Mod as well as investigated modifications with exclusively sulfuric acid in order to elucidate the impacts of doping the AC with such a heteroatom. Additionally, since the proposed optimum point is on the outskirts of the design space, a further and deeper investigation into the surface modification technique employed in this thesis (e.g. using the edge point described above as a centre point) would be advisable. As part of such investigations, the presence (and/or quantity) of heteroatom-containing species (S and/or N) could be used as the dependent variable to shine more light on the mechanism of such modifications.

9. Conclusions & Future Work

Climate change and the global temperature rise are increasingly concerning issues, stemming in part from excessive amounts of anthropogenic carbon dioxide emissions. These CO_2 emissions are largely ascribed to the dependency of the modern world on fossil fuels. Therefore, in order to minimise the impacts on the climate, alternative energy sources are attracting ever-more attention. Within the plethora of available energy sources, biomass-based power can be viewed as carbon-neutral and one of the most attainable options for decarbonising the energy sector. Moreover, if bioenergy is coupled with carbon capture and storage (in an approach known as BECCS), the process of energy generation can be made carbon negative.

Yet this technique is not without its drawbacks and limitations. A major hurdle, which constitutes an additional monetary and environmental concern, is production of waste ash in large quantities. This research, therefore, aims to address the issue of CO_2 emissions *via* valorisation of biomass combustion ash to CO_2 sorbents, thus, proposing a method for management of a portion of this novel waste stream. This entailed, first, fulfilling the objective of extraction (followed by characterisation) of a virgin carbon from an industrial-grade biomass combustion bottom ash (BA) as well as investigations of CO_2 adsorption (in terms of kinetics, equilibrium and working capacity) for the produced material. Then, in order to develop a stronger affinity towards CO_2, the virgin carbon was activated both physically and chemically. Out of these two activation approaches, the physically activated carbon was deemed more appropriate for further studies, namely, investigation of different pelletisation pathways and surface chemical modification. Below a collection of tables is provided to ease comparison between each of the BA-derived carbonaceous adsorbents. Details describing the reasoning behind the observed changes are extensively discussed in the respective chapters featuring the results of other characterisation techniques.

Table 9.*1* describes the key textural properties of the studied BA-derived carbons (in powder-form), whilst

Table 9.*2* hones into their CO_2 adsorption behaviour and Table 9.3 describes their composition. Further,

Table 9.*4* is focused on the pelletised adsorbents. Finally, Figures 9.1 and 9.2 present the comparative TGA uptake of the produced sorbents.

Table 9.1: Surface properties based on BET N_2 adsorption isotherm at 77K.

Name	S_{BET}	Micropore volume	N_2 isotherm	Hysteresis loop
Virgin Carbon	4.6 m^2/g	0.00087 cm^3/g	Type I	No
Chem-Act	643.6 m^2/g	0.2934 cm^3/g	Type VI	H_4 (closed)
Phys-Act	248.0 m^2/g	0.0936 cm^3/g	Type VI	H_4 (closed)
Chem-Mod	221.0 m^{2s}/g	0.0633 cm^3/g	Type VI	H_4 (open)

Table 9.2: CO_2 adsorption behaviour.

Name	CO_2 uptake, mmol/g			Isotherm model		Heat of adsorption	Fractional coverage after 40 cycles
	25 °C	50°C	75°C	Equilibrium	Kinetic		
Virgin Carbon	0.53	0.34	0.14	Double-site Langmuir	PFO	27 kJ/mol	~88%
Chem-Act	1.93	1.29	0.84	Triple-site Langmuir	Avrami	30.5 kJ/mol	~85%
Phys-Act	1.04	0.69	0.43	Toth	Modified Ritchie	26.5 kJ/mol	~96%
Chem-Mod	1.39	0.96	0.61	Triple-site Langmuir	Modified Ritchie	30.5 kJ/mol	~95%

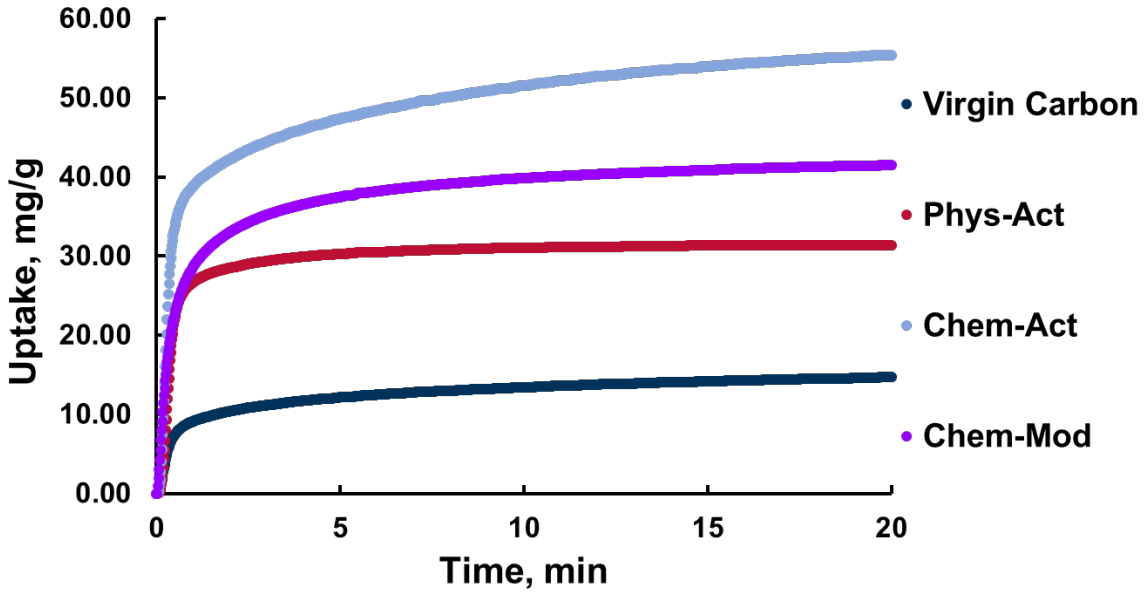

Figure 9.1: CO_2 adsorption plots of the produced sorbents at 1 bar and 50 °C.

Table 9.3: Composition of powder-form BA-derived adsorbents.

Name	Ultimate Analysis, wt%			Proximate Analysis, wt%			
	C	H	N	Moisture	VOC	Fixed C	Ash
Virgin Carbon	60.07	3.16	0.42	3.4	37.1	34.4	25.1
Chem-Act	39.34	2.05	0.00	13.5	20	33	33.5
Phys-Act	54.47	1.00	0.26	1.5	7	49	42.5
Chem-Mod	65.45	1.38	1.43	7.2	21.3	58.4	13.1

Table 9.4: Comparison of pelletised adsorbents.

Name	Crush Strength, N/mm	CO_2 uptake at 50 °C, mmol/g	S_{BET}, m^2/g	Proximate Analysis, wt%			
				Moisture	VOC	Fixed C	Ash
VCP	1.054	0.25	4.0	2	40.5	36	21.5
P-A	N/S	0.71	334.0	1	8.5	57.5	33
A-P	0.794	0.51	120.2	1	14.5	53.5	31

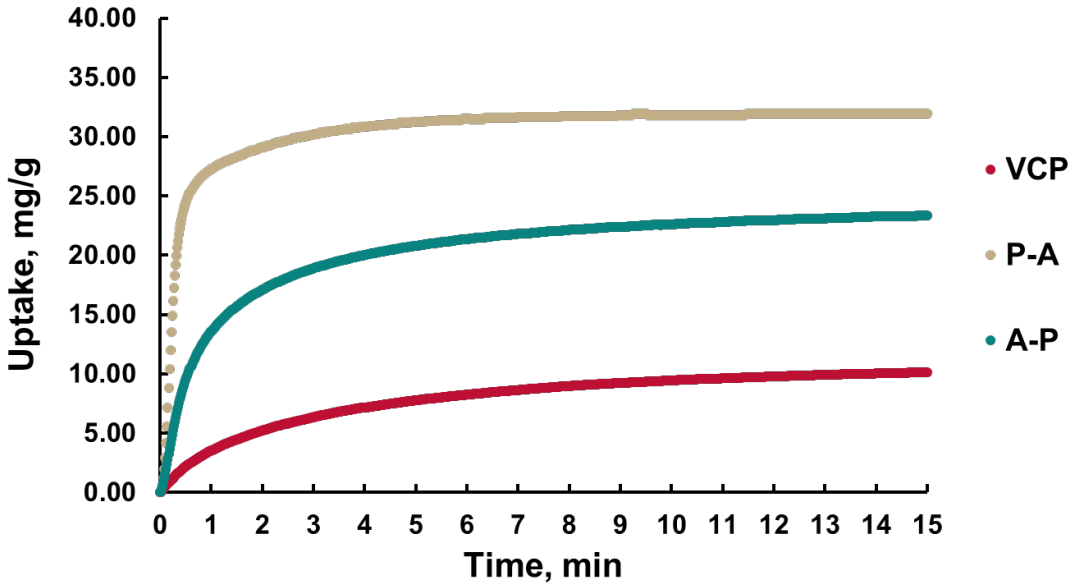

Figure 9.2: CO_2 adsorption plots of the produced pellets at 1 bar and 50 °C.

As a result of these investigations, future practitioners would be able to inform their studies on the application of BA-derived adsorbents in the realm of CO_2 adsorption as well as generally within the realm of activated carbons as adsorbents. The latter is particularly important as the scaling up of the laboratory-based technologies is an ever-existing challenge.

Future work may focus on improving mechanical properties of the pellets (utilising appropriate industrial-grade equipment) as well as apply the adsorbents in a real flue gas environment to assess their performance under low concentrated CO_2 streams, investigate the aspects of selectivity over N_2 as well as resistance to moisture. Further, alternative modification techniques and novel functional groups can be grafted onto the surface of the adsorbents to investigate their efficacy in the context of CO_2 adsorption.

10. Bibliography

[1] United Nations, “Summary of the Paris Agreement,” *United Nations Framew. Conv. Clim. Chang.*, pp. 27–52, 2015.

[2] NASA, “Graphic: Earth’s temperature record.” [Online]. Available: https://climate.nasa.gov/climate_resources/9/graphic-earths-temperature-record/. [Accessed: 29-Sep-2020].

[3] UK Government, “Climate Change Act 2008 CONTENTS,” vol. 2050, no. November, pp. 1–226, 2008.

[4] S. A. Montzka, E. J. Dlugokencky, and J. H. Butler, “Non-CO_2 greenhouse gases and climate change,” *Nature*, vol. 476, no. 7358, pp. 43–50, 2011.

[5] N. Jones, “Troubling milestone for CO_2,” *Nat. Geosci.*, vol. 6, no. 8, p. 589, 2013.

[6] F. Joos and R. Spahni, “Rates of change in natural and anthropogenic radiative forcing over the past 20,000 years,” *Proc. Natl. Acad. Sci. U. S. A.*, vol. 105, no. 5, pp. 1425–1430, 2008.

[7] NASA, “The relentless rise of carbon dioxide – Climate Change: Vital Signs of the Planet.” [Online]. Available: https://climate.nasa.gov/climate_resources/24/graphic-the-relentless-rise-of-carbon-dioxide/. [Accessed: 29-Sep-2020].

[8] C. Le Quéré *et al.*, “Global Carbon Budget 2018 (pre-print),” *Earth Syst. Sci. Data Discuss.*, vol. pre print, no. November, pp. 1–54, 2018.

[9] R. B. Jackson *et al.*, “Global energy growth is outpacing decarbonization,” *Environ. Res. Lett.*, vol. 13, no. 12, 2018.

[10] T. Tanner and L. Horn-Phathanothai, “IPCC Report,” *National Weather Service: Weather and Climate*. pp. 1–31, 2011.

[11] H. Ritchie, M. Roser, and P. Rosado, “CO_2 and Greenhouse Gas Emissions - Our World in Data,” *OurWorldInData.org*, 2020. .

[12] Her Majesty's Government, “Joint Statement from the Department of Natural Resources of Canada and the Department of Energy and Climate Change of the United Kingdom concerning Carbon Capture and Storage,” no. April 2012. pp. 1–3, 2014.

[13] M. Bui *et al.*, “Carbon capture and storage (CCS): The way forward,” *Energy Environ. Sci.*, vol. 11, no. 5, pp. 1062–1176, 2018.

[14] Committee on Climate Change, “Fourth Carbon Budget Review – part 2,” no. December, p. 90, 2013.

[15] IPCC, “Climate Change 2014,” 2014.

[16] R. R. Bottoms, “Process for separating acidic gases, United States Patent office,” 1930.

[17] C. H. Yu, C. H. Huang, and C. S. Tan, “A review of CO_2 capture by absorption and adsorption,” *Aerosol Air Qual. Res.*, vol. 12, no. 5, pp. 745–769, 2012.

[18] H. A. Patel, J. Byun, and C. T. Yavuz, “Carbon Dioxide Capture Adsorbents: Chemistry and Methods,” *ChemSusChem*, vol. 10, no. 7, pp. 1303–1317, Apr. 2017.

[19] S. V. Vassilev, D. Baxter, L. K. Andersen, and C. G. Vassileva, “An overview of the composition and application of biomass ash. Part 1. Phase-mineral and chemical composition and classification,” *Fuel*, vol. 105, pp. 40–76, 2013.

[20] T. F. de Aquino *et al.*, “CO_2 adsorption capacity of zeolites synthesized from coal fly ashes,” *Fuel*, vol. 276, no. May 2019, p. 118143, 2020.

[21] A. Dindi, D. V. Quang, L. F. Vega, E. Nashef, and M. R. M. Abu-Zahra, “Applications of fly ash for CO_2 capture, utilization, and storage,” *J. CO_2 Util.*, vol. 29, no. June 2018, pp. 82–102, 2019.

[22] M. Ahmaruzzaman, “A review on the utilization of fly ash,” *Prog. Energy Combust. Sci.*, vol. 36, no. 3, pp. 327–363, 2010.

[23] Office for National Statistics, “UK Environmental Accounts: 2019,” *United Kingdom Natl. Accounts - Blue B.*, vol. 2011, no. 1, pp. 1–15, 2019.

[24] P. E. Allen and G. P. Hammond, “Bioenergy utilization for a low carbon future in the UK: the evaluation of some alternative scenarios and projections,” *BMC Energy*, vol. 1, no. 1, pp. 1–24, 2019.

[25] I. Staffell, R. Green, R. Gross, T. Green, and L. Clark, “Electric Insights Quarterly January to March 2020,” 2020.

[26] P. W. Griffin, G. P. Hammond, and J. B. Norman, “Industrial decarbonisation of the pulp and paper sector: A UK perspective,” *Appl. Therm. Eng.*, vol. 134, no. December 2017, pp. 152–162, 2018.

[27] É. J. M. Bastien, “Towards Circular Economy : Wood ash management for biomass CHP plants in the UK,” KTH Royal Institute of Technology, 2020.

[28] BEIS, “IMPLEMENTING THE END OF UNABATED COAL BY 2025 Government response to unabated coal closure consultation,” 2018.

[29] B. P. Spigarelli and S. K. Kawatra, “Opportunities and challenges in carbon dioxide capture,” *J. CO_2 Util.*, vol. 1, pp. 69–87, 2013.

[30] D. Toporov, *Combustion of Pulverised Coal in a Mixture of Oxygen and Recycled Flue Gas*. Elsevier, 2014.

[31] X. Li *et al.*, “Oxy-fuel combustion for carbon capture and storage in internal combustion engines – A review,” *Int. J. Energy Res.*, no. August, pp. 1–18, 2021.

[32] B. Metz, O. Davidson, L. Meyer, H. de Coninck, and M. Loos, “IPCC Special Report on Carbon Dioxide Capture and Storage,” 2005.

[33] S. Yadav and S. S. Mondal, “A review on the progress and prospects of oxy-fuel carbon capture and sequestration (CCS) technology,” *Fuel*, vol. 308, no. August 2021, p. 122057, 2022.

[34] X. Wang and C. Song, “Carbon Capture From Flue Gas and the Atmosphere: A Perspective,” *Front. Energy Res.*, vol. 8, no. December, 2020.

[35] S. Masoudi Soltani, A. Lahiri, H. Bahzad, P. Clough, M. Gorbounov, and Y. Yan, “Sorption-enhanced Steam Methane Reforming for Combined CO_2 Capture and Hydrogen Production: A State-of-the-Art Review,” *Carbon Capture Sci. Technol.*, vol. 1, no. August, p. 100003, Dec. 2021.

[36] M. Cao *et al.*, “A carbon molecular sieve membrane-based reactive separation process for pre-combustion CO_2 capture,” *J. Memb. Sci.*, vol. 605, no. February, p. 118028, 2020.

[37] W. L. Theo, J. S. Lim, H. Hashim, A. A. Mustaffa, and W. S. Ho, “Review of pre-combustion capture and ionic liquid in carbon capture and storage,” *Appl. Energy*, vol. 183, pp. 1633–1663, 2016.

[38] E. Portillo, B. Alonso-Fariñas, F. Vega, M. Cano, and B. Navarrete, “Alternatives for oxygen-selective membrane systems and their integration into the oxy-fuel combustion process: A review,” *Sep. Purif. Technol.*, vol. 229, no. January, p. 115708, 2019.

[39] Politecnico di Milano - Alstom UK, “European best practice guidelines for assessment of CO_2 capture technologies,” 2011.

[40] N. Otsuka, “Fireside Corrosion,” in *Shreir’s Corrosion*, Elsevier, 2010, pp. 457–481.

[41] C. Scholes, M. Ho, and D. Wiley, “Membrane-Cryogenic Post-Combustion Carbon Capture of Flue Gases from NGCC,” *Technologies*, vol. 4, no. 2, p. 14,

Apr. 2016.

[42] R. Zevenhoven and P. Kilpinen, “Flue gases and fuel gases,” *Control Pollut. Flue Gases Fuel Gases*, pp. 2.1-2.12, 2001.

[43] A. Bosoaga, O. Masek, and J. E. Oakey, “CO_2 Capture Technologies for Cement Industry,” *Energy Procedia*, vol. 1, no. 1, pp. 133–140, 2009.

[44] D. Sachde and G. T. Rochelle, “Absorber intercooling configurations using aqueous piperazine for capture from sources with 4 to 27% CO_2,” *Energy Procedia*, vol. 63, pp. 1637–1656, 2014.

[45] P. García-Gutiérrez, “Carbon Capture and Utilisation processes : a techno-economic assessment of synthetic fuel production from CO_2,” University of Sheffield, 2016.

[46] J. Wilcox, *Carbon capture*. 2012.

[47] R. Bounaceur, N. Lape, D. Roizard, C. Vallieres, and E. Favre, “Membrane processes for post-combustion carbon dioxide capture: A parametric study,” *Energy*, vol. 31, no. 14, pp. 2556–2570, 2006.

[48] F. Vega, M. Cano, S. Camino, L. M. G. Fernández, E. Portillo, and B. Navarrete, “Solvents for Carbon Dioxide Capture,” in *Carbon Dioxide Chemistry, Capture and Oil Recovery*, vol. 32, InTech, 2018, pp. 137–144.

[49] B. Lv, B. Guo, Z. Zhou, and G. Jing, “Mechanisms of CO_2 Capture into Monoethanolamine Solution with Different CO_2 Loading during the Absorption/Desorption Processes,” *Environ. Sci. Technol.*, vol. 49, no. 17, pp. 10728–10735, 2015.

[50] F. A. Chowdhury, H. Yamada, T. Higashii, K. Goto, and M. Onoda, “CO_2 capture by tertiary amine absorbents: A performance comparison study,” *Ind. Eng. Chem. Res.*, vol. 52, no. 24, pp. 8323–8331, 2013.

[51] N. Lai *et al.*, “CO_2 Capture With Absorbents of Tertiary Amine Functionalized Nano–SiO2,” *Front. Chem.*, vol. 8, no. February, pp. 1–9, 2020.

[52] F. O. Ochedi, J. Yu, H. Yu, Y. Liu, and A. Hussain, *Carbon dioxide capture using liquid absorption methods: a review*, vol. 19, no. 1. Springer International Publishing, 2021.

[53] B. Petrovic and S. Masoudi Soltani, “Optimization of Post Combustion CO_2 Capture from a Combined-Cycle Gas Turbine Power Plant via Taguchi Design of Experiment,” *Processes*, vol. 7, no. 6, p. 364, Jun. 2019.

[54] M. Rabensteiner, G. Kinger, M. Koller, and C. Hochenauer, “Pilot plant study of

aqueous solution of piperazine activated 2-amino-2-methyl-1-propanol for post combustion carbon dioxide capture," *Int. J. Greenh. Gas Control*, vol. 51, pp. 106–117, 2016.

[55] G. T. Rochelle, "Amine Scrubbing for CO_2 Capture," *Science*. 2009.

[56] W. R. Elliott, "Front-End Engineering Design (FEED) Study for a Carbon Capture Plant Retrofit to a Natural Gas-Fired Gas Turbine Combined Cycle Power Plant," 2022.

[57] Global CCS Institute, "Global Status of CCS, Targeting Climate Change,2019," 2019.

[58] J. Gibbins, "The Petra Nova CO_2 capture project – why not open it up?," *UKCCSRC*, 2022. [Online]. Available: https://ukccsrc.ac.uk/the-petra-nova-co2-capture-project-why-not-open-it-up/.

[59] S. Winberg, "Testimony by Steven E. Winberg Assistant Secretary for Fossil Energy U.S. Department of Energy Before the U.S. Senate Committee on Energy and Natural Resources," 2020.

[60] M. A. (Memoria. U. of N. S. J. Abdi, M. M. (National I. O. C. . Golkar, and A. (Memorial U. of N. Meisen, "Improve contaminant control in amine systems," *Hydrocarb. Process.*, no. 63, pp. 102C – 102–I, 2001.

[61] N. E. Flø *et al.*, "Results from MEA Degradation and Reclaiming Processes at the CO_2 Technology Centre Mongstad," *Energy Procedia*, vol. 114. pp. 1307–1324, 2017.

[62] D. Danaci, P. A. Webley, and C. Petit, "Guidelines for Techno-Economic Analysis of Adsorption Processes," *Front. Chem. Eng.*, vol. 2, no. January, pp. 1–11, 2021.

[63] D. Kearns, H. Liu, and C. Consoli, "Technology Readiness and Costs of CCS," 2021.

[64] J. Freeman, "Chevron natural gas carbon capture technology testing project," 2021.

[65] T. M. McDonald, D. M. D'Alessandro, R. Krishna, and J. R. Long, "Enhanced carbon dioxide capture upon incorporation of N,N′- dimethylethylenediamine in the metal-organic framework CuBTTri," *Chem. Sci.*, vol. 2, no. 10, pp. 2022–2028, 2011.

[66] S. Sircar, "Basic research needs for design of adsorptive gas separation processes," *Ind. Eng. Chem. Res.*, vol. 45, no. 16, pp. 5435–5448, 2006.

[67] R. K. Sinnott and G. Towler, *Chemical Engineering Design : SI edition.* Butterworth-Heinemann, 2009.

[68] R. T. Yang, *Adsorbents: Fundamentals and Applications*. 2003.

[69] A. A. Adelodun, K. H. Kim, J. C. Ngila, and J. Szulejko, “A review on the effect of amination pretreatment for the selective separation of CO_2,” *Appl. Energy*, vol. 158, pp. 631–642, 2015.

[70] B. Petrovic, M. Gorbounov, and S. Masoudi Soltani, “Impact of Surface Functional Groups and Their Introduction Methods on the Mechanisms of CO_2 Adsorption on Porous Carbonaceous Adsorbents,” *Carbon Capture Sci. Technol.*, vol. 3, p. 100045, Jun. 2022.

[71] M. L. McGlashan, “Manual of symbols and terminology for physicochemical quantities and units,” *Pure Appl. Chem.*, vol. 21, no. 1, pp. 1–44, 1970.

[72] C. Geankoplis, J., *Transport processes and separation process principles (Includes Unit Operations)*. 2003.

[73] B. Petrovic, M. Gorbounov, and S. Masoudi Soltani, “Influence of surface modification on selective CO_2 adsorption: A technical review on mechanisms and methods,” *Microporous Mesoporous Mater.*, vol. 312, no. September 2020, p. 110751, Jan. 2021.

[74] D. D. Do, *Adsorption Analysis: Equilibria and Kinetics*, vol. 2, no. Imperial College Press. 1998.

[75] W. Kast, “Principles of adsorption and adsorption processes,” *Chem. Eng. Process. Process Intensif.*, vol. 19, no. 2, p. 118, 1985.

[76] R. B. Bird, W. E. Stewart, and E. N. Lightfoot, *Transport phenomena, R. B. Bird, W. E. Stewart, and E. N. Lightfoot, John Wiley and Sons, Inc., New York(1960). 780 pages.$11.50*, vol. 7, no. 2. 1961.

[77] S. Ghanbari and G. Kamath, “Dynamic simulation and mass transfer study of carbon dioxide capture using biochar and mgo-impregnated activated carbon in a swing adsorption process,” *Energy and Fuels*, vol. 33, no. 6, pp. 5452–5463, 2019.

[78] M. Suzuki, *Adsorption engineering, Chemical engineering monographs : Vol. 25*. 1991.

[79] I. K. Petrushenko, N. A. Ivanov, and K. B. Petrushenko, “Theoretical investigation of carbon dioxide adsorption on Li^+-decorated nanoflakes,” *Molecules*, vol. 26, no. 24, pp. 1–14, 2021.

[80] H. A. Patel, J. Byun, and C. T. Yavuz, “Carbon Dioxide Capture Adsorbents: Chemistry and Methods,” *ChemSusChem*, vol. 10, no. 7, pp. 1303–1317, Apr. 2017.

[81] S. Wang, Z. Tian, S. Dai, and D. E. Jiang, “Optimal Size of a Cylindrical Pore for Post-Combustion CO_2 Capture,” *J. Phys. Chem. C*, vol. 121, no. 40, pp. 22025–22030, 2017.

[82] J. Rouquerol, F. Rouquerol, P. Llewellyn, G. Maurin, and K. S. W. Sing, *Adsorption by Powders and Porous Solids: Principles, Methodology and Applications: Second Edition*. 2013.

[83] J. U. Keller and R. Staudt, *GAS ADSORPTION EQUILIBRIA Experimental Methods and Adsorptive Isotherms*. Boston: Springer, 2005.

[84] E. J. Bottani and J. M. D. Tascón, *Adsorption by carbons*. Elsevier, 2008.

[85] M. M. Dubinin, “Physical Adsorption of Gases and Vapors in Micropores,” in *Progress in Surface and Membrane Science*, vol. 9, ACADEMIC PRESS, INC., 1975, pp. 1–70.

[86] M. Thommes *et al.*, “Physisorption of gases, with special reference to the evaluation of surface area and pore size distribution (IUPAC Technical Report),” *Pure Appl. Chem.*, vol. 87, no. 9–10, pp. 1051–1069, 2015.

[87] M. D. Donohue and G. L. Aranovich, “Adsorption Hysteresis in Porous Solids,” *J. Colloid Interface Sci.*, vol. 205, no. 1, pp. 121–130, Sep. 1998.

[88] D. Spanjaard and M. C. Desjonqueres, “Electronic Theory of Chemisorption,” in *Interaction of Atoms and Molecules with Solid Surfaces*, Springer, 1990, pp. 255–323.

[89] P. A. Webley and D. Danaci, “CO_2 Capture by Adsorption Processes,” in *Carbon Capture and Storage*, Royal Society of Chemistry, 2019, pp. 106–167.

[90] Y. C. Chiang and R. S. Juang, “Surface modifications of carbonaceous materials for carbon dioxide adsorption: A review,” *J. Taiwan Inst. Chem. Eng.*, vol. 71, pp. 214–234, 2017.

[91] J. R. Pels, F. Kapteijn, J. A. Moulijn, Q. Zhu, and K. M. Thomas, “Evolution of nitrogen functionalities in carbonaceous materials during pyrolysis,” *Carbon N. Y.*, vol. 33, no. 11, pp. 1641–1653, 1995.

[92] X. Zhang *et al.*, “Nitrogen enriched biochar modified by high temperature CO_2-ammonia treatment: Characterization and adsorption of CO_2,” *Chem. Eng. J.*, vol. 257, pp. 20–27, 2014.

[93] X. Zhang *et al.*, “Preparation of nitrogen-doped microporous modified biochar by high temperature CO_2-NH_3 treatment for CO_2 adsorption: Effects of temperature,” *RSC Adv.*, vol. 6, no. 100, pp. 98157–98166, 2016.

[94] S. Hosseini *et al.*, “Adsorption of carbon dioxide using activated carbon impregnated with Cu promoted by zinc,” *J. Taiwan Inst. Chem. Eng.*, vol. 52, pp. 109–117, 2015.

[95] V. P. Mulgundmath, R. A. Jones, F. H. Tezel, and J. Thibault, “Fixed bed adsorption for the removal of carbon dioxide from nitrogen: Breakthrough behaviour and modelling for heat and mass transfer,” *Sep. Purif. Technol.*, vol. 85, pp. 17–27, 2012.

[96] H. Yang, Y. Yuan, and S. C. E. Tsang, “Nitrogen-enriched carbonaceous materials with hierarchical micro-mesopore structures for efficient CO_2 capture,” *Chem. Eng. J.*, vol. 185–186, pp. 374–379, 2012.

[97] M. G. Plaza, C. Pevida, A. Arenillas, F. Rubiera, and J. J. Pis, “CO_2 capture by adsorption with nitrogen enriched carbons,” *Fuel*, vol. 86, no. 14 SPEC. ISS., pp. 2204–2212, 2007.

[98] S. Nakao, K. Yogo, K. Goto, T. Kai, and H. Yamada, “Advanced CO_2 capture technologies: Absorption, adsorption, and membrane separation methods,” *Book*, 2019. .

[99] Y. C. Chang and D. H. Chen, “Recovery of gold(III) ions by a chitosancoated magnetic nano-adsorbent,” *Gold Bull.*, vol. 39, no. 3, pp. 98–102, 2006.

[100] S. Youk, J. P. Hofmann, B. Badamdorj, A. Völkel, M. Antonietti, and M. Oschatz, “Controlling pore size and pore functionality in sp2-conjugated microporous materials by precursor chemistry and salt templating,” *J. Mater. Chem. A*, vol. 8, no. 41, pp. 21680–21689, 2020.

[101] P. A. Webley and D. Danaci, “Chapter 5. CO_2 Capture by Adsorption Processes,” in *Carbon Capture and Storage*, M. Bui and N. Mac Dowell, Eds. Cambridge: Royal Society of Chemistry, 2019, pp. 106–167.

[102] L. An *et al.*, “Novel Nitrogen-Doped Porous Carbons Derived from Graphene for Effective CO_2 Capture,” *Ind. Eng. Chem. Res.*, vol. 58, no. 8, pp. 3349–3358, Feb. 2019.

[103] B. Sreenivasulu, D. V. Gayatri, I. Sreedhar, and K. V. Raghavan, “A journey into the process and engineering aspects of carbon capture technologies,” *Renew. Sustain. Energy Rev.*, vol. 41, pp. 1324–1350, Jan. 2015.

[104] M. Wang *et al.*, “Adsorption and regeneration study of polyethylenimine-impregnated millimeter-sized mesoporous carbon spheres for post-combustion CO_2 capture,” *Appl. Energy*, vol. 168, pp. 282–290, Apr. 2016.

[105] L. Joss, M. Gazzani, and M. Mazzotti, “Rational design of temperature swing adsorption cycles for post-combustion CO_2 capture,” *Chem. Eng. Sci.*, vol. 158, pp. 381–394, Feb. 2017.

[106] K. Sumida *et al.*, “Carbon Dioxide Capture in Metal–Organic Frameworks,” *Chem. Rev.*, vol. 112, no. 2, pp. 724–781, Feb. 2012.

[107] C. Dhoke, A. Zaabout, S. Cloete, and S. Amini, “Review on reactor configurations for adsorption-based CO_2 capture,” *Ind. Eng. Chem. Res.*, vol. 60, no. 10, pp. 3779–3798, 2021.

[108] H. Chalmers, M. Leach, M. Lucquiaud, and J. Gibbins, “Valuing flexible operation of power plants with CO_2 capture,” *Energy Procedia*, vol. 1, no. 1, pp. 4289–4296, Feb. 2009.

[109] F. Normann, S. Ó. Gararsdóttir, R. Skagestad, A. Mathisen, and F. Johnsson, “Partial Capture of Carbon Dioxide from Industrial Sources - A Discussion on Cost Optimization and the CO_2 Capture Rate,” *Energy Procedia*, vol. 114, no. November 2016, pp. 113–121, 2017.

[110] M. Luberti, G. D. Oreggioni, and H. Ahn, “Design of a rapid vacuum pressure swing adsorption (RVPSA) process for post-combustion CO_2 capture from a biomass-fuelled CHP plant,” *J. Environ. Chem. Eng.*, vol. 5, no. 4, pp. 3973–3982, Aug. 2017.

[111] P. A. Webley and J. Zhang, “Microwave assisted vacuum regeneration for CO_2 capture from wet flue gas,” *Adsorption*, vol. 20, no. 1, pp. 201–210, Jan. 2014.

[112] M. Auta, N. D. Amat Darbis, A. T. Mohd Din, and B. H. Hameed, “Fixed-bed column adsorption of carbon dioxide by sodium hydroxide modified activated alumina,” *Chem. Eng. J.*, vol. 233, pp. 80–87, Nov. 2013.

[113] C. A. Grande, R. P. L. Ribeiro, E. L. G. Oliveira, and A. E. Rodrigues, “Electric swing adsorption as emerging CO_2 capture technique,” *Energy Procedia*, vol. 1, no. 1, pp. 1219–1225, Feb. 2009.

[114] L. Riboldi and O. Bolland, “Evaluating Pressure Swing Adsorption as a CO_2 separation technique in coal-fired power plants,” *Int. J. Greenh. Gas Control*, vol. 39, no. 7491, pp. 1–16, 2015.

[115] T. L. P. Dantas *et al.*, “Modeling of the fixed - bed adsorption of carbon dioxide

and a carbon dioxide - nitrogen mixture on zeolite 13X," *Brazilian J. Chem. Eng.*, vol. 28, no. 3, pp. 533–544, Sep. 2011.

[116] C. Dhoke *et al.*, "Demonstration of the Novel Swing Adsorption Reactor Cluster Concept in a Multistage Fluidized Bed with Heat-Transfer Surfaces for Postcombustion CO_2 Capture," *Ind. Eng. Chem. Res.*, vol. 59, no. 51, pp. 22281–22291, Dec. 2020.

[117] G. Hofer, G. Schöny, J. Fuchs, and T. Pröll, "Investigating wall-to-bed heat transfer in view of a continuous temperature swing adsorption process," *Fuel Process. Technol.*, vol. 169, pp. 157–169, Jan. 2018.

[118] F. Raganati, R. Chirone, and P. Ammendola, "Calcium-looping for thermochemical energy storage in concentrating solar power applications: Evaluation of the effect of acoustic perturbation on the fluidized bed carbonation," *Chem. Eng. J.*, vol. 392, p. 123658, Jul. 2020.

[119] E. R. Monazam, J. Spenik, and L. J. Shadle, "Fluid bed adsorption of carbon dioxide on immobilized polyethylenimine (PEI): Kinetic analysis and breakthrough behavior," *Chem. Eng. J.*, vol. 223, pp. 795–805, May 2013.

[120] S. Yaghoobi-Khankhajeh, R. Alizadeh, and R. Zarghami, "Adsorption modeling of CO_2 in fluidized bed reactor," *Chem. Eng. Res. Des.*, vol. 129, pp. 111–121, Jan. 2018.

[121] W.-C. Yang and J. Hoffman, "Exploratory Design Study on Reactor Configurations for Carbon Dioxide Capture from Conventional Power Plants Employing Regenerable Solid Sorbents," *Ind. Eng. Chem. Res.*, vol. 48, no. 1, pp. 341–351, Jan. 2009.

[122] J. Zhang, P. A. Webley, and P. Xiao, "Effect of process parameters on power requirements of vacuum swing adsorption technology for CO_2 capture from flue gas," *Energy Convers. Manag.*, vol. 49, no. 2, pp. 346–356, Feb. 2008.

[123] K. Kim, Y. Son, W. B. Lee, and K. S. Lee, "Moving bed adsorption process with internal heat integration for carbon dioxide capture," *Int. J. Greenh. Gas Control*, vol. 17, pp. 13–24, Sep. 2013.

[124] G. Mondino, C. A. Grande, R. Blom, and L. O. Nord, "Moving bed temperature swing adsorption for CO_2 capture from a natural gas combined cycle power plant," *Int. J. Greenh. Gas Control*, vol. 85, pp. 58–70, Jun. 2019.

[125] O. H. P. Gunawardene, C. A. Gunathilake, K. Vikrant, and S. M. Amaraweera, *Carbon Dioxide Capture through Physical and Chemical Adsorption Using*

Porous Carbon Materials: A Review, vol. 13, no. 3. 2022.

[126] S. Boycheva, D. Zgureva, H. Lazarova, and M. Popova, “Comparative studies of carbon capture onto coal fly ash zeolites Na-X and Na–Ca-X,” *Chemosphere*, vol. 271, p. 129505, May 2021.

[127] B. Petrovic, M. Gorbounov, S. Ozmen, P. Clough, and S. M. Soltani, “Synthesis of Nanoporous Type A and X Zeolite Mixtures from Biomass Combustion Fly Ash for Post-Combustion Carbon Capture,” in *2022 IEEE 22nd International Conference on Nanotechnology (NANO)*, 2022, pp. 221–224.

[128] B. Petrovic, M. Gorbounov, A. Lahiri, and S. M. Soltani, “Biomass Combustion Fly Ash-Derived Nanoporous Zeolites for Post-Combustion Carbon Capture,” in *2021 IEEE 21st International Conference on Nanotechnology (NANO)*, 2021, vol. 2021-July, pp. 233–236.

[129] K. Margeta and A. Farkaš, “Introductory Chapter: Zeolites - From Discovery to New Applications on the Global Market,” in *Zeolites - New Challenges*, IntechOpen, 2020.

[130] T. Y. S. Ng, T. L. Chew, Y. F. Yeong, Z. A. Jawad, and C.-D. Ho, “Zeolite RHO Synthesis Accelerated by Ultrasonic Irradiation Treatment,” *Sci. Rep.*, vol. 9, no. 1, p. 15062, Oct. 2019.

[131] J. Y. Lai, L. H. Ngu, and S. S. Hashim, “A review of CO_2 adsorbents performance for different carbon capture technology processes conditions,” *Greenh. Gases Sci. Technol.*, vol. 11, no. 5, pp. 1076–1117, Oct. 2021.

[132] S. Rostami, A. Nakhaei Pour, A. Salimi, and A. Abolghasempour, “Hydrogen adsorption in metal- organic frameworks (MOFs): Effects of adsorbent architecture,” *Int. J. Hydrogen Energy*, vol. 43, no. 14, pp. 7072–7080, Apr. 2018.

[133] Z. R. Herm, E. D. Bloch, and J. R. Long, “Hydrocarbon Separations in Metal–Organic Frameworks,” *Chem. Mater.*, vol. 26, no. 1, pp. 323–338, Jan. 2014.

[134] M. H. Yap, K. L. Fow, and G. Z. Chen, “Synthesis and applications of MOF-derived porous nanostructures,” *Green Energy Environ.*, vol. 2, no. 3, pp. 218–245, Jul. 2017.

[135] T. Bae *et al.*, “Environmental Science post-combustion carbon dioxide capture †,” pp. 128–138, 2013.

[136] T. T. T. Nguyen, J.-B. Lin, G. K. H. Shimizu, and A. Rajendran, “Separation of

CO_2 and N_2 on a hydrophobic metal organic framework CALF-20," *Chem. Eng. J.*, vol. 442, p. 136263, Aug. 2022.

[137] A. K. Rajagopalan, A. M. Avila, and A. Rajendran, "Do adsorbent screening metrics predict process performance? A process optimisation based study for post-combustion capture of CO_2," *Int. J. Greenh. Gas Control*, vol. 46, pp. 76–85, Mar. 2016.

[138] M. Younas *et al.*, "Recent progress and remaining challenges in post-combustion CO_2 capture using metal-organic frameworks (MOFs)," *Prog. Energy Combust. Sci.*, vol. 80, p. 100849, 2020.

[139] S. G. Subraveti, S. Roussanaly, R. Anantharaman, L. Riboldi, and A. Rajendran, "Techno-economic assessment of optimised vacuum swing adsorption for post-combustion CO_2 capture from steam-methane reformer flue gas," *Sep. Purif. Technol.*, vol. 256, no. August 2020, p. 117832, 2021.

[140] J.-B. Lin *et al.*, "A scalable metal-organic framework as a durable physisorbent for carbon dioxide capture," *Science (80-.).*, vol. 374, no. 6574, pp. 1464–1469, Dec. 2021.

[141] P. Silva, S. M. F. Vilela, J. P. C. Tomé, and F. A. Almeida Paz, "Multifunctional metal-organic frameworks: From academia to industrial applications," *Chem. Soc. Rev.*, vol. 44, no. 19, pp. 6774–6803, 2015.

[142] PrometheanParticles, "OUR TECHNOLOGY Continuous, Industrial-scale, Cost-effective Nanomaterial Manufacturing." [Online]. Available: https://prometheanparticles.co.uk/our-technology/.

[143] Barclays, "Barclays invest in Northern Irish carbon capture company, MOF Technologies," *2022*. [Online]. Available: https://home.barclays/news/press-releases/2022/10/barclays-invest-in-mof-technologies-/.

[144] X. Gao, S. Yang, L. Hu, S. Cai, L. Wu, and S. Kawi, "Carbonaceous materials as adsorbents for CO_2 capture: synthesis and modification," *Carbon Capture Sci. Technol.*, vol. 3, p. 100039, Jun. 2022.

[145] C. Rodriguez Correa, T. Hehr, A. Voglhuber-Slavinsky, Y. Rauscher, and A. Kruse, "Pyrolysis vs. hydrothermal carbonization: Understanding the effect of biomass structural components and inorganic compounds on the char properties," *J. Anal. Appl. Pyrolysis*, vol. 140, pp. 137–147, Jun. 2019.

[146] C. Quan, R. Su, and N. Gao, "Preparation of activated biomass carbon from pine sawdust for supercapacitor and CO_2 capture," *Int. J. Energy Res.*, vol. 44,

no. 6, pp. 4335–4351, May 2020.

[147] G. Huang, Y. Liu, X. Wu, and J. Cai, “Activated carbons prepared by the KOH activation of a hydrochar from garlic peel and their CO_2 adsorption performance,” *New Carbon Mater.*, vol. 34, no. 3, pp. 247–257, Jun. 2019.

[148] R. Nandi, M. K. Jha, S. K. Guchhait, D. Sutradhar, and S. Yadav, “Impact of KOH Activation on Rice Husk Derived Porous Activated Carbon for Carbon Capture at Flue Gas alike Temperatures with High CO_2/N_2 Selectivity,” *ACS Omega*, vol. 8, no. 5, pp. 4802–4812, Feb. 2023.

[149] K. Kiełbasa *et al.*, “Carbon Dioxide Adsorption over Activated Carbons Produced from Molasses Using H_2SO_4, H_3PO_4, HCl, NaOH, and KOH as Activating Agents,” *Molecules*, vol. 27, no. 21, p. 7467, Nov. 2022.

[150] Y. Ji, C. Zhang, X. J. Zhang, P. F. Xie, C. Wu, and L. Jiang, “A high adsorption capacity bamboo biochar for CO_2 capture for low temperature heat utilization,” *Sep. Purif. Technol.*, vol. 293, p. 121131, Jul. 2022.

[151] M. M. Bade, A. A. Dubale, D. F. Bebizuh, and M. Atlabachew, “Highly Efficient Multisubstrate Agricultural Waste-Derived Activated Carbon for Enhanced CO_2 Capture,” *ACS Omega*, vol. 7, no. 22, pp. 18770–18779, Jun. 2022.

[152] G. K. Parshetti, S. Chowdhury, and R. Balasubramanian, “Biomass derived low-cost microporous adsorbents for efficient CO_2 capture,” *Fuel*, vol. 148, pp. 246–254, May 2015.

[153] A. Jain, R. Balasubramanian, and M. P. Srinivasan, “Hydrothermal conversion of biomass waste to activated carbon with high porosity: A review,” *Chem. Eng. J.*, vol. 283, pp. 789–805, Jan. 2016.

[154] G. Xu, Y. Lv, J. Sun, H. Shao, and L. Wei, “Recent Advances in Biochar Applications in Agricultural Soils: Benefits and Environmental Implications,” *CLEAN - Soil, Air, Water*, vol. 40, no. 10, pp. 1093–1098, Oct. 2012.

[155] N. Abuelnoor, A. AlHajaj, M. Khaleel, L. F. Vega, and M. R. M. Abu-Zahra, “Activated carbons from biomass-based sources for CO_2 capture applications,” *Chemosphere*, vol. 282, p. 131111, Nov. 2021.

[156] S. Ciuta, F. Patuzzi, M. Baratieri, and M. J. Castaldi, “Enthalpy changes during pyrolysis of biomass: Interpretation of intraparticle gas sampling,” *Appl. Energy*, vol. 228, pp. 1985–1993, Oct. 2018.

[157] J. Li *et al.*, “Selective preparation of biomass-derived porous carbon with controllable pore sizes toward highly efficient CO_2 capture,” *Chem. Eng. J.*,

vol. 360, pp. 250–259, Mar. 2019.

[158] A. Pal *et al.*, “A benchmark for CO_2 uptake onto newly synthesized biomass-derived activated carbons,” *Appl. Energy*, vol. 264, p. 114720, Apr. 2020.

[159] S. Li, X. Yuan, S. Deng, L. Zhao, and K. B. Lee, “A review on biomass-derived CO_2 adsorption capture: Adsorbent, adsorber, adsorption, and advice,” *Renewable and Sustainable Energy Reviews*, vol. 152. 2021.

[160] M. R. Ketabchi, S. Babamohammadi, W. G. Davies, M. Gorbounov, and S. Masoudi Soltani, “Latest advances and challenges in carbon capture using bio-based sorbents: A state-of-the-art review,” *Carbon Capture Sci. Technol.*, vol. 6, no. October 2022, p. 100087, Mar. 2023.

[161] J. Pallarés, A. González-Cencerrado, and I. Arauzo, “Production and characterization of activated carbon from barley straw by physical activation with carbon dioxide and steam,” *Biomass and Bioenergy*, vol. 115, pp. 64–73, Aug. 2018.

[162] L. Leng *et al.*, “An overview on engineering the surface area and porosity of biochar,” *Sci. Total Environ.*, vol. 763, p. 144204, Apr. 2021.

[163] B. Zhang, P. Liu, Z. Huang, and J. Liu, “Adsorption Equilibrium and Diffusion of CH_4 , CO_2 , and N_2 in Coal-Based Activated Carbon,” *ACS Omega*, vol. 8, no. 11, pp. 10303–10313, Mar. 2023.

[164] A. E. Ogungbenro, D. V. Quang, K. A. Al-Ali, L. F. Vega, and M. R. M. Abu-Zahra, “Physical synthesis and characterization of activated carbon from date seeds for CO_2 capture,” *J. Environ. Chem. Eng.*, vol. 6, no. 4, pp. 4245–4252, Aug. 2018.

[165] M. Danish, V. Parthasarthy, and M. K. Al Mesfer, “CO_2 capture using activated carbon synthesized from date stone: breakthrough, equilibrium, and mass-transfer zone,” *Carbon Lett.*, vol. 31, no. 6, pp. 1261–1272, Dec. 2021.

[166] N. A. Rashidi, A. Bokhari, and S. Yusup, “Evaluation of kinetics and mechanism properties of CO_2 adsorption onto the palm kernel shell activated carbon,” *Environ. Sci. Pollut. Res.*, vol. 28, no. 26, pp. 33967–33979, Jul. 2021.

[167] M. J. Prauchner, S. da C. Oliveira, and F. Rodríguez-Reinoso, “Tailoring Low-Cost Granular Activated Carbons Intended for CO_2 Adsorption,” *Front. Chem.*, vol. 8, Nov. 2020.

[168] A. Ligero, M. Calero, A. Pérez, R. R. Solís, M. J. Muñoz-Batista, and M. Á.

Martín-Lara, “Low-cost activated carbon from the pyrolysis of post-consumer plastic waste and the application in CO_2 capture,” *Process Saf. Environ. Prot.*, vol. 173, no. March, pp. 558–566, 2023.

[169] M. Molina-Sabio and F. Rodríguez-Reinoso, “Role of chemical activation in the development of carbon porosity,” *Colloids Surfaces A Physicochem. Eng. Asp.*, vol. 241, no. 1–3, pp. 15–25, 2004.

[170] C. Quan, Y. Zhou, J. Wang, C. Wu, and N. Gao, “Biomass-based carbon materials for CO_2 capture: A review,” *J. CO_2 Util.*, vol. 68, p. 102373, Feb. 2023.

[171] S. Wang *et al.*, “Development of high-performance adsorbent using KOH-impregnated rice husk-based activated carbon for indoor CO_2 adsorption,” *Chem. Eng. J.*, vol. 437, p. 135378, Jun. 2022.

[172] H. Yuan, J. Chen, D. Li, H. Chen, and Y. Chen, “5 Ultramicropore-rich renewable porous carbon from biomass tar with excellent adsorption capacity and selectivity for CO_2 capture,” *Chem. Eng. J.*, vol. 373, pp. 171–178, Oct. 2019.

[173] L. K. C. de Souza, A. A. S. Gonçalves, L. S. Queiroz, J. S. Chaar, G. N. da Rocha Filho, and C. E. F. da Costa, “Utilization of acai stone biomass for the sustainable production of nanoporous carbon for CO_2 capture,” *Sustain. Mater. Technol.*, vol. 25, p. e00168, Sep. 2020.

[174] K. Labus, S. Gryglewicz, and J. Machnikowski, “Granular KOH-activated carbons from coal-based cokes and their CO_2 adsorption capacity,” *Fuel*, vol. 118, pp. 9–15, Feb. 2014.

[175] C. Zhang, S. Sun, S. He, and C. Wu, “Direct air capture of CO_2 by KOH-activated bamboo biochar,” *J. Energy Inst.*, vol. 105, pp. 399–405, Dec. 2022.

[176] S.-Y. Lee *et al.*, “Preparation and characterization of pitch-based nanoporous carbons for improving CO_2 capture,” *J. Solid State Chem.*, vol. 215, pp. 201–205, Jul. 2014.

[177] D. Li, T. Ma, R. Zhang, Y. Tian, and Y. Qiao, “Preparation of porous carbons with high low-pressure CO_2 uptake by KOH activation of rice husk char,” *Fuel*, vol. 139, pp. 68–70, Jan. 2015.

[178] Z.-F. Gao, B.-Q. Wang, J. Yin, and Y.-P. Zeng, “Corrosion behavior of alumina-based ceramic core materials in caustic alkali solutions,” *Int. J. Appl. Ceram. Technol.*, vol. 16, no. 1, pp. 335–345, Jan. 2019.

[179] J. J. Manyà, B. González, M. Azuara, and G. Arner, “Ultra-microporous adsorbents prepared from vine shoots-derived biochar with high CO_2 uptake and CO_2/N_2 selectivity,” *Chem. Eng. J.*, vol. 345, no. November 2017, pp. 631–639, Aug. 2018.

[180] X. Yuan *et al.*, “Solving two environmental issues simultaneously: Waste polyethylene terephthalate plastic bottle-derived microporous carbons for capturing CO_2,” *Chem. Eng. J.*, vol. 397, no. May, 2020.

[181] A. Houshmand, W. M. A. W. Daud, and M. S. Shafeeyan, “Exploring potential methods for anchoring amine groups on the surface of activated carbon for CO_2 adsorption,” *Sep. Sci. Technol.*, vol. 46, no. 7, pp. 1098–1112, Apr. 2011.

[182] T. Li *et al.*, “Covalent Grafting of Organic Molecules onto Activated Carbon by a Single Step,” *BioResources*, vol. 8, no. 2, pp. 2300–2309, Mar. 2013.

[183] M. Keramati and A. A. Ghoreyshi, “Improving CO_2 adsorption onto activated carbon through functionalization by chitosan and triethylenetetramine,” *Phys. E Low-dimensional Syst. Nanostructures*, vol. 57, pp. 161–168, Mar. 2014.

[184] A. Houshmand, M. S. Shafeeyan, A. Arami-Niya, and W. M. A. W. Daud, “Anchoring a halogenated amine on the surface of a microporous activated carbon for carbon dioxide capture,” *J. Taiwan Inst. Chem. Eng.*, vol. 44, no. 5, pp. 774–779, 2013.

[185] M. Gorbounov, J. Taylor, B. Petrovic, and S. Masoudi Soltani, “To DoE or not to DoE? A Technical Review on & Roadmap for Optimisation of Carbonaceous Adsorbents and Adsorption Processes,” *South African J. Chem. Eng.*, vol. 41, no. July, pp. 111–128, Jul. 2022.

[186] H. M. Smallwood, “Design of Experiments in Industrial Research,” *Anal. Chem.*, vol. 19, no. 12, pp. 950–952, 1947.

[187] S. Sircar, “Pressure Swing Adsorption,” *Ind. Eng. Chem. Res.*, vol. 41, no. 6, pp. 1389–1392, Mar. 2002.

[188] D. Danaci, M. Bui, C. Petit, and N. MacDowell, “En Route to Zero Emissions for Power and Industry with Amine-Based Post-combustion Capture,” *Environmental Science and Technology*, vol. 55, no. 15. 2021.

[189] A. Khuri and S. Mukhopadhyay, “Response Surface Experiments and Designs,” in *Handbook of Design and Analysis of Experiments*, 1st ed., A. Dean, M. Morris, J. Stufken, and D. Bingham, Eds. CRC Press LLC, 2015, pp. 198–235.

[190] D. Montgomery, *Design and Analysis of Experiments*, 8th ed. John Wiley & Sons, Incorporated, 2017.

[191] A. Ghasemi and S. Zahediasl, “Normality tests for statistical analysis: A guide for non-statisticians,” *Int. J. Endocrinol. Metab.*, vol. 10, no. 2, pp. 486–489, Apr. 2012.

[192] R. Davis and P. John, “Application of Taguchi-Based Design of Experiments for Industrial Chemical Processes,” *Stat. Approaches With Emphas. Des. Exp. Appl. to Chem. Process.*, 2018.

[193] G. E. P. Box and K. B. Wilson, “On the Experimental Attainment of Optimum Conditions,” *J. R. Stat. Soc. Ser. B*, 1951.

[194] A. Alaoui, K. E. L. Kacemi, K. E. L. Ass, and S. Kitane, “Application of box-behnken design to determine the optimal conditions of reductive leaching of MnO2 from manganese mine tailings,” *Trans. Indian Inst. Met.*, vol. 68, no. 5, 2015.

[195] S. L. C. Ferreira *et al.*, “Statistical designs and response surface techniques for the optimization of chromatographic systems,” *Journal of Chromatography A*, vol. 1158, no. 1–2. 2007.

[196] S. Khalili, B. Khoshandam, and M. Jahanshahi, “Optimization of production conditions for synthesis of chemically activated carbon produced from pine cone using response surface methodology for CO_2 adsorption,” *RSC Adv.*, vol. 5, no. 114, pp. 94115–94129, 2015.

[197] P. Yu *et al.*, “Activated carbon-based CO_2 uptake evaluation at different temperatures: The correlation analysis and coupling effects of the preparation conditions,” *Journal of CO_2 Utilization*, vol. 40. 2020.

[198] N. A. Rashidi and S. Yusup, “Production of palm kernel shell-based activated carbon by direct physical activation for carbon dioxide adsorption,” *Environ. Sci. Pollut. Res.*, vol. 26, no. 33, pp. 33732–33746, 2019.

[199] I. Hapazari, V. Ntuli, and W. Parawira, “Evaluation of single-step steam pyrolysis-activated carbons from Lesotho agro-forestry residues,” *Tanzania J. Sci.*, 2011.

[200] S. García, M. V. Gil, C. F. Martín, J. J. Pis, F. Rubiera, and C. Pevida, “Breakthrough adsorption study of a commercial activated carbon for pre-combustion CO_2 capture,” *Chem. Eng. J.*, vol. 171, no. 2, pp. 549–556, 2011.

[201] F. H. B. Baldovino, N. P. Dugos, S. A. Roces, A. T. Quitain, and T. Kida,

"Process optimization of carbon dioxide adsorption using nitrogen-functionalized graphene oxide via response surface methodology approach," *ASEAN J. Chem. Eng.*, vol. 17, no. 2, pp. 106–113, 2017.

[202] M. Gorbounov, E. Diaz-Vasseur, R. Panek, and S. M. Soltani, "Impact of Production Pathway on Nanoporosity of Carbonaceous Sorbents for CO_2 Adsorption," in *2023 IEEE 23rd International Conference on Nanotechnology (NANO)*, 2023, vol. 1, pp. 249–254.

[203] S. H. Tang and M. A. Ahmad Zaini, "Development of activated carbon pellets using a facile low-cost binder for effective malachite green dye removal," *J. Clean. Prod.*, vol. 253, p. 119970, 2020.

[204] A. Pal, I. I. El-Sharkawy, B. B. Saha, S. Jribi, T. Miyazaki, and S. Koyama, "Experimental investigation of CO_2 adsorption onto a carbon based consolidated composite adsorbent for adsorption cooling application," *Appl. Therm. Eng.*, vol. 109, pp. 304–311, Oct. 2016.

[205] A. Pal *et al.*, "Ionic liquid as a new binder for activated carbon based consolidated composite adsorbents," *Chem. Eng. J.*, vol. 326, pp. 980–986, 2017.

[206] N. Saeidi and M. N. Lotfollahi, "Effects of Powder Activated Carbon Particle Size on Activated Carbon Monolith's Properties," *Mater. Manuf. Process.*, vol. 31, no. 12, pp. 1634–1638, 2016.

[207] N. Saeidi and M. N. Lotfollahi, "A procedure to form powder activated carbon into activated carbon monolith," *Int. J. Adv. Manuf. Technol.*, vol. 81, no. 5–8, pp. 1281–1288, 2015.

[208] B. Pendyal, M. M. Johns, W. E. Marshall, M. Ahmedna, and R. M. Rao, "The effect of binders and agricultural by-products on physical and chemical properties of granular activated carbons," *Bioresour. Technol.*, vol. 68, no. 3, pp. 247–254, 1999.

[209] I. Skoczko and R. Guminski, "Research on the Development of Technologies for the Production of Granulated Activated Carbons Using Various Binders," *Materials (Basel).*, vol. 13, no. 22, p. 5180, Nov. 2020.

[210] L. H. Liu, Y. Lin, Y. Y. Liu, H. Zhu, and Q. He, "Effect of binders on performance of granular carbons from sewage sludge," *Zhongguo Huanjing Kexue/China Environ. Sci.*, vol. 34, no. 12, pp. 3133–3141, 2014.

[211] A. C. Deiana, D. L. Granados, L. M. Petkovic, M. F. Sardella, and H. S. Silva,

"Use of grape must as a binder to obtain activated carbon briquettes," *Brazilian J. Chem. Eng.*, vol. 21, no. 4, pp. 585–591, 2004.

[212] E. Schroeder, K. Thomauske, B. Oechsler, S. Herberger, S. Baur, and A. Hornung, "Activated Carbon from Waste Biomass," in *Progress in Biomass and Bioenergy Production*, no. August 2014, InTech, 2011.

[213] A. P. Carvalho, A. S. Mestre, J. Pires, M. L. Pinto, and M. E. Rosa, "Granular activated carbons from powdered samples using clays as binders for the adsorption of organic vapours," *Microporous Mesoporous Mater.*, vol. 93, no. 1–3, pp. 226–231, Jul. 2006.

[214] L. Liu, Y. Lin, Y. Liu, and Q. He, "Effect of Binders on Porous Properties, Surface Chemical Properties and Adsorption Characteristics of Granular Adsorbents from Sewage Sludge," *Mater. Sci.*, vol. 20, no. 4, Dec. 2014.

[215] U. B. Deshannavar, P. G. Hegde, Z. Dhalayat, V. Patil, and S. Gavas, "Production and characterization of agro-based briquettes and estimation of calorific value by regression analysis: An energy application," *Mater. Sci. Energy Technol.*, vol. 1, no. 2, pp. 175–181, Dec. 2018.

[216] E. Narooei, D. Mohebbi-Kalhori, A. Samimi, and M. Zivdar, "Preparation and characteristics' evaluation of zeolite/activated carbon composite granules, using high shear mixer granulator," *Mater. Res. Express*, vol. 6, no. 12, p. 125532, Dec. 2019.

[217] N. Ben Halima, "Poly(vinyl alcohol): review of its promising applications and insights into biodegradation," *RSC Adv.*, vol. 6, no. 46, pp. 39823–39832, 2016.

[218] M. Moniruzzaman, A. Akib, R. Shakil, S. Khatun, C. Kumar Roy, and A.-N. Chowdury, "Influence of Binder in the Fabrication of AC-Based High-Performance Electrochemical Supercapacitors," *ECS Trans.*, vol. 107, no. 1, pp. 18357–18365, Apr. 2022.

[219] A. Altwala, "Biomass-derived Activated Carbon for Energy Storage Applications," University of Nottingham, 2022.

[220] U. of Warwick, "Scanning Electron Microscopy (SEM)," 2010. [Online]. Available: https://warwick.ac.uk/fac/sci/physics/current/postgraduate/regs/mpagswarwick/ex5/techniques/structural/sem3/.

[221] J. Konopka, "Options for quantitative analysis of light elements by SEM/EDS,"

Thermo Fisher Scientific Technical Note 52523, 2013. [Online]. Available: https://assets.thermofisher.com/TFS-Assets/CAD/Warranties/TN52523_E_0713M_LightElement_H.pdf.

[222] M. Thompson, “AMC Technical Briefs,” 2008.

[223] ASTM D 7582-15, “Standard Test Methods for Proximate Analysis of Coal and Coke by Macro,” *Program*, vol. i, pp. 1–9, 2012.

[224] J. P. Simonin, “On the comparison of pseudo-first order and pseudo-second order rate laws in the modeling of adsorption kinetics,” *Chem. Eng. J.*, vol. 300, pp. 254–263, 2016.

[225] Y. Zheng, “Evaluation of a New Method to Estimate the Micropore Volume and External Surface Area of Single-walled Carbon Nanotubes,” The University of Tennessee, 2008.

[226] ASTM International, “ASTM Standard D6556 − 14 Standard Test Method for Carbon Black - Total and External Surface Area by Nitrogen Adsorption,” 2012.

[227] L. Desmurs *et al.*, “Determination of Microporous and Mesoporous Surface Areas and Volumes of Mesoporous Zeolites by Corrected t -Plot Analysis,” *ChemNanoMat*, vol. 8, no. 4, Apr. 2022.

[228] A. Galarneau, F. Villemot, J. Rodriguez, F. Fajula, and B. Coasne, “Validity of the t-plot method to assess microporosity in hierarchical micro/mesoporous materials,” *Langmuir*, vol. 30, no. 44, pp. 13266–13274, 2014.

[229] E. P. Barrett, L. G. Joyner, and P. P. Halenda, “The Determination of Pore Volume and Area Distributions in Porous Substances. I. Computations from Nitrogen Isotherms,” *J. Am. Chem. Soc.*, vol. 73, no. 1, pp. 373–380, Jan. 1951.

[230] M. Chalaris, R. Kosheleva, and A. Mitropoulos, “Theories and Trends in Porosimetry,” *Asp. Min. Miner. Sci.*, vol. 10, no. 3, pp. 1168–1175, 2023.

[231] K. V. Kumar, S. Gadipelli, C. A. Howard, W. Kwapinski, and D. J. L. Brett, “Probing adsorbent heterogeneity using Toth isotherms,” *J. Mater. Chem. A*, vol. 9, no. 2, pp. 944–962, 2021.

[232] J. Wang and X. Guo, “Adsorption kinetic models: Physical meanings, applications, and solving methods,” *J. Hazard. Mater.*, vol. 390, no. November 2019, p. 122156, 2020.

[233] G. Calzaferri, S. H. Gallagher, and D. Brühwiler, “Multiple equilibria describe

the complete adsorption isotherms of nonporous, microporous, and mesoporous adsorbents," *Microporous Mesoporous Mater.*, vol. 330, p. 111563, Jan. 2022.

[234] A. Hossain, H. H. Ngo, and W. Guo, "Introductory of Microsoft Excel SOLVER Function - Spreadsheet Method for Isotherm and Kinetics Modelling of Metals Biosorption in Water and Wastewater," *J. water Sustain.*, vol. 3, no. 4, pp. 223–237, 2013.

[235] J. Zhang *et al.*, "Carboxylic functionalized mesoporous polymers for fast, highly efficient, selective and reversible adsorption of ammonia," *Chem. Eng. J.*, vol. 448, p. 137640, Nov. 2022.

[236] K. Vijayaraghavan, T. Padmesh, K. Palanivelu, and M. Velan, "Biosorption of nickel(II) ions onto Sargassum wightii: Application of two-parameter and three-parameter isotherm models," *J. Hazard. Mater.*, vol. 133, no. 1–3, pp. 304–308, May 2006.

[237] S. Masoudi Soltani, S. Kazemi Yazdi, S. Hosseini, and I. Bayestie, "Lead removal from aqueous solution using non-modified and nitric acid-modified charred carbon from the pyrolysis of used cigarette filters," *Desalin. Water Treat.*, vol. 53, no. 1, pp. 126–138, Jan. 2015.

[238] M. Mozaffari Majd, V. Kordzadeh-Kermani, V. Ghalandari, A. Askari, and M. Sillanpää, "Adsorption isotherm models: A comprehensive and systematic review (2010−2020)," *Sci. Total Environ.*, vol. 812, no. xxxx, 2022.

[239] N. Ayawei, A. N. Ebelegi, and D. Wankasi, "Modelling and Interpretation of Adsorption Isotherms," *J. Chem.*, vol. 2017, 2017.

[240] R. Chen, J. Liu, and X. Dai, "Adsorption equilibrium of ammonia and water on porous adsorbents at low pressure: Machine learning-based models," *J. Clean. Prod.*, p. 134351, Sep. 2022.

[241] J. López-Luna *et al.*, "Linear and nonlinear kinetic and isotherm adsorption models for arsenic removal by manganese ferrite nanoparticles," *SN Appl. Sci.*, vol. 1, no. 8, pp. 1–19, 2019.

[242] W. Mozgawa, M. Król, J. Dyczek, and J. Deja, "Investigation of the coal fly ashes using IR spectroscopy," *Spectrochim. Acta - Part A Mol. Biomol. Spectrosc.*, vol. 132, pp. 889–894, 2014.

[243] M. Niinipuu, "Tailoring residue-derived carbon materials for the removal of wastewater contaminants," Umeå University, 2019.

[244] T. Somanathan, K. Prasad, K. K. Ostrikov, A. Saravanan, and V. M. Krishna, “Graphene oxide synthesis from agro waste,” *Nanomaterials*, vol. 5, no. 2, pp. 826–834, 2015.

[245] S. Potgieter-Vermaak, N. Maledi, N. Wagner, J. H. P. Van Heerden, R. Van Grieken, and J. H. Potgieter, “Raman spectroscopy for the analysis of coal: a review,” *J. Raman Spectrosc.*, vol. 42, no. 2, pp. 123–129, Feb. 2011.

[246] Edinburgh Instruments, “What is Raman Spectroscopy,” 2023. [Online]. Available: https://www.edinst.com/blog/what-is-raman-spectroscopy/. [Accessed: 15-Jun-2023].

[247] University of Toronto (TRACES Centre), “Understanding Raman Spectroscopy. Principles and Theory,” 2021.

[248] M. Gorbounov, B. Petrovic, A. Lahiri, and S. M. Soltani, “Application of Nanoporous Carbon, Extracted from Biomass Combustion Ash, in CO_2 Adsorption,” in *2021 IEEE 21st International Conference on Nanotechnology (NANO)*, 2021, vol. 2021-July, pp. 229–232.

[249] BEIS, “Energy Trends UK, October to December 2020,” 2021.

[250] ASTM, “ASTM D3172-13, Standard Practice for Proximate Analysis of Coal and Coke,” 2013. [Online]. Available: https://www.astm.org/Standards/D3172.htm.

[251] A. L. Yaumi, M. Z. A. Bakar, and B. H. Hameed, “Melamine-nitrogenated mesoporous activated carbon derived from rice husk for carbon dioxide adsorption in fixed-bed,” *Energy*, vol. 155, pp. 46–55, 2018.

[252] L. D. M. Torquato, P. M. Crnkovic, C. A. Ribeiro, and M. S. Crespi, “New approach for proximate analysis by thermogravimetry using CO_2 atmosphere: Validation and application to different biomasses,” *J. Therm. Anal. Calorim.*, vol. 128, no. 1, pp. 1–14, 2017.

[253] S. Masoudi Soltani, S. K. Yazdi, and S. Hosseini, “Effects of pyrolysis conditions on the porous structure construction of mesoporous charred carbon from used cigarette filters,” *Appl. Nanosci.*, vol. 4, no. 5, pp. 551–569, 2014.

[254] S. Masoudi Soltani, S. K. Yazdi, S. Hosseini, and M. K. Gargari, “Effect of nitric acid modification on porous characteristics of mesoporous char synthesized from the pyrolysis of used cigarette filters,” *J. Environ. Chem. Eng.*, vol. 2, no. 3, pp. 1301–1308, 2014.

[255] N. A. Rashidi, S. Yusup, M. M. Ahmad, N. M. Mohamed, and B. H. Hameed,

"Activated Carbon from the Renewable Agricultural Residues Using Single Step Physical Activation: A Preliminary Analysis," *APCBEE Procedia*, vol. 3, pp. 84–92, 2012.

[256] D. Mainganye, T. Ojumu, and L. Petrik, "Synthesis of Zeolites Na-P1 from South African Coal Fly Ash: Effect of Impeller Design and Agitation," *Materials (Basel).*, vol. 6, no. 5, pp. 2074–2089, May 2013.

[257] P. Chindaprasirt and U. Rattanasak, "Characterization of porous alkali-activated fly ash composite as a solid absorbent," *Int. J. Greenh. Gas Control*, vol. 85, no. April, pp. 30–35, 2019.

[258] M. Assad Munawar *et al.*, "Biomass ash characterization, fusion analysis and its application in catalytic decomposition of methane," *Fuel*, vol. 285, no. July 2020, p. 119107, 2021.

[259] P. Raizada, P. Shandilya, P. Singh, and P. Thakur, " Solar light-facilitated oxytetracycline removal from the aqueous phase utilizing a H 2 O 2 /ZnWO 4 /CaO catalytic system ," *J. Taibah Univ. Sci.*, vol. 11, no. 5, pp. 689–699, 2017.

[260] M. Gómez *et al.*, "Development of mesoporous materials from biomass ash with future applications as adsorbent materials," *Microporous Mesoporous Mater.*, vol. 299, no. January, 2020.

[261] V. H. Pham *et al.*, "Chemical functionalization of graphene sheets by solvothermal reduction of a graphene oxide suspension in N-methyl-2-pyrrolidone," *J. Mater. Chem.*, vol. 21, no. 10, pp. 3371–3377, 2011.

[262] Sudesh, N. Kumar, S. Das, C. Bernhard, and G. D. Varma, "Effect of graphene oxide doping on superconducting properties of bulk MgB2," *Supercond. Sci. Technol.*, vol. 26, no. 9, 2013.

[263] M. Gorbounov, B. Petrovic, S. Ozmen, P. Clough, and S. Masoudi Soltani, "Activated carbon derived from Biomass combustion bottom ash as solid sorbent for CO_2 adsorption," *Chem. Eng. Res. Des.*, vol. 194, pp. 325–343, Jun. 2023.

[264] M. R. Derrick, D. Stulik, and J. M. Landry, *Infrared Spectroscopy in Conservation Science*. Los Angeles, 1999.

[265] A. Nuhnen and C. Janiak, "A practical guide to calculate the isosteric heat/enthalpy of adsorption via adsorption isotherms in metal–organic frameworks, MOFs," *Dalt. Trans.*, vol. 49, no. 30, pp. 10295–10307, 2020.

[266] K. N. Son, G. E. Cmarik, J. C. Knox, J. A. Weibel, and S. V. Garimella,

"Measurement and Prediction of the Heat of Adsorption and Equilibrium Concentration of CO_2 on Zeolite 13X," *J. Chem. Eng. Data*, vol. 63, no. 5, pp. 1663–1674, May 2018.

[267] E. Maruccia *et al.*, "Revealing the competitive effect of N_2 and H_2O towards CO_2 adsorption in N-rich ordered mesoporous carbons," *Mater. Today Sustain.*, vol. 21, p. 100270, Mar. 2023.

[268] C. E. Wilmer, O. K. Farha, Y. S. Bae, J. T. Hupp, and R. Q. Snurr, "Structure-property relationships of porous materials for carbon dioxide separation and capture," *Energy Environ. Sci.*, vol. 5, no. 12, pp. 9849–9856, 2012.

[269] T. Boublík and K. Aim, "Heats of vaporization of simple non-spherical molecule compounds," *Collect. Czechoslov. Chem. Commun.*, vol. 37, no. 11, pp. 3513–3521, 1972.

[270] R. M. Stephenson and S. Malanowski, *Handbook of the Thermodynamics of Organic Compounds*. Dordrecht: Springer Netherlands, 1987.

[271] S. Keskin, T. M. van Heest, and D. S. Sholl, "Can Metal–Organic Framework Materials Play a Useful Role in Large-Scale Carbon Dioxide Separations?," *ChemSusChem*, vol. 3, no. 8, pp. 879–891, Aug. 2010.

[272] T. Fischer *et al.*, "Post-treatment strategies for pyrophoric KOH-activated carbon nanofibres," *RSC Adv.*, vol. 14, no. 6, pp. 3845–3856, 2024.

[273] J. H. Taylor and S. Masoudi Soltani, "Carbonaceous adsorbents in the removal of aquaculture pollutants: A technical review of methods and mechanisms," *Ecotoxicol. Environ. Saf.*, vol. 266, no. September, p. 115552, Nov. 2023.

[274] A. Linares-Solano, M. A. Lillo-Ródenas, J. P. Marco-Lozar, M. Kunowsky, and A. J. Romero-Anaya, "NaOH and KOH for preparing activated carbons used in energy and environmental applications," *Res. Appl. Energy, Environ. Econ.*, vol. 20, no. 4, pp. 59–92, 2014.

[275] R. Wang, S. C. Xi, D. Y. Wang, M. Dou, and B. Dong, "Defluorinated Porous Carbon Nanomaterials for CO_2 Capture," *ACS Appl. Nano Mater.*, vol. 4, no. 10, pp. 10148–10154, 2021.

[276] M. . Lillo-Ródenas, D. Cazorla-Amorós, and A. Linares-Solano, "Understanding chemical reactions between carbons and NaOH and KOH: An insight into the chemical activation mechanism," *Carbon N. Y.*, vol. 41, no. 2, pp. 267–275, Feb. 2003.

[277] Z. Heidarinejad, M. H. Dehghani, M. Heidari, G. Javedan, I. Ali, and M.

Sillanpää, “Methods for preparation and activation of activated carbon: a review,” *Environ. Chem. Lett.*, vol. 18, no. 2, pp. 393–415, Mar. 2020.

[278] G. E. Harimisa, N. W. C. Jusoh, L. S. Tan, K. Shameli, N. A. Ghafar, and A. Masudi, “Synthesis of potassium hydroxide-treated activated carbon via one-step activation method,” *J. Phys. Conf. Ser.*, vol. 2259, no. 1, p. 012009, Apr. 2022.

[279] K. Jedynak and B. Charmas, “Adsorption properties of biochars obtained by KOH activation,” *Adsorption*, vol. 2023, no. June, Jul. 2023.

[280] E. Raymundo-Piñero, P. Azaïs, T. Cacciaguerra, D. Cazorla-Amorós, A. Linares-Solano, and F. Béguin, “KOH and NaOH activation mechanisms of multiwalled carbon nanotubes with different structural organisation,” *Carbon N. Y.*, vol. 43, no. 4, pp. 786–795, 2005.

[281] T. Otowa, R. Tanibata, and M. Itoh, “Production and adsorption characteristics of MAXSORB: High-surface-area active carbon,” *Gas Sep. Purif.*, vol. 7, no. 4, pp. 241–245, Jan. 1993.

[282] J. Liu *et al.*, “Spherical potassium intercalated activated carbon beads for pulverised fuel CO_2 post-combustion capture,” *Carbon N. Y.*, vol. 94, pp. 243–255, Nov. 2015.

[283] B. Sajjadi, T. Zubatiuk, D. Leszczynska, J. Leszczynski, and W. Y. Chen, “Chemical activation of biochar for energy and environmental applications: A comprehensive review,” *Reviews in Chemical Engineering*, vol. 35, no. 7. pp. 777–815, 2019.

[284] T. P. Kaloni, M. Upadhyay Kahaly, Y. C. Cheng, and U. Schwingenschlögl, “K-intercalated carbon systems: Effects of dimensionality and substrate,” *EPL (Europhysics Lett.*, vol. 98, no. 6, p. 67003, Jun. 2012.

[285] Merck, “IR Spectrum Table & Chart,” 2023. [Online]. Available: https://www.sigmaaldrich.com/GB/en/technical-documents/technical-article/analytical-chemistry/photometry-and-reflectometry/ir-spectrum-table. [Accessed: 13-Jun-2023].

[286] N. E. Williams, O. A. Oba, and N. P. Aydinlik, “Modification, Production, and Methods of KOH-Activated Carbon,” *ChemBioEng Rev.*, vol. 9, no. 2, pp. 164–189, 2022.

[287] M. S. Shafeeyan, W. M. A. W. Daud, A. Houshmand, and A. Shamiri, “A review on surface modification of activated carbon for carbon dioxide

adsorption," *J. Anal. Appl. Pyrolysis*, vol. 89, no. 2, pp. 143–151, 2010.

[288] "Map: Organic Chemistry (Wade), Infrared Spectra of Some Common Functional Groups," *LibreTexts*, 2020. [Online]. Available: https://chem.libretexts.org/@go/page/45261.

[289] R. C. Bansal and M. Goyal, *Activated carbon adsorption*. Taylor & Francis Group, CRC Press, 2005.

[290] G. Aguilar-Armenta, M. E. Patiño-Iglesias, and R. Leyva-Ramos, "Adsorption Kinetic Behaviour of Pure CO_2, N_2 and CH_4 in Natural Clinoptilolite at Different Temperatures," *Adsorpt. Sci. Technol.*, vol. 21, no. 1, pp. 81–91, Feb. 2003.

[291] Y. Hattori, K. Kaneko, and T. Ohba, "Adsorption Properties," in *Comprehensive Inorganic Chemistry II*, Elsevier, 2013, pp. 25–44.

[292] N. A. Oladoja, "A critical review of the applicability of Avrami fractional kinetic equation in adsorption-based water treatment studies," *Desalin. Water Treat.*, vol. 57, no. 34, pp. 15813–15825, 2016.

[293] M. Songolzadeh, M. Soleimani, and M. Takht Ravanchi, "Using modified Avrami kinetic and two component isotherm equation for modeling of CO_2/N_2 adsorption over a 13X zeolite bed," *J. Nat. Gas Sci. Eng.*, vol. 27, pp. 831–841, Nov. 2015.

[294] É. C. Lima, M. A. Adebayo, and F. M. Machado, *Kinetic and equilibrium models of adsorption*, vol. 0, no. 9783319188744. 2015.

[295] J. Rojas, D. Suarez, A. Moreno, J. Silva-Agredo, and R. A. Torres-Palma, "Kinetics, Isotherms and Thermodynamic Modeling of Liquid Phase Adsorption of Crystal Violet Dye onto Shrimp-Waste in Its Raw, Pyrolyzed Material and Activated Charcoals," *Appl. Sci.*, vol. 9, no. 24, p. 5337, Dec. 2019.

[296] E. C. N. Lopes, F. S. C. dos Anjos, E. F. S. Vieira, and A. R. Cestari, "An alternative Avrami equation to evaluate kinetic parameters of the interaction of Hg(II) with thin chitosan membranes," *J. Colloid Interface Sci.*, vol. 263, no. 2, pp. 542–547, Jul. 2003.

[297] N. Sivarajasekar and R. Baskar, "Adsorption of Basic Magenta II onto H2SO4 activated immature Gossypium hirsutum seeds: Kinetics, isotherms, mass transfer, thermodynamics and process design," *Arab. J. Chem.*, vol. 12, no. 7, pp. 1322–1337, Nov. 2019.

[298] E. S. Sanz-Pérez, M. Olivares-Marín, A. Arencibia, R. Sanz, G. Calleja, and M. M. Maroto-Valer, "CO_2 adsorption performance of amino-functionalized SBA-

15 under post-combustion conditions," *Int. J. Greenh. Gas Control*, vol. 17, pp. 366–375, Sep. 2013.

[299] D. S. Dao, H. Yamada, and K. Yogo, "Enhancement of CO_2 Adsorption/Desorption Properties of Solid Sorbents Using Tetraethylenepentamine/Diethanolamine Blends," *ACS Omega*, vol. 5, no. 37, pp. 23533–23541, Sep. 2020.

[300] J. Singh, H. Bhunia, and S. Basu, "Adsorption of CO_2 on KOH activated carbon adsorbents: Effect of different mass ratios," *J. Environ. Manage.*, vol. 250, p. 109457, Nov. 2019.

[301] S. Wang *et al.*, "Development of High-Performance Adsorbent Using Koh-Impregnated Rice Husk-Based Activated Carbon for Indoor CO_2 Adsorption," *SSRN Electron. J.*, 2021.

[302] M. Gorbounov, B. Petrovic, S. Ozmen, P. Clough, D. Bekmuratova, and S. M. Soltani, "Development of Nanoporosity on a Biomass Combustion Ash-derived Carbon for CO_2 Adsorption," in *2022 IEEE 22nd International Conference on Nanotechnology (NANO)*, 2022, pp. 245–248.

[303] H. Dai, H. Zhao, S. Chen, and B. Jiang, "A Microwave-Assisted Boudouard Reaction: A Highly Effective Reduction of the Greenhouse Gas CO_2 to Useful CO Feedstock with Semi-Coke," *Molecules*, vol. 26, no. 6, p. 1507, Mar. 2021.

[304] H. Marsh and F. Rodríguez-Reinoso, "Activation Processes (Thermal or Physical)," in *Activated Carbon*, vol. 2, 2006, pp. 243–321.

[305] H. . Boehm, "Surface oxides on carbon and their analysis: a critical assessment," *Carbon N. Y.*, vol. 40, no. 2, pp. 145–149, Feb. 2002.

[306] S. S. Barton and B. H. Harrison, "Acidic surface oxide structures on carbon and graphite—I," *Carbon N. Y.*, vol. 13, no. 4, pp. 283–288, Aug. 1975.

[307] B. Sajjadi, W. Y. Chen, and N. O. Egiebor, "A comprehensive review on physical activation of biochar for energy and environmental applications," *Rev. Chem. Eng.*, vol. 35, no. 6, pp. 735–776, 2019.

[308] M. Keiluweit, P. S. Nico, M. Johnson, and M. Kleber, "Dynamic molecular structure of plant biomass-derived black carbon (biochar)," *Environ. Sci. Technol.*, vol. 44, no. 4, pp. 1247–1253, 2010.

[309] G. de la Puente, J. J. Pis, J. A. Menéndez, and P. Grange, "Thermal stability of oxygenated functions in activated carbons," *J. Anal. Appl. Pyrolysis*, vol. 43, no. 2, pp. 125–138, Oct. 1997.

[310] V. Bernal, L. Giraldo, and J. Moreno-Piraján, “Physicochemical Properties of Activated Carbon: Their Effect on the Adsorption of Pharmaceutical Compounds and Adsorbate–Adsorbent Interactions,” *C*, vol. 4, no. 4, p. 62, Nov. 2018.

[311] O. R. Harvey, B. E. Herbert, L. J. Kuo, and P. Louchouarn, “Generalized two-dimensional perturbation correlation infrared spectroscopy reveals mechanisms for the development of surface charge and recalcitrance in plant-derived biochars,” *Environ. Sci. Technol.*, vol. 46, no. 19, pp. 10641–10650, 2012.

[312] M. J. Antal and M. Grønli, “The art, science, and technology of charcoal production,” *Ind. Eng. Chem. Res.*, vol. 42, no. 8, pp. 1619–1640, 2003.

[313] S. Sam, S. P. Malinga, and N. Mabuba, “Carbon Nanodots Embedded on a Polyethersulfone Membrane for Cadmium(II) Removal from Water,” *Membranes (Basel).*, vol. 11, no. 2, p. 114, Feb. 2021.

[314] N. Álvarez-Gutiérrez, M. V. Gil, F. Rubiera, and C. Pevida, “Kinetics of CO_2 adsorption on cherry stone-based carbons in CO_2/CH_4 separations,” *Chem. Eng. J.*, vol. 307, pp. 249–257, 2017.

[315] C. Kim, H. S. Cho, S. Chang, S. J. Cho, and M. Choi, “An ethylenediamine-grafted Y zeolite: a highly regenerable carbon dioxide adsorbent via temperature swing adsorption without urea formation,” *Energy Environ. Sci.*, vol. 9, no. 5, pp. 1803–1811, 2016.

[316] J. Hao *et al.*, “Hierarchical structure N, O-co-doped porous carbon/carbon nanotube composite derived from coal for supercapacitors and CO_2 capture,” *Nanoscale Adv.*, vol. 2, no. 2, pp. 878–887, 2020.

[317] S. Himeno, T. Komatsu, and S. Fujita, “High-Pressure Adsorption Equilibria of Methane and Carbon Dioxide on Several Activated Carbons,” *J. Chem. Eng. Data*, vol. 50, no. 2, pp. 369–376, Mar. 2005.

[318] R. V. Siriwardane, M.-S. Shen, E. P. Fisher, and J. Losch, “Adsorption of CO_2 on Zeolites at Moderate Temperatures,” *Energy & Fuels*, vol. 19, no. 3, pp. 1153–1159, May 2005.

[319] A. Gutierrez-Ortega, R. Nomen, J. Sempere, J. B. Parra, M. A. Montes-Morán, and R. Gonzalez-Olmos, “A fast methodology to rank adsorbents for CO_2 capture with temperature swing adsorption,” *Chem. Eng. J.*, vol. 435, p. 134703, May 2022.

[320] G. Jaria, V. Calisto, V. I. Esteves, and M. Otero, “Overview of relevant economic and environmental aspects of waste-based activated carbons aimed at adsorptive water treatments,” *J. Clean. Prod.*, vol. 344, no. February, p. 130984, 2022.

[321] Y. Wang, T. Du, Z. Qiu, Y. Song, S. Che, and X. Fang, “CO_2 adsorption on polyethylenimine-modified ZSM-5 zeolite synthesized from rice husk ash,” *Mater. Chem. Phys.*, vol. 207, pp. 105–113, 2018.

[322] G. Selvaraju and N. K. A. Bakar, “Production of a new industrially viable green-activated carbon from Artocarpus integer fruit processing waste and evaluation of its chemical, morphological and adsorption properties,” *J. Clean. Prod.*, vol. 141, pp. 989–999, 2017.

[323] Y. Zhang, X. Song, Y. Xu, H. Shen, X. Kong, and H. Xu, “Utilization of wheat bran for producing activated carbon with high specific surface area via NaOH activation using industrial furnace,” *J. Clean. Prod.*, vol. 210, pp. 366–375, 2019.

[324] S. Banerjee, S. Mukherjee, A. LaminKa-ot, S. R. Joshi, T. Mandal, and G. Halder, “Biosorptive uptake of Fe^{2+}, Cu^{2+} and As^{5+} by activated biochar derived from Colocasia esculenta: Isotherm, kinetics, thermodynamics, and cost estimation,” *J. Adv. Res.*, vol. 7, no. 5, pp. 597–610, 2016.

[325] S. Mondal, K. Bobde, K. Aikat, and G. Halder, “Biosorptive uptake of ibuprofen by steam activated biochar derived from mung bean husk: Equilibrium, kinetics, thermodynamics, modeling and eco-toxicological studies,” *J. Environ. Manage.*, vol. 182, pp. 581–594, 2016.

[326] S. Pap, T. Šolević Knudsen, J. Radonić, S. Maletić, S. M. Igić, and M. Turk Sekulić, “Utilization of fruit processing industry waste as green activated carbon for the treatment of heavy metals and chlorophenols contaminated water,” *J. Clean. Prod.*, vol. 162, pp. 958–972, 2017.

[327] G. Selvaraju and N. K. A. Bakar, “Production of a new industrially viable green-activated carbon from Artocarpus integer fruit processing waste and evaluation of its chemical, morphological and adsorption properties,” *J. Clean. Prod.*, vol. 141, pp. 989–999, 2017.

[328] “UK Biomass Policy Statement.” Department for Business Energy & Industrial Strategy, p. 45, 2021.

[329] X. Yuan *et al.*, “ Sustainability-inspired upcycling of waste polyethylene

terephthalate plastic into porous carbon for CO_2 capture ," *Green Chem.*, vol. 24, no. 4, pp. 1494–1504, 2022.

[330] J. Y. Lai and L. H. Ngu, "Comparative laboratory cost analysis of various activated carbon activation process," *IOP Conf. Ser. Mater. Sci. Eng.*, vol. 1195, no. 1, p. 012018, 2021.

[331] T. L. Tan and G. B. Lebron, "Determination of carbon dioxide, carbon monoxide, and methane concentrations in cigarette smoke by fourier transform infrared spectroscopy," *J. Chem. Educ.*, vol. 89, no. 3, pp. 383–386, 2012.

[332] ASTM International, "ASTM Standard D6175 - 03 Standard Test Method for Radial Crush Strength of Extruded Catalyst and Catalyst," 2003.

[333] K. K. Robinson, R. L. Mieville, and H. Schroeder, "Development of Carbon Adsorption Blocks for Evaporative Loss Control," *Mega-Carbon Company*, 2003. [Online]. Available: https://citeseerx.ist.psu.edu/document?repid=rep1&type=pdf&doi=f0da35661233a31d09689063ad833c455862da57. [Accessed: 27-Jan-2023].

[334] X. Zhao *et al.*, "Design and optimization of NiMg/ceria-zirconia catalyst pellets," *Powder Technol.*, vol. 357, pp. 214–222, 2019.

[335] Z. Zhou, E. Duff, D. Kumar, and H. Weiner, "ETHANOL MANUFACTURING PROCESS OVER CATALYST HAVING IMPROVED RADAL CRUSH STRENGTH," 2016.

[336] D. Garg, R. Quinn, F. C. Wilhelm, G. Alptekin, M. Dubovik, and M. Schaefer, "HYDROGEN PRODUCTION USING COMPLEX METAL OXDE PELLETS," 2011.

[337] J. Liu *et al.*, "Structured Binder-Free Al-β Zeolite for Acid-Catalyzed Dehydration," *ACS Appl. Nano Mater.*, vol. 4, no. 11, pp. 11997–12005, Nov. 2021.

[338] W. Somyanonthanakun, R. Ahmed, V. Krongtong, and S. Thongmee, "Studies on the adsorption of Pb(II) from aqueous solutions using sugarcane bagasse-based modified activated carbon with nitric acid: Kinetic, isotherm and desorption," *Chem. Phys. Impact*, vol. 6, p. 100181, Jun. 2023.

[339] İ. Demiral, C. Samdan, and H. Demiral, "Enrichment of the surface functional groups of activated carbon by modification method," *Surfaces and Interfaces*, vol. 22, p. 100873, Feb. 2021.

[340] M. S. Shafeeyan, A. Houshmand, A. Arami-Niya, H. Razaghizadeh, and W. M.

A. W. Daud, “Modification of activated carbon using nitration followed by reduction for carbon dioxide capture,” *Bull. Korean Chem. Soc.*, vol. 36, no. 2, pp. 533–538, 2015.

[341] G. Zhang, S. Sun, D. Yang, J.-P. Dodelet, and E. Sacher, “The surface analytical characterization of carbon fibers functionalized by H2SO4/HNO3 treatment,” *Carbon N. Y.*, vol. 46, no. 2, pp. 196–205, Feb. 2008.

[342] J.-H. Kim *et al.*, “Impact of the oxygen functional group of nitric acid-treated activated carbon on KOH activation reaction,” *Carbon Lett.*, vol. 29, no. 3, pp. 281–287, Jun. 2019.

[343] J. J. Ternero-Hidalgo, J. M. Rosas, J. Palomo, M. J. Valero-Romero, J. Rodríguez-Mirasol, and T. Cordero, “Functionalization of activated carbons by HNO3 treatment: Influence of phosphorus surface groups,” *Carbon N. Y.*, vol. 101, pp. 409–419, May 2016.

[344] K. Krishnan, “Raman spectra of organic compounds,” *Proc. Indian Acad. Sci. - Sect. A*, vol. 54, no. 2, pp. 89–98, Aug. 1961.

[345] P. Maziarka *et al.*, “Tailoring of the pore structures of wood pyrolysis chars for potential use in energy storage applications,” *Appl. Energy*, vol. 286, p. 116431, Mar. 2021.

[346] W. J. Braida, J. J. Pignatello, Y. Lu, P. I. Ravikovitch, A. V. Neimark, and B. Xing, “Sorption Hysteresis of Benzene in Charcoal Particles,” *Environ. Sci. Technol.*, vol. 37, no. 2, pp. 409–417, Jan. 2003.

Appendix A: CO_2 Adsorption Isotherms

Table A.1: Virgin Carbon's (BA-100-P) CO_2 adsorption isotherms at various temperatures.

0 °C		10 °C	
P, mbara	V, cm^3_{STP}/g	P, mbara	V, cm^3_{STP}/g
0.457441	0.514962	0.657635	0.458561
1.13541	0.938539	1.566883	0.818766
1.890286	1.331883	2.55835	1.149416
2.694018	1.705653	3.603416	1.46213
3.539714	2.065913	4.683038	1.761004
4.414248	2.412354	5.791668	2.050141
5.317506	2.748772	6.928632	2.328084
6.245131	3.07529	8.079563	2.597267
7.193847	3.391349	9.25538	2.858657
8.156834	3.697857	10.40879	3.10854
9.147729	3.999155	13.46419	3.713749
10.13446	4.286558	16.583	4.290556
11.14142	4.569443	19.73987	4.829781
12.15068	4.841287	22.95805	5.346761
13.15761	5.116111	26.20825	5.839064
14.18804	5.369977	29.51288	6.310218
15.21714	5.620676	32.7925	6.759336
16.26288	5.868657	36.12197	7.193175
17.34355	6.114177	39.46517	7.604602
18.43397	6.360579	42.79978	8.00095
19.51744	6.598001	46.16443	8.383528
20.61178	6.832132	49.62864	8.76255
21.73497	7.067503	56.6495	9.489484
22.85634	7.285745	63.68751	10.1728
23.97542	7.507893	71.03283	10.83054
25.06409	7.722165	78.4042	11.45775
26.15737	7.935205	85.61813	12.04272
27.25083	8.139164	92.86708	12.59968
28.37412	8.344131	100.1041	13.13439
29.49987	8.541548	146.2583	16.00881
30.61508	8.73428	199.1577	18.62054
31.82672	8.942198	248.3026	20.61471
32.96633	9.136458	298.1688	22.34462
34.0856	9.315203	348.3076	23.87594
35.25321	9.495345	398.6606	25.24202
36.38043	9.677235	449.0675	26.47666
37.52608	9.861736	499.0104	27.58376
38.6771	10.03817	548.6363	28.59578

39.79295	10.20955	598.6775	29.55093
40.95087	10.37884	649.3217	30.43997
42.07779	10.54289	698.8301	31.25721
43.23202	10.70948	748.5657	32.02044
44.42321	10.87641	798.5077	32.75106
45.63262	11.0455	848.2806	33.42182
46.79174	11.20553	898.2247	34.06851
47.91478	11.35624	948.6242	34.68524
54.38815	12.17527	999.0742	35.28312
60.99123	12.9565		
67.48809	13.66912		
74.12961	14.3533		
80.75214	14.99404		
87.50742	15.61422		
93.9806	16.18252		
100.7851	16.75182		
145.2421	19.86921		
199.0949	22.78982		
248.6577	24.95947		
298.4067	26.78708		
348.5058	28.39423		
398.7427	29.8107		
449.0197	31.07947		
499.0874	32.22187		
549.2421	33.27096		
599.1393	34.22192		
648.613	35.10648		
699.3461	35.94505		
748.4962	36.68977		
798.477	37.40865		
848.8055	38.09453		
898.8524	38.74205		
948.4444	39.3641		
998.8549	39.96422		

20 °C		30 °C	
P, mbara	V, cm^3_{STP}/g	P, mbara	V, cm^3_{STP}/g
0.828645	0.394267	0.980338	0.334259
1.923453	0.680387	2.21272	0.560685
3.080402	0.942113	3.503662	0.764437
4.284157	1.186197	4.825303	0.95542
5.51441	1.420101	6.167344	1.137538
6.781325	1.646095	7.53447	1.313559
8.042626	1.861936	8.901288	1.484349
9.327167	2.071294	10.30876	1.651451

10.65004	2.276876	13.95608	2.060525
13.93883	2.76661	17.56042	2.436462
17.33936	3.234819	21.14513	2.784836
20.80671	3.676066	24.72698	3.116088
24.27785	4.099806	28.35653	3.442247
27.72235	4.493812	31.98099	3.749442
31.19818	4.872598	35.64342	4.054229
34.66677	5.230893	39.46645	4.364391
38.22835	5.593546	43.32125	4.656238
41.84824	5.94131	47.07098	4.928933
45.34794	6.266895	50.73043	5.20002
48.98912	6.594996	58.30419	5.70972
56.25735	7.211472	65.90576	6.198681
63.50962	7.796867	73.37942	6.653793
70.74623	8.340819	81.02494	7.100226
78.1607	8.867285	88.74823	7.523279
85.47032	9.364311	96.21866	7.930909
92.88819	9.840713	146.4284	10.26113
100.3068	10.29692	199.0824	12.25205
146.3333	12.79061	248.6162	13.85183
199.9582	15.12707	298.8277	15.26422
249.5313	16.95356	349.0295	16.52447
298.7618	18.5237	398.6332	17.65411
348.4114	19.92983	449.4474	18.72338
398.5463	21.20798	499.3386	19.68385
448.5558	22.36918	548.5481	20.55127
498.9738	23.44062	598.5909	21.37155
549.2044	24.42536	648.9487	22.14923
598.7116	25.31725	698.4156	22.85869
649.2801	26.18252	748.2324	23.54791
699.4723	26.98345	798.8351	24.18861
748.4557	27.72076	849.0568	24.81813
798.4772	28.44952	898.5965	25.39411
848.7186	29.12506	949.4212	25.98134
898.24	29.76927	998.9	26.49527
949.0594	30.39734		
998.5594	30.99544		

40 °C	
P, mbara	V, cm^3_{STP}/g
1.097704	0.287273
2.442732	0.468956
3.83691	0.631383
5.257293	0.784039
6.680701	0.929799

8.12103	1.071356
9.569694	1.208268
13.23316	1.539778
16.95679	1.844753
20.67474	2.131179
24.43248	2.418145
28.16165	2.687725
31.98104	2.940387
35.70188	3.186757
39.52567	3.427055
43.25034	3.652903
47.18705	3.886255
51.03817	4.110265
58.69864	4.536102
66.44227	4.943633
74.03443	5.334854
81.72102	5.6966
89.32432	6.055255
96.96479	6.396894
146.7916	8.3779
199.0645	10.10456
248.9942	11.51624
298.9012	12.789
348.4639	13.92368
398.9921	14.96586
448.7658	15.90367
498.4821	16.76118
549.0981	17.61155
598.7632	18.37324
648.7434	19.10721
698.6221	19.79021
748.8347	20.39856
798.423	21.01636
848.4366	21.60526
898.6324	22.16922
948.5197	22.68752
999.0079	23.22708

Table A.2: Chemically Activated Carbon's (ChAB) CO_2 adsorption isotherms at various temperatures.

0 °C		10 °C	
P, mbara	V, cm^3_{STP}/g	P, mbara	V, cm^3_{STP}/g
0.002612	0.778179	0.003808	0.787415
0.016553	1.54871	0.026519	1.558699
0.0574	2.301843	0.092233	2.306507
0.141528	3.024842	0.227649	3.00793
0.284814	3.71205	0.446368	3.675115
0.491757	4.3688	0.755226	4.288734
0.752611	4.9734	1.128201	4.860648
1.09156	5.548407	1.583606	5.386199
1.477927	6.091403	2.105987	5.875656
1.92171	6.606017	2.66969	6.331711
2.394409	7.092803	3.290669	6.762011
2.906356	7.56345	3.946232	7.168843
3.454593	8.001515	4.61641	7.554145
4.012585	8.429219	5.320274	7.919851
4.6241	8.838489	6.042202	8.273861
5.243032	9.23223	6.785313	8.611458
5.881804	9.609412	7.556612	8.940078
6.54055	9.984319	8.358546	9.264047
7.209177	10.34099	9.165613	9.568229
7.89046	10.68626	9.974943	9.867819
8.584355	11.02364	12.03819	10.54985
9.28977	11.35039	14.19339	11.20995
9.996568	11.67156	16.37494	11.83108
10.72044	11.98437	18.59396	12.43618
11.48167	12.29364	20.86369	12.99867
12.26123	12.59942	23.14334	13.54256
13.00908	12.89079	25.46429	14.07579
13.76609	13.17947	27.84175	14.59599
14.56008	13.46137	30.17923	15.08049
15.33134	13.73357	32.53815	15.55065
16.14237	14.00883	34.96235	16.02983
16.94577	14.26908	37.46804	16.49074
17.75364	14.53658	39.91614	16.94816
18.55541	14.79085	42.46189	17.3944
19.40034	15.05477	44.92555	17.82259
20.23854	15.31899	47.44243	18.2467
21.09977	15.57513	50.00023	18.66662
21.94602	15.83367	54.97438	19.43165
22.82181	16.08606	60.05938	20.18349
23.6485	16.32495	65.07189	20.89477

24.48794	16.55037	70.13213	21.59342
25.35079	16.79241	75.19771	22.2617
26.1918	17.0169	80.42347	22.92947
27.05092	17.2483	85.53724	23.55703
27.93176	17.47894	90.23565	24.12078
28.79382	17.69997	95.51456	24.74629
29.65368	17.92321	144.8647	29.73107
30.52499	18.14364	198.9278	34.29916
31.39071	18.35573	249.2207	37.99541
32.31533	18.57542	299.3836	41.28642
33.20396	18.77751	349.3878	44.31838
34.14631	18.99814	399.5956	47.1126
35.01629	19.2122	449.7006	49.73023
35.91629	19.41064	499.3801	52.15762
36.80836	19.61631	548.5204	54.42797
37.68039	19.81459	598.426	56.61936
38.59752	20.0235	648.4426	58.71385
39.48806	20.21322	698.3836	60.69
40.38781	20.4079	748.7714	62.62308
41.33026	20.6068	798.2946	64.44876
42.23149	20.80303	848.2484	66.19755
43.23219	21.01286	898.1415	67.89676
44.1562	21.20516	948.2886	69.53723
45.15814	21.4091	998.388	71.15758
46.09313	21.60052		
47.05723	21.80135		
47.95875	21.99466		
52.57	22.86451		
57.14343	23.68761		
61.67569	24.47668		
66.34425	25.26187		
70.96239	25.99925		
75.55982	26.72611		
80.32201	27.44234		
84.61719	28.06866		
89.06655	28.71225		
93.79222	29.38015		
98.1369	29.97353		
144.2281	35.50023		
199.1443	40.96275		
248.7025	45.2109		
298.7486	49.04647		
348.925	52.53955		
399.1136	55.76669		

449.3041	58.76416
499.4813	61.56321
549.4302	64.17829
598.7687	66.62489
648.8835	68.97597
699.0623	71.22273
749.1536	73.34232
798.4077	75.35418
848.5129	77.29712
898.4518	79.17032
948.4548	80.97722
998.5735	82.73081
749.1536	73.34232
798.4077	75.35418
848.5129	77.29712
898.4518	79.17032
948.4548	80.97722
998.5735	82.73081

20 °C		30 °C	
P, mbara	V, cm^3_{STP}/g	P, mbara	V, cm^3_{STP}/g
0.00534	0.782011	0.007882	0.780668
0.044979	1.541508	0.069751	1.524536
0.152794	2.257462	0.229468	2.207763
0.360175	2.917684	0.529375	2.820088
0.66925	3.525926	0.932953	3.359084
1.080902	4.074087	1.450044	3.839523
1.587672	4.571324	2.041163	4.279923
2.156379	5.029752	2.708179	4.668527
2.790854	5.442807	3.411501	5.037161
3.454906	5.837823	4.178531	5.368182
4.157174	6.206478	4.960542	5.677188
4.90122	6.545693	5.756797	5.978495
5.68223	6.866804	6.57571	6.262488
6.493388	7.177602	7.460899	6.527054
7.294955	7.477445	8.336546	6.779365
8.120903	7.756411	9.243477	7.017127
8.951324	8.027482	10.1306	7.245734
9.800159	8.289003	12.4586	7.796293
11.99679	8.899464	14.84581	8.297549
14.25766	9.477796	17.31215	8.766215
16.5685	10.01538	19.77284	9.219548
18.94004	10.53305	22.30101	9.641455
21.31029	11.02994	24.84899	10.03353
23.77323	11.50601	27.3816	10.42879

26.21054	11.96	29.9463	10.79769
28.74067	12.41375	32.55747	11.1579
31.31016	12.83932	35.14484	11.49347
33.80806	13.24842	37.76414	11.83804
36.37241	13.65094	40.42773	12.17675
38.98486	14.04368	43.13084	12.50705
41.54265	14.41802	45.77293	12.81259
44.18099	14.79683	48.39715	13.13536
46.73356	15.16229	53.65099	13.69971
49.347	15.51385	59.08639	14.25935
54.49651	16.17702	64.49658	14.81401
59.65417	16.81533	69.84867	15.33189
65.02287	17.45833	75.16159	15.82023
70.3333	18.05315	80.72934	16.32956
75.60393	18.62746	86.09474	16.79642
80.82644	19.18095	91.13672	17.22407
86.08089	19.71834	96.24899	17.63717
90.95049	20.20486	145.7977	21.18295
96.25488	20.7206	199.596	24.43611
145.3898	24.8904	249.323	27.09681
198.9953	28.73027	299.4267	29.5321
249.4985	31.89462	349.3382	31.76973
299.7547	34.74144	398.5378	33.82279
349.5081	37.33541	448.7542	35.77802
398.8544	39.72377	498.8754	37.63791
448.7476	41.98362	549.0231	39.40186
498.9618	44.12863	598.3435	41.00603
549.1683	46.16079	648.3244	42.59304
599.2074	48.07935	698.4271	44.13836
649.0167	49.91103	748.8673	45.59932
698.2139	51.63924	798.3605	46.98843
749.3823	53.36466	848.5024	48.33551
798.4752	54.9599	898.22	49.67461
848.6566	56.50558	948.7307	50.99506
898.4965	57.98799	999.3046	52.258
948.4139	59.4502		
999.1759	60.87966		

40 °C	
P, mbara	V, cm^3_{STP}/g
0.012197	0.775035
0.104412	1.497816
0.34233	2.139053
0.723774	2.696212
1.230598	3.181699

1.823046	3.609195
2.506797	3.98559
3.226997	4.333006
4.007884	4.640792
4.820953	4.927109
5.665601	5.198274
6.559257	5.449231
7.450748	5.687375
8.389463	5.915164
9.30305	6.138341
10.25192	6.352982
12.61638	6.830408
15.0869	7.250783
17.57408	7.646403
20.07558	8.033436
22.63196	8.398146
25.16834	8.748933
27.73618	9.088938
30.32979	9.408653
32.99404	9.719673
35.64058	10.02121
38.30755	10.33036
40.96926	10.60787
43.64486	10.86982
46.3349	11.14708
49.03924	11.41957
54.4371	11.92297
59.98344	12.41255
65.4583	12.8924
70.93049	13.33293
76.50386	13.77712
81.9265	14.19668
87.41143	14.59398
92.55553	14.96231
97.96782	15.35246
146.9753	18.37861
199.3831	21.12803
249.3336	23.45299
298.589	25.52673
348.6114	27.5018
398.653	29.34279
448.9125	31.08377
499.2519	32.68374
549.1358	34.22995

598.5318	35.71495
648.6494	37.10859
698.8323	38.4581
748.3956	39.7197
798.674	40.99407
848.9913	42.18055
898.3207	43.32693
948.7413	44.45299
998.7156	45.54987

Table A.3: Physically Activated Carbon's (AC-Opt) CO_2 adsorption isotherms at various temperatures.

0 °C		10 °C	
P, mbara	V, cm^3_{STP}/g	P, mbara	V, cm^3_{STP}/g
0.339034	0.653044	0.499792	0.600214
0.961043	1.1858	1.342066	1.065811
1.661521	1.684212	2.279952	1.492588
2.419926	2.160706	3.281529	1.89707
3.226567	2.620686	4.324788	2.282096
4.067793	3.065968	5.396001	2.654163
4.934016	3.49542	6.499548	3.013036
5.828172	3.910511	7.617657	3.358992
6.74608	4.315443	8.770221	3.699563
7.686557	4.708602	9.910627	4.023668
8.641201	5.092819	12.92288	4.79406
9.612308	5.465677	16.00025	5.533243
10.58657	5.833844	19.14493	6.238001
11.56661	6.189596	22.31473	6.9056
12.57603	6.525974	25.56218	7.55002
13.60177	6.861775	28.86838	8.166863
14.61648	7.190605	32.22988	8.751267
15.64226	7.503822	35.6	9.312855
16.68103	7.816611	38.96387	9.852476
17.74482	8.122833	42.42653	10.38429
18.81852	8.430296	45.82732	10.88436
19.9052	8.727725	49.27834	11.36949
20.98113	9.015641	56.60138	12.3332
22.07656	9.307587	63.91088	13.23817
23.17684	9.583257	71.39979	14.10104
24.26794	9.85366	79.03355	14.92115
25.38165	10.12843	86.5441	15.68498
26.48901	10.39283	93.9928	16.41084
27.60396	10.65509	101.5236	17.09956
28.79221	10.92966	144.6693	20.49803
29.92238	11.18139	199.4989	23.90123
31.09023	11.44202	248.2711	26.36685
32.21713	11.68735	297.947	28.50908
33.3447	11.93258	348.9259	30.44367
34.55619	12.17711	398.6449	32.10057
35.71701	12.4158	448.303	33.58945
36.88363	12.64793	498.6186	34.94588
38.00699	12.87198	548.0526	36.16073
39.14779	13.09153	598.3153	37.30449
40.33477	13.3199	649.0005	38.37148

41.5417	13.55004	698.8956	39.34879
42.73842	13.76371	748.3771	40.24934
43.86653	13.96808	798.1632	41.10177
45.07147	14.18607	848.2823	41.9051
46.29495	14.40131	898.7987	42.66355
47.43919	14.59778	948.0194	43.37771
48.82575	14.83428	999.3158	44.07531
55.22668	15.8575		
61.69704	16.81746		
68.30888	17.73008		
74.93089	18.58555		
81.66212	19.40607		
88.28819	20.17059		
95.23051	20.93109		
144.2001	25.35067		
199.2857	29.08811		
248.3025	31.74187		
298.3275	34.00705		
348.5502	35.9775		
398.4573	37.68494		
448.7248	39.20307		
498.4302	40.54503		
548.5062	41.76564		
598.5276	42.88086		
648.6557	43.9073		
698.8857	44.84941		
748.6951	45.72279		
798.9333	46.52828		
848.8486	47.28444		
898.6459	47.99698		
948.8895	48.67387		
998.6714	49.32272		

20 °C		30 °C	
P, mbara	V, cm^3_{STP}/g	P, mbara	V, cm^3_{STP}/g
0.651749	0.538051	0.782429	0.484229
1.688339	0.919828	1.985663	0.791477
2.828873	1.261235	3.25711	1.070725
4.01242	1.583909	4.581744	1.32749
5.223196	1.893533	5.918674	1.573014
6.468048	2.188625	7.293334	1.81117
7.724536	2.475288	8.668962	2.039271
9.01244	2.752693	10.055	2.259596
10.33419	3.023059	13.64509	2.78511
13.68286	3.670829	17.32711	3.289908

17.09632	4.283546	20.96064	3.750849
20.67703	4.875783	24.65135	4.195435
24.30583	5.441595	28.36068	4.629033
27.98752	5.9849	32.10893	5.039851
31.49735	6.473197	35.81582	5.436298
35.20751	6.972293	39.58108	5.821548
39.02845	7.463377	43.46218	6.211223
42.82173	7.937597	47.25846	6.571792
46.74566	8.399358	51.38123	6.945272
50.46789	8.821153	59.39476	7.649911
57.92406	9.620709	67.18036	8.290345
65.90536	10.42122	75.19059	8.919384
73.51507	11.14258	83.24205	9.518015
81.69438	11.87891	91.19258	10.08568
89.26713	12.52578	99.08286	10.62095
97.09662	13.1631	145.5881	13.38171
144.8356	16.4848	199.3321	15.98635
199.337	19.51947	250.2812	18.09065
250.5337	21.88618	300.7069	19.88858
300.7011	23.88346	350.633	21.46661
351.2227	25.65779	401.0848	22.9104
400.7184	27.20884	451.4743	24.22603
450.927	28.62605	500.8365	25.38295
501.2651	29.93029	550.699	26.49026
550.5562	31.09085	600.6977	27.48573
600.3808	32.1752	650.3585	28.40861
650.0978	33.18723	700.5821	29.28299
700.1862	34.13583	750.7979	30.10336
750.5987	35.02471	801.0987	30.85764
801.0973	35.85691	850.9037	31.5837
851.1823	36.64229	900.8438	32.32668
901.1657	37.38584	948.6633	32.95507
949.078	38.04894	998.4292	33.57207
998.6178	38.72844		

40 °C	
P, mbara	V, cm^3_{STP}/g
0.909894	0.429582
2.226482	0.68204
3.616486	0.903616
5.039454	1.108912
6.477289	1.308938
7.979901	1.506908
9.496237	1.693038
10.94543	1.870829

14.787	2.303141
18.70534	2.70391
22.60919	3.091272
26.5832	3.471873
30.41807	3.815628
34.50767	4.161378
38.44029	4.497806
42.57545	4.826302
46.5699	5.140059
50.39513	5.42577
58.51354	6.01418
66.81073	6.578106
74.78465	7.10185
82.87995	7.608812
90.87588	8.083304
99.04453	8.558682
147.4209	11.02514
200.5138	13.26207
250.2144	15.06834
298.5472	16.6053
348.8248	18.08715
400.8583	19.45312
448.3318	20.59934
500.9198	21.76946
548.7523	22.7455
598.8238	23.7162
650.7955	24.67728
698.8836	25.47694
751.0533	26.286
801.3114	27.02933
850.7881	27.72071
899.253	28.36219
948.6244	29.00121
998.5278	29.61574

Table A.4: Chemically Modified Activated Carbon's (AC-Mod) CO_2 adsorption isotherms at various temperatures.

0 °C		10 °C	
P, mbara	V, cm^3_{STP}/g	P, mbara	V, cm^3_{STP}/g
3.7843574	3.83923168	0.6530179	0.373392275
9.115485	6.999996903	1.5818027	0.968010217
15.289629	9.783655847	2.6456212	1.587589003
22.187788	12.24670104	3.7688644	2.179999778
30.288924	14.56201416	4.9429068	2.750207566
38.640417	16.50157892	6.1612557	3.300933431
60.650062	20.66028904	7.5733988	3.807068783
87.204348	24.3348686	8.3784808	4.066111294
112.6183	27.02242277	9.0948149	4.443644715
138.11253	29.253074	9.7046512	4.643130496
164.401	31.20165616	10.274885	4.977198062
190.35194	32.89343662	11.392699	5.115514253
216.2482	34.49555176	12.114066	5.540672907
242.47984	35.90985775	12.929349	5.824468054
268.18568	37.12141612	13.474413	6.134103611
293.96032	38.24020038	14.234988	6.336717625
320.79967	39.25993948	14.789989	6.497505702
346.47657	40.17715187	16.08278	6.673726224
372.39356	40.98904917	16.874348	6.859192106
398.24943	41.82999605	18.170452	7.033282606
424.35598	42.62159783	18.856188	7.162705114
450.05293	43.44478532	19.220182	7.333955467
476.51056	44.21340198	20.157723	7.582155057
502.02084	44.91437088	20.87154	7.877242397
528.01643	45.61442509	21.681255	8.107947061
554.1351	46.22273726	22.523687	8.382943239
579.68974	46.84441408	23.331686	8.702600614
605.71055	47.38306241	24.250677	8.872032076
631.3748	48.0586795	25.053903	9.115795123
657.71525	48.66849109	25.87912	9.281043649
683.56518	49.11845472	26.717051	9.492002481
728.89108	49.99357217	27.644658	9.634820407
735.22315	50.06978077	28.461522	9.873586692
780.91148	50.82919214	29.358006	10.08019541
787.14549	50.94153327	30.219777	10.1799075
812.69597	51.36610867	31.078105	10.22472605
838.69783	51.8261588	31.959741	10.44123388
864.52563	52.23934792	32.896752	10.64012379
910.75315	52.82842955	33.753763	10.85269441
936.71806	53.24994175	35.08589	11.03568007

942.51981	53.39270948	35.888457	11.20556143
968.73943	53.68311784	36.713406	11.42107172
1014.3095	54.25931799	37.380464	11.62468623
1040.2197	54.58726649	38.32754	11.82176797
1066.0896	55.04717274	39.224815	12.02975887
		39.711732	12.12970889
		40.173745	12.26222521
		41.176981	12.31808549
		42.396123	12.47888167
		43.254451	12.70890574
		44.085628	12.86710959
		44.623541	12.99960975
		45.579754	13.07265618
		85.052167	18.31894059
		115.03605	21.33096968
		144.74551	23.6566845
		178.16896	25.87780063
		211.92142	27.84151723
		245.48406	29.53687656
		279.24649	31.14449874
		312.33289	32.50595975
		346.32839	33.83034592
		379.27114	34.95529442
		413.12052	36.09932609
		447.1894	37.04901032
		479.97568	38.02070309
		513.7661	39.03768818
		547.28063	39.79347033
		600.39741	41.08503028
		614.3528	41.34753301
		667.49677	42.42375681
		700.91047	43.09446824
		734.4741	43.7230734
		768.03383	44.46492973
		781.35928	44.72030295
		835.26282	45.62246647
		868.6773	46.15370534
		901.99225	46.72092992
		935.30428	47.23600798
		968.86328	47.74846861
		1002.2965	48.19258039
		1035.7881	48.70246288
		1069.1623	49.21437393
		1102.8628	49.59466631

1136.4246	50.03159684
1169.8815	50.40181721
1190.5298	50.82485949
1215.858	51.1175666

20 °C		30 °C	
P, mbara	V, cm^3_{STP}/g	P, mbara	V, cm^3_{STP}/g
1.2559942	0.604334225	1.6844845	0.448950287
2.6067392	1.16931177	3.4316544	0.865812105
4.0251337	1.709066898	5.2269854	1.263186641
5.5001097	2.226536058	8.0114611	1.900431965
7.5934071	2.90111246	9.4723412	2.205991851
8.8242074	3.295520428	10.836664	2.524565832
9.8891727	3.612743396	12.491989	2.732589977
11.185278	3.992791821	13.821738	3.067287578
12.276862	4.283249725	15.264208	3.249416251
13.365404	4.579933783	16.66363	3.448902123
14.491829	4.840378959	18.139612	3.644720562
15.615738	5.115560191	19.703411	3.925041204
16.946944	5.4270859	21.061371	4.115527482
18.076413	5.693384207	22.465035	4.29847572
19.206281	5.944891996	24.459453	4.471501014
20.353104	6.19199672	26.089226	4.848337503
21.510785	6.432613111	27.432213	5.078120134
22.653373	6.674117881	28.890839	5.310294674
23.805494	6.908133594	30.274106	5.582418162
24.975098	7.133524995	32.2023	5.740191222
26.133844	7.362946684	33.873527	6.004965358
27.28226	7.595505831	35.415736	6.19809559
28.441794	7.820427482	37.085898	6.368376281
29.789556	8.060720132	38.789707	6.554828167
30.97069	8.271385625	40.419611	6.783210738
32.1297	8.487553026	42.055471	6.984045466
33.334134	8.685759432	43.84484	7.122565112
34.513416	8.886411548	45.592631	7.336173213
35.696795	9.094110267	47.383993	7.576199226
36.880845	9.283148371	49.167151	7.768179084
38.072963	9.476753667	50.719555	7.913141012
39.281642	9.651765774	52.445218	8.153832047
40.488733	9.847818495	54.323883	8.311179576
41.689734	10.0368343	55.804628	8.513416996
42.731516	10.35069385	57.441554	8.725310328
44.100596	10.5105589	75.940922	10.26557347
45.308491	10.63532787	94.965875	11.6728966
46.477032	10.74039336	115.28788	12.98259257

47.777245	10.9314732	133.84037	14.11743931
48.930299	11.13555338	153.43743	15.16805205
50.172625	11.29678942	172.04173	16.12185315
51.328716	11.48939038	191.60631	17.05346653
52.52057	11.61119025	210.44492	17.91112865
53.841447	11.70057702	229.65652	18.71149721
55.088406	11.83730059	248.58426	19.43741514
56.794733	12.09648341	267.62089	20.14924039
58.13044	12.22408728	286.29089	20.83681316
80.269513	14.68025163	305.03923	21.5714783
108.43542	17.14234255	324.66326	22.20663118
132.08316	18.97319438	364.35509	23.34107546
157.51119	20.75030787	402.52983	24.39618014
182.62258	22.21131335	440.92545	25.33845548
207.2712	23.55240731	479.00034	26.26459339
232.47005	24.7399869	517.2453	27.23251017
257.23989	25.91771053	555.40388	28.11338225
282.46122	26.9154961	593.71332	28.93206547
306.91473	27.84164159	631.93367	29.69227561
332.37826	28.78170481	670.21427	30.30833565
357.21178	29.60619116	708.32032	30.94722026
401.5127	30.94762003	746.81583	31.54006887
426.34966	31.66242827	784.97136	32.25947333
452.25021	32.46401074	823.16171	32.98851307
457.1023	32.65361145		
482.29404	33.34133012		
527.44589	34.4308898		
552.38363	35.02716102		
577.20594	35.66554616		
602.21549	36.25463062		
627.27016	36.74187827		
652.21824	37.22579021		
677.3553	37.72168921		
701.89395	38.25448213		
726.98443	38.81470904		
752.12405	39.21921371		
776.98937	39.73490582		
801.94802	40.15531434		
826.85533	40.57266175		
852.08723	40.90756993		
876.63951	41.30810602		
901.65561	41.78181829		
926.85757	42.17361054		
951.88043	42.58372092		

976.76031	42.96603099
1001.4736	43.24046821
1026.8654	43.57220115
1051.625	43.81668502

40 °C	
P, mbara	V, cm^3_{STP}/g
1.9633303	0.313163056
3.9601332	0.617245346
5.9927513	0.911944239
8.6292777	1.216396561
10.436006	1.496563877
12.261544	1.805011944
13.930781	2.017195465
15.427696	2.18694475
28.597613	3.840490091
45.34192	5.574333512
59.508054	6.81966014
73.97593	8.00674464
89.151927	9.013793857
102.90109	9.927056502
117.99099	10.85587069
132.69809	11.66471821
147.10463	12.37586297
162.07612	13.12926696
176.33802	13.80024844
191.03361	14.52169738
206.73947	15.30244398
221.71079	15.8291355
235.31807	16.46101917
250.1204	17.03703101
264.38587	17.49683993
278.83785	17.97540279
294.58797	18.59415446
309.35495	19.11264818
323.93328	19.59445167
338.5939	20.04830168
353.09218	20.47868575
366.90216	21.03577718
381.8567	21.53371065
397.36515	21.99061879
412.0446	22.30166341
426.36289	22.70324127
440.54438	23.01024593
455.91697	23.36331586

470.66857	23.87086601
485.59259	24.46817412
500.32388	24.85307425
514.50989	25.18053928
529.41134	25.50217131
544.1954	25.80229154
558.9142	26.1129655
573.68028	26.44570583
588.21607	26.91168959
603.06975	27.29700857
617.57856	27.63493718
632.28211	27.92950188
646.90879	28.24608115
661.74347	28.45962538
676.08978	28.76269302
690.96421	29.08493619
705.44638	29.54122709
720.31751	29.99746938
734.81376	30.33392674
749.66983	30.49891144
783.64668	31.08525369
794.27688	31.27049357
808.69208	31.46672853
822.99946	31.86715347
838.17387	32.23106888
852.40321	32.67172751
867.44937	32.95297878
881.8461	33.12060095
896.42282	33.29932154
911.03714	33.57112594
925.92015	33.73374284
940.01693	34.10828338
955.15945	34.531178
970.06703	34.9025127
984.94476	35.01980985
1018.77	35.44417255

Appendix B: N_2 Adsorption Isotherms at 77 K

Table B1: Virgin Carbon's (BA-100-P) BET Adsorption & Desorption data.

Adsorption		Desorption	
P/Po	V, cm^3_{STP}/g	P/Po	V, cm^3_{STP}/g
0.000254	0.0042194	0.993184	5.40005401
0.000351	0.00846479	0.975043	3.38694657
0.00045	0.01102453	0.941733	2.42677003
0.000549	0.01312346	0.906125	1.98849825
0.000648	0.01518435	0.880398	1.77607409
0.000775	0.01773369	0.855377	1.63529599
0.000888	0.01984448	0.830253	1.54493277
0.000989	0.02075926	0.80532	1.47523784
0.001078	0.02167541	0.780187	1.4164563
0.001158	0.02175262	0.754767	1.3522985
0.001228	0.02167041	0.73028	1.26614302
0.001291	0.02084928	0.705081	1.22342488
0.001347	0.02022253	0.680111	1.18268322
0.001396	0.0189306	0.655155	1.14529424
0.001523	0.02027677	0.630028	1.10493179
0.001643	0.01774318	0.605077	1.06662831
0.001746	0.01818378	0.580081	1.01024532
0.001841	0.01742924	0.554954	0.97138295
0.001925	0.01673128	0.530024	0.9399546
0.002	0.0158177	0.504504	0.90747299
0.002066	0.0150519	0.479616	0.86614869
0.002126	0.01401876	0.455009	0.81638512
0.002179	0.01311152	0.429465	0.78023512
0.002227	0.01199233	0.404569	0.74092277
0.002328	0.01152594	0.379584	0.69497574
0.002428	0.01137229	0.354529	0.66604335
0.002529	0.01072647	0.329372	0.61984404
0.00263	0.01055654	0.304543	0.56629337
0.00273	0.01050268	0.279463	0.53879802
0.002831	0.01000807	0.254497	0.47478204
0.002931	0.01005982	0.229473	0.40228827
0.003032	0.00953869	0.204293	0.47708036
0.003133	0.00968313	0.179494	0.39743739
0.003232	0.0098762	0.128882	0.14187022
0.003333	0.00959595		
0.003434	0.00960489		
0.003534	0.00972301		
0.003634	0.00942403		
0.003734	0.00951435		

0.003835	0.00962207
0.003936	0.00945016
0.004036	0.00967395
0.004136	0.01007416
0.004236	0.00984646
0.004336	0.01004685
0.004437	0.01002423
0.004536	0.01050973
0.004636	0.01022916
0.004736	0.01037727
0.004836	0.01097394
0.004937	0.01081099
0.005037	0.01104659
0.005136	0.01140899
0.005236	0.01189409
0.005335	0.0116237
0.005435	0.01229804
0.005535	0.01256052
0.005635	0.01267777
0.005734	0.01311018
0.005833	0.01330997
0.005932	0.0137612
0.006031	0.01438904
0.00613	0.01458719
0.006231	0.01432829
0.006329	0.01489109
0.006428	0.01539266
0.006527	0.01604173
0.006626	0.01631045
0.008013	0.006468
0.008405	0.00680108
0.00917	0.00944217
0.009562	0.0026572
0.010305	0.02782165
0.01419	0.05902393
0.017642	0.08020433
0.023295	0.12848505
0.029231	0.15724816
0.034949	0.17101702
0.040497	0.20563809
0.052329	0.27529961
0.063884	0.32061566
0.075335	0.36410509
0.092772	0.45362092

0.110173	0.51090957
0.139154	0.64549412
0.160831	0.70389014
0.191115	0.79461277
0.2211	0.87905144
0.250763	0.89346314
0.280799	0.95310963
0.321055	1.01112042
0.345459	1.06344594
0.370643	1.11263034
0.395596	1.11183925
0.420514	1.13436895
0.445588	1.15612869
0.470572	1.18757778
0.495553	1.21424403
0.520577	1.22583475
0.545575	1.23172169
0.570631	1.2332246
0.595524	1.26705455
0.620563	1.30504391
0.645655	1.30930721
0.670569	1.32645349
0.69553	1.34508771
0.720631	1.3889097
0.7457	1.41709072
0.770605	1.4659045
0.795758	1.48312268
0.820027	1.54102504
0.845057	1.57857151
0.869903	1.67958111
0.894934	1.82825497
0.919966	1.99738661
0.939739	2.2185525
0.959676	2.5619522
0.979376	3.33218298
0.99376	10.5942731
0.994408	17.7447361
0.995131	29.0585731
0.99617	46.5814032
0.997154	73.5342668

Table B2: Chemically Activated Carbon's (ChAB) BET Adsorption & Desorption data.

Adsorption		Desorption	
P/Po	V, cm^3_{STP}/g	P/Po	V, cm^3_{STP}/g
1.16E-07	5.05573923	0.998942	249.3154328
1.3E-07	10.1117346	0.986432	234.4965153
1.67E-07	15.1679224	0.968793	229.7134836
2.53E-07	20.2207481	0.942543	226.4128962
3.04E-07	25.2767012	0.906807	223.6653726
4.59E-07	32.3483175	0.881335	222.2004949
6.4E-07	39.4201655	0.856103	221.0915456
1E-06	46.4910154	0.830989	220.2285564
1.57E-06	53.5596153	0.805973	219.3727169
2.84E-06	60.6228249	0.780733	218.7053853
4.35E-06	67.6805498	0.755426	217.9491812
9.22E-06	77.7514023	0.730319	217.3338525
1.94E-05	87.790001	0.705108	216.8831765
4.02E-05	97.7625912	0.680445	216.0967586
8.29E-05	107.578693	0.655376	215.5886792
0.000174	117.238265	0.630085	215.3524649
0.000367	126.530967	0.60512	214.5420593
0.000775	135.20526	0.580297	213.9293741
0.00179	144.332849	0.555521	213.2443241
0.003853	152.495876	0.530296	212.680509
0.007194	159.431408	0.505048	212.1693234
0.011759	165.091563	0.480542	210.4046354
0.013196	166.488087	0.474725	210.0725333
0.015041	168.097301	0.429964	208.0370588
0.019488	171.693764	0.404988	207.3988145
0.025537	175.255823	0.379891	206.7544819
0.02995	177.03299	0.354835	206.1211052
0.03464	179.067994	0.329778	205.5161934
0.040552	181.157619	0.304795	204.7814877
0.045086	182.580736	0.280109	203.877805
0.050031	184.086585	0.2549	203.0549857
0.055253	185.24648	0.229715	202.1380871
0.060249	186.37546	0.204799	201.1757041
0.065171	187.481676	0.179973	199.939293
0.070392	188.331429	0.130591	196.5407665
0.075494	189.203377		
0.080308	190.112394		
0.085541	190.850774		
0.090677	191.486551		
0.095547	192.171659		
0.100284	192.811974		

0.120154	194.767467
0.14066	196.48952
0.151085	197.132637
0.160426	197.989118
0.170743	198.356903
0.180681	198.942417
0.200253	200.215699
0.210479	200.636659
0.220442	201.1257
0.250632	202.133374
0.280514	203.342533
0.320994	204.350692
0.345658	204.926601
0.370115	205.770643
0.395514	206.249349
0.420471	206.964979
0.445581	207.397157
0.470325	208.142828
0.495606	208.535942
0.520666	208.912633
0.545399	209.696221
0.570632	210.194813
0.595691	210.687845
0.620543	211.329814
0.645775	211.746818
0.670809	212.299705
0.695532	213.141075
0.72083	213.74349
0.745592	214.644969
0.770993	215.071255
0.795742	215.821786
0.821039	216.449893
0.84569	217.501551
0.870686	218.674411
0.895828	219.719229
0.919322	221.096176
0.938997	222.753116
0.940309	223.040354
0.950681	223.688938
0.977375	228.350592
0.981753	229.663464
0.98553	231.011341
0.986285	231.479756
0.988936	232.424073

0.998942	249.315433

Table B3: Physically Activated Carbon's (AC-Opt) BET Adsorption & Desorption data.

Adsorption		Desorption	
P/Po	V, cm^3_{STP}/g	P/Po	V, cm^3_{STP}/g
1.55E-07	5.0637921	0.997981	108.8658
3.54E-07	10.1259532	0.978802	103.8316
6.25E-07	15.1879745	0.958565	102.2771
1.07E-06	20.2452105	0.930628	101.0279
1.85E-06	25.2979662	0.905741	99.98146
3.82E-06	30.3400978	0.880222	99.24188
1.04E-05	35.3725503	0.855266	98.44295
3.27E-05	40.3518863	0.830169	97.81758
0.000106	45.1412168	0.80526	97.10793
0.000333	49.5593703	0.780011	96.65514
0.001294	54.0590111	0.755129	96.06801
0.0036	57.6223479	0.730067	95.48441
0.007798	60.1661754	0.704918	94.97492
0.012512	61.7779596	0.679876	94.44004
0.016893	62.8457561	0.654976	93.90708
0.019897	63.5707513	0.629907	93.35426
0.025518	64.4296744	0.604621	92.97805
0.034131	65.6430104	0.579949	92.34186
0.040264	66.2777849	0.554603	91.8627
0.051484	67.4353131	0.52994	91.10241
0.055085	67.9528643	0.504932	90.41174
0.060479	68.347208	0.480268	89.39189
0.065348	68.7369836	0.455775	87.67821
0.070221	69.0967225	0.430368	86.09647
0.075088	69.4824576	0.405513	84.94904
0.080113	69.9037684	0.380632	83.82616
0.085097	70.3212191	0.354922	82.9575
0.090332	70.6961097	0.329873	81.95399
0.095373	71.0318611	0.304893	81.03781
0.100208	71.3638639	0.280044	80.01013
0.138606	73.3267814	0.255008	78.98882
0.160241	74.1343994	0.229912	78.14807
0.190334	75.543467	0.205021	77.11243
0.22019	76.9814026	0.180076	75.94797
0.250245	78.1912831	0.129621	73.85507
0.280208	79.4218081		
0.3204	80.982111		
0.34499	82.0039004		

0.369878	82.9594998
0.394949	83.8104695
0.419621	84.840674
0.444928	85.5718808
0.469591	86.548513
0.4949	87.2122222
0.519626	88.1100965
0.54461	88.9220972
0.569655	89.6295316
0.594892	90.4203728
0.619846	91.1947885
0.644836	91.9475782
0.669658	92.7222749
0.694791	93.2821625
0.719453	94.0063025
0.744553	94.5808172
0.769298	95.2879459
0.79415	95.9397106
0.819311	96.422937
0.843904	97.0630058
0.868728	97.8544256
0.893667	98.5963318
0.918435	99.400163
0.937982	100.196514
0.957649	101.143538
0.976931	102.842023
0.978775	102.963524
0.997981	108.865792

Table B4: Chemically Modified Carbon's (AC-Mod) BET Adsorption & Desorption data.

Adsorption		Desorption	
P/Po	V, cm^3_{STP}/g	P/Po	V, cm^3_{STP}/g
2.37E-07	2.026857419	0.978983	81.2826
2.81E-07	4.054574361	0.95858	79.66889
3.7E-07	6.080389541	0.931056	78.55889
5.13E-07	8.104891665	0.905857	77.96637
1.03E-06	10.12504006	0.880845	77.43646
1.96E-06	12.14077279	0.855778	77.04157
3.14E-06	14.14850697	0.830836	76.58882
5.25E-06	16.139653	0.805737	76.41462
8.79E-06	18.10799472	0.780674	76.12845
1.37E-05	20.04588993	0.75522	75.84766
2.27E-05	21.93240692	0.730107	75.60801
3.66E-05	23.74143018	0.705239	75.40726
5.73E-05	25.48290542	0.680299	75.12508
9.03E-05	27.21548765	0.655269	74.90616
0.000148	29.00316289	0.630165	74.71012
0.000303	30.90389702	0.60516	74.69475
0.000547	32.6977877	0.580277	74.41064
0.000892	34.35810791	0.55476	74.23796
0.001337	35.87284509	0.530215	74.13928
0.001871	37.254217	0.505104	73.99538
0.002494	38.53286533	0.480601	73.048
0.003167	39.6998084	0.45508	71.77332
0.003889	40.78268553	0.430108	70.86281
0.004654	41.793469	0.404771	70.49443
0.005457	42.74	0.379848	69.89481
0.006347	43.66598797	0.354597	69.71328
0.007567	44.19043461	0.329732	69.21855
0.008308	44.39198628	0.304707	68.81312
0.009204	44.87100106	0.279617	68.4092
0.010103	45.12400703	0.254852	67.85
0.013572	45.88374218	0.229667	67.03281
0.015067	46.06699174	0.204685	66.6958
0.022568	47.37469648	0.179593	66.24219
0.025129	47.6516507	0.129422	64.64977
0.034127	48.72361213		
0.034909	49.05559886		
0.04042	49.44612177		
0.051673	50.28055779		
0.054982	50.78784117		
0.060061	51.13984785		
0.065062	51.69201726		

0.06992	52.21054629
0.075054	52.6629407
0.079961	53.02203027
0.085276	53.1062145
0.08996	53.55938068
0.095074	53.97379272
0.100057	54.33742458
0.120284	55.05982846
0.140262	55.58341774
0.169907	56.5488906
0.189904	57.44152541
0.22029	58.24360153
0.250166	59.00691966
0.280209	59.85531794
0.320466	60.75536909
0.345136	61.56999659
0.370057	62.41285993
0.395118	62.97028702
0.419959	63.67745564
0.445123	64.19698328
0.469943	64.82134184
0.495089	65.36293284
0.520031	65.92202381
0.544932	66.25969498
0.569755	66.82256549
0.594897	67.27927912
0.619739	67.93293243
0.644768	68.51441153
0.669934	68.79162169
0.694817	69.33962012
0.719743	69.98558558
0.744971	70.44195971
0.7699	70.90046389
0.794932	71.30198582
0.819785	72.12289826
0.844901	72.58315577
0.869809	73.2635258
0.894748	74.03578432
0.919828	74.81226318
0.939616	75.71874003
0.959571	76.7304956
0.979159	78.61627892
0.980924	78.7826052
0.985229	79.96639354

0.986233	80.15793474
0.987845	80.67081923
0.990095	81.40622391
0.99071	81.52409074
0.991894	81.98420462
0.993191	82.6583828
0.994095	83.26781089
0.995287	83.89147696
0.996061	84.62680127
0.998119	86.19866649

Table B5: Virgin Carbon Pellet's (VCP) BET Adsorption & Desorption data.

Adsorption		Desorption	
P/Po	V, cm^3_{STP}/g	P/Po	V, cm^3_{STP}/g
0.001909	0.009350824	0.998875	0.39116594
0.0041	0.011723232	0.983392	0.179842774
0.006318	0.013508487	0.963164	0.157578712
0.00895	0.008784381	0.94075	0.146965592
0.010734	0.011451839	0.905193	0.133232738
0.012382	0.012829645	0.880583	0.122242391
0.017627	0.017242181	0.855349	0.121776104
0.023656	0.017777201	0.830632	0.115553175
0.029331	0.019206075	0.805377	0.115819714
0.03505	0.020384646	0.780505	0.111988212
0.046722	0.02474844	0.755564	0.106791196
0.058251	0.02779589	0.730501	0.104250042
0.06957	0.032484762	0.705526	0.102222359
0.081404	0.03246946	0.680385	0.101154833
0.098654	0.034486552	0.655063	0.097161958
0.116172	0.036423842	0.629406	0.095233035
0.139356	0.03834535	0.604248	0.097026055
0.161817	0.041041108	0.578904	0.095860321
0.192002	0.048412973	0.554383	0.09065944
0.222131	0.048375018	0.52937	0.090345902
0.251941	0.053698137	0.503775	0.091213912
0.282218	0.053397694	0.479086	0.080491278
0.32196	0.057021738	0.454258	0.081717962
0.346471	0.059561638	0.428903	0.076181943
0.371594	0.061234146	0.404002	0.069911156
0.396484	0.064822195	0.379316	0.068899941
0.42131	0.066792341	0.354075	0.068844346
0.446346	0.06963395	0.328897	0.065512988
0.471285	0.070593921	0.304078	0.060156962
0.496174	0.07354703	0.278934	0.062479496
0.521218	0.074765257	0.253776	0.062449643
0.546122	0.076842673	0.229035	0.057966015
0.57102	0.079092621	0.203974	0.055208604
0.596042	0.080554891	0.178824	0.055067599
0.62081	0.084158256	0.128079	0.045136608
0.645735	0.088986776		
0.670807	0.089486486		
0.695689	0.092590959		
0.720662	0.09294726		
0.745658	0.094932204		
0.770205	0.104259886		

0.795572	0.105422399
0.820276	0.109376811
0.845248	0.113133752
0.87121	0.112814207
0.895922	0.120131268
0.920784	0.129650399
0.951148	0.141085516
0.980846	0.162832294
0.998875	0.39116594

Table B6: Pelletised-then-Activated (P-A) sample's BET Adsorption & Desorption data.

Adsorption		Desorption	
P/Po	V, cm^3_{STP}/g	P/Po	V, cm^3_{STP}/g
3.42E-07	2.02028118	0.999436	137.28729
2.75E-07	4.040868986	0.986768	126.7765054
3E-07	6.061720643	0.966454	125.4885095
2.73E-07	8.081715651	0.941036	124.4022622
2.72E-07	10.10180363	0.90485	123.4655512
2.89E-07	14.14762407	0.880442	122.9384877
3.45E-07	18.19347249	0.85556	122.322411
4.46E-07	22.23878812	0.830167	121.9575427
6.23E-07	26.28396652	0.80545	121.422238
9.14E-07	30.32840136	0.780449	120.9107544
1.67E-06	34.3711604	0.755136	120.5574764
2.75E-06	38.41169033	0.730271	120.079664
4.54E-06	42.4497826	0.705214	119.6810675
8E-06	46.48103339	0.680225	119.245986
1.44E-05	50.501932	0.65531	118.7208105
2.56E-05	54.50230877	0.630138	118.1931358
4.1E-05	58.47278011	0.604979	117.7953194
7.57E-05	62.38751574	0.580198	117.2744865
0.000157	66.20660813	0.555142	116.7948982
0.000325	69.86765223	0.5303	116.2354586
0.000668	73.31147911	0.505288	115.6741894
0.001563	76.87556135	0.480908	114.4217741
0.003213	79.993308	0.475506	113.941971
0.005736	82.59089243	0.450866	112.2590554
0.009135	84.15144321	0.405248	110.1840197
0.013379	85.71910063	0.380405	109.0967838
0.015228	86.11164762	0.35499	108.3116379
0.019538	87.27162676	0.330072	107.483834
0.025823	88.53677605	0.305238	106.4961676
0.030279	89.14138005	0.280052	105.5715132
0.03494	89.91557047	0.255176	104.6408382
0.040696	90.62364054	0.230319	103.6219245
0.045001	91.28372977	0.205273	102.7025234
0.050839	91.81200927	0.180289	101.6213153
0.055625	92.29796113	0.130319	99.28687929
0.060377	92.85194455		
0.065595	93.26284093		
0.070666	93.62053287		
0.075387	94.15468726		
0.080726	94.52499833		
0.08558	95.02423225		

0.090725	95.37493006
0.095683	95.72862805
0.100244	96.15471901
0.120587	97.2031011
0.140478	98.25483799
0.150235	98.89381478
0.160744	99.30632889
0.170785	99.71612162
0.200248	101.1735413
0.210439	101.6093713
0.220396	102.192535
0.230708	102.6403377
0.24067	103.0838721
0.270584	104.1980899
0.300585	105.4374991
0.345953	106.9512608
0.370609	107.9037851
0.395758	108.7217404
0.420602	109.604935
0.445541	110.3708521
0.470373	111.1523734
0.495507	111.9555958
0.520555	112.6923805
0.545591	113.3782427
0.570422	114.0955586
0.595427	114.826147
0.620588	115.456229
0.64547	116.1756964
0.67067	116.7237343
0.695452	117.416006
0.720659	117.9702651
0.745517	118.6359747
0.770538	119.2031953
0.795721	119.693007
0.820762	120.2231575
0.845497	120.9595098
0.870758	121.4247314
0.895536	122.141811
0.920595	122.7422064
0.950581	123.7297627
0.979195	125.4310358
0.980517	125.5234437
0.985178	126.033895
0.986329	126.2646989

0.988498	126.4827204
0.999436	137.28729

Table B7: Activated-then-Pelletised (A-P) sample's BET Adsorption & Desorption data.

Adsorption		Desorption	
P/Po	V, cm^3_{STP}/g	P/Po	V, cm^3_{STP}/g
4.95E-07	4.04325575	0.997853	48.11747279
1.55E-06	8.09683466	0.976763	46.88742851
6.95E-06	12.1570224	0.955045	46.57982993
3.25E-05	16.2779729	0.929827	46.29535779
0.000341	20.486775	0.904844	45.98171393
0.001887	24.1524324	0.879477	45.84561442
0.005144	26.870162	0.854419	45.74252886
0.009449	28.9370898	0.829482	45.58201794
0.01399	30.4879381	0.804332	45.65945905
0.016335	31.4553044	0.778877	45.56957774
0.021771	32.147777	0.754382	45.49226957
0.028596	32.6414395	0.729278	45.43618947
0.034312	33.2290262	0.704138	45.36818805
0.035242	33.3594755	0.679302	45.23628547
0.040765	33.6533088	0.654037	45.27659781
0.051699	34.1986205	0.629254	45.17914925
0.055366	34.3828035	0.604088	45.08739513
0.06034	34.6116489	0.579063	44.96862803
0.065226	34.7972291	0.554138	44.88958775
0.070353	34.9834842	0.529005	44.80142793
0.075159	35.1565726	0.503511	44.66720088
0.080186	35.3067831	0.479253	44.43330297
0.085212	35.4632267	0.454056	44.04316965
0.103832	35.8802004	0.429571	43.50187352
0.138689	36.503588	0.404181	43.09735923
0.161018	36.8855065	0.379001	42.85998201
0.191161	37.3652771	0.353976	42.67136213
0.221223	37.7764999	0.328927	42.47875211
0.25121	38.1820793	0.304045	42.25668379
0.281101	38.5690032	0.278995	42.01882893
0.321451	39.0247125	0.253983	41.7942516
0.345921	39.360467	0.229077	41.53226601
0.370966	39.6796059	0.204074	41.26746092
0.395984	39.9659067	0.179065	40.97598613
0.420989	40.2710001	0.128495	40.31622691
0.445852	40.5512109		
0.470872	40.8175377		
0.495968	41.0898901		
0.520734	41.35187		
0.54572	41.6115839		
0.570696	41.8706911		

0.595688	42.1145096
0.620544	42.3408817
0.645661	42.5848095
0.670507	42.8097568
0.695539	43.0426089
0.720536	43.2362697
0.745374	43.4749192
0.770316	43.6893739
0.795395	43.915005
0.820235	44.1354651
0.845321	44.3494732
0.870225	44.6060778
0.895067	44.8918103
0.919978	45.1751029
0.950033	45.5859675
0.979503	46.3751989
0.997853	48.1174728

Appendix C: Pore Size Distribution data

Table C.1: Virgin Carbon's (BA-100-P) Pore Size Distribution data.

Average Pore Diameter, nm	Pore Volume, $cm^3/g \cdot nm$
92.74777588	1.19306E-05
40.71824953	2.62454E-05
24.56259126	4.06875E-05
18.19679855	5.63835E-05
14.7237113	5.46388E-05
12.33580718	4.01837E-05
10.58403924	3.8206E-05
9.237182911	3.96525E-05
8.159836735	6.78349E-05
7.297735648	0.000153375
6.580846352	5.11575E-05
5.97027784	6.23976E-05
5.448916574	6.57868E-05
4.99456408	9.56868E-05
4.596124021	0.000105091
4.243760991	0.00023644
3.927694793	0.000142916
3.643658809	0.000107366
3.383782362	0.00012573
3.14754368	0.000232207
2.934406051	0.00034471
2.734509105	0.00020331
2.548582037	0.000266936
2.376856245	0.000363941
2.215355482	0.000152912
2.062695864	0.000398186
1.918954235	0.000523384
1.782183139	0.00012624
92.74777588	1.19306E-05
40.71824953	2.62454E-05
24.56259126	4.06875E-05
18.19679855	5.63835E-05
14.7237113	5.46388E-05
12.33580718	4.01837E-05
10.58403924	3.8206E-05
9.237182911	3.96525E-05
8.159836735	6.78349E-05
7.297735648	0.000153375
6.580846352	5.11575E-05
5.97027784	6.23976E-05

5.448916574	6.57868E-05
4.99456408	9.56868E-05
4.596124021	0.000105091
4.243760991	0.00023644
3.927694793	0.000142916
3.643658809	0.000107366
3.383782362	0.00012573
3.14754368	0.000232207
2.934406051	0.00034471
2.734509105	0.00020331
2.548582037	0.000266936
2.376856245	0.000363941
2.215355482	0.000152912
2.062695864	0.000398186
1.918954235	0.000523384
1.782183139	0.00012624

Table C.2: Chemically Activated Carbon's (ChAB) Pore Size Distribution data.

Average Pore Diameter, nm	Pore Volume, $cm^3/g \cdot nm$
76.61668395	0.000101628
41.72516471	0.000202197
25.66162365	0.000378467
19.23104708	0.000592871
15.7065516	0.000705033
13.2866337	0.000787388
11.5175019	0.001092824
10.15684859	0.001082458
9.074679148	0.001623854
8.198949362	0.001620331
7.473187929	0.001355158
6.866228421	0.003320548
6.345678346	0.002289164
5.888262424	0.000871009
5.488351532	0.005611308
5.137096385	0.004649888
4.824078527	0.006074091
4.539528832	0.005269972
4.279416801	0.005212416
4.045808651	0.025685558
3.917473635	0.021004439
3.694243406	0.017796458
3.443317257	0.009386507
3.270728552	0.010287941
3.108765085	0.010864853
2.956324334	0.010847836
2.812244406	0.015667512
2.676196024	0.022642377
2.54516222	0.02002645
2.417947668	0.02445807
2.295493694	0.027359924
2.176718063	0.040276548
1.988028942	0.062979608
76.61668395	0.000101628
41.72516471	0.000202197
25.66162365	0.000378467
19.23104708	0.000592871
15.7065516	0.000705033
13.2866337	0.000787388
11.5175019	0.001092824
10.15684859	0.001082458
9.074679148	0.001623854

8.198949362	0.001620331
7.473187929	0.001355158
6.866228421	0.003320548
6.345678346	0.002289164
5.888262424	0.000871009
5.488351532	0.005611308
5.137096385	0.004649888
4.824078527	0.006074091
4.539528832	0.005269972
4.279416801	0.005212416
4.045808651	0.025685558
3.917473635	0.021004439
3.694243406	0.017796458
3.443317257	0.009386507
3.270728552	0.010287941
3.108765085	0.010864853
2.956324334	0.010847836
2.812244406	0.015667512
2.676196024	0.022642377
2.54516222	0.02002645
2.417947668	0.02445807
2.295493694	0.027359924
2.176718063	0.040276548
1.988028942	0.062979608

Table C.3: Physically Activated Carbon's (AC-Opt) Pore Size Distribution data.

Average Pore Diameter, nm	Pore Volume, $cm^3/g \cdot nm$
57.6863409	6.07589E-05
34.35056922	0.000117675
24.48074308	0.000258362
19.04616926	0.000309374
15.59988695	0.000544422
13.21966312	0.000602963
11.47127166	0.00096341
10.12263071	0.000758576
9.056321939	0.00133733
8.190417079	0.001647987
7.467470199	0.001724418
6.857205636	0.00221372
6.336457216	0.002635897
5.883566524	0.003200102
5.483036579	0.002297786
5.131561645	0.005151568
4.81617616	0.004038036
4.532944504	0.008150789
4.277212385	0.008001609
4.043986315	0.014153356
3.831814928	0.027860717
3.632448736	0.026730257
3.446671677	0.020480948
3.275025627	0.02154868
3.111148176	0.015834319
2.956865018	0.021460163
2.812789357	0.020158016
2.67623672	0.025226955
2.545324294	0.025849363
2.418731483	0.019482727
2.296510716	0.028453136
2.177444805	0.034349706
1.985130073	0.027092334
57.6863409	6.07589E-05
34.35056922	0.000117675
24.48074308	0.000258362
19.04616926	0.000309374
15.59988695	0.000544422
13.21966312	0.000602963
11.47127166	0.00096341
10.12263071	0.000758576
9.056321939	0.00133733

8.190417079	0.001647987
7.467470199	0.001724418
6.857205636	0.00221372
6.336457216	0.002635897
5.883566524	0.003200102
5.483036579	0.002297786
5.131561645	0.005151568
4.81617616	0.004038036
4.532944504	0.008150789
4.277212385	0.008001609
4.043986315	0.014153356
3.831814928	0.027860717
3.632448736	0.026730257
3.446671677	0.020480948
3.275025627	0.02154868
3.111148176	0.015834319
2.956865018	0.021460163
2.812789357	0.020158016
2.67623672	0.025226955
2.545324294	0.025849363
2.418731483	0.019482727
2.296510716	0.028453136
2.177444805	0.034349706
1.985130073	0.027092334

Table C.4: Chemically Modified Carbon's (AC-Mod) Pore Size Distribution data.

Average Pore Diameter, nm	Pore Volume, $cm^3/g \cdot nm$
57.71203723	6.19476E-05
34.50339656	0.000104786
24.51491412	0.000139074
19.09318276	0.000222715
15.63606665	0.000254642
13.24214644	0.000436001
11.47879515	0.000195113
10.12407491	0.000482246
9.042815315	0.000599154
8.165974379	0.000637104
7.446284099	0.000642046
6.839300838	0.001161166
6.316862026	0.001016715
5.861807927	0.001041171
5.137184922	0.001106681
4.818961715	0.001357095
4.535334223	0.000716275
4.279359164	0.001401701
4.046331268	0.014204769
3.82990487	0.020448115
3.628950911	0.015848272
3.442928509	0.00551061
3.269921484	0.011622919
3.107823057	0.001511966
2.955542832	0.010740408
2.811854429	0.008521473
2.674521636	0.008900129
2.543907392	0.015267201
2.417708802	0.025626
2.295081775	0.006029591
2.175457961	0.011117707
1.983727636	0.027273665
57.71203723	6.19476E-05
34.50339656	0.000104786
24.51491412	0.000139074
19.09318276	0.000222715
15.63606665	0.000254642
13.24214644	0.000436001
11.47879515	0.000195113
10.12407491	0.000482246
9.042815315	0.000599154
8.165974379	0.000637104

7.446284099	0.000642046
6.839300838	0.001161166
6.316862026	0.001016715
5.861807927	0.001041171
5.137184922	0.001106681
4.818961715	0.001357095
4.535334223	0.000716275
4.279359164	0.001401701
4.046331268	0.014204769
3.82990487	0.020448115
3.628950911	0.015848272
3.442928509	0.00551061
3.269921484	0.011622919
3.107823057	0.001511966
2.955542832	0.010740408
2.811854429	0.008521473
2.674521636	0.008900129
2.543907392	0.015267201
2.417708802	0.025626
2.295081775	0.006029591
2.175457961	0.011117707
1.983727636	0.027273665

Table C.5: Virgin Carbon Pellet's (VCP) Pore Size Distribution data.

Average Pore Diameter, nm	Pore Volume, $cm^3/g \cdot nm$
50.13083136	1.73976E-05
33.1828698	2.35606E-05
20.85324919	4.45112E-05
16.57249545	7.26534E-05
13.67647508	9.05978E-05
11.6212594	0.000121747
10.07707684	0.00017425
8.871033957	0.000163252
7.908604346	0.000203091
7.118133324	0.00028645
6.451115852	0.000278791
5.888248224	0.000391564
5.401170418	0.000525363
4.970695383	0.000391121
4.60275924	0.000401044
4.267904637	0.000525588
3.969807073	0.000734122
3.699112459	0.00069269
3.453652924	0.000743077
3.228285723	0.000987942
3.01747736	0.000975313
2.830633502	0.001064096
2.647337018	0.000921964
2.482658813	0.001037849
2.32495597	0.001101691
2.177317109	0.000829593
2.037270028	0.001395986
1.904339998	0.001634883
1.775292249	0.001318857
1.65150542	0.001304212
50.13083136	1.73976E-05
33.1828698	2.35606E-05
20.85324919	4.45112E-05
16.57249545	7.26534E-05
13.67647508	9.05978E-05
11.6212594	0.000121747
10.07707684	0.00017425
8.871033957	0.000163252
7.908604346	0.000203091
7.118133324	0.00028645
6.451115852	0.000278791
5.888248224	0.000391564

5.401170418	0.000525363
4.970695383	0.000391121
4.60275924	0.000401044
4.267904637	0.000525588
3.969807073	0.000734122
3.699112459	0.00069269
3.453652924	0.000743077
3.228285723	0.000987942
3.01747736	0.000975313
2.830633502	0.001064096
2.647337018	0.000921964
2.482658813	0.001037849
2.32495597	0.001101691
2.177317109	0.000829593
2.037270028	0.001395986
1.904339998	0.001634883
1.775292249	0.001318857
1.65150542	0.001304212

Table C.6: Pelletised-then-Activated (P-A) sample's Pore Size Distribution data.

Average Pore Diameter, nm	Pore Volume, $cm^3/g \cdot nm$
59.58545	0.002218
34.43718	0.00414
21.66768	0.005857
17.37233	0.006854
14.46438	0.008075
12.3583	0.008784
10.8242	0.009911
9.614366	0.011013
8.633277	0.011759
7.842432	0.012845
7.174955	0.01375
6.60868	0.014779
6.121573	0.016083
5.692203	0.017419
5.314153	0.018399
4.9828	0.01978
4.682204	0.021055
4.412899	0.022615
4.166216	0.024207
3.945978	0.028225
3.899581	0.02984
3.697924	0.03544
3.361857	0.042106
3.195841	0.045613
3.036335	0.047905
2.888757	0.050422
2.749166	0.053665
2.614133	0.056623
2.48622	0.059633
2.362846	0.063073
2.242032	0.065963
2.123965	0.069675
1.889982	0.077815
59.58545	0.002218
34.43718	0.00414
21.66768	0.005857
17.37233	0.006854
14.46438	0.008075
12.3583	0.008784
10.8242	0.009911
9.614366	0.011013
8.633277	0.011759

7.842432	0.012845
7.174955	0.01375
6.60868	0.014779
6.121573	0.016083
5.692203	0.017419
5.314153	0.018399
4.9828	0.01978
4.682204	0.021055
4.412899	0.022615
4.166216	0.024207
3.945978	0.028225
3.899581	0.02984
3.697924	0.03544
3.361857	0.042106
3.195841	0.045613
3.036335	0.047905
2.888757	0.050422
2.749166	0.053665
2.614133	0.056623
2.48622	0.059633
2.362846	0.063073
2.242032	0.065963
2.123965	0.069675
1.889982	0.077815

Table C.7: Activated-then-Pelletised (A-P) sample's Pore Size Distribution data.

Average Pore Diameter, nm	Pore Volume, $cm^3/g \cdot nm$
53.14251	1.33561E-05
33.50926	3.26543E-05
24.15641	7.90849E-05
18.82544	5.61576E-05
15.4221	6.6218E-05
13.07154	0.000158327
9.021528	4.62912E-05
8.166225	0.000148804
7.446844	0.000230406
6.842312	0.000590181
6.053774	0.00010985
5.474294	0.000640563
5.121904	0.000986345
4.808375	0.000700926
4.525157	0.000892598
4.265438	0.001602329
4.033226	0.003465054
3.820221	0.00632966
3.623155	0.0100997
3.438898	0.007646576
3.265053	0.004406422
3.103305	0.003507504
2.951276	0.003864053
2.807787	0.005072808
2.6711	0.005831735
2.540005	0.005615084
2.414177	0.007336099
2.292178	0.00757184
2.17279	0.008825085
1.979943	0.010312358
53.14251	1.33561E-05
33.50926	3.26543E-05
24.15641	7.90849E-05
18.82544	5.61576E-05
15.4221	6.6218E-05
13.07154	0.000158327
9.021528	4.62912E-05
8.166225	0.000148804
7.446844	0.000230406
6.842312	0.000590181
6.053774	0.00010985
5.474294	0.000640563

5.121904	0.000986345
4.808375	0.000700926
4.525157	0.000892598
4.265438	0.001602329
4.033226	0.003465054
3.820221	0.00632966
3.623155	0.0100997
3.438898	0.007646576
3.265053	0.004406422
3.103305	0.003507504
2.951276	0.003864053
2.807787	0.005072808
2.6711	0.005831735
2.540005	0.005615084
2.414177	0.007336099
2.292178	0.00757184
2.17279	0.008825085
1.979943	0.010312358